

A STUDY ON CO-FREE HYDROGEN PRODUCTION FROM
HYDROCARBONS AND CO_x ELIMINATION THROUGH PRE-COMBUSTION

by

Belkız Merve Eropak

B.S., Chemical Engineering, Boğaziçi University, 2009

M.S., Chemical Engineering, Boğaziçi University, 2011

Submitted to the Institute for Graduate Studies in
Science and Engineering in partial fulfillment of
the requirements for the degree of
Doctor of Philosophy

Graduate Program in Chemical Engineering
Boğaziçi University

2020

to my parents

ACKNOWLEDGEMENTS

First of all, I would like to express my gratitude sincerely to my thesis supervisor Prof. Ahmet Erhan Aksoylu for his guidance, encouragement and trust in me. He devoted his time to guide me and shared his knowledge and expertise in catalysis and reaction engineering. It was a privilege for me to work with Prof. Aksoylu during my Ph.D. thesis.

I would like to express my endless appreciations for Dr. Burcu Selen Çağlayan for her guidance during my Ph.D. years. Besides the efforts in XPS, Raman Spectroscopy analysis and adsorption studies, she never hesitated to spend her time and effort for me.

I am very grateful to Prof. Ramazan Yıldırım, Prof. Hüsnü Atakül, Assoc. Prof. Hasan Bedir, and Assoc. Prof. Alper Uzun for accepting to be a member of the thesis committee, sparing their valuable time for reading and commenting on my thesis.

Very special thanks to Ali Uzun for his undeniable support on any matter as well as his valuable help in experiments. I would also like to thank Aybüke Leba and Cihat Öztepe for their invaluable friendship and everlasting support.

I also would like to thank Dr. Melek Selcen Başar for being there whenever I needed her help. I feel lucky to work with her. Heartfelt thanks to Gözde Öztürk for her valuable friendship and accompanying me in intensive experiment days. Most sincere thanks are for Feyza Gökaliiler for her guidance in the beginning of my Ph.D. years. I would also like to thank 411/A and its members. It feel very lucky for belonging to 411/A laboratory. All colleagues in the Department of Chemical Engineering at Boğazici University deserve my intimate thanks for their kindness and cheerfulness.

Cordial thanks are for Bilgi Dedeoğlu for his technical assistance and friendly attitude during my Ph.D. years. Heartfelt thanks are for Melike Gürbüz, Murat Düzgünoğlu, Başak Ünen, Dilek Kirkoç and Yakup Bal for their friendship and kindness to me. I would also like to thank Bilge Gedik Uluocak for her significant effort in SEM analyses.

Finally; I would like to thank all my family for their patience, encouragement, understanding and intimate support all these years. They believed in me and loved me all the time. This thesis would not have been possible without their everlasting support.

Financial support provided by Presidency of Republic of Turkey Department of Strategy and Budget (Ministry of Development) through project 2016K121160 and TÜBİTAK through projects 215M312 and 214M170 are gratefully acknowledged.

ABSTRACT

A STUDY ON CO-FREE HYDROGEN PRODUCTION FROM HYDROCARBONS AND CO_x ELIMINATION THROUGH PRE-COMBUSTION

The goal of this research study is to design and develop active, stable and selective alkali promoted Pt-based catalysts and activated carbon-based adsorbents for CO_x elimination to be used in CO-free hydrogen production and CO₂ removal. Firstly, Pt-Re-Na/CeO₂ and Pt-Re-Na/TiO₂ catalysts were designed and prepared for WGS reaction. The effect of Na loading, support type, reaction temperature, feed type and composition (H₂O/CO ratio) on WGS performance were considered as the experimental parameters. Among the prepared catalysts, sequentially impregnated 1%Pt-1%Re-2%Na/CeO₂ exhibited the highest performance under Realistic Feed with H₂O/CO=6.7. Serial OSR-WGS tests were also conducted for two OSR feed compositions having different O/C ratio and the highest real WGS activity was achieved over sequentially impregnated 1%Pt-1%Re-1%Na/CeO₂ at 350°C as 43.0% CO conversion. The freshly reduced and spent forms of the catalyst samples were characterized by SEM, XPS, XRD and Raman spectroscopy. Combined evaluation of the Na1s and Ce3d spectra of the highly active catalysts, suggests the NaO_x species should be more influential than CeO_x species in the WGS reaction mechanisms. Surface formate and carbonate species under reaction conditions were examined in *operando* FTIR-DRIFTS-MS tests over Pt-Re-Na/CeO₂ catalysts. The combined evaluation of WGS performance and OSC results indicated that structural OSC (S-OSC) and effective OSC (E-OSC) have both significant effect on WGS performance. E-OSC values of the catalysts were found in direct accordance with their performance results. In the adsorbent design part, CO₂ and CH₄ adsorption capacities of AC-based NaOH impregnated samples were determined for various “temperature-pressure range” couples, their selective adsorption capacities were measured under CO₂-CH₄ gas mixtures through using a novel methodology developed by our group, and the adsorption on the samples was modelled. The best performing adsorbent in terms of selective CO₂ adsorption under CO₂:CH₄=1:1 and 1:9 was determined as AC6-200, which is the air oxidized AC doped with Na.

ÖZET

HİDROKARBONLARDAN CO'DAN ARINDIRILMIŞ HİDROJEN ÜRETİMİ VE ÖN YANMA YOLUYLA CO_x GİDERİMİ ÜZERİNE BİR ÇALIŞMA

Bu çalışmanın amacı, CO içermeyen hidrojen üretimi ve CO₂ giderilmesinde kullanılacak CO_x eliminasyonu için aktif, kararlı ve seçici alkali destekli Pt bazlı katalizörler ve aktif karbon bazlı adsorbanlar tasarlamak ve geliştirmektir. İlk olarak, Pt-Re-Na/CeO₂ ve Pt-Re-Na/TiO₂ katalizörleri, WGS reaksiyonu için tasarlanmış ve hazırlanmıştır. Na yüklemesi, destek tipi, reaksiyon sıcaklığı, besleme tipi ve kompozisyonun (H₂O/CO oranı) WGS performansı üzerindeki etkisi deneysel parametreler olarak kabul edilmiştir. Farklı O/C oranına sahip iki OSR besleme akışı için seri OSR-WGS testleri de yapılmıştır. Gerçekçi besleme altındaki en yüksek performansı %1Pt-%1Re-%2Na/CeO₂ katalizörü verirken; en yüksek gerçek WGS aktivitesi, 350°C'de %43.0 CO dönüşümü olarak sırayla empregne edilmiş %1Pt-%1Re-%1Na/CeO₂ üzerinde elde edilmiştir. Numunelerin yeni indirgenmiş ve kullanılmış biçimleri SEM, XPS, XRD ve Raman spektroskopisi ile karakterize edilmiştir. Yüksek aktivite gösteren katalizörlerin Na1 ve Ce3d spektrumları değerlendirildiğinde, WGS reaksiyon mekanizmalarında NaO_x gruplarının CeO_x gruplarına göre daha etkili olduğu görülmüştür. Pt-Re-Na/CeO₂ katalizörleri üzerinde bir WGS reaksiyon mekanizması önermeyi amaçlayarak yapılan FTIR-DRIFTS-MS testlerinde, reaksiyon koşulları altında yüzeyde oluşan format ve karbonat grupları incelenmiştir. WGS performansı ve OSC sonuçlarının birlikte değerlendirildiğinde, yapısal OSC (S-OSC) ve efektif OSC'nin (E-OSC) WGS performansı üzerinde önemli bir etkiye sahip olduğu görülmüştür. Katalizörlerin E-OSC değerleri aktivite sonuçları ile korelasyon göstermiştir. Adsorban tasarım bölümünde, AC bazlı NaOH emdirilmiş numunelerin çeşitli "sıcaklık-basınç aralığı" değerleri için CO₂ ve CH₄ adsorpsiyon kapasiteleri belirlenmiş, CO₂-CH₄ gaz karışımları altında seçici adsorpsiyon kapasiteleri ölçülmüştür. Grubumuz tarafından geliştirilen yeni bir metodoloji ile numuneler üzerindeki adsorpsiyon modellenmiştir. CO₂:CH₄=1:1 ve 1:9 altında seçici CO₂ adsorpsiyonu açısından en iyi performans gösteren adsorban, hava ile oksitlenmiş ve Na eklenmiş AC olan AC6-200 olarak belirlenmiştir.

TABLE OF CONTENTS

ACKNOWLEDGEMENTS	iv
ABSTRACT	vi
ÖZET	vii
LIST OF FIGURES	xi
LIST OF TABLES	xxiv
LIST OF SYMBOLS	xxvi
LIST OF ACRONYMS/ABBREVIATIONS	xxvii
1. INTRODUCTION	1
2. LITERATURE SURVEY	5
2.1. Fuel Processor-Fuel Cell Technology	5
2.2. Oxidative Steam Reforming	6
2.2.1. Pt-Ni Bimetallic OSR Catalysts.....	7
2.3. Water-Gas Shift Reaction.....	8
2.3.1. Au-Based WGS Catalysts.....	10
2.3.2. Pt-Based WGS Catalysts	12
2.4. Oxygen Storage Capacity	15
2.5. CO ₂ Removal.....	17
2.5.1. CO ₂ Adsorption	17
2.5.2. Activated Carbon (AC) Supported CO ₂ Adsorption	18
2.5.2. Selective CO ₂ Adsorption.....	23
3. EXPERIMENTAL WORK	26
3.1. Materials	26
3.1.1. Gases and Liquids.....	26
3.1.2. Chemicals	27
3.2. Experimental Systems	28
3.2.1. Catalyst and Adsorbent Preparation Systems	28
3.2.2. Catalytic Reaction System	30
3.2.3. Product Analysis Systems.....	34
3.2.4. Catalyst Characterization Systems	35

3.2.4.1. Scanning Electron Microscopy-Energy Dispersive X-Ray ...	35
3.2.4.2. X-Ray Diffraction	35
3.2.4.3. X-Ray Photoelectron Spectroscopy	35
3.2.4.4. Raman Spectroscopy	36
3.2.4.5. CO Chemisorption	36
3.2.4.6. Total Surface Area-Total Pore Volume	36
3.2.5. Fourier Transform Infrared Spectroscopy - Mass Spectroscopy (FTIR-DRIFTS-MS) System	37
3.2.6. Gravimetric Gas Sorption Analysis – Mass Spectrometry (IGA-MS) System	40
3.3. Catalyst/Adsorbent Preparation and Pretreatment	43
3.3.1. Oxidative Steam Reforming Catalyst (Pt-Ni/ δ -Al ₂ O ₃).....	43
3.3.2. Water Gas Shift Catalysts	45
3.3.2.1. Preparation of CeO ₂ Support.....	45
3.3.2.2. Preparation of Pt-Re-Na/CeO ₂ and Pt-Re-Na/TiO ₂	45
3.3.3. Activated Carbon Based Adsorbents	47
3.4. Single WGS and serial OSR-WGS Reaction Tests	48
3.4.1. WGS Performance Tests.....	48
3.4.2. Serial OSR-WGS Performance Tests	52
3.5. In-situ and operando FTIR-DRIFTS-MS Studies	54
3.6. Oxygen Storage Capacity (OSC) Analysis	55
3.7. Adsorption Tests	58
4. RESULTS AND DISCUSSION	60
4.1. WGS Performance of Pt-Re-Na/CeO ₂ and Pt-Re-Na/TiO ₂ Catalysts for Realistic Synthetic Feeds	60
4.1.1. WGS Performance Tests Conducted under Ideal Feeds.....	62
4.1.2. WGS Performance Tests Conducted under Realistic Feeds.....	70
4.2. WGS Performance of Pt-Re-Na/CeO ₂ and Pt-Re-Na/TiO ₂ Catalysts under Real Feed in Serial OSR-WGS System	79
4.3. Characterization of Pt-Re-Na/CeO ₂ and Pt-Re-Na/TiO ₂ Catalysts	83
4.3.1. XRD Analysis	83
4.3.2. SEM Analysis	87
4.3.3. XPS Analysis	91

4.3.4. Raman Spectroscopy Analysis	101
4.3.5. CO Chemisorption As a Measure of Dispersion	105
4.4. <i>In situ</i> Characterization of Pt-Re-Na/CeO ₂ System and <i>Operando</i> Analysis of WGS Mechanism on its Sites by FTIR-DRIFTS-MS	106
4.5. Analysis of “WGS Performance-Oxygen Storage Capacity” Relation for Pt- Re-Na/CeO ₂ and Pt-Re-Na/TiO ₂ Catalysts.....	117
4.5.1. Oxygen Storage Capacity Tests.....	119
4.6. Combined Evaluation of Performance, Characterization and FTIR-DRIFTS Tests Results Conducted on Tri-metallic WGS Catalysts	124
4.7. Selective CO ₂ Adsorption over Activated Carbon Based Adsorbents	127
4.7.1. Determination of Selective Adsorption Capacities of an Adsorbent under Flow of Multicomponent gas Mixtures	128
4.7.2. Pure Carbon Dioxide and Methane Adsorption Studies	131
4.7.3. Selective Adsorption Tests	139
4.7.4. High Pressure Adsorption Tests	144
4.7.5. Adsorption Modelling Studies on AC6 and AC7 Adsorbents.....	148
4.7.6. SEM Analysis of Adsorbents.....	156
4.7.7. BET Surface Area and Total Pore Volume Analysis	158
5. CONCLUSION	160
5.1. Conclusions	160
5.2. Recommendations	166
REFERENCES	168
APPENDIX A: TIME-ON-STREAM ACTIVITY DATA OF INDIVIDUAL WGS TESTS.....	190
APPENDIX B: TIME-ON-STREAM ACTIVITY DATA OF SERIAL OSR-WGS TESTS.....	198

LIST OF FIGURES

Figure 2.1.	Surface groups.....	19
Figure 2.2.	Adsorption capacities of CO ₂ , CH ₄ , N ₂	24
Figure 3.1.	Schematic diagram of the impregnation system.	29
Figure 3.2.	Schematic diagram of the deposition precipitation system.	29
Figure 3.3.	Schematic diagram of the system used for (a) HCl, (b) HNO ₃ and (c) DI water treatments of activated carbons.	30
Figure 3.4.	Schematic diagram of OSR-WGS reaction system.....	33
Figure 3.5.	Schematic representation of FTIR-DRIFTS-MS system	39
Figure 3.6.	Schematic diagram of the Intelligent Gravimetric Analyzer (IGA)	41
Figure 3.7.	Schematic diagram of the gravimetric gas sorption analysis system.....	42
Figure 3.8.	Pretreatment and reduction procedure for Pt-Ni/ δ -Al ₂ O ₃ catalyst.....	44
Figure 4.1.	Effect of temperature on catalytic activity for ideal feed #1 (3% CO, 15% H ₂ O, 82% Ar; H ₂ O/CO=5)	63
Figure 4.2.	Effect of temperature on catalytic activity for ideal feed #2 (3% CO, 6% H ₂ O, 91% Ar; H ₂ O/CO=2).....	63
Figure 4.3.	Effect of H ₂ O/CO feed ratio on the catalytic activity of 1%Pt-1%Re-1%Na/CeO ₂ (Re-Na coimp.).....	64

Figure 4.4.	Effect of H ₂ O/CO feed ratio on the catalytic activity of 1%Pt-1%Re-1%Na/CeO ₂	65
Figure 4.5.	Effect of H ₂ O/CO feed ratio on the catalytic activity of 1%Pt-1%Re-2%Na/CeO ₂	65
Figure 4.6.	Effect of H ₂ O/CO feed ratio on the catalytic activity of 1%Pt-1%Re-1%Na/TiO ₂	66
Figure 4.7.	Effect of Re-Na impregnation procedure on the catalytic activity of 1%Pt-1%Re-1%Na/CeO ₂ under ideal feed #1 (3% CO, 15% H ₂ O, 82% Ar; H ₂ O/CO=5).....	67
Figure 4.8.	Effect of Re-Na impregnation procedure on the catalytic activity of 1%Pt-1%Re-1%Na/CeO ₂ under ideal feed #2 (3% CO, 6% H ₂ O, 91% Ar; H ₂ O/CO=2).....	67
Figure 4.9.	Effect of Na loading on the catalytic activity for ideal feed #1 (3% CO, 15% H ₂ O, 82% Ar; H ₂ O/CO=5).....	68
Figure 4.10.	Effect of Na loading on the catalytic activity for ideal feed #2 (3% CO, 6% H ₂ O, 91% Ar; H ₂ O/CO=2).....	69
Figure 4.11.	Effect of support type on the catalytic activity for ideal feed #1 (3% CO, 15% H ₂ O, 82% Ar; H ₂ O/CO=5).....	69
Figure 4.12.	Effect of support type on the catalytic activity for ideal feed #2 (3% CO, 6% H ₂ O, 91% Ar; H ₂ O/CO=2).....	70
Figure 4.13.	Temperature dependence of (a) catalytic activity and (b) net H ₂ production for realistic feed #1 (4.9% CO, 32.7% H ₂ O, 30% H ₂ , 10.4% CO ₂ , 22% Ar; H ₂ O/CO=6.7).....	71

Figure 4.14.	Temperature dependence of (a) catalytic activity and (b) net H ₂ production for realistic feed #2 (2.1% CO, 34.1% H ₂ O, 23.7% H ₂ , 12.3% CO ₂ , 27.8% Ar; H ₂ O/CO=16.2)	72
Figure 4.15.	Effect of Re-Na impregnation procedure on the catalytic activity of 1%Pt-1%Re-1%Na/CeO ₂ under realistic feed #1 conditions (4.9% CO, 32.7% H ₂ O, 30% H ₂ , 10.4% CO ₂ , 22% Ar, H ₂ O/CO=6.7)	73
Figure 4.16.	Effect of Re-Na impregnation procedure on the catalytic activity of 1%Pt-1%Re-1%Na/CeO ₂ under realistic feed #2 conditions (2.1% CO, 34.1% H ₂ O, 23.7% H ₂ , 12.3% CO ₂ , 27.8% Ar, H ₂ O/CO=16.2)	74
Figure 4.17.	Effect of Na loading on the catalytic activity of Pt-Re-Na/CeO ₂ under realistic feed #1 conditions (4.9% CO, 32.7% H ₂ O, 30% H ₂ , 10.4% CO ₂ , 22% Ar, H ₂ O/CO=6.7).....	75
Figure 4.18.	Effect of Na loading on the catalytic activity of Pt-Re-Na/CeO ₂ under realistic feed #2 conditions (2.1% CO, 34.1% H ₂ O, 23.7% H ₂ , 12.3% CO ₂ , 27.8% Ar, H ₂ O/CO=16.2).....	75
Figure 4.19.	Effect of support type on the catalytic activity of Pt-Re-Na catalysts under realistic feed #1 (4.9% CO, 32.7% H ₂ O, 30% H ₂ , 10.4% CO ₂ , 22% Ar, H ₂ O/CO=6.7).....	76
Figure 4.20.	Effect of support type on the catalytic activity of Pt-Re-Na catalysts under realistic feed #2 (2.1% CO, 34.1% H ₂ O, 23.7% H ₂ , 12.3% CO ₂ , 27.8% Ar, H ₂ O/CO=16.2).....	76
Figure 4.21.	Catalyst activities at different feed conditions and temperatures	78
Figure 4.22.	CO conversion and net H ₂ production percentages for each catalyst at different temperatures under realistic feed #1 and 2 conditions	78

Figure 4.23.	6 h TOS OSR and WGS activities over sequentially impregnated 1%Pt-1%Re-1%Na/CeO ₂ under 14% CH ₄ , 9.3% O ₂ , 56% H ₂ O, 20.7% Ar (H ₂ O/CO=4, O/C=1.33) feed flow at 300°C, 350°C and 400°C	80
Figure 4.24.	6 h TOS OSR and WGS activities over sequentially impregnated 1%Pt-1%Re-1%Na/CeO ₂ under 14% CH ₄ , %6.7 O ₂ , %56 H ₂ O, %23.3 Ar (H ₂ O/CO=4, O/C=0.95 feed flow at 300°C, 350°C and 400°C	81
Figure 4.25.	OSR activity and real WGS performance data obtained in serial OSR-WGS tests conducted under 14% CH ₄ , 9.3% O ₂ , 56% H ₂ O, 20.7% Ar (H ₂ O/CO=4, O/C=1.33); WGS temperatures are 300°C, 350°C and 400°C; H ₂ concentrations are given on a dry basis	82
Figure 4.26.	OSR activity and real WGS performance data obtained in serial OSR-WGS tests conducted under 14% CH ₄ , 6.7% O ₂ , 56% H ₂ O, 23.3% Ar (H ₂ O/CO=4, O/C=0.95); WGS temperatures are 300°C, 350°C and 400°C; H ₂ concentrations are given on a dry basis	83
Figure 4.27.	XRD Profiles of sequentially impregnated 1%Pt-1%Re-1%Na/CeO ₂ , 1%Pt-1%Re-2%Na/CeO ₂ and 1%Pt-1%Re-3%Na/CeO ₂ catalysts	84
Figure 4.28.	XRD Profiles of sequentially impregnated 1%Pt-1%Re-1%Na/TiO ₂ catalyst	85
Figure 4.29.	SEM image of coimpregnated %1Pt-%1Re-%1Na/CeO ₂ catalyst (x100000).....	88
Figure 4.30.	SEM image of sequentially impregnated %1Pt-%1Re-%1Na/CeO ₂ catalyst (x100000).....	88

Figure 4.31.	SEM image of sequentially impregnated %1Pt-%1Re-%2Na/CeO ₂ catalyst (x100000).....	89
Figure 4.32.	SEM image of sequentially impregnated %1Pt-%1Re-%1Na/TiO ₂ catalyst (x100000).....	90
Figure 4.33.	SEM image of sequentially impregnated %1Pt-%1Re-%3Na/CeO ₂ catalyst (x100000).....	90
Figure 4.34.	SEM image of sequentially impregnated 1%Pt-1%Re-2%Na/CeO ₂ catalyst after reaction (x100000).....	91
Figure 4.35.	XP Spectra showing the Ce3d region of freshly reduced and spent (real feed #1, 350°C) catalyst samples (v: Ce ³⁺ , u: Ce ⁴⁺).....	94
Figure 4.36.	XP Spectra showing the Na1s region of freshly reduced and spent (real feed #1, 350°C) catalyst samples	96
Figure 4.37.	XP Spectra showing the O1s region of freshly reduced and spent (real feed #1, 350°C) catalyst samples	97
Figure 4.38.	XP Spectra showing the Pt4f region of freshly reduced and spent (real feed #1, 350°C) catalyst samples	99
Figure 4.39.	XP Spectra showing the Re4f region of freshly reduced and spent (real feed #1, 350°C) catalyst samples	100
Figure 4.40.	XP Spectra showing the Ti2p region of freshly reduced and spent (real feed #1, 350°C) 1%Pt-1%Re-1%Na/TiO ₂ sample	101
Figure 4.41.	Raman spectra of freshly reduced and spent forms of CeO ₂ supported catalyst samples subjected to RF #1 and RF#2 at 350°C.....	102

Figure 4.42.	The expanded Raman spectra of freshly reduced and spent 1%Pt-1%Re-2%Na/CeO ₂ supported catalyst samples subjected to RF #1 and RF#2 at 350°C	103
Figure 4.43.	Raman spectra of freshly reduced and spent 1%Pt-1%Re-1%Na/CeO ₂ catalyst samples subjected to RF #1 and RF #2 at 350°C.....	104
Figure 4.44.	The expanded Raman spectra of freshly reduced and spent 1%Pt-1%Re-1%Na/TiO ₂ supported catalyst samples subjected to RF #1 and RF #2 at 350°C	105
Figure 4.45.	Characteristic FTIR-DRIFT spectrum	107
Figure 4.46.	FTIR-DRIFT spectra obtained over CeO ₂ at 300°C under various feed flows.....	109
Figure 4.47.	MS signals of CO ₂ and H ₂ molecules in the exit stream of FTIR-DRIFTS system during 1% CO adsorption at 300°C over in-situ reduced support and catalyst samples	110
Figure 4.48.	MS signals of CO ₂ and H ₂ molecules in the exit stream of FTIR-DRIFTS system under 1.36%CO-2.72%H ₂ O feed flow at 300°C over in-situ reduced support and catalyst samples	110
Figure 4.49.	2000-2300 cm ⁻¹ region of the FTIR-DRIFT spectra obtained over CeO ₂ at 300°C under various feed flows	111
Figure 4.50.	FTIR-DRIFT spectra obtained over 1%Pt-1%Re-1%Na/CeO ₂ at 300°C under various feed flows	112
Figure 4.51.	1700-2300 cm ⁻¹ region of the FTIR-DRIFT spectra obtained over 1%Pt-1%Re-1%Na/CeO ₂ at 300°C under various feed flows	115

Figure 4.52.	FTIR-DRIFT spectra obtained over 1%Pt-1%Re-3%Na/CeO ₂ at 300°C under various feed flows	115
Figure 4.53.	Oxygen Storage Capacities of catalysts tested at 350°C under DRF #1 (H ₂ O/CO=6.7).....	120
Figure 4.54.	Oxygen Storage Capacities of catalysts tested at 350°C under DRF #2 (H ₂ O/CO=16.2).....	121
Figure 4.55.	Effective OSCs and CO conversions of the samples obtained at 350°C under DRF #1 (H ₂ O/CO=6.7).....	123
Figure 4.56.	Effective OSCs and CO conversions of the samples obtained at 350°C under DRF #2 (H ₂ O/CO=16.2).....	124
Figure 4.57.	Comparison of normalized MS partial pressures in blank and adsorption tests at RT for 500-600 mbar pressure range with 50% CO ₂ -50% CH ₄ mixture	130
Figure 4.58.	Change of IGA pressure and adsorbent weight with respect to time for the adsorption test conducted at RT for 500-600 mbar pressure range with 50% CO ₂ -50% CH ₄ mixture	130
Figure 4.59.	Mass uptake (%) of AC6-200 under pure 50 ml/min CO ₂ flow	132
Figure 4.60.	Mass uptake (%) of AC6-200 under pure 50 ml/min CH ₄ flow	133
Figure 4.61.	Mass uptake (%) comparison of AC6-200 under pure 50 ml/min CO ₂ flow and 50 ml/min CH ₄ flow (1000 mbar data).....	133
Figure 4.62.	Mass uptake (%) of AC6-250 under pure 50 ml/min CO ₂ flow	134

Figure 4.63.	Mass uptake (%) of AC6-250 under pure 50 ml/min CH ₄ flow	135
Figure 4.64.	Mass uptake (%) comparison of AC6-200 under pure 50 ml/min CO ₂ flow and 50 ml/min CH ₄ flow (1000 mbar data)	135
Figure 4.65.	Mass uptake (%) of AC6-300 under pure 50 ml/min CO ₂ flow	136
Figure 4.66.	Mass uptake (%) of AC6-300 under pure 50 ml/min CH ₄ flow	137
Figure 4.67.	Mass uptake (%) comparison of AC6-300 under pure 50 ml/min CO ₂ flow and 50 ml/min CH ₄ flow (1000 mbar data).....	137
Figure 4.68.	Adsorbed amounts of CO ₂ and CH ₄ on AC6-200, AC6-250 and AC6-300 under pure 50 ml/min CO ₂ flow and 50 ml/min CH ₄ flow at RT (1000 mbar data)	138
Figure 4.69.	Adsorbed amounts of CO ₂ and CH ₄ on AC7-125, AC7-200 and AC7-250 under pure 50 ml/min CO ₂ flow and 50 ml/min CH ₄ flow at RT (1000 mbar data)	139
Figure 4.70.	Mass uptake (%) of AC6-200 at different flow compositions	140
Figure 4.71.	Mass uptake (mg/g adsorbent) of AC6-200 at RT under 25 ml/min CO ₂ -25 ml/min CH ₄ flow	141
Figure 4.72.	Adsorbed CO ₂ /CH ₄ ratio on AC6-200 at RT and 0-1000 mbar under 25 ml/min CO ₂ - 25 ml/min CH ₄ flow	141
Figure 4.73.	Mass uptake (mg/g adsorbent) of AC6-200 at RT under 5 ml/min CO ₂ -45 ml/min CH ₄ flow	142
Figure 4.74.	Adsorbed CO ₂ /CH ₄ ratio on AC6-200 at RT and 0-1000 mbar under 5 ml/min CO ₂ - 45 ml/min CH ₄ flow	142

Figure 4.75.	Adsorbed amounts of CO ₂ and CH ₄ on AC6-200 at RT under 25 ml/min CO ₂ -25 ml/min CH ₄ flow.....	143
Figure 4.76.	Adsorbed amounts of CO ₂ and CH ₄ on AC6-200 at RT under 5 ml/min CO ₂ -45 ml/min CH ₄ flow.....	144
Figure 4.77.	Mass uptake (%) on AC6-200 under different feed compositions in the 0-5000 mbar pressure range.	145
Figure 4.78.	Mass uptakes (mg/g adsorbent) of CO ₂ and CH ₄ on AC6-200 under 45 ml/min CO ₂ -45 ml/min CH ₄ flow (50% CO ₂ -50% CH ₄).....	147
Figure 4.79.	Mass uptakes (mg/g adsorbent) of CO ₂ and CH ₄ on AC6-200 under 9 ml/min CO ₂ -81 ml/min CH ₄ flow (10% CO ₂ -90% CH ₄).....	147
Figure 4.80.	The adsorbed mass ratio of CO ₂ :CH ₄ under CO ₂ -CH ₄ mixture feed flows in the pressure range of 0-5000 mbar.....	148
Figure 4.81.	Freundlich isotherms for CO ₂ adsorption over AC6-200 under different temperatures (◆) 25°C, (■) 120°C, and (▲) 200°C.....	150
Figure 4.82.	Freundlich isotherms for CH ₄ adsorption over AC6-200 under different temperatures (◆) 25°C, (■) 120°C, and (▲) 200°C.....	150
Figure 4.83.	D-R isotherms for CO ₂ adsorption over AC6-200 under different temperatures (◆) 25°C, (■) 120°C, and (▲) 200°C.....	151
Figure 4.84.	D-R isotherms for CH ₄ adsorption over AC6-200 under different temperatures (◆) 25°C, (■) 120°C, and (▲) 200°C.....	151
Figure 4.85.	SEM images of (a) AC6-200 and (b) AC6-300 adsorbents (x50000). ...	156

Figure 4.86.	BSEs of (a) AC6-200 (b) AC6-250 and (c) AC6-300 adsorbents (x50000)	157
Figure 4.87.	SE (a,c)and BSE (b,d) images of AC6-200 and AC7-200 adsorbents (x5000).....	157
Figure 4.88.	Pore size distributions of AC adsorbents	159
Figure A.1.	Temperature dependence of time-on-stream activity data for coimpregnated 1%Pt-1%Re-1%Na/CeO ₂ catalyst under ideal feed #1 (H ₂ O/CO=5).....	190
Figure A.2.	Temperature dependence of time-on-stream activity data for coimpregnated 1%Pt-1%Re-1%Na/CeO ₂ catalyst under ideal feed #2 (H ₂ O/CO=2).....	190
Figure A.3.	Temperature dependence of time-on-stream activity data for coimpregnated 1%Pt-1%Re-1%Na/CeO ₂ catalyst under realistic feed #1 (H ₂ O/CO=6.7).....	191
Figure A.4.	Temperature dependence of time-on-stream activity data for coimpregnated 1%Pt-1%Re-1%Na/CeO ₂ catalyst under realistic feed #2 (H ₂ O/CO=16.2).....	191
Figure A.5.	Temperature dependence of time-on-stream activity data for sequentially impregnated 1%Pt-1%Re-1%Na/CeO ₂ catalyst under ideal feed #1 (H ₂ O/CO=5).....	192
Figure A.6.	Temperature dependence of time-on-stream activity data for sequentially impregnated 1%Pt-1%Re-1%Na/CeO ₂ catalyst under ideal feed #2 (H ₂ O/CO=2).....	192

Figure A.7.	Temperature dependence of time-on-stream activity data for sequentially impregnated 1%Pt-1%Re-1%Na/CeO ₂ catalyst under realistic feed #1 (H ₂ O/CO=6.7).	193
Figure A.8.	Temperature dependence of time-on-stream activity data for sequentially impregnated 1%Pt-1%Re-1%Na/CeO ₂ catalyst under realistic feed #2 (H ₂ O/CO=16.2).	193
Figure A.9.	Temperature dependence of time-on-stream activity data for sequentially impregnated 1%Pt-1%Re-2%Na/CeO ₂ catalyst under ideal feed #1 (H ₂ O/CO=5)	194
Figure A.10.	Temperature dependence of time-on-stream activity data for sequentially impregnated 1%Pt-1%Re-2%Na/CeO ₂ catalyst under ideal feed #2 (H ₂ O/CO=2)	194
Figure A.11.	Temperature dependence of time-on-stream activity data for sequentially impregnated 1%Pt-1%Re-2%Na/CeO ₂ catalyst under realistic feed #1 (H ₂ O/CO=6.7).	195
Figure A.12.	Temperature dependence of time-on-stream activity data for sequentially impregnated 1%Pt-1%Re-2%Na/CeO ₂ catalyst under realistic feed #2 (H ₂ O/CO=16.2).	195
Figure A.13.	Temperature dependence of time-on-stream activity data for sequentially impregnated 1%Pt-1%Re-1%Na/TiO ₂ catalyst under ideal feed #1 (H ₂ O/CO=5)	196
Figure A.14.	Temperature dependence of time-on-stream activity data for sequentially impregnated 1%Pt-1%Re-1%Na/TiO ₂ catalyst under ideal feed #2 (H ₂ O/CO=2)	196

Figure A.15.	Temperature dependence of time-on-stream activity data for sequentially impregnated 1%Pt-1%Re-1%Na/TiO ₂ catalyst under realistic feed #1 (H ₂ O/CO=6.7).	197
Figure A.16.	Temperature dependence of time-on-stream activity data for sequentially impregnated 1%Pt-1%Re-1%Na/CeO ₂ catalyst under realistic feed #2 (H ₂ O/CO=16.2).	197
Figure B.1.	6 h TOS OSR and WGS activities over coimpregnated 1%Pt-1%Re-1%Na/CeO ₂ under 14% CH ₄ , 9.3% O ₂ , 56% H ₂ O, 20.7% Ar (H ₂ O/CO=4, O/C=1.33) feed flow at 300°C, 350°C and 400°C.....	198
Figure B.2.	6 h TOS OSR and WGS activities over coimpregnated 1%Pt-1%Re-1%Na/CeO ₂ under 14% CH ₄ , %6.7 O ₂ , %56 H ₂ O, %23.3 Ar (H ₂ O/CO=4, O/C=0.95) feed flow at 300°C, 350°C and 400°C.....	198
Figure B.3.	6 h TOS OSR and WGS activities over sequentially impregnated 1%Pt-1%Re-1%Na/CeO ₂ under 14% CH ₄ , 9.3% O ₂ , 56% H ₂ O, 20.7% Ar (H ₂ O/CO=4, O/C=1.33) feed flow at 300°C, 350°C and 400°C.....	199
Figure B.4.	6 h TOS OSR and WGS activities over sequentially impregnated 1%Pt-1%Re-1%Na/CeO ₂ under 14% CH ₄ , %6.7 O ₂ , %56 H ₂ O, %23.3 Ar (H ₂ O/CO=4, O/C=0.95) feed flow at 300°C, 350°C and 400°C.....	199
Figure B.5.	6 h TOS OSR and WGS activities over sequentially impregnated 1%Pt-1%Re-2%Na/CeO ₂ under 14% CH ₄ , 9.3% O ₂ , 56% H ₂ O, 20.7% Ar (H ₂ O/CO=4, O/C=1.33) feed flow at 300°C, 350°C and 400°C.....	200
Figure B.6.	6 h TOS OSR and WGS activities over sequentially impregnated 1%Pt-1%Re-2%Na/CeO ₂ under 14% CH ₄ , %6.7 O ₂ , %56 H ₂ O, %23.3 Ar (H ₂ O/CO=4, O/C=0.95) feed flow at 300°C, 350°C and 400°C.....	200

- Figure B.7. 6 h TOS OSR and WGS activities over sequentially impregnated 1%Pt-1%Re-1%Na/TiO₂ under 14% CH₄, 9.3% O₂, 56% H₂O, 20.7% Ar (H₂O/CO=4, O/C=1.33) feed flow at 300°C, 350°C and 400°C 201
- Figure B.8. 6 h TOS OSR and WGS activities over sequentially impregnated 1%Pt-1%Re-1%Na/TiO₂ under 14% CH₄, %6.7 O₂, %56 H₂O, %23.3 Ar (H₂O/CO=4, O/C=0.95) feed flow at 300°C, 350°C and 400°C 201

LIST OF TABLES

Table 3.1.	Specifications and applications of the gases used	26
Table 3.2.	Specifications and applications of the liquids used	27
Table 3.3.	Chemicals used in catalyst and adsorbent preparation.	27
Table 3.4.	Gas analysis conditions for OSR and/or WGS reaction system	34
Table 3.5.	Pt-Re-Na catalysts and applied impregnation methods.....	45
Table 3.6.	List of modified activated carbon adsorbents.....	48
Table 3.7.	WGS performance test feed compositions	49
Table 3.8.	Summary of the performed WGS experiments	50
Table 3.9.	Serial OSR-WGS feed compositions	52
Table 3.10.	Summary of the performed OSR-WGS experiments	53
Table 3.11.	Diluted realistic and inert feed compositions used in OSC analysis	56
Table 3.12.	Experiments conducted over catalysts for OSC analysis	56
Table 4.1.	Lattice contents and crystallite sizes of CeO ₂ and reduced samples	87
Table 4.2.	Ce ³⁺ contents (%) of freshly reduced and spent catalysts under realistic feed #1 and realistic feed #2 conditions	93

Table 4.3.	The Pt dispersion values of catalyst samples	106
Table 4.4.	Langmuir isotherm parameters for CO ₂ adsorption	152
Table 4.5.	Langmuir isotherm parameters for CH ₄ adsorption	152
Table 4.6.	Freundlich isotherm parameters for CO ₂ adsorption.....	154
Table 4.7.	Freundlich isotherm parameters for CH ₄ adsorption.....	154
Table 4.8.	Dubinin-Radushkevich (D-R) isotherm parameters for CO ₂ adsorption.	155
Table 4.9.	Dubinin-Radushkevich (D-R) isotherm parameters for CH ₄ adsorption	155
Table 4.10.	BET surface areas and total pore volumes of modified AC adsorbents.	158

LIST OF SYMBOLS

a	Lattice constant
d	Lattice spacing
E	Characteristic energy
E_1	Heat of adsorption for the first layer
E_L	Heat of adsorption for the second and higher layers
$f_{i,in}$	Molar flow rate of species i in the feed stream
$f_{i,out}$	Molar flow rate of species i in the product stream
P	Equilibrium pressure
P_0	Saturation pressure
P_{gas}	Pressure of the gas
P_T	Total Pressure
R	Universal gas constant
T_{gas}	Temperature of the gas
V_{gas}	Volume of the gas
n_{gas}	Moles of the gas
\dot{n}_{gas}	Molar flow rate of the gas
MW_{gas}	Molecular weight of the gas
$v_{i,gas}$	Volumetric flow rate of the gas
W	Adsorbed volume
W_0	Saturated adsorption capacity
β	Line broadening at half the maximum intensity
ΔH_{298}°	Standard enthalpy of reaction
λ	X-ray wavelength
θ	Bragg angle
τ	Mean crystallite size
v	Adsorbed gas quantity
v_m	Monolayer adsorbed quantity

LIST OF ACRONYMS/ABBREVIATIONS

AC	Activated Carbon
ATR	Auto-thermal Reforming
BSE	Back Scattering Electron
CCS	Carbon dioxide Capture and Storage
D-R	Dubinin- Radushkevich
DE	Distributed Energy
DI	Deionized
DRF	Diluted Realistic Feed
DRIFTS	Diffuse Reflectance Infrared Fourier Transform Spectroscopy
DSMS	Dynamic Sampling Mass Spectrometer
EDX	Energy Dispersive X-Ray
E-OSC	Effective Oxygen Storage Capacity
FC	Fuel Cell
FP	Fuel Processor
FTIR	Fourier Transform Infrared Spectroscopy
GC	Gas Chromatograph
GHSV	Gas Hourly Space Velocity
GTL	Gas to liquid
HPLC	High Performance Liquid Chromatography
HTS	High Temperature Shift
IF	Ideal Feed
IGA	Intelligent Gravimetric Analyzer
LTS	Low Temperature Shift
MAC	Microwave Activated Carbon
MCT	Mercury-Cadmium-Telluride
MFC	Mass Flow Controller
MOF	Metal Organic Framework

MS	Mass Spectroscopy
MW	Molecular Weight
OD	Outer Diameter
OSC	Oxygen Storage Capacity
OSCC	Oxygen Storage Capacity, Complete
OSR	Oxidative Steam Reforming
PEMFC	Proton Exchange Membrane Fuel Cell
PEM	Proton Exchange Membrane
PGM	Platinum Group Metal
PID	Proportional-integral-derivative
POX	Partial Oxidation
PROX	Preferential Oxidation
PSA	Pressure Swing Adsorption
PSD	Pore Size Distribution
RF	Realistic Feed
RT	Room Temperature
SEM	Scanning Electron Microscopy
SE	Secondary Electron
S-OSC	Structural Oxygen Storage Capacity
SR	Steam Reforming
SS	Stainless Steel
TCD	Thermal Conductivity Detector
TOF	Turn-over Frequency
TOS	Time-on-stream
T-OSC	Total Oxygen Storage Capacity
TOX	Total Oxidation
TPD	Temperature Programmed Desorption
TPO	Temperature Programmed Oxidation
TPR	Temperature Programmed Reduction
TPV	Total Pore Volume
TSA	Total Surface Area

VSA	Vacuum Swing Adsorption
WGS	Water-Gas Shift
XP	X-Ray Photoelectron
XPS	X-Ray Photoelectron Spectroscopy
XRD	X-Ray Diffraction

1. INTRODUCTION

The severity of global warming imposes effective, life cycle based, decarbonization in energy sector regardless of primary energy source, production type, process used and final product obtained (electricity, heat, etc). Even a conventional production through fossil fuel combustion should be coupled with an efficient carbon capture technology in order to decrease its emission per “unit energy produced” basis. Continuous increase in energy demand pushing up both peak and base-load demands while intermittent nature of most of sustainable routes and losses occur during distribution impose diverting the energy production from conventional large central facilities coupled with vertical distribution to distributed units having efficiency levels equivalent to central production coupled with smart grids.

Hydrogen has been emphasized as an important clean and environmentally benign energy carrier and it has been tried to take the place of traditional hydrocarbon fuels, regarding its advantages such as reducing the greenhouse gas emissions, high energy content and economic extent among hydrocarbon fuels (Cormos, 2011). On site hydrogen production via Fuel Processors (FP) seems to be the most promising and suitable alternative eliminating the disadvantage of hydrogen storage (Moreño *et al.*, 2008).

Among a variety of fuel cells operating with different fuels and electrolytes, proton exchange membrane fuel cells (PEMFC) seems to be the most viable fuel cell technology for small scale stationary applications like energy or combined heat and energy generation in houses, apartments due to its compactness, modularity, high power density and fast response (Ahmed and Krumpelt, 2001; Avci *et al.*, 2002). As proliferation of PEMFC technology depends on the availability of hydrogen, small-scale hydrogen production technologies have gained importance for electric generation through the use of new technologies like combined fuel processor- fuel cell systems (Wang *et al.*, 2011; Zeng *et al.*, 2010). Thus, the use of combined FP and proton exchange membrane fuel cell (FP-PEMFC) systems in small stationary units, like houses and small scale businesses, has become an attractive research area. Energy production through FP-PEMFC is fully sustainable when bio-methane (*or third generation bio-based fuels*) is used as the fuel.

Hydrogen can be produced by reforming a hydrocarbon fuel into a hydrogen rich gas mixture. Fuel processing units generally consist of reforming, water-gas shift and CO oxidation stages (Ersöz *et al.*, 2006). There are several methods for hydrocarbon reforming, namely steam reforming, partial oxidation reforming, oxidative steam reforming. The exit gas stream of the reforming reactor contains relatively high carbon monoxide quantity that is poisonous for the electrocatalysts of the PEMFC anode, which able to operate with less than 100 ppm CO. Thus, it is necessary to use a CO clean-up system (Sopeña *et al.*, 2007). A widespread CO clean-up system widely used generally consists of several water-gas shift (WGS) and preferential oxidation (PROX) reactors run in series. In our prototype and demo-scale FPs, an Oxidative Steam Reforming reactor, a single WGS reactor operating near thermodynamic limit and a highly selective PROX reactor are aimed to be combined and run in a serial fashion in production of CO-free hydrogen to be used in electricity production via FP-PEMFC combined systems.

Today, the industrial WGS process takes place in a series of adiabatic converters where the effluent from the reformer system is processed in two WGS reactors (HTS and LTS units, respectively). The aim of combining these units is to benefit from both fast reaction kinetics at higher temperatures and higher conversion levels can be achieved at lower temperatures (Leppelt *et al.*, 2006). HTS is mainly conducted over $\text{Fe}_2\text{O}_3/\text{Cr}_2\text{O}_3$ oxide catalysts at 350-500 °C and reduces the CO concentration to around 3%, while LTS is conducted over $\text{Cu}/\text{ZnO}/\text{Al}_2\text{O}_3$ catalysts at 180-240°C for reducing the CO concentration down to about 0.5-1% (Ratnasamy *et al.*, 2009).

Conventional WGS catalysts does not meet the required properties and performance characteristic criteria for FP operation. Maintaining high activity after repeated start-up and shut-down cycles; stable operation under feeds having oxygen and excess water; thermal stability; and low methanation activity are some of the performance criteria, which industrial WGS catalysts fail to satisfy. Moreover, the two step (HTS and LTS) WGS reactors are not appropriate for small scale hydrogen production applications, as they present the bulkiest part of the whole fuel processor. Therefore, there has been a profound research interest in the design and development of active, non-pyrophoric, robust Platinum-group metal (PGM) based and metal oxide supported WGS catalysts (Li *et al.*, 2011; Colussi *et al.*, 2014). In the literature, Pt and Au based WGS catalysts have been reported to have promising WGS

performance. A single WGS reactor, which utilizes a highly active and stable catalyst, operating at HTS-LTS transition temperatures, i.e. 250-350°C, is preferred over the conventional use of serial HTS and LTS reactors in FP operations (Gonzalez-Castaño *et al.*, 2014).

Thermal power plants fed by fossil fuels, including coal, oil and gas generate CO₂ as a by-product accounts for 40% of total CO₂ emissions. Since reducing CO₂ emissions is crucial for environmental concerns, there is a growing interest on CO₂ capture technologies. Although combined FP-PEMFC systems release lower “amount of CO₂ per unit energy produced” compared to conventional systems, these systems need a CO₂ capturing unit for CO₂-free energy production as well. CO₂ capture technologies also provide an advantageous way for many issues, such as selective separation of CO₂ from the natural gas reserves, flue gas mixture or the shifted-syngas (CO + H₂) prior to the generation of electricity. CO₂ concentrations lower than 15% in the effluent stream of WGS units, account for low thermodynamic driving force available for CO₂ capture. The requirement for achieving a high level of CO₂ removal leads to a rise in fixed and operational costs, which impose developing cost effective, advanced CO₂ capture processes utilizing adsorbents, absorbents or membranes (Gomes and Yee, 2002). Adsorption seems to be the most promising technology due to its reasonable removal efficiency, especially by using solid sorbents that offers potential energy savings with lower capital and operating costs (Garcia *et al.*, 2011; Balsamo *et al.*, 2013).

The successful operation of the adsorption process depends on the availability of a CO₂ adsorbent having the following key properties: (i) reversible and selective adsorption of CO₂ over CH₄, H₂, and/or CO, (ii) relatively fast kinetics of adsorption and desorption of CO₂ (Beaver *et al.*, 2009). Activated carbon (AC) based adsorbents with their large surface area and suitable porosity, are widely used for carbon dioxide removal in carbon dioxide emission abatement (Jang and Park, 2012).

The aim of the current study is to design and develop efficient catalysts and adsorbents for CO_x elimination to be used in various applications including CO-free hydrogen production from hydrocarbons and CO₂ elimination through pre-combustion technologies.

In this context, Na promoted Pt-Re/CeO₂ and Pt-Re/TiO₂ catalysts having high activity, selectivity and stability under ideal and realistic WGS feed conditions were designed, prepared and tested. In catalyst design; Na loading, impregnation procedure and support type were used as the parameters. The effect of reaction temperature, feed type and composition (H₂O/CO ratio) were examined in the performance tests. The real performance of the WGS catalysts were tested in a serial OSR-WGS reactor system using the OSR catalyst studied in the previous studies, i.e. 0.2%Pt-10%Ni/ δ -Al₂O₃ (Gökaliler, 2012; Başar, 2016; Öztepe, 2017). The prepared catalysts were characterized by X-Ray diffraction (XRD) for identifying the crystalline phases, X-Ray Photoelectron Spectroscopy (XPS) for analyzing the oxidation states, Raman Spectroscopy for structural characterization and abundance of coke formation, and Scanning Electron Microscopy/Electron dispersive X-Ray (SEM-EDX) for studying microstructural formations. CO chemisorption was also carried out in order to see the level of metal dispersion. A detailed *in-situ* and *operando* FTIR-DRIFTS-MS study was performed in order to interpret the WGS reaction mechanism, and structure-mechanism-performance relation. Oxygen storage capacity of the catalysts were also measured and WGS performance-oxygen storage capacity relation was investigated. High performance AC based, chemically modified adsorbents for selective CO₂ capture were designed and developed through an experimental design procedure having AC pretreatment type, type and loading of additives, temperature and adsorbate gas composition as the parameters. Total surface area and pore volume distribution of the adsorbents were determined by performing N₂ adsorption.

Chapter 2 contains a comprehensive literature survey on theoretical background of fuel processor and fuel cell technologies, followed by detailed information about fuel processing reactions as well as CO₂ adsorption and activated carbon adsorbents. The experimental systems and procedures used in catalyst and adsorbent preparation in the current study are presented in Chapter 3. The results of performance tests, characterization, FTIR-DRIFTS-MS, oxygen storage capacity and adsorption tests and related discussions can be found in Chapter 4. Finally, the conclusions that are drawn from this research and the recommendations for future studies are summarized in Chapter 5.

2. LITERATURE SURVEY

2.1. Fuel Processor – Fuel Cell Technology

Fuel cell technologies have received extensive interest in recent years, owing to their high efficiencies and low emissions, showing regard to the environmental problems related with fossil fuel combustion causing climate change. Fuel cells can take the place of batteries via providing 1kW to 5kW power for telecom sites without noise and emissions. Electronic systems can benefit from on-site or direct DC power supply that is provided by such systems. Fuel cells (FCs), which are classified according to the type of electrolytes employed, are electrochemical devices that convert the chemical energy of H₂ or H₂-rich fuels directly into electricity. There are different types of fuel cells that contributes different applications, which generally have high temperature requirement. Among the various fuel cells, proton exchange membrane fuel cells (PEMFCs) are considered as the most suitable technology for small scale and stationary applications, due to their high power density, mechanical robustness, low operation temperature and fast start-up properties (Ghenciu, 2002).

The use of combined fuel processor-PEM fuel cell (FP-PEMFC) systems in small-scale stationary electricity production is expected to be well proliferated in foreseeable future as the part of distributed energy (DE) production systems connected to smart grids. On site hydrogen production via FP seems to be the most promising and suitable alternative to hydrogen storage, which still has technological hurdles. PEMFC is one of the most viable fuel cell type for small-scale stationary applications, like energy and/or combined heat and energy generation in houses, apartments, small scale businesses, etc.

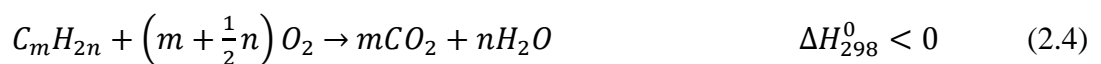
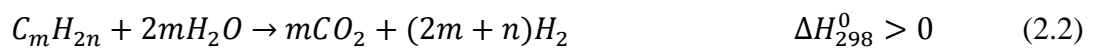
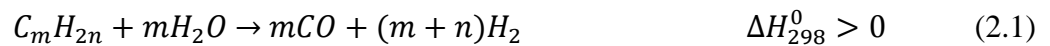
In hydrogen production from hydrocarbons by using FPs, significant amount of CO production is unavoidable as hydrogen is produced and enriched by the series of catalytic reforming and water-gas shift units of the fuel processor. The CO level in the downstream of the reformer is reduced by the shift reactions, but further CO removal is a necessity in order to decrease CO content to the required levels for stable operation of PEMFC. CO concentration at the exit of a FP should be less than 40 ppm not to deactivate platinum-

electro catalyst in PEMFC as its anode catalyst is sensitive to even traces of CO at the low operation temperature of PEMFC (Çağlayan *et al.*, 2005; Ahmed *et al.*, 2006).

In a FP, three catalytic reactions in series are operated to produce CO-free hydrogen to be fed to a fuel cell, which are reforming reactions (i.e. steam reforming, partial oxidation, oxidative steam reforming), water-gas shift reaction and preferential CO oxidation, respectively. It should be noted that CO concentration at the exit of a FP should be less than 40 ppm not to deactivate platinum-electro catalyst in PEMFC as its anode catalyst is sensitive to even traces of CO at the low operation temperature of PEMFC (Çağlayan *et al.*, 2005; Ahmed *et al.*, 2006).

2.2. Oxidative Steam Reforming (OSR)

Steam reforming (SR) process is the common industrial method for hydrogen production, though it is highly endothermic and SR reactors need to possess large heat transfer areas. Therefore, it is not suitable for on-site FP-FC applications due to the need of large reactor size. On the other hand, partial oxidation (POX) has higher reaction rates but lower hydrogen yield with respect to SR. Besides, POX tends to coke formation which deactivates catalyst (Rowshanzamir *et al.*, 2012). Faster kinetic of POX allows the use of smaller reactor compared to those used for SR. However, depending on the nature of the catalyst, the amount of oxidant in the feed and the residence time, POX reaction may turn to total oxidation (TOX).



Oxidative steam reforming (OSR) is a combination of steam reforming and partial/total oxidation, and profitable in terms of economic and technical aspects. Combining exothermic oxidation and endothermic steam reforming provide energy efficiency which ensures the temperature control and reduction in hot-spot formation; therefore, suppresses the catalyst deactivation due to sintering or coking. OSR reduces coke formation and increases hydrogen yield. The special case of OSR is named as autothermal steam reforming (ATR) when zero heat requirement is attained. In OSR, changing the hydrogen concentration and H₂/CO ratio in the product stream can be manipulated through changing the H₂O/O₂ feeding ratio. This is significant in the production of syngas for especially large-scale gas-to-liquid (GTL) plants. Additionally, OSR reactors are advantageous in terms of design as they have compact size, quick response feature, and inexpensive material requirement (Cai *et al.*, 2008; Hagh, 2004; Souza *et al.*, 2007; Rowshanzamir *et al.*, 2012).

Nickel and noble metals are known to be catalytically active metals in the steam reforming process. Although Ni is less active than some noble metals and more prone to deactivation (e.g., by coking), steam reforming (Equation 2.1) of hydrocarbons on Ni promoted catalysts is the conventional, cheapest and highly efficient process for providing synthesis gas (H₂ + CO) and for large scale hydrogen production (Çağlayan *et al.*, 2005; Gupta, 2009; Schadel *et al.*, 2009).

POX reaction is a rapid reaction with quick response and higher reaction rates than SR reaction and can be conducted in the presence or absence of catalyst. The non-catalytic process operates at high temperatures (1100-1500°C), whereas the catalytic one at much lower range of temperatures (600-900°C). The catalyst should be very active also in SR reaction to ensure complete conversion of the hydrocarbon fuel. Most commonly used catalysts are refractory supported Ni and noble metal based (e.g., Rh, Pt, Pd, Ir, Ru, and Re) catalysts in the form of pellets and monoliths (Hu and Ruckenstein, 2004; Reuse *et al.*, 2004; Vita *et al.*, 2010).

2.2.1. Pt-Ni Bimetallic OSR Catalysts

Nickel based catalysts are generally used for OSR reactions, however they suffer from catalyst deactivation due to carbon deposition and sintering. Noble metal based catalysts

such as Pt, Rh, and Pd, show very high activity in OSR reaction at low concentrations resulting with a high resistance to coke deposition (Vita *et al.*, 2015). Bimetallic Pt–Ni system was found to exhibit superior activity at relatively low temperatures depending on the presence of close – but distinct – Pt and Ni sites (Çağlayan *et al.*, 2005). The addition of Pt to Ni/CeO₂ catalyst was also observed to promote the decomposition of dehydrogenated and acetate species to hydrogen, methane, CO and carbonate species. The segregation of Pt on the surface of the Ni particles was observed to minimize the formation of nickel carbide and also promoted catalyst stability (Moraes *et al.*, 2016).

In the study concerning with the OSR performance tests of Pt–Ni/δ-Al₂O₃ bimetallic catalysts, optimum Ni:Pt weight ratio was found around 50 depending on suppressed methanation and enhanced hydrogen production activities of these catalysts (Gökaliiler *et al.*, 2008). The performance specs of the catalyst with optimum loading were specified by conducting the experiments under different feed compositions for the OSR reactor at various temperatures (Başar *et al.*, 2016).

2.3. Water-Gas Shift Reaction

Water- gas shift reaction (Equation 2.5) was previously established for the purpose of hydrogen production as a part of ammonia synthesis (Duarte de Farias *et al.*, 2008; Sanchez *et al.*, 2013). More recently, growing attention has paid on WGS reaction, since it is an intermediate step for hydrogen production. WGS process has an essential importance for the preliminary CO clean-up and extra hydrogen production. The effluent stream of the reformer contains CO, CO₂, H₂, H₂O, O₂ and CH₄. CO content in the effluent of the reformer system decreases from 10% to 0.5-1% in the WGS unit. Due to the other components present in the feed stream of WGS unit, side reactions such as methanation reaction (Equation 2.6) can occur depending on the reaction conditions, catalyst type, and H₂O/CO ratio (Duarte de Farias *et al.*, 2008; Choung *et al.*, 2005; Sanchez *et al.*, 2013).



The WGS reaction is a reversible, equilibrium limited, and moderately exothermic reaction ($\Delta H = -41.2$ kJ/mol). Due to the exothermicity of the reaction, the reaction shifts backwards at high temperatures. High CO conversion levels are met at low temperatures, whereas the kinetics of WGS reaction is enhanced at high temperatures. Commercially, WGS process takes place in serial reactors, namely high temperature shift stage (HTS) at 300-400°C and low temperature shift stage (LTS) at 200-260°C to handle this contradiction (Natesakhawat *et al.*, 2006; Leppelt *et al.*, 2006).

Due to the necessity of a low CO content hydrogen stream for the PEM fuel cell, selective catalysts are required. The overall selectivity is dependent on the efficiency of the catalysts in each segment of the fuel processor. Conventionally used catalysts for WGS reaction include Fe-Cr oxide mixtures ($\text{Fe}_3\text{O}_4/\text{Cr}_2\text{O}_3$) for HTS and Cu-Zn oxide ($\text{Cu}/\text{ZnO}/\text{Al}_2\text{O}_3$) for LTS (Song, 2002; Mhadeshwar and Vlachos, 2005; Rhodes *et al.*, 2002). These types of catalysts, however, are pyrophoric and deactivate if exposed to air and condensed water; thus, they are not suitable to be used in FP of the FP-PEMFC systems due to the transient operation mode of those systems.

A suitable WGS catalyst for fuel cell applications, needs to be (i) non-pyrophoric, (ii) free of pre-reduction treatment, (iii) robust in cycles of rapid heating and cooling, (iv) having fast kinetics, and (v) reach conversion levels close to thermodynamic barrier. Since conventional catalysts are pyrophoric after activation and/or require strict reduction conditions, researchers focused on the development of low-loading robust noble metal-based catalysts that are non-pyrophoric with high activity at low-temperatures. Noble metal-based catalysts including Pd (Wang and Gorte, 2003; Bi *et al.*, 2009), Ru (Panagiotopoulou and Kondarides, 2004), Rh (Cornaglia *et al.*, 2012), Pt (Jacobs *et al.*, 2003; Meunier *et al.*, 2007) and Au (Andreeva *et al.*, 2002) supported on reducible single (CeO_2 , TiO_2 , ZrO_2 , ThO_2) and mixed oxides can potentially satisfy the requirement of fuel cells, i.e. low (less than 5 ppm) CO content level in the hydrogen gas stream produced (Xu *et al.*, 2012; Vignatti *et al.*, 2011; Song, 2002; Kalamaras *et al.*, 2008; Kalamaras *et al.*, 2012).

2.3.1. Au-Based WGS Catalysts

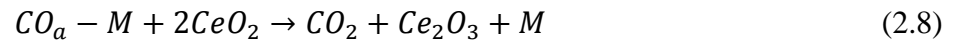
Regarding the literature, gold-based catalysts are proposed to have potential to be used effectively in fuel cell technology. Although bulk metallic gold typically exhibits a very low chemical and catalytic activity, it has become the subject of a lot of attention due to its unusual catalytic properties when dispersed on some oxide supports. Another reason behind developing the gold-based catalysts is the relatively low and stable price and greater availability of gold compared with the platinum, besides their promising technical performance (Cameron *et al.*, 2003; Rodriguez, 2011). By the use of transmission FTIR experiments, Au atoms were determined to be active sites for WGS reaction by many researchers (Çağlayan and Aksoylu, 2011; Wang *et al.*, 2012).

High activity and stability of Pt/CeO₂ catalysts for the WGS reaction has led researchers to investigate Au/CeO₂ catalysts. On the contrary to the Au/Fe₂O₃ catalysts, Au/CeO₂ system does not have unstability problem (Corti *et al.*, 2005). According to the study of Boaro *et al.*, the behaviours of gold and platinum based catalysts were not in great accordance, especially in the 423–513 K, temperature range. The performance of gold was superior to platinum under feed conditions imitating the outlet stream of the reforming reactor. In terms of supports, CeO₂- ZrO₂ mixed oxide catalysts showed the ability of redox and structural characteristic modification on ZrO₂, and it is concluded that the most important issue for the reaction mechanism is the metal-support interface (Boara *et al.*, 2009).

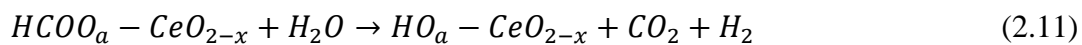
Pilasombat and coworkers have investigated the effects of gold precursor deposition method (Deposition–Precipitation (DP), Co-Precipitation (CP), Urea Gelation Co-precipitation (UGC)), the concentration and composition of the washing solution, the nature of the gold precursor (HAuCl₄, AuBr₃), the drying method, the Ce:Zr mole ratio in the support on the activity and stability of Au/ceria–zirconia catalysts. The highest activity was achieved on the mixed oxide support with Ce:Zr mole ratio 1:1. HAuCl₄ gold precursor was used in deposition precipitation technique, and drying under vacuum at room temperature was determined to be the most effective choice (Pilasombat *et al.*, 2012).

Particle size and structure, which is affected by preparation method, structure of the support and catalyst pretreatment have great importance on the activity of gold-based catalysts (Haruta, 1997; El-Moemen *et al.*, 2009). The study performed by Çağlayan and Aksoylu, examined the effect of preparation method by applying impregnation and deposition precipitation, effect of Re addition, metal addition sequence, space velocity and H₂O/CO ratio on the Au-Re/ceria performance. The results indicated that gold addition by deposition precipitation technique on impregnated Re/ceria catalysts exhibited higher CO conversion values owing to higher dispersion. It is also determined that Au–Re/ceria catalyst showed higher activity for WGS reaction under high H₂O/CO feeding ratios (Çağlayan and Aksoylu, 2011). Additional H₂ production beside CO conversion was obtained for 1%Au–0.5%Re/CeO₂ catalyst with high H₂O/CO ratios under realistic feed conditions (Çağlayan, 2011). Gökaliler *et al.* have investigated the power-law kinetics of WGS reaction on this catalyst at 280–325°C range under realistic feed conditions, which is essential for the reactor design. Determined reaction orders with respect to CO, H₂O, CO₂ and H₂ partial pressures, were 0.75, 2.0, –0.34 and –0.60, respectively (Gökaliler *et al.*, 2013).

Bunluesin *et al.* have reported the general redox mechanism on the surface of the cerium oxide catalysts containing deposited precious metals. Carbon monoxide adsorbs on precious metal surfaces and reduces cerium oxide producing CO₂, and the reduced cerium oxide is reoxidized by water to form H₂ as shown in the equations (Equation 2.7-2.9) below.



However this redox mechanism is not valid for the catalytic behavior of Au/CeO₂, as it was encountered in the CO and water pulse experiments on Au/CeO₂ that CO₂ and H₂ were formed at the same time when H₂O was added. This may results from an associative mechanism shown in the following two equations (Equation 2.10 and 2.11) (Sakurai *et al.*, 2005; Chen *et al.*, 2008).



2.3.2. Pt-Based WGS Catalysts

Pt based catalysts are found to be most active among all the investigated noble metals (Panagiotopoulou and Kondarides, 2006; Olympiou *et al.*, 2007; Radhakrishnan *et al.*, 2006). Ru is an active and less costly catalyst than Pt for WGS reaction, however it has a disadvantage of methanation at WGS conditions. According to the results of the study, Pt-CeO₂, Ru-CeO₂ and Pt-Ru alloy-CeO₂ catalysts were examined; Pt-Ru alloy-CeO₂ did not exhibit an improved activity with respect to Pt-CeO₂. On the other hand, methane generation was reduced by the alloy formation (Xu *et al.*, 2012).

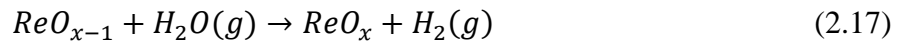
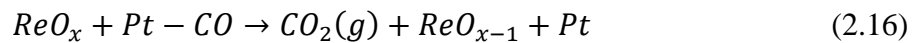
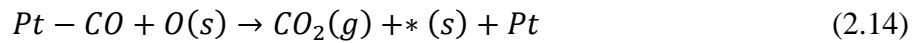
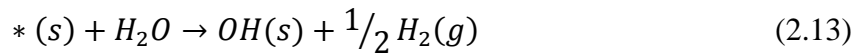
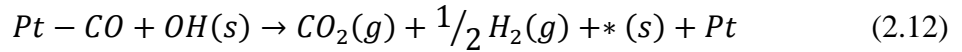
In a temperature programmed DRIFTS study, it has been proposed that Pt particle size had slight effect on turnover frequency (s⁻¹) of WGS reaction. According to the results presented, the reaction rate highly depends on the length of Pt-CeO₂ interface, which is found directly related with platinum loading and mean particle size (Kalamaras *et al.*, 2011).

The reasons of WGS activities of Pt/SiO₂, Pt/CeO₂ and Pt/TiO₂ were studied via *in-situ* diffuse reflection infrared Fourier transform spectroscopy (DRIFTS). DRIFTS spectra showed that reduced ceria was the only active support, which promoted the WGS reaction on surface bridging OH groups that react with CO to form formate intermediates. However Pt/SiO₂ has showed higher activity than CeO₂ and followed a monofunctional redox mechanism on metallic Pt sites. More than one order of magnitude greater CO conversion turnover rate implied that the reaction proceeds faster on Pt/CeO₂ than on Pt/SiO₂ showing that there exists a bifunctional metal-support mechanism. Pt/TiO₂ was the most active one among all the catalysts. The WGS reaction on Pt/TiO₂ was also catalyzed via a bifunctional metal-support mechanism, but not through same mechanism over Pt/CeO₂. The potential mechanism involves the activation of CO and water on the metal and the support, respectively. Platinum enhances the reduction of Ti⁴⁺ ions to Ti³⁺, and creates oxygen vacancy sites on the support for efficient water activation (Vignatti *et al.*, 2010).

WGS reaction was also studied on Pt/CeO₂, Pt/ZrO₂ and Pt/Ce_xZr_{1-x}O_x by Vignatti and coworkers. Pt/Ce_xZr_{1-x}O_x catalysts with $x > 0.5$ were determined to be more active than Pt/CeO₂, Pt/ZrO₂ and Pt/Ce_xZr_{1-x}O_x with $x < 0.5$. Ce_xZr_{1-x}O_x supports were prepared by sol-gel method. Zr(OC₃H₇)₄ (70% en propan-1-ol, Aldrich) precursor dissolved in 100 mL of isopropyl alcohol solution was slowly added (1 mL min⁻¹) at 30 °C to 100 mL of an aqueous solution of Ce(NO₃)₃·6H₂O (Aldrich) stirred at 500 rpm. Platinum-supported catalysts were prepared by incipient wetness impregnation method at 30°C with an aqueous solution of tetraamine platinum nitrate (Pt(NH₃)₄](NO₃)₂) (Aldrich, 99.9%). The increase in activity is explained by the increased surface area and reducibility led by the addition of Zr to ceria. The DRIFTS experiments confirmed that the stability of formate species is higher on Zr-rich supports. According to the associative mechanism of WGS, the formate formation rate increases with the surface OH group concentration. Introduction of zirconia into Pt/CeO₂ enhances the reducibility of the catalyst by increasing Ce³⁺ defect sites (Vignatti *et al.*, 2011). Superior performance of mixed oxide supported Pt over Pt/CeO₂ and Pt/ZrO₂ is approved by many researchers. Hui Li and coworkers were carried out a WGS study on Pt/Ce_{0.6}Zr_{0.4}O₂ and this catalyst showed higher conversion levels compared to Pt/CeO₂ and Pt/ZrO₂, led by the high oxygen storage capacity (Li *et al.*, 2013). Furthermore, the results of another study agreed that Pt/Ce_xZr_{1-x}O₂ catalysts exhibits superior WGS activity in comparison with the Pt/CeO₂, resulting from the increased site reactivity of Pt across the metal-support interface by the addition of Zr⁴⁺. The introduction of zirconium into ceria decreases the Ce⁴⁺/Ce³⁺ reduction energy, and adsorbed CO on Pt reacts with the partially reducible oxide component at the interface to form CO₂ (Kalamaras *et al.*, 2011).

Another promising WGS catalyst, Pt/TiO₂, showed better activity than Pt/CeO₂ which was deactivated with time due to the formation of stable carbonate on the ceria surface. However, time-on-stream (TOS) data showed that Pt sintering caused the deactivation of Pt/TiO₂, and an improvement, such as through Re addition, was very promising for overcoming Pt sintering. This addition also leads to catalysts having more stable performance (Azzam *et al.*, 2007). In their following study, Azzam *et al.* discovered that the reaction between CO adsorbed on Pt and OH groups on TiO₂ is the rate determining step following the reaction steps given in equations (Equation 2.12-2.15).

Since ReO_x could not be reduced completely under WGS reaction temperature (300°C), some oxidized form of rhenium was present during the reaction. Hence ReO_x provides an extra redox mechanism for WGS reaction shown in equations (Equation 2.16, 2.17) (Azzam *et al.*, 2008).



There are other studies examined the effect of introducing a second metal on the WGS performance of the catalysts. Researchers have shown great interest to Pt–Re bimetallic catalysts as a viable option for WGS process (Wei *et al.*, 2012). Choung *et al.* has also carried out a study on Pt-Re catalysts. They have reported that the addition of Re to $\text{Pt/Ce}_{0.46}\text{Zr}_{0.54}\text{O}_2$ enhanced the rate of WGS reaction over a temperature range of $250\text{--}400^\circ\text{C}$ using a feed gas of 6.9% CO, 10.4% CO_2 , 31.1% H_2 , 31.0% H_2O and 20.7% N_2 . The Pt dispersion has found to be higher in these catalysts compared with the monometallic Pt catalyst (Choung *et al.*, 2005).

Addition of Ni into Pt-based catalysts have also taken great importance from researchers as an alternative WGS catalyst. The control of heat of reaction for the exothermic reactions would be easier with a high conductive material. Easy fabrication of Ni metal powder and reduced reactor volumes were other advantages of these catalysts. Pt-Ni/ γ - Al_2O_3 catalysts have also found highly selective and active for the WGS reaction, and increase in Ni loading from 5 wt% to 15 wt% resulted an increase in activity (Çağlayan

and Aksoylu, 2009). In the study of Wang *et al.*, Pt-Ni catalysts were compared with the monometallic ones. Additionally, different supports were tried in order to achieve highest activity and selectivity. In terms of the catalytic activity, Pt-Ni bimetallic catalysts can be ordered $\text{CeO}_2 > \text{HSA-ZrO}_2 > \text{TiO}_2 \sim \gamma\text{-Al}_2\text{O}_3 > \text{SiO}_2 > \text{LSA-ZrO}_2$, where HSA and LSA are high surface area and low surface area. At similar CO conversions, the catalyst sequence for the production of the undesirable CH_4 was determined to be $\text{SiO}_2 > \text{CeO}_2 \sim \gamma\text{-Al}_2\text{O}_3 > \text{TiO}_2 \sim \text{HSA-ZrO}_2$. Considering these results, it was concluded that activity improvement and methanation inhibition can be achieved by using CeO_2 -based mixed oxide supports (Wang *et al.*, 2014).

2.4. Oxygen Storage Capacity

Ceria is the most important and extensively investigated material, which is widely used as a WGS reaction support due to its redox property and was established to greatly enhance the reaction rates involving redox steps, where it can act as an oxygen resource (Aneggi *et al.*, 2006; Zhou *et al.*, 2018). Effectiveness of CeO_2 in WGS reaction originates from its excellent oxygen storage capacity (OSC), which is related to the reversible $\text{Ce}^{4+}/\text{Ce}^{3+}$ redox cycles through rapid formation and elimination of oxygen vacancies in CeO_2 (Min *et al.*, 2018; Zhou *et al.*, 2018). It is reported that OSC of CeO_2 can be enhanced by the presence of precious metals such as Pt, Pd and Rh (Kakuta *et al.*, 1997). The pronounced enhancement is supposed to result from active sites at the metal- CeO_2 interface, due to the higher reaction rates than the sum of the rates over CeO_2 and the metal individually (Cargnello *et al.*, 2013).

OSC can generally be classified into two categories according to the reactivity of the O species: total OSC and dynamic OSC. The first one represents the total amount of transferable oxygen both on surface and bulk oxygen at a fixed temperature and is entitled as oxygen storage capacity complete (OSCC) (Yao *et al.*, 1984; Duprez *et al.*, 2001; Aneggi *et al.*, 2006). The second one accounts for the reactive oxygen species and readily available oxygen atoms, containing primarily the surface oxygen and oxygen vacancies. Since Dynamic OSC concerns with the mobility of oxygen, the temperature increase results with the increase in discrepancy between dynamic OSC and total OSC. However, a direct correlation between total OSC and dynamic OSC cannot be expressed due to the fact that total OSC can be measured under thermodynamic equilibrium, whereas dynamic OSC is a kinetic feature, which expresses the rate of oxygen release from the material (Li *et al.*, 2019).

OSC of the catalysts can be quantified by different methods such as TPR, chemisorption and pulse injection (Yao *et al.*, 1984; Swanson *et al.*, 2008). The most conventional method applied in the literature is pulse injection, in which the catalyst is subjected to O₂ pulses, followed by one or more CO pulses (Swanson *et al.*, 2008). The total amount of CO₂ produced after single pulses of O₂ and CO, respectively, is designated as the OSC. When a fully oxidized sample is subjected to consecutive pulses of CO until CO₂ production ceases, the total amount of CO₂ produced is termed as the OSC complete (OSCC). In chemisorption method, available sites on catalyst surface can be examined by obtaining total and reversible adsorption isotherms of oxygen, while TPR gives information about highest amount of transferable oxygen on catalysts surface (Yao *et al.*, 1984).

The review study conducted by Li *et al.* about OSC of CeO₂ mention about the parameters that affect OSC of the catalysts. Besides the properties such as structure and composition; pretreatment, temperature and aging conditions have great effect on OSC (Li *et al.*, 2019). This review, which includes many studies on oxygen storage capacity of CeO₂ catalysts, also indicates that introducing PGM results with quantitative improvement of OSC. It is also stated that catalytic activity is mostly correlated with the dynamic OSC rather than total OSC. In another study on OSC of CeO₂ reported that Hf⁴⁺ and Sn⁴⁺ doped CeO₂ is achieved to have an enhanced OSC by constructing an unstable CeO₂ crystal structure (Min *et al.*, 2018). Optimum loading of La³⁺ doping on CeO₂- γ -Al₂O₃, i.e. 0.08, is also found to increase the OSC and enhance the stability of the catalyst (Wang *et al.*, 2015). The addition of small amounts of Pt, Pd, Rh metals over CeO₂-ZrO₂ and CeO₂-ZrO₂-Y₂O₃ mixed oxides, is also found to enhance the OSC accordingly (Kai *et al.*, 2007).

Another method for improving OSC of the catalysts, is reductive treatments applied on support materials. The study performed by Morikawa *et al.*, showed that reductive treatments from 700°C to 1000°C prior to Pt addition, significantly improved the complete oxygen storage capacity (OSCC) of ACZ (composite of Al₂O₃ and CeZrO₄) (Morikawa *et al.*, 2009).

2.5. CO₂ Removal

Carbon dioxide capture and storage (CCS) technologies have crucial importance on satisfying the energy demand without contributing to global warming in the forthcoming years. These technologies save the time needed for the renewable energy technologies to bring cost down and to lead necessary advances, while enabling cleaner use of fossil fuels during the transition period (Plaza *et al.*, 2010).

CO₂ removal technologies such as absorption, adsorption, gas separation membrane, cryogenic separation, etc. seem to have the greatest near-term potential for Carbon Capture and Storage (CCS) applications, as they can be adapted to existing units. Nowadays, commercial CO₂ capture technologies such as chemical absorption via monoethanolamine (MEA), followed by direct injection into geological formations are not preferred due to their high energy requirement and cost. Among the possible CO₂-capture technologies, adsorption coupled with an effective regeneration process needing low energy, becomes a promising alternative because of the great removal efficiency, and reusable nature of the adsorbents used (Balsamo *et al.*, 2013, Garcia *et al.*, 2011; Shen *et al.*, 2010).

A cost-effective regeneration can be carried out either by increasing the temperature (Temperature Swing Adsorption, TSA) or by decreasing the pressure, to atmospheric value (Pressure Swing Adsorption, PSA) or vacuum level (Vacuum Swing Adsorption, VSA) (Tlili *et al.*, 2009; Gomes and Yee, 2002). The success of the adsorption process depends on the development of regenerable adsorbents that have high capacity, high selectivity and good regenerability (Siriwardane *et al.*, 2001; Shen *et al.*, 2010).

2.5.1. CO₂ Adsorption

Porous materials such as zeolites, activated carbon materials (AC), supported amines, metal oxides, metal carbonates, metal–organic frameworks (MOFs) have been the mostly studied adsorbents for their use in CO₂ separation from energy-generating coal-fired power plants. (Pevida *et al.*, 2008; Yang *et al.*, 2008; Garcia *et al.*, 2011). Among these adsorbents, activated carbon (AC) and aluminosilicate zeolite molecular sieves are the most promising candidates for CO₂ adsorption because of their high adsorption capacities, rapid

adsorption kinetics and low regeneration energies. Zeolites usually have high CO₂ uptake, however they suffer from a performance decay under humid flue gas environment while supported amines are susceptible to thermal and oxidative degradation despite their superior CO₂ adsorption capacity and selectivity. Activated carbon materials have been investigated in many studies as sorbents in a wide range of industrial applications, owing to their highly developed porosities, wide availability and low cost relative to other solid adsorbents. They are the most attractive candidate adsorbent materials for both post-combustion and, in particular, pre-combustion CO₂ capture (Sun *et al.*, 2013, Garcia *et al.*, 2011).

2.5.2. Activated Carbon (AC) Supported CO₂ Adsorption

Carbonaceous materials is any types of substances that can produce activated carbon such as wood, lignite, anthracite or bone. ACs are processed carbonaceous products with a complicated porous structure and high surface area arising predominant contribution of micropores (Biniak *et al.*, 1997; Dali *et al.*, 2012). The most important raw materials for the production of AC are wood, coal, lignite, coconut shell and peat. The produced ACs have different properties, such as pore structure and surface area influencing the adsorption capacity, depending on the nature of the precursor, the nature of the activating agent, washing steps and the conditions used during activation process (Auer *et al.*, 1998; Sun *et al.*, 2013).

Structural modification of AC is an important parameter for CO₂ adsorption properties. As an example, mesostructured silica impregnated with paratoluene sulfonic acid has been used for preparing KOH activated template carbons. Although the commercial AC displays a larger pore development than the activated template carbons, it has a considerably lower adsorption capacity. This outcome indicates that the capture capacity of the AC does not only depends on the textural properties such as, BET surface area or pore volume, but also on the pore size distribution. The CO₂ adsorption capacity was observed to be higher in the presence of narrow micropores (<1 nm) (Sevilla and Fuertes, 2012). This result has been approved by another research group, who has studied modified carbon fibers. The narrowest microporous carbon has given the best adsorption capacity values (Lee and Park, 2013).

There are atoms, other than carbon, form surface functional groups which contribute to the adsorption behavior of the ACs through acid–base interactions. Surface functional groups (which are formed from these heteroatoms) and the delocalized electrons of the carbon structure determine the acidic and basic characteristic of the AC surface (Shafeeyan *et al.*, 2010). Oxygen is an important heteroatom, which commonly occurs in the form of carboxylic, lactone, phenol, carbonyl, pyrone, chromene, quinone, and ether groups (Figure 2.1) These functional groups have been postulated as the sources of surface acidity (Li *et al.*, 2002; Shafeeyan *et al.*, 2010).

Basicity of AC can be defined by the following characteristics: (i) resonating π electrons of carbon aromatic rings that attract protons, and (ii) basic surface functionalities (e.g., nitrogen containing groups) that are capable of binding with protons. Oxygen containing surface functionalities such as chromene, ketone, and pyrone were pointed out as the indicator of carbon surface basicity (Figure 2.1) (Shafeeyan *et al.*, 2010).

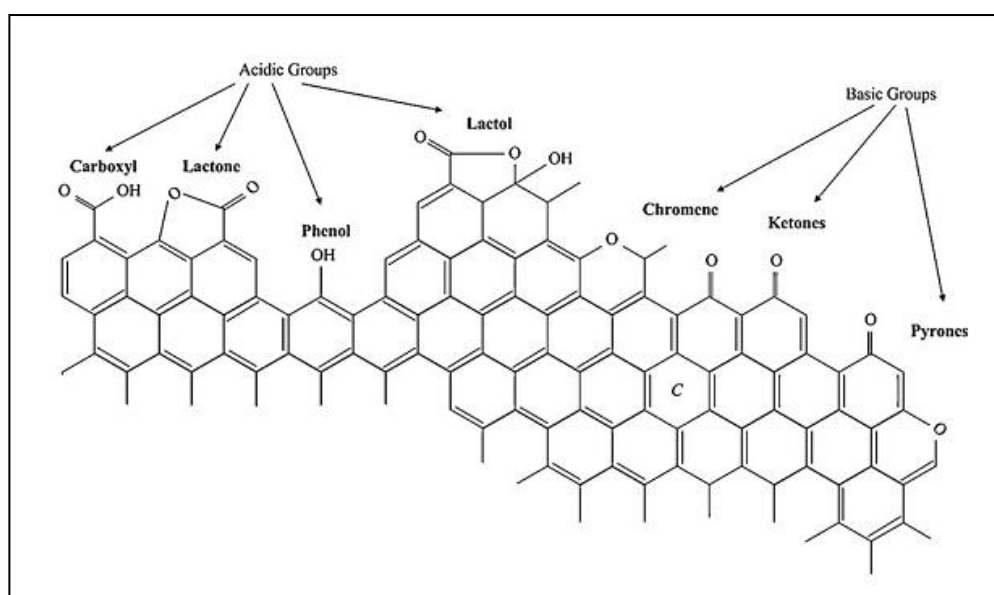


Figure 2.1. Surface groups.

It has been reported that creating base functional groups on AC would be useful for increasing the capacity of AC to adsorb CO_2 . Introduction of nitrogen containing functional groups is made through either reaction with nitrogen containing reagents, such as NH_3 , nitric acid, and amine, or activation with nitrogen containing precursors such as polyethylenimine

(PEI), acridine and carbazole (Li *et al.*, 2002; Shafeeyan *et al.*, 2010; Maroto *et al.*, 2005; Arenillas *et al.*, 2005).

Several researchers have confirmed that the decomposition of oxygen functional groups at elevated temperatures increases basicity of the carbon surface (Otake and Jenkins, 1993; Darmstadt and Roy, 2003). This is due to the fact that strongly acidic functionalities (such as carboxylic, anhydrides and lactones) decompose at lower temperatures, while the weakly acidic functionalities (such as carbonyl, phenol and quinone) decompose at higher temperatures (Papirer *et al.*, 1987; Dandekar *et al.*, 1998).

One of the most common procedures used for creation of nitrogen surface groups is the reaction with nitrogen containing reagents (such as NH_3 and amines) (Lee and Park, 2013). Several authors have studied thermal treatment of carbons in an ammonia atmosphere (Shafeeyan *et al.*, 2011). In order to form a basic surface, two different methods, heat treatment and ammonia treatment (amination) were applied to activated carbon. By means of TPD, XPS, and FTIR analysis, amination was found to be a suitable modification technique in order to obtain efficient CO_2 adsorbents (Shafeeyan *et al.*, 2010). In their following study, the effect of oxygen surface groups before introduction of basic nitrogen functionalities to the carbon surface has been investigated, and it was found that oxidation preceding high temperature amination is proposed as a suitable modification technique for improving the performance of activated carbon adsorbent, especially at relatively high temperature (Shafeeyan *et al.*, 2011).

C. Pevida and colleagues have performed similar analysis for surface chemistry via TPD and X-ray photoelectron spectroscopy, and performance of CO_2 capture was determined by using a thermogravimetric analyzer. The results indicated that ammonia treatment at temperatures higher than 600°C has incorporated nitrogen mainly into aromatic rings, while at lower temperatures nitrogen was introduced into more labile functionalities (Pevida *et al.*, 2008). However, various amine groups on AC surfaces have the drawback of pore blockage, which decrease the physical adsorption capacity of the carbon dioxide (Plaza *et al.*, 2011).

The improvement of the adsorptive properties of ACs using metallic species, such as salts of chromium, copper, iron and zinc has been reported to be effective on activated carbons. The presence of copper oxides significantly led to an increase in the carbon dioxide adsorption capacity of the carbons resulting from the electron-donor features of copper oxide nanoparticles (Kim *et al.*, 2010). Nickel oxide loading effect on CO₂ adsorption capacity of AC has also been studied by Jang *et al.*, and it was concluded that nickel oxide on the activated carbons led to an increase in the carbon dioxide adsorption capacity (Jang *et al.*, 2012).

The effect of impregnation of Cr₂O and Fe₂O₃ and promotion by Zn²⁺ on CO₂ adsorption properties of AC has been investigated by Somy *et al.* There, CO₂ adsorption properties were examined via volumetric adsorption apparatus at ambient temperature and low pressures. The results have indicated that the amount of CO₂ adsorbed on Cr₂O impregnated AC is higher than both the unimpregnated and Fe₂O₃ impregnated one. Slurry type impregnation was determined to be more effective than solution impregnation (Somy *et al.*, 2009).

Sun and coworkers have investigated the surface affinity of spherical AC beads to CO₂. The beads were prepared by carbonization and activation of phenolic resins which promoted further by nitrogen incorporation. N₂ physisorption and scanning electron microscope (SEM) were used for characterization. The adsorption tests were carried out at both ambient and elevated pressures by using either thermal gravimetric or high pressure volumetric analysis method. The AC beads used in this study are found to have reasonable CO₂ uptakes with fast adsorption kinetics. The results have indicated that AC beads are suitable solid adsorbents for pre-combustion CO₂ capture where CO₂ partial pressure is relatively higher (Sun *et al.*, 2013).

In another study conducted by Balsamo *et al.* adsorption tests, for which CO₂ inlet concentration (1–15% by vol.) and temperature were used as the parameters, were carried out on activated carbon produced from coal tar pitch and furfural. In the preparation of the samples, 50:50 wt% coal tar pitch to furfural ratio was used, and concentrated H₂SO₄ (drops of H₂SO₄ were added to the mixtures with continuous stirring) treatment was applied to the mixture until solidification. Solid product was further steam activated at 800°C for 1 h in order to obtain porous structure. The results have confirmed that CO₂ can be easily desorbed

to permit full carbon regeneration, which means CO₂ adsorption is reversible. Researchers did not observe any loss in adsorption capacity during 15 consecutive adsorption–desorption cycles. The most suitable desorbing temperature was found to be 100°C for 70–80% regeneration level (Balsamo *et al.*, 2013).

Enhancement in CO₂ adsorption capacities has been observed for air and HNO₃ oxidized forms of AC samples upon Na₂CO₃ impregnation by Çağlayan and Aksoylu. DRIFTS study results have indicated the formation of carboxylic acid groups on the HNO₃ oxidized adsorbents, which are anchoring sites for the precursors. Accordingly, uniform distribution of the Na particles with high dispersion were observed on the samples prepared by Na₂CO₃ impregnation onto HNO₃ oxidized AC support. Additionally, high temperature He treatment has been found beneficial in further stabilization and enhanced basicity of the AC adsorbent surface (Çağlayan and Aksoylu, 2013).

2.5.3. Selective CO₂ Adsorption

Separation of CO₂ from natural gas source or flue gas of thermal power plant have led the researchers concentrate on selective CO₂ adsorbents. Since the mixture contains carbon dioxide, nitrogen and methane along with minor percentage of moisture and other gases like SO_x and NO_x, there is a need for the adsorbent material possessing high selectivity and adsorption capacity for CO₂ (Grande *et al.*, 2013; Sawant *et al.*, 2012).

Carbon dioxide, methane, carbon monoxide and nitrogen adsorption properties of the horn shaped carbon nanotubes were determined by volumetric measurements up to 850 mm Hg. According to the study, the carbon nanotubes showed high adsorption capacity for CO₂ at 303 K and 850 mmHg pressure, with high selectivity over N₂ (Sawant *et al.*, 2012).

In the literature, there is an intensive research on the adsorption of CH₄ and CO₂ on activated carbons and carbon molecular sieves (Lozano-Castello *et al.*, 2002; Belmabkhout *et al.*, 2004). The adsorption of CO₂ is determined to be stronger than CH₄ and the loading of both gases depend on specific parameters of the adsorbent like surface area, pore volume, surface groups, particle density, etc. (Grande *et al.*, 2013).

Grande *et al.* have examined high-pressure adsorption of 10-20% CO₂ and balanced CH₄ containing CO₂-CH₄ mixtures on activated carbon. CO₂ adsorption is more than CH₄ in all the conditions tested, however the selectivity of the adsorbent is not very high. The results were compared with three mathematical models, multi-site Langmuir (MSL), Virial, Sips, and the fitted data have showed a very good agreement (Grande *et al.*, 2013).

Three kinds of activated carbons were prepared and characterized by XRD, FTIR and texture property tests, in order to analyze the effect of preparation method on adsorption. Nitrogen, phosphoric acid and KOH solutions were used in the carbonization step and the ACs prepared were named as W-AC, P-AC, and K-AC. Regarding the results of the study, P-AC is found as an excellent adsorbent for separating CO₂-CH₄ mixed gas due to its high separation coefficient of $\alpha_{\text{CO}_2, \text{CH}_4}$ (Yang *et al.*, 2011).

Carbon type developed from different sources affects the activity and selectivity; as an example, almond shell-sourced carbon has superior CO₂/N₂ selectivity over those obtained from olive stones. Amination process led to greater carbon yield and a shorter soaking time. Aminated almond shells also did not exhibit any deactivation during two-step cyclic adsorption/desorption (Plaza *et al.*, 2010; Plaza *et al.*, 2011).

Martin and coworkers have studied CO₂ capture process under post-combustion and pre-combustion conditions, and determined the effects of pore volume and pore length on adsorption. It was found that CO₂ capture on AC under post-combustion conditions (1bar and 298K) needs exclusively smaller micropores. Maxima CO₂ retention capacities under post-combustion conditions can only be found for carbons having high micropore volume with pore sizes below 0.6nm. 98–100wt% CO₂ capture capacity has been reached for highly activated carbons with pore sizes centered in the supermicroporosity range (1.5–2nm) (Martin *et al.*, 2010). Pore size distribution can be controlled with changing the stabilization temperature. The stabilization temperature have an influence on the amount of nitrogen groups formed, as determined by XPS, which enhances the specific adsorbent-adsorbate interaction for CO₂ (Hsiao *et al.*, 2011).

Garcia and coworkers conducted experiments over a commercial activated carbon aiming to explain the influence of adsorption pressure and temperature on CO₂ pre-

combustion capture process. In the tests the pressures were from 5 to 15 bar, and temperatures from 25 to 65°C. The influent gas stream used in the experiments consisted of CO₂/H₂/N₂ gases with 20/70/10 volume ratios at normal conditions. The CO₂ partial pressure was determined to be the most important parameter for CO₂ capture capacity and breakthrough time, which is the time it takes for CO₂ to be detected at the adsorption column outlet. Linear increase in CO₂ capture capacity and the breakthrough time was observed with increasing CO₂ partial pressure. On the contrary, as the temperature increased, both response variables decreased. The maximum values for CO₂ capture capacity and breakthrough time were achieved at 25°C for a stream having 20% CO₂ at partial pressure of 3 bar (Garcia *et al.*, 2011).

Adsorption separation of CO₂, CH₄, and N₂ on microwave activated carbon (MAC) has been investigated by Yi and coworkers. Based on the adsorption equilibrium data obtained by a static volume instrument experiment for CO₂, CH₄ and N₂ on MAC, the adsorption capacities were found in the following order: CO₂>CH₄>N₂. Two adsorption models, Langmuir and Toth, were used to fit the adsorption isotherms. Toth model is found to be more suitable than Langmuir model. The adsorption capacities of the ternary mixtures were predicted by Langmuir and Toth models, and comparison was given in Figure 2.2. It was conferred that a loss in adsorption amount has occurred for each component compared to

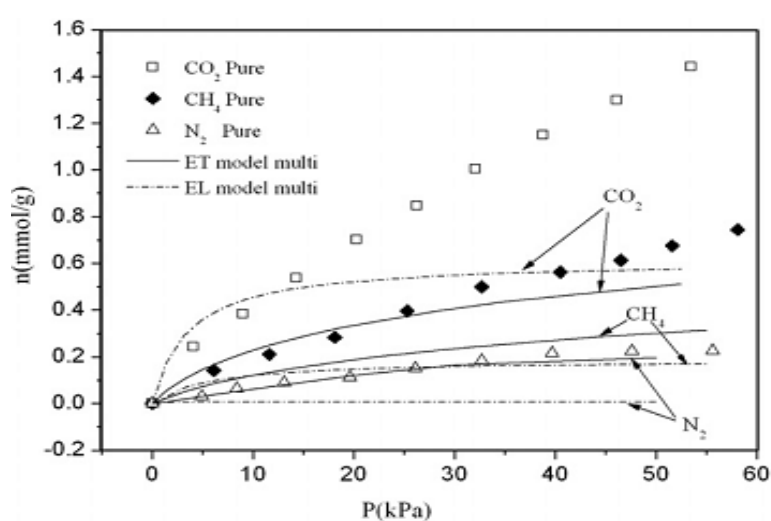


Figure 2.2. Adsorption capacities of CO₂, CH₄, N₂.

the capacity determined from the tests conducted with the pure component, which is an indication of the competitive adsorption. Fortunately, the amount of adsorbed CO₂ still dominates the adsorption system in the ternary mixtures. The selectivity for the separation of the binary mixtures, CO₂/CH₄, CO₂/N₂ and CH₄/N₂, were estimated by using a methodology based on the determination of the equation of state for the Gibbs free energy of desorption of the solid adsorbent, and the highest separation factors were obtained for the CO₂/N₂ and CO₂/CH₄ system (Yi *et al.*, 2013).

Yin *et al.* have examined the effects of pore size and oxygen-containing surface groups on AC for CO₂ separation from synthesis gas. It was found that CO₂ adsorption capacity of AC depends on pores of <0.7 nm under pressure swing adsorption, PSA, condition, and oxygen-containing surface groups on AC have little effect on CO₂ adsorption. Effects of K, Ca, Si, Al and Fe on CO₂ adsorption were investigated, and it was determined that only K addition leads to an enhancement in CO₂ adsorption (Yin *et al.*, 2013).

The interaction of water and CO₂ on carbon materials in adsorption processes gathers great interest from the researchers. Vacuum swing adsorption studies were performed by Xu and coworkers in order to investigate the effect of water on CO₂ adsorption, and separation processes. Simulations and experiments have implied that there was little effect of CO₂ and water on each other's adsorption on the activated carbon. Recovery and purity of CO₂, obtained via single bed vacuum swing experiment, was found to be almost identical in the presence of water as in the dry case (Xu *et al.*, 2013). Low effect of the existence of water vapor on CO₂ capture from flue gas was also approved by other researchers (Xu *et al.*, 2011; Ribeiro *et al.*, 2009).

3. EXPERIMENTAL WORK

3.1. Materials

3.1.1. Gases and Liquids

All of the gases used in this research were supplied by Linde Group, İstanbul. The specifications and applications of the gases and liquids employed in this research are listed in Table 3.1 and Table 3.2.

Table 3.1. Specifications and applications of the gases used.

Gas	Specification	Application
Argon	99.998%	Inert, GC Carrier Gas
Carbon dioxide	99.995%	Reactant, Adsorbate
Carbon monoxide	99.999%	Reactant
Dry air	99.998%	GC 6-way pneumatic valve
Hydrogen	99.995%	Reactant, Reducing Agent
Methane	99.995%	Reactant, Adsorbate
Nitrogen	99.998%	Air treatment
Oxygen	99.998%	Reactant, Air treatment

Table 3.2. Specifications and applications of the liquids used.

Liquid	Specification	Application
Nitrogen	Adv. Tech. R&D Center, Boğaziçi University	FTIR detector
Water	Deionized	Aqueous solution, Reactant

3.1.2. Chemicals

The list of chemicals used for catalyst and adsorbent preparation are given in Table 3.3. All chemicals used are research grade.

Table 3.3. Chemicals used for catalyst and adsorbent preparation.

Chemical	Formula	Specification	Source	MW (g/gmol)
Activated Carbon	C	ROX 0.8	Norit	12.01
Aluminum oxide	γ -Al ₂ O ₃	Catalyst support, high surface area	Alfa Aesar	101.96
Ammonium perhenate	NH ₄ ReO ₄	99.999%	Sigma- Aldrich	268.24
Cerium (III) nitrate hexahydrate	Ce(NO ₃) ₃ .6H ₂ O	99.99%	Sigma- Aldrich	434.23
Hydrochloric acid	HCl	37% aq. solution	Merck	36.46
Nickel (II) nitrate hexahydrate	Ni(NO ₃) ₂ .6H ₂ O	99+%	Merck	290.81
Nitric acid	HNO ₃	65% aq. solution	Merck	63.01
Sodium carbonate	Na ₂ CO ₃	99.9+%	Merck	105.99
Sodium hydroxide	NaOH	Pellet, pure	Merck	40.00

Table 3.3. Chemicals used for catalyst and adsorbent preparation (con't).

Chemical	Formula	Specification	Source	MW (g/gmol)
Sodium nitrate	NaNO ₃	99.0%	Carlo Erba Reagents	84.995
Tetraammine platinum (II) nitrate	Pt(NH) ₄ (NO ₃) ₂	99.995%	Sigma-Aldrich	387.22
Titanium (IV) oxide	TiO ₂	Anatase, 99.9%	Alfa Aesar	79.87

3.2. Experimental Systems

3.2.1. Catalyst and Adsorbent Preparation Systems

The system used for preparing catalysts by incipient-to-wetness impregnation method includes a Retsch UR1 ultrasonic mixer providing uniform mixing, a Büchner flask, a KNF Neuberger vacuum pump, a Masterflex computerized-drive peristaltic pump used for contacting the precursor solution to be impregnated with the support material, a beaker containing the precursor solution and silicone tubing (Figure 3.1).

In this method, specified amount of support (2-5 g) was placed in the Büchner flask and kept under vacuum both before and after the addition of the precursor solution. Since trapped air in the pores of the support could prevent penetration of the solutions, vacuum pump was used to remove the trapped air, i.e. to evacuate the support and to give a uniform distribution of the active component. Before impregnating the solution, the support material was mixed by using ultrasonic mixer for 30 minutes under vacuum. The peristaltic pump was used to feed the precursor solution at a rate of 0.5 ml/min via silicone tubing to the support material in the Büchner flask. The slurry was mixed in the ultrasonic mixer during the impregnation in order to maintain uniform distribution of the precursor solution. After the addition of precursor solution, the slurry was ultrasonically mixed for an additional 90 minutes under vacuum. The obtained thick slurry was dried overnight in the oven.

The system used for catalyst preparation by homogeneous deposition precipitation method includes a Julabo ED-13 water bath circulator, a beaker, a Heidolph RZR 2021 overhead stirrer and a Mettler Toledo SevenGO pH meter (Figure 3.2).

The adsorbent preparation system, which was used for HCl and HNO₃ treatments of activated carbons consists of an Electro-mag heating mantle, a soxhlet apparatus, a thimble, a condenser, a round bottom flask, a 2 L beaker and a Heidolph MR 3001 magnetic stirrer depending on the treatment type (Figure 3.3).

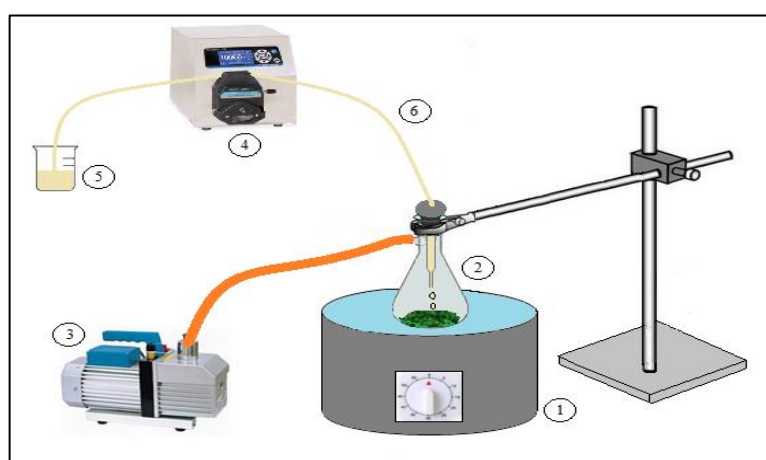


Figure 3.1. Schematic diagram of the impregnation system (1. Ultrasonic mixer, 2. Büchner flask, 3. Vacuum pump, 4. Peristaltic pump, 5. Beaker, 6. Silicone tubing) (Başar, 2016).

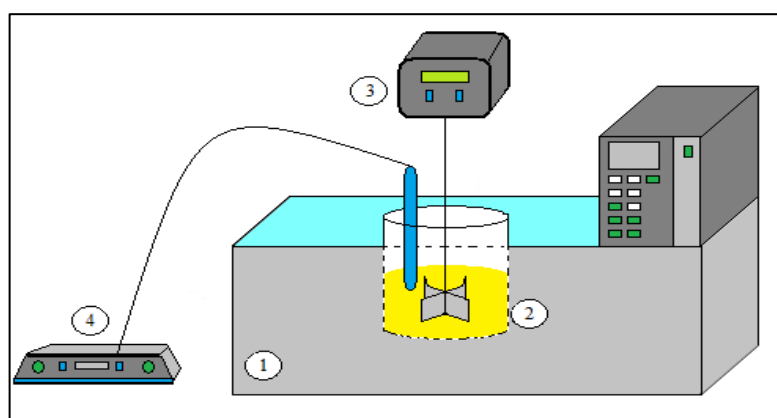


Figure 3.2. Schematic diagram of the deposition precipitation system 1. Ultrasonic mixer or water bath circulator, 2. Beaker, 3. Overhead stirrer, 4. pH meter (Başar, 2016).

The air oxidation treatment and calcination of the activated carbon samples were carried out in a Lenton tube furnace equipped with a Eurotherm 91e controller; the N_2 , O_2 , and He gases were supplied from pressurized cylinders by gas regulators and Brooks/Aalborg mass flow controllers.

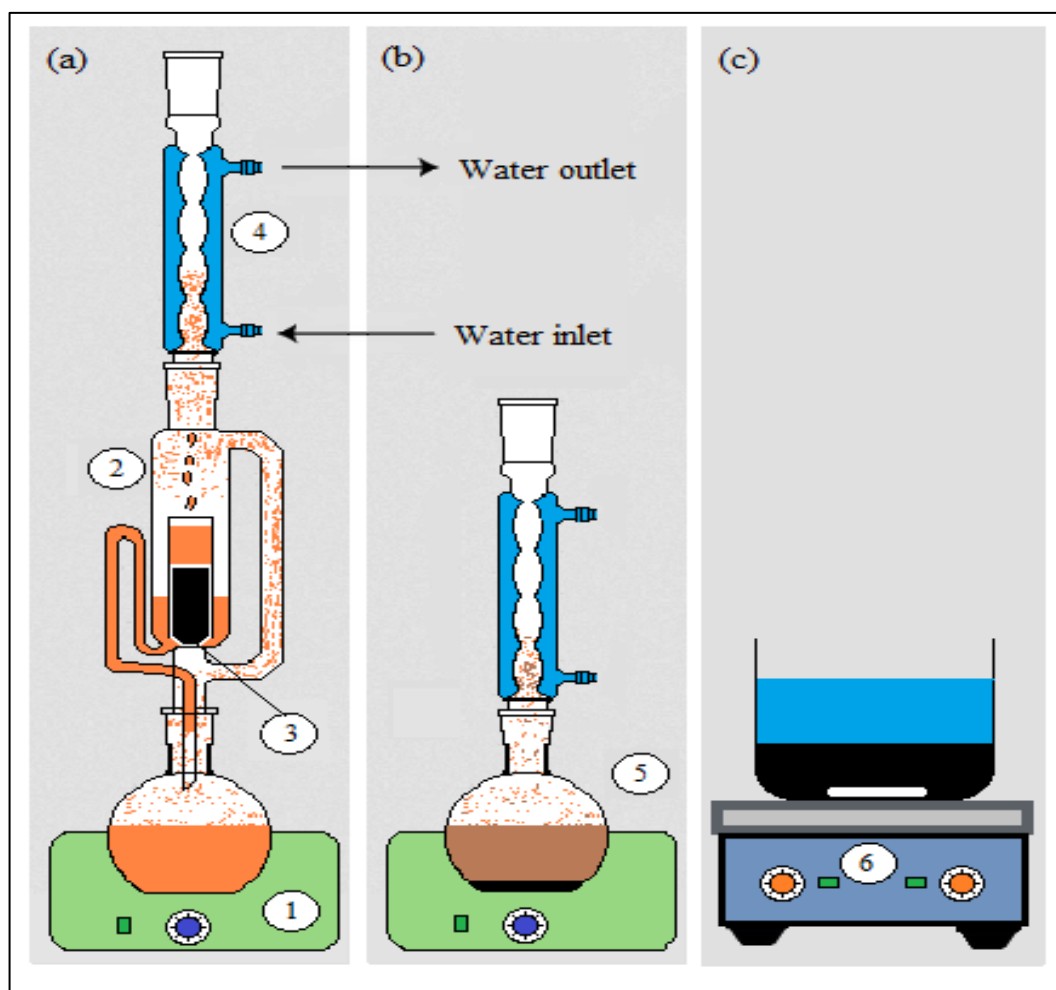


Figure 3.3. Schematic diagram of the system used for (a) HCl, (b) HNO_3 and (c) DI water treatments of activated carbons - 1. Heater, 2. Soxhlet apparatus, 3. Thimble, 4. Condenser, 5. Flask, 6. Magnetic stirrer (Başar, 2016).

3.2.2. Catalytic Reaction System

The catalytic reaction system used in this study was designed and constructed in the Catalysis and Reaction Engineering Laboratory of Chemical Engineering Department, Boğaziçi University and involves three main sections: feed, reaction and product analysis

(Figure 3.4). The reaction system included two consecutive reactors in order to enable testing the response of WGS catalyst performance to the changes in OSR feed composition.

The feed section was composed of mass flow control systems, 1/4", 1/8" and 1/16" SS tubing, valves and fittings for feeding liquid water and gaseous species, i.e. argon, oxygen, methane, carbon monoxide, carbon dioxide and hydrogen. The high purity gases were supplied by pressurized cylinders and were passed through gas flow regulators. The flow rates of the gasses were controlled by Brooks Instrument mass flow controllers and the set values were adjusted by two Brooks Instrument 0154 series control boxes. On-off valves were placed in front of the mass flow controllers to protect them from possible back-pressure fluctuations. In order to meter the flow of individual species and adjust desired feed composition, each gas was fed from an independent line. It was possible to divert the flow direction of feed gases before entering OSR reactor through the bypass line by using a three way valve, so that the feed mixture allowed to come to an equilibrated state.

Water was introduced to the system at constant flow rates using a Jasco PU-2089 Plus quaternary gradient pump. In order to feed water in gaseous state, the 1/16" SS tubing through which water was allowed to flow and the whole reactant mixing zone were kept at 135 ± 5 °C using a heating tape, a 16-gauge wire K type sheathed thermocouple and Shimaden SR91 temperature controller. The heating tape was covered with ceramic wool insulation to prevent heat losses.

The reactants, metered and mixed in the feed section, were allowed to flow to the first reaction section. At the exit of the first reactor it was possible to divert the flow direction of OSR product gases before entering the second reactor via a bypass line by using a three way valve so that the OSR product composition could be measured using gas chromatographs. If this was not the case, the exit stream of first reactor was allowed to flow into the second reactor by 1/4" SS tubing which was heated up to 135 ± 5 °C using a Cole-Parmer heating tape. Reaction sections were composed of two 47 cm×20 cm×20 cm furnaces with 3.4 cm OD each controlled by a Shimaden FP23 programmable temperature controller, K-type sheathed thermocouples and a down-flow, 55 cm long 1/4" OD SS tubular microreactors. During the reaction tests, the catalyst beds which were stabilized by silane treated glass wool were placed in the center of the reactors. Ceramic glass wool insulations were placed on top

and bottom ends of the reactors furnace in order to prevent heat loss and provide a stable temperature profile.

The product stream leaving the reactor involves steam. Since steam is known to damage the gas chromatograph (GC) packed column, two cold traps were placed before GC inlet in order to condense water. The line between the cold traps and the reactor was kept at 135 ± 5 °C to avoid any condensation of steam along the SS tubing.

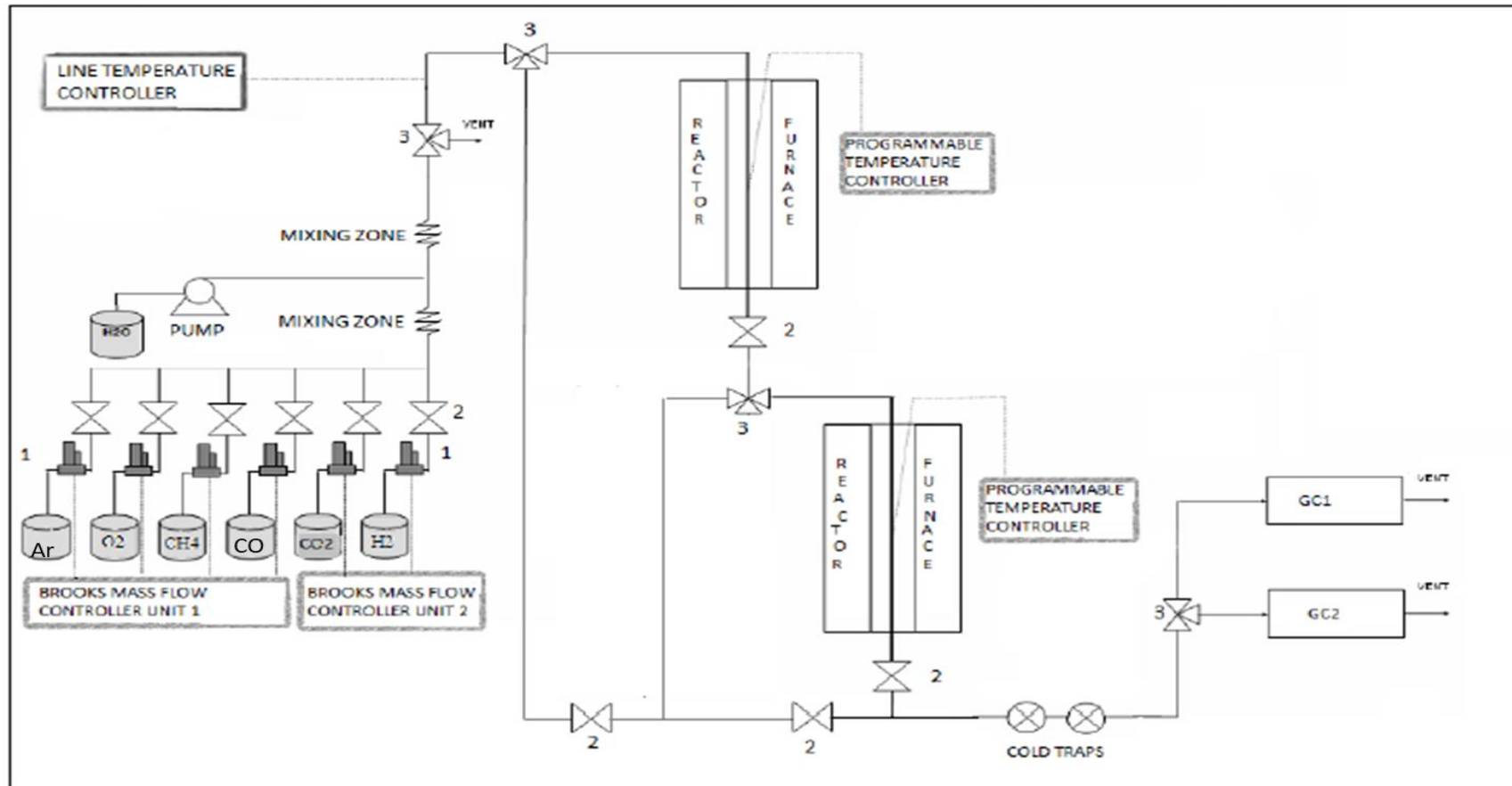


Figure 3.4. Schematic representation of OSR-WGS reaction system (1) MFC, (2) On-off valve, (3) Three-way valve (Gökaliler, 2012).

3.2.3. Product Analysis Systems

Two parallel Agilent Technologies 6850 GCs equipped with Molecular Sieve 5A and Hayesep D columns were used for analyzing gas mixtures in serial OSR-WGS reactions. In WGS reaction tests, only GC2 with Hayesep D column was used, since O₂ is not a reactant or a product in this reaction. Analysis conditions of the GCs are given in Tables 3.4.

Table 3.4. Gas analysis conditions for OSR and/or WGS reaction system.

	GC1	GC2
Column Packing Material	Molecular Sieve 5A	Hayesep D
Column Temperature	40°C	40°C
Column Length x ID	2m x 3mm	3m x 3mm
Carrier Gas	Argon	Argon
Carrier Gas Flow Rate	15 ml/min	15 ml/min
Detector Type	TCD	TCD
Detector Temperature	150°C	150°C
Inlet Temperature	100°C	100°C
Sample Loop Volume	1 ml	1 ml
Gases Analyzed	H ₂ , CH ₄ , CO, O ₂	H ₂ , CH ₄ , CO, CO ₂

Before proceeding with the experiments, the GCs were calibrated by known values of the species to be analyzed under the conditions given in Table 3.4 by reading the area under the peak calculated by the integrator. Using this procedure, volume versus peak area curves were constructed for each gas and the corresponding calibration factors were determined by linear regression.

3.2.4. Catalyst Characterization Systems

This part involves the analytical and spectroscopic techniques and systems, which are used to characterize the physical, microstructural and electronic properties of the catalyst samples prepared and to examine the changes during and/or after reaction of the freshly reduced catalyst samples.

3.2.4.1. Scanning Electron Microscopy and Energy Dispersive X-Ray. Micrographs of the freshly reduced and spent catalyst samples as well as the adsorbent samples were acquired by SEM and SEM-EDX to analyze their microstructure and morphology, to clarify their quantitative/qualitative elemental analysis and to obtain information on the dispersion of the metals on the catalyst surface. The tests were conducted in a Philips XL 30 ESEM-FEG system having a maximum resolution of 2 nm. Back-scattered electron (BSE) images were also obtained for modified activated carbon samples besides the secondary electron (SE) images at high resolution. The analyses were performed in the Advanced Technologies Research and Development Center of Boğaziçi University.

3.2.4.2. X-Ray Diffraction. The crystalline phases of the catalyst samples were identified by using a Rigaku D/MAX-Ultima+/PC X-ray diffraction equipment having an X-ray generator with Cu target and scan speed of 2°/min. The analyses were performed in the Advanced Technologies Research and Development Center of Boğaziçi University.

3.2.4.3. X-Ray Photoelectron Spectroscopy. The extent of electronic interaction between metal components of the freshly reduced samples as well as the oxidation states of the metallic species present on the fresh and spent samples was investigated through determination the amounts of metallic phases by X-ray photoelectron spectroscopy. The analyses were performed in the Advanced Technologies Research and Development Center of Boğaziçi University using a Thermo Scientific K-Alpha X-ray Photoelectron Spectrometer.

3.2.4.4. Raman Spectroscopy. The possible coke formations on spent catalyst samples were examined with Raman spectroscopy. Raman spectra of the freshly reduced and spent catalyst samples were obtained by using a Renishaw in Via Raman microscope with the following operation parameters: 514 nm 20 mW Ar⁺ laser as the excitation source, laser intensity of ~10 mW, 5 s acquisition time; a total of 20 accumulation/spectrum.

3.2.4.5. CO Chemisorption. Pt dispersion was measured by CO Chemisorption to quantify the total amount of metal available for reaction using Hiden Analytical CATLAB. The samples were reduced *in situ* prior to CO uptake measurements. The CO uptake analyses were performed at room temperature with 60 ml/min He flow via injecting 0.1 ml pulses involving 5% CO over the catalyst samples. A CO/Pt stoichiometry of 1 was assumed for dispersion calculations.

3.2.4.6. Total Surface Area-Total Pore Volume. Total surface area and pore volume distribution of the adsorbents were measured by performing N₂ adsorption at liquid nitrogen temperature via 3-Flex Surface Characterization Micromeritics using a multi-point technique and the Brunauer-Emmett-Teller (BET) equation and Dubinin-Raduskevich Method, respectively.

The BET equation can be written as follows:

$$\frac{1}{v[(P_0/P)-1]} = \frac{(c-1)}{v_m c} \left(\frac{P}{P_0}\right) + \frac{1}{v_m c} \quad (3.1)$$

Where P and P₀ are the equilibrium and saturation pressure of adsorbates at the temperature of adsorption, v is the adsorbed gas quantity, and v_m is the monolayer adsorbed gas quantity. The BET constant, c, can be expressed as:

$$c = \exp\left(\frac{E_1 - E_L}{RT}\right) \quad (3.2)$$

Where E_1 is the heat of adsorption for the first layer and E_L is that for the second and higher layers, R is the universal gas constant and T is the adsorption temperature.

Dubinin-Raduskevich equation, which describes the adsorption of microporous adsorbents such as activated carbon, is given as follows:

$$\frac{W}{W_0} = \exp \left[- \left(\frac{RT}{E} \ln \left(\frac{P}{P_0} \right) \right)^2 \right] \quad (3.3)$$

Where W and W_0 imply the adsorbed volume (cc/g) and saturated adsorption capacity (cc/g), respectively. R expresses the universal gas constant; T , temperature (K); E , characteristic energy (J/mol) and P_0 saturated steam pressure (mm Hg).

3.2.5. Fourier Transform Infrared Spectroscopy-Mass Spectrometry (FTIR-DRIFTS-MS) System

The FTIR absorbance spectra have been collected on a Bruker Vertex 70V equipped with a Mercury-Cadmium-Telluride (MCT) detector. PIKE technologies DRIFTS cell with ZnSe window with PIKE Technologies temperature controller and Brooks mass flow controllers allowed thermal treatments under controlled atmospheres and spectrum scanning at controlled temperatures (25-375°C).

A Hiden Analytical HPR-20 Quartz Inert Capillary Mass Spectrometer was connected to the FTIR-DRIFTS system outlet to provide online real-time data representing the outlet mixture composition. In order to be used in steam containing experiments, New Era Pump System brand syringe pump was used.

Figure 3.5 shows the schematic representation of the FTIR-DRIFTS-MS system. The feed section was composed of mass flow control systems, 1/4", 1/8" and 1/16" stainless steel tubing and fittings for feeding gaseous mixtures with controlled compositions, i.e. carbon monoxide,

carbon dioxide, methane, hydrogen, helium and argon. The high purity gases were supplied by pressurized cylinders and were passed through the gas flow regulators. The flow rates of the gasses were controlled by Brooks Instrument mass flow controllers and the set values of were adjusted by two Brooks Instrument 0154 series control boxes. Three-way valves, which were placed in the outlet of the mass flow controllers, provide two side flow opportunity through the line which steam was not included and the one with steam included. In order to meter the flow of individual species and adjust desired feed ratios, each gas was fed from an independent line. The liquid water was introduced into the reaction system at constant flow rate via New Era Pump System syringe pump. To feed water in the gaseous state, 1/16" stainless steel tubing, through which water was allowed to flow and the whole reactant mixing zone were kept about at $140\pm 5^{\circ}\text{C}$ by using a Cole-Parmer heating tape covered with ceramic wool insulation, a 16-gauge wire K type sheathed thermocouple and EMKO PID temperature controller. The line from the FTIR outlet to the MS entrance was also heated to $40\pm 5^{\circ}\text{C}$ as a precaution to prevent condensation of water, which was already used in the amount that does not condense even at room temperature.

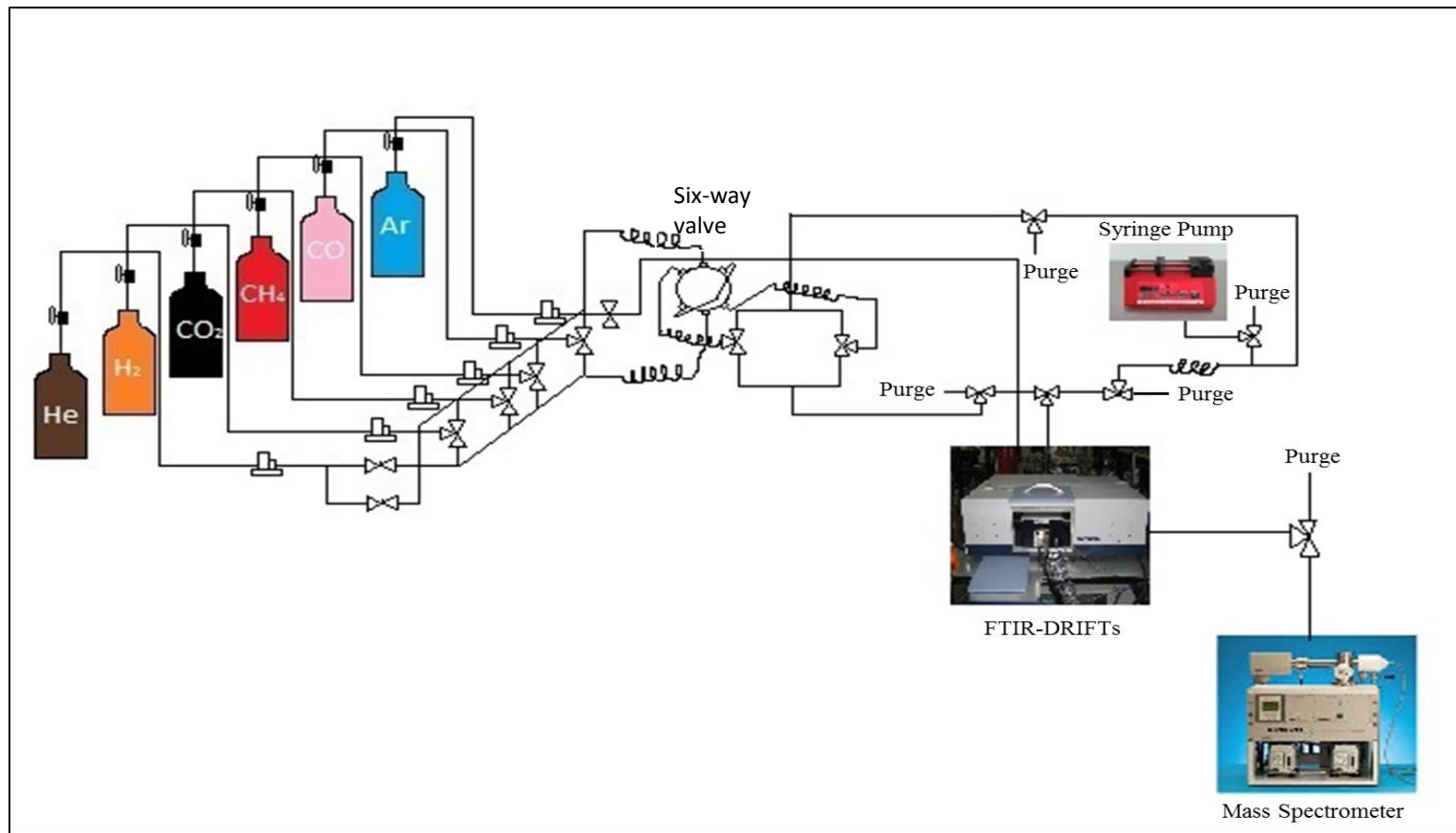


Figure 3.5. Schematic representation of FTIR-DRIFTS-MS system.

3.2.6. Gravimetric Gas Sorption Analysis- Mass Spectrometry System (IGA-MS)

The gravimetric gas sorption analysis system included a Hiden Isochema Intelligent Gravimetric Analyzer IGA-003 Dynamic Mixed Gas Sorption Analyzer (Figure 3.6) and a Hiden Analytical Dynamic Sampling Mass Spectrometer (DSMS). It was designed to study the single/mixed gas sorption equilibrium isotherms and sorption kinetics on materials such as activated carbons, zeolites, polymers and catalysts from vacuum to high pressures (up to 20 bar) in the temperature range from -190 °C to 1000 °C by using gravimetric technique with a resolution of 0.1 µg. The system enabled a broad range of experiments to be performed by using several accessories including vacuum pump, standard furnace, cryofurnace, humidifier, pressurizer, etc. In sorption tests, pressure was changed ramp-wise and then held constant during sorption at the set point. Weight data were acquired and analyzed in real time to determine kinetic parameters and to predict the exact point of equilibrium mass uptake. Equilibrium points (pressure vs. weight data) were collected and plotted as an isotherm. The combination of gravimetric sorption measurement and unadsorbed/evolved gas analysis provided a reliable tool for material characterization, thermal decomposition and desorption processes and also temperature programmed (TPO-TPR-TPD) techniques. The oxygen storage capacity tests were performed by taking advantage of this feature of the device. The calculations were based on monitoring the change in weight of the sample subjected to WGS reaction conditions with increasing temperature of sample up to 800°C under inert atmosphere.

IGA was designed and programmed to work in two pressure/control modes; which were static and dynamic pressure modes. In static mode, a single component gas was supplied by pressurized cylinder through a gas pressure regulator and sent directly to IGA chamber without controlling the flow via MFC. In dynamic pressure mode, one or more gases were supplied by pressurized cylinders through gas pressure regulators and MFCs at constant pressure and at constant flow rate to IGA chamber (e.g. multicomponent sorption). There was always some flow of gas into or out of the IGA chamber to maintain constant pressure inside. Dynamic mode of IGA was used in all oxygen storage capacity and adsorption-desorption tests of this study.

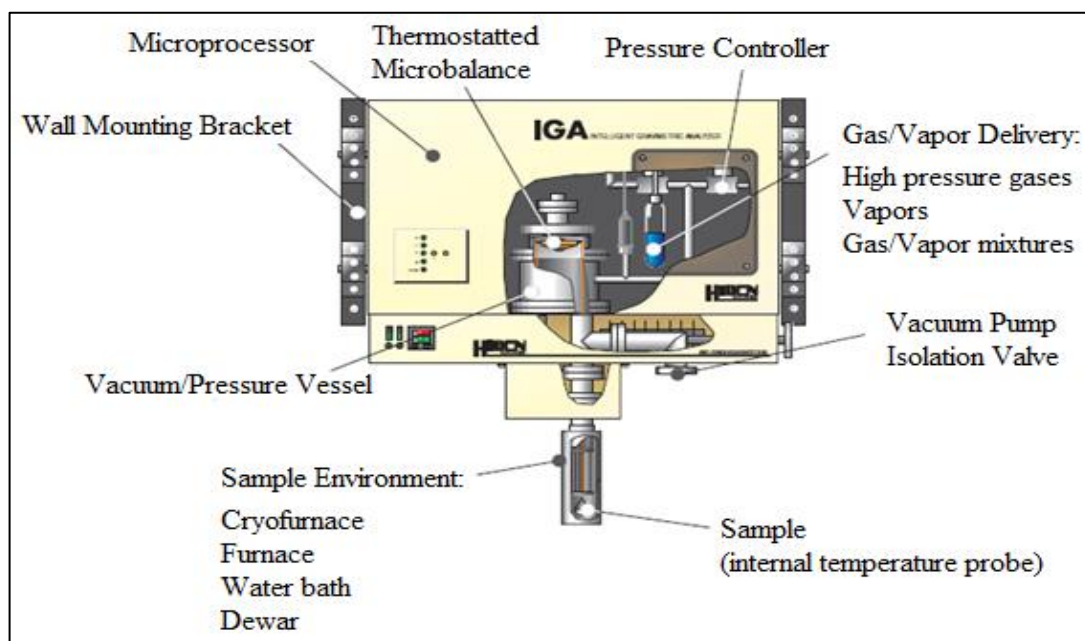


Figure 3.6. Schematic diagram of the Intelligent Gravimetric Analyzer (IGA).

The feed section of the gravimetric gas sorption analysis system included Brooks model 5850E MFCs for controlled flow of the inlet gases, i.e. CO₂, CH₄, H₂, CO and He, which were supplied by pressurized cylinders, a NE-300 model New Era Pump Systems Inc. syringe pump for water feed, and 1/4", 1/8", 1/16" Swagelok stainless steel tubings, valves and fittings (Figures 3.7). On-off valves were placed at the exit of mass flow controllers to protect them from possible back pressure. K-type sheathed thermocouple was placed inside the water transfer line and connected to the temperature controller (Shimaden SR91) with ± 0.1 K sensitivity. In order to send the system trace amount of water, NE-300 model New Era Pump Systems Inc. syringe pump was used. The system also involved pressurizer, Parker ABP1 model back pressure regulator (BPR) and Keller LEO1 digital manometer to perform high pressure analysis. Syringe pump was used to supply water to the system in the OSC tests of WGS catalysts, whereas back pressure regulator was used in high pressure adsorption-desorption tests of the modified activated carbon adsorbents. In order to conduct the tests e.g. at 5 bar, the gases were sent at 7 bar from the gas pressure regulators first to the mass flow controllers then to the pressurizer, whose high volume enabled to prepare homogeneous and pressurized gas mixture, the BPR opening was adjusted in such a way that the digital manometer displays a constant value of 5 bar and the extra gas mixture was purged from the other outlet of the BPR.

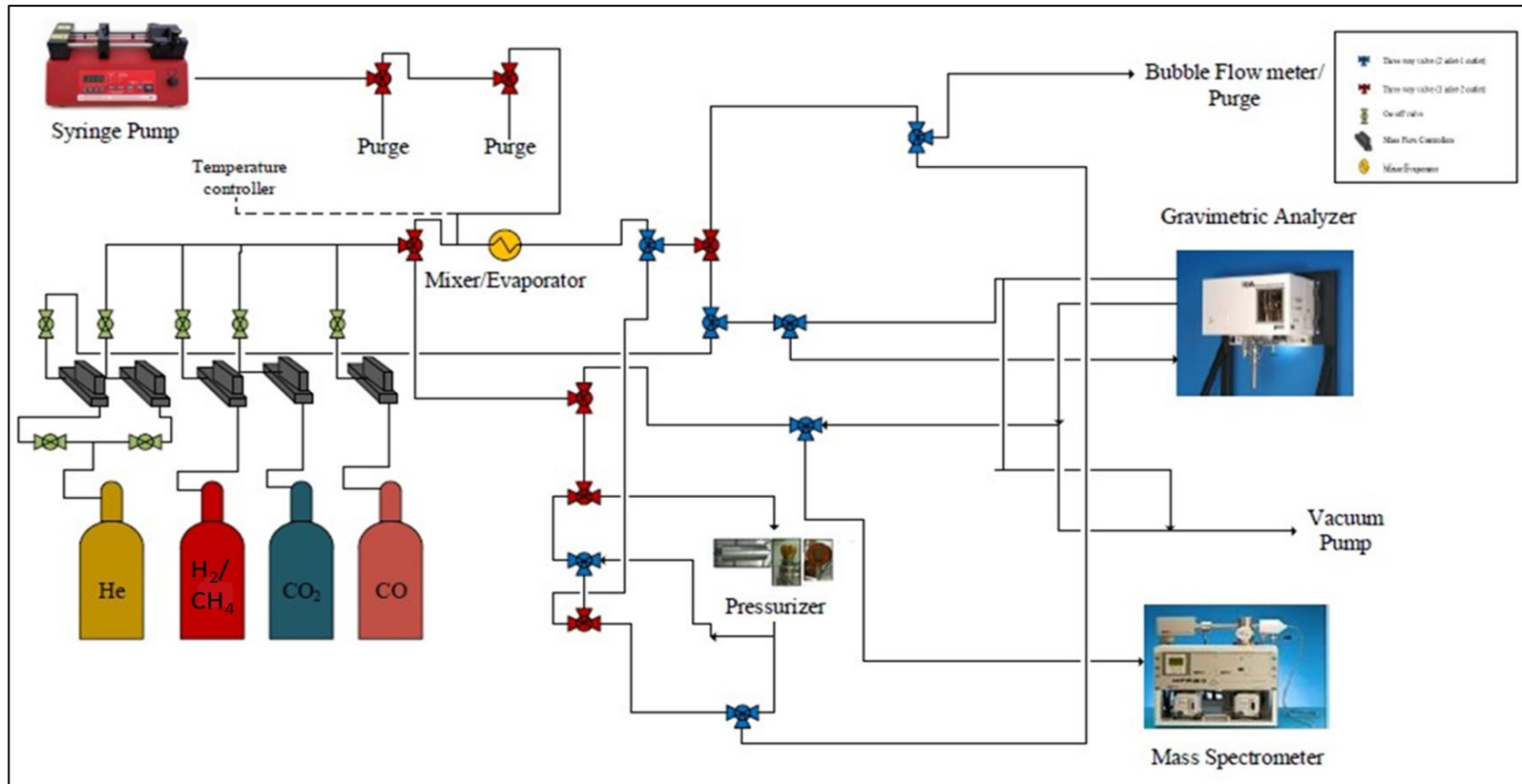


Figure 3.7. Schematic diagram of the gravimetric gas sorption analysis system (Öztürk, 2018).

3.3. Catalyst/Adsorbent Preparation and Pretreatment

In this study, six sets of catalysts were prepared, one for oxidative steam reforming reaction and five for water-gas shift reaction. Also a set of AC based adsorbents were prepared with different pretreatments and calcination temperatures.

3.3.1. Oxidative Steam Reforming Catalyst (Pt-Ni/ δ -Al₂O₃)

γ -Al₂O₃ pellets was crushed and sieved into 250-354 μm (45-60 mesh) particle size. In order to modify the support into δ -Al₂O₃, which has an appropriate surface area and also exhibits high thermal stability, γ -Al₂O₃ was dried at 200°C for 2 hours and calcined at 900°C for 4 hours in a muffle furnace.

The bimetallic Pt-Ni/ δ -Al₂O₃ catalyst (0.2%Pt-10%Ni) was prepared by a sequential route in which Pt solution was impregnated over initially prepared and calcined Ni/ δ -Al₂O₃ catalyst, which was prepared by the incipient-to-wetness impregnation method using aqueous solution of Ni(NO₃)₂.6H₂O as explained in Section 3.2.1. The precursor solutions were prepared by dissolving calculated amount of precursor salt in definite amounts of deionized water (ca. 1.1 ml DI water/g support). The resulting slurry that was obtained at the end of first impregnation, was then left drying overnight at 110°C and calcined at 600°C for 4h to obtain NiO/ δ -Al₂O₃. Similarly, aqueous solution of Pt(NH₄)₄(NO₃)₂ was impregnated over obtained monometallic catalyst. The resulting slurry involving two metals was dried overnight at 110°C and finally calcined at 500°C for 4 hours.

In order to obtain high catalytic activities, a pretreatment involving the reduction of the active metals from the oxide state, which is formed during the calcinations, to the metallic state is required prior to the reaction, since catalysts in their oxide forms are usually inactive for the reactions.

Temperature programmed reduction studies have shown that reduction using pure H₂ flow at 500°C K for 4 hours is a suitable procedure for pretreating the bimetallic Pt-Ni catalyst (Ma, 1995). Ma has also reported that during reduction, the water in the catalyst may cause premature sintering, which may lead to deactivation before the reaction. Considering

these issues, the following stepwise pretreatment and reduction procedure was followed for the bimetallic OSR catalyst.

After placing the catalyst into the constant temperature zone of the microreactor, inert flow was set to 50 ml/min for 7 minutes to remove O₂ from the system at RT. The gas flow was then switched from Ar to H₂ and it was set to flow at 20 ml/min. Reduction was started by heating the catalyst from RT to 150°C at a rate of 10°C/min. The temperature was kept constant at 150°C for 30 minutes for the removal of adsorbed water. Third step involved heating the sample from 150°C to 300°C at a rate of 5°C/min, followed by an isothermal segment of 30 minutes at 300°C for the removal of crystalline water. The temperature was then increased from 300°C to 500°C at a rate of 2°C/min and finally kept constant at 500°C for 4 hours. After reduction, the system was allowed to cool down to ca. 150°C under H₂ flow. Below this temperature, the gas flow was switched to Ar and it was allowed to flow at 5 ml/min overnight to sweep H₂ from the system prior to the catalytic tests (Figure 3.8).

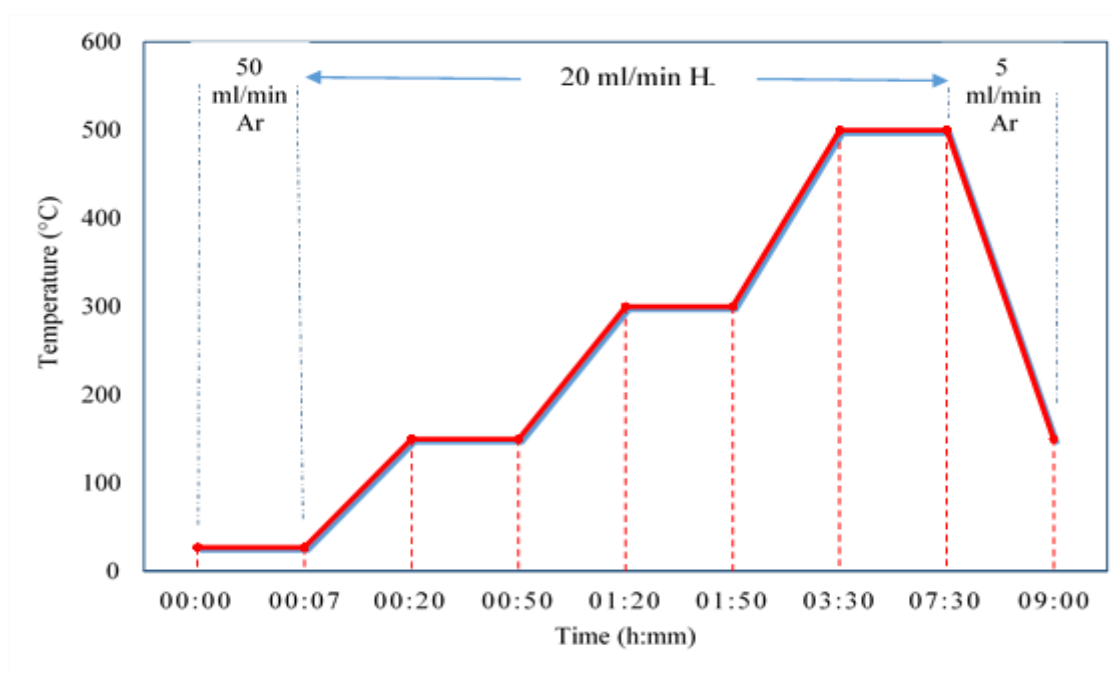


Figure 3.8. Pretreatment and reduction procedure for Pt-Ni/ δ -Al₂O₃ catalyst.

3.3.2. Water Gas Shift Catalysts

3.3.2.1. Preparation of CeO₂ support

Support material was prepared via homogeneous precipitation of cerium (III) nitrate hexahydrate and NaCO₃. Briefly, aqueous Na₂CO₃ solution was slowly added to the cerium-precursor containing solution, which was kept at 60°C and stirred at 200 rpm in a water bath. Addition of sodium carbonate solution continued until the pH value reached to 8. The resulting suspension was left mixing for an hour in the water bath at 60°C under controlled temperature and pH. Afterwards, it was filtered by using Watman filter paper under vacuum, and washed with deionized water several times. It was then dried overnight at 110°C and finally calcined in a muffle furnace at 400°C for 4h (Çağlayan, 2011).

3.3.2.2. Preparation of Pt-Re-Na/CeO₂ and Pt-Re-Na/TiO₂

Trimetallic Pt-Re-Na/CeO₂ catalysts were prepared via two different methods, namely coimpregnation and sequential impregnation of rhenium and sodium metal precursors (NH₄ReO₄ and NaNO₃). Catalysts, which were prepared with different impregnation techniques and different Na loadings were listed in Table 3.5. In order to examine the effect of support type, Pt-Re-Na/TiO₂ catalyst was also prepared with the same metal loadings.

Tablo 3.5. Pt-Re-Na catalysts and applied impregnation methods.

1%Pt-1%Re-1%Na/CeO ₂ _1	Na-Re coimpregnation, Pt sequential impregnation
1%Pt-1%Re-1%Na/CeO ₂ _2	Na-Re-Pt sequential impregnation
1%Pt-1%Re-2%Na/CeO ₂	Na-Re-Pt sequential impregnation
1%Pt-1%Re-3%Na/CeO ₂	Na-Re-Pt sequential impregnation
1%Pt-1%Re-1%Na/TiO ₂	Na-Re-Pt sequential impregnation

1%Pt-1%Re-1%Na/CeO₂_1 catalyst was prepared via Pt impregnation subsequent to Na-Re coimpregnation. 2 g of CeO₂ support in an erlenmeyer was placed into the ultrasonic mixer and left 25 minutes under vacuum to discharge the pores. In order to prepare Re-

Na/CeO₂ catalyst, sodium nitrate (NaNO₃) and ammonium perrhenate (NH₄ReO₄) aqueous solution, which contains 1% Re and 1% Na was confected (using ca. 1.25 ml DI water/g support). The signified solution was impregnated over support material under vacuum via peristaltic pump. Resulting slurry was left in the ultrasonic mixer under vacuum during 1.5 h. It was then left drying overnight at 110°C and calcined at 400°C in the muffle furnace for 2h to obtain Re-Na/CeO₂. Pt(NH₃)₄(NO₃)₂ aqueous solution (using ca. 1.1 ml DI water/g support), which includes 1% Pt, was impregnated over promoted support by following the same procedures. Slurry form of Pt-Re-Na/CeO₂ was left drying overnight at 110°C and calcined at 400°C in the muffle furnace for 4h.

1%Pt-1%Re-1%Na/CeO_{2_2}, 1%Pt-1%Re-2%Na/CeO₂, 1%Pt-1%Re-3%Na/CeO₂ catalysts were prepared via sequential impregnation of Na, Re and Pt impregnation. In the first step, NaNO₃ aqueous solution was impregnated over CeO₂ support with intended loadings (1-2-3%). Samples were dried overnight at 110°C and calcined at 400°C in the muffle furnace for 2h to obtain Na/CeO₂. Second impregnation step was carried out with NH₄ReO₄ aqueous solution. Drying and calcination steps were repeated under same conditions. Lastly, Pt(NH₃)₄(NO₃)₂ aqueous solution was added using peristaltic pump. After impregnation period, obtained slurry was left drying overnight at 110°C and calcined at 400°C in the muffle furnace for 4h.

In the preparation stage of 1%Pt-1%Re-1%Na/TiO₂, 99.9% anatase TiO₂ was used as support material. Impregnation and calcination steps in the preparation procedure were applied in the same way with sequential impregnated Pt-Re-Na/CeO₂ catalysts.

3.3.3. Activated Carbon Based Adsorbents

The modified activated carbon adsorbents used in this study were prepared by subjecting the commercial activated carbon to different oxidative, alkali and thermal treatments as described below:

Commercial activated carbon pellets (NORIT ROX 0.8) were crushed and sieved into 354-250 μm (45-60 mesh) particle size referred to as AC0. Then, approximately 20 g of AC0 was placed in an extraction thimble and was washed at 448 K with 200 ml of 2 N HCl solution for 12 hours in a Soxhlet apparatus system to remove the ash and sulfur content in the adsorbent. After the extraction process was completed, the slurry was then rinsed with deionized(DI) water several times and washed with 300 ml DI water for 6 hours to remove HCl remaining on the activated carbon surface (Figure 3.3a). Finally, the slurry was dried at 110°C overnight. This support is referred to as AC1.

10 g of AC1 was oxidized in a quartz down flow reactor in a tube furnace under the flow of 10 ml/min O₂-190 ml/min N₂ (5% O₂-95% N₂) mixture for 10 hours at 723 K in the system as described in Section 3.2.1. Heating the activated carbon up to the oxidation temperature and cooling down to the RT processes were done under the flow of 150 ml/min N₂. The air oxidized AC material obtained through this procedure is referred to as AC2.

10 g of AC1 was put into a round bottom flask containing 350 ml of 5 N HNO₃ solution and washed at 448 K under total reflux for 3 hours (Figure 3.3b). The suspension was allowed to precipitate throughout the night. The resulting precipitate was put in a 2 L beaker with 1.5 L DI water. The mixture was boiled at 523 K at 250 rpm, until 300 ml of the DI water (ca. 4 hours) evaporated (Figure 3.3c) and was again allowed to precipitate through the night. The rinsing procedure with DI water was repeated several times until there was no precipitation (i.e. the solution had a homogeneous appearance). Then the solution was filtrated using vacuum filtration. Obtained AC was dried at 383 K overnight. The nitric acid oxidized AC material obtained through this procedure is referred to as AC3.

AC6 was prepared via impregnation of NaOH solution. NaOH solution, which has 10% Na content and ca. 2.1 ml DI/g AC, was impregnated over 3-5 g AC2 under vacuum.

The obtained slurry was dried at 388 K overnight and then subjected to calcination at different temperatures under flow of 5% O₂- 95%N₂ mixture for 2h. The calcination temperatures were 200, 250 and 300°C. The samples were named according to the calcination temperatures as AC6-200, AC6-250 and AC6-300. The same impregnation procedure was also applied to AC3. The slurry was dried at 388 K overnight and was calcined at 175, 200 and 250°C. The resulting adsorbents were named as AC7-175, AC7-200 and AC7-250.

Table 3.6. List of modified activated carbon adsorbents.

Name	Treatment Type
AC0	NORIT ROX
AC1	HCl washed AC0
AC2	Air oxidized AC1
AC3	HNO ₃ oxidized AC1
AC6-200	NaOH impregnated and calcined (200°C) AC2
AC6-250	NaOH impregnated and calcined (250°C) AC2
AC6-300	NaOH impregnated and calcined (300°C) AC2
AC7-175	NaOH impregnated and calcined (175°C) AC2
AC7-200	NaOH impregnated and calcined (200°C) AC2
AC7-250	NaOH impregnated and calcined (250°C) AC2

3.4. Single WGS and serial OSR-WGS Reaction Tests

3.4.1. WGS Performance Tests:

WGS reaction tests were performed under two types of feed, namely ideal and realistic feeds. In WGS performance tests, two different H₂O/CO ratio were used for each type of feed. Feed conditions used in performance tests are given in Table 3.7. Tests conducted under each feed composition were performed at 3 different temperatures, i.e. 300°C, 350°C

and 400°C. Each performance test was conducted over 75 mg freshly reduced catalyst samples for 6h TOS by keeping GHSV as $120000 \text{ ml g}_{cat}^{-1} \text{ h}^{-1}$.

Table 3.7. WGS performance test feed compositions.

Reaction Condition	Feed Composition	H₂O/CO
Ideal #1	3% CO, 15% H ₂ O, 82% Ar	5
Ideal #2	3% CO, 6% H ₂ O, 91% Ar	2
Realistic #1	4.9% CO, 32.7% H ₂ O, 30% H ₂ , 10.4% CO ₂ , 22% Ar	6.7
Realistic #2	2.1% CO, 34.1% H ₂ O, 23.7% H ₂ , 12.3% CO ₂ , 27.8% Ar	16.2

Before starting the performance tests, freshly reduced catalyst samples were heated to reaction temperature under inert (Ar) flow. In order to obtain homogeneous and stable feed composition, feed flow was sent to purge for 1.5 hour before entering the reactor. TOS performance tests were started by directing the feed flow through reactor. The first product analysis was carried out at 30 minutes TOS and it was proceeded during 6 hours to receive data every 1 hour. WGS reaction tests were performed in the first reactor of the reaction system presented in Figure 3.4. The summary of the WGS experiments are given in Table 3.8.

Table 3.8. Summary of the performed WGS experiments.

Experiment #	Catalyst	Feed	Temperature (°C)
1	1%Pt-1%Re-1%Na/CeO ₂ _1	Ideal #1	300
2	1%Pt-1%Re-1%Na/CeO ₂ _1	Ideal #1	350
3	1%Pt-1%Re-1%Na/CeO ₂ _1	Ideal #1	400
4	1%Pt-1%Re-1%Na/CeO ₂ _1	Ideal #2	300
5	1%Pt-1%Re-1%Na/CeO ₂ _1	Ideal #2	350
6	1%Pt-1%Re-1%Na/CeO ₂ _1	Ideal #2	400
7	1%Pt-1%Re-1%Na/CeO ₂ _1	Realistic #1	300
8	1%Pt-1%Re-1%Na/CeO ₂ _1	Realistic #1	350
9	1%Pt-1%Re-1%Na/CeO ₂ _1	Realistic #1	400
10	1%Pt-1%Re-1%Na/CeO ₂ _1	Realistic #2	300
11	1%Pt-1%Re-1%Na/CeO ₂ _1	Realistic #2	350
12	1%Pt-1%Re-1%Na/CeO ₂ _1	Realistic #2	400
13	1%Pt-1%Re-1%Na/CeO ₂ _2	Ideal #1	300
14	1%Pt-1%Re-1%Na/CeO ₂ _2	Ideal #1	350
15	1%Pt-1%Re-1%Na/CeO ₂ _2	Ideal #1	400
16	1%Pt-1%Re-1%Na/CeO ₂ _2	Ideal #2	300
17	1%Pt-1%Re-1%Na/CeO ₂ _2	Ideal #2	350
18	1%Pt-1%Re-1%Na/CeO ₂ _2	Ideal #2	400
19	1%Pt-1%Re-1%Na/CeO ₂ _2	Realistic #1	300
20	1%Pt-1%Re-1%Na/CeO ₂ _2	Realistic #1	350
21	1%Pt-1%Re-1%Na/CeO ₂ _2	Realistic #1	400
22	1%Pt-1%Re-1%Na/CeO ₂ _2	Realistic #2	300
23	1%Pt-1%Re-1%Na/CeO ₂ _2	Realistic #2	350
24	1%Pt-1%Re-1%Na/CeO ₂ _2	Realistic #2	400
25	1%Pt-1%Re-2%Na/CeO ₂	Ideal #1	300
26	1%Pt-1%Re-2%Na/CeO ₂	Ideal #1	350
27	1%Pt-1%Re-2%Na/CeO ₂	Ideal #1	400

Table 3.8. Summary of the performed WGS experiments (con't.).

Experiment #	Catalyst	Feed	Temperature (°C)
28	1%Pt-1%Re-2%Na/CeO ₂	Ideal #2	300
29	1%Pt-1%Re-2%Na/CeO ₂	Ideal #2	350
30	1%Pt-1%Re-2%Na/CeO ₂	Ideal #2	400
31	1%Pt-1%Re-2%Na/CeO ₂	Realistic #1	300
32	1%Pt-1%Re-2%Na/CeO ₂	Realistic #1	350
33	1%Pt-1%Re-2%Na/CeO ₂	Realistic #1	400
34	1%Pt-1%Re-2%Na/CeO ₂	Realistic #2	300
35	1%Pt-1%Re-2%Na/CeO ₂	Realistic #2	350
36	1%Pt-1%Re-2%Na/CeO ₂	Realistic #2	400
37	1%Pt-1%Re-3%Na/CeO ₂	Realistic #1	350
38	1%Pt-1%Re-3%Na/CeO ₂	Realistic #1	400
39	1%Pt-1%Re-1%Na/TiO ₂	Ideal #1	300
40	1%Pt-1%Re-1%Na/TiO ₂	Ideal #1	350
41	1%Pt-1%Re-1%Na/TiO ₂	Ideal #1	400
42	1%Pt-1%Re-1%Na/TiO ₂	Ideal #2	300
43	1%Pt-1%Re-1%Na/TiO ₂	Ideal #2	350
44	1%Pt-1%Re-1%Na/TiO ₂	Ideal #2	400
45	1%Pt-1%Re-1%Na/TiO ₂	Realistic #1	300
46	1%Pt-1%Re-1%Na/TiO ₂	Realistic #1	350
47	1%Pt-1%Re-1%Na/TiO ₂	Realistic #1	400
48	1%Pt-1%Re-1%Na/TiO ₂	Realistic #2	300
49	1%Pt-1%Re-1%Na/TiO ₂	Realistic #2	350
50	1%Pt-1%Re-1%Na/TiO ₂	Realistic #2	400

3.4.2. Serial OSR- WGS Performance Tests:

WGS reactor was located after OSR reactor in a fuel processor, hence OSR product stream was fed to WGS reactor. Therefore it was considered that performing serial OSR-WGS performance tests of prepared WGS catalysts is also important in order to examine catalytic performance under real feed conditions.

Serial tests of WGS catalysts were conducted in the reaction system presented in Figure 3.4 as the first reactor of the system is OSR reactor and the second one is WGS reactor. Parameters of serial tests were based on the performance results of OSR over 0.2%Pt-10%Ni/ δ -Al₂O₃ obtained in the previous studies conducted under various conditions (Başar, 2016; Öztepe, 2017). The conditions, which gave high OSR activity, were specified and fixed for all serial OSR-WGS tests. OSR reaction temperature was fixed at 450°C for all serial OSR-WGS tests. Temperature effect was examined for WGS reaction, which occurred after OSR reaction. All serial tests were conducted at 3 different WGS reaction temperatures, i.e. 300°C, 350°C and 400°C. Two different feed flow compositions were used in serial tests. Feed flow compositions were determined regarding CO composition obtained in the exit stream of OSR reactor in the previous studies. In order to be able to observe the feed composition effect clearly, produced CO amounts at the exit of OSR reactor were tried to be chosen relatively different. Feed flow compositions, which were used in serial tests are presented in Table 3.9 with S/C and O/C ratios. The summary of the serial OSR-WGS tests are given in Table 3.10.

Table 3.9. Serial OSR-WGS feed compositions.

Feed Flow Compositions	S/C	O/C
14% CH ₄ , 9.3% O ₂ , 56% H ₂ O, 20.7% Ar	4	1.33
14% CH ₄ , 6.7% O ₂ , 56% H ₂ O, 23.3% Ar	4	0.95

Table 3.10. Summary of the performed OSR-WGS experiments.

Experiment #	Catalyst	Feed	Temperature (°C)
1	1%Pt-1%Re-1%Na/CeO ₂ _1	Real#1	300
2	1%Pt-1%Re-1%Na/CeO ₂ _1	Real#1	350
3	1%Pt-1%Re-1%Na/CeO ₂ _1	Real#1	400
4	1%Pt-1%Re-1%Na/CeO ₂ _1	Real#2	300
5	1%Pt-1%Re-1%Na/CeO ₂ _1	Real#2	350
6	1%Pt-1%Re-1%Na/CeO ₂ _1	Real#2	400
7	1%Pt-1%Re-1%Na/CeO ₂ _2	Real#1	300
8	1%Pt-1%Re-1%Na/CeO ₂ _2	Real#1	350
9	1%Pt-1%Re-1%Na/CeO ₂ _2	Real#1	400
10	1%Pt-1%Re-1%Na/CeO ₂ _2	Real#2	300
11	1%Pt-1%Re-1%Na/CeO ₂ _2	Real#2	350
12	1%Pt-1%Re-1%Na/CeO ₂ _2	Real#2	400
13	1%Pt-1%Re-2%Na/CeO ₂	Real#1	300
14	1%Pt-1%Re-2%Na/CeO ₂	Real#1	350
15	1%Pt-1%Re-2%Na/CeO ₂	Real#1	400
16	1%Pt-1%Re-2%Na/CeO ₂	Real#2	300
17	1%Pt-1%Re-2%Na/CeO ₂	Real#2	350
18	1%Pt-1%Re-2%Na/CeO ₂	Real#2	400
19	1%Pt-1%Re-1%Na/TiO ₂	Real#1	300
20	1%Pt-1%Re-1%Na/TiO ₂	Real#1	350
21	1%Pt-1%Re-1%Na/TiO ₂	Real#1	400
22	1%Pt-1%Re-1%Na/TiO ₂	Real#2	300
23	1%Pt-1%Re-1%Na/TiO ₂	Real#2	350
24	1%Pt-1%Re-1%Na/TiO ₂	Real#2	400

3.5. *In situ* and *operando* FTIR-DRIFTS-MS Studies

FTIR-DRIFTS-MS analysis of WGS reaction over sequentially impregnated 1%Pt-1%Re-1%Na/CeO₂ and 1%Pt-1%Re-3%Na/CeO₂, were performed via Bruker Vertex 70V equipped with a Mercury-Cadmium-Telluride (MCT) detector combined with Hiden Mass Spectrometre. The FTIR-DRIFTS system, which includes Pike Technologies DRIFTS cell with ZnSe window, PIKE Technologies temperature controller and a feed section involving Brooks mass flow controllers allowed thermal treatments under controlled atmospheres and spectrum scanning at controlled temperatures (20-300°C).

Figure 3.5 shows the schematic representation of FTIR-DRIFTS-MS system. The feed section was composed of mass flow controllers, 1/4", 1/8" and 1/16" stainless steel tubings and fittings, 6-way valves for feeding gaseous mixtures and controlled compositions, i.e. carbon monoxide, carbon dioxide, hydrogen, helium and argon. Steam was fed to the system via New Era Pump System syringe pump with specified volumetric flow rate. Steam feed stream was passed through perfectly heated lines and combined with gaseous feed stream.

4 cm⁻¹ resolution, 128 scans and 4000-800 cm⁻¹ wave number range were used in FTIR spectra. Catalyst sample in powder form was placed into the Drift cell sample cup, and smoothing apparatus was used in order to obtain a smooth sample surface for the analysis. Outside of the Drift cell was held in inert atmosphere with 5 ml/min Ar flow. Activity screening via MS made the precision of the catalyst sample weight crucial, and it was provided that the weight of the samples in each analysis to be 25±2 mg.

Catalyst samples were reduced in-situ before each FTIR-DRIFTS-MS analysis by following the same procedure with WGS performance reaction tests. By this procedure, samples were reduced under 15% H₂ containing inert (He) flow by giving a 9°C/min ramp from RT to 375°C, and dwell 2 hours at this temperature. In order to sweep out the sample surface, He flush was applied during 1 hour. Then temperature was set to WGS reaction temperature (300°C). In all tests, total feed flow was fixed at 50 ml/min.

Before analysis, background spectrum was taken under He flow at analysis temperature (300°C). Spectra were obtained every ten minutes during 30 minutes, and feed

mixture sequence sent over catalyst surface was introduced as follows: (i) He flow during 30 minutes, (ii) 1% CO containing He gas mixture during 30 minutes, (iii) He flush after 1% CO adsorption during 30 minutes, (iv) 1.36% CO-2.72% H₂O containing He gas mixture as WGS ideal feed, (v) He flush after WGS ideal feed during 30 minutes. 30 minute spectra were used in comparisons, since surface did not come to equilibrium at the first 10 minutes, but equilibrated after 20 minutes.

3.6. Oxygen Storage Capacity (OSC) Analysis

“Total Oxygen Storage Capacity” (T-OSC) analysis of catalysts were carried out over 75 mg *in-situ* reduced catalyst by fixing the GHSV at $40000 \text{ ml g}_{\text{cat}}^{-1} \text{ h}^{-1}$, following the reaction experiments conducted under 50 ml/min feed flow.

Each catalyst was tested at 350°C, the temperature at which the highest activity and stability was achieved in WGS performance tests. Tests were conducted under the flow of Diluted Realistic Feed #1 (DRF #1) and Diluted Realistic Feed #2 (DRF #2), which are given in Table 3.11. The same CO: H₂O: H₂: CO₂ ratios were used in Diluted Feed #1 and #2 as those in Realistic Feed # 1 and Realistic Feed # 2, respectively, used in the performance tests. The reason of the dilution is that temperature inside IGA system can be increased up to 40°C, and water condensation emerge as a problem at this temperature with realistic feed compositions. The feed flow was diluted up to the point that water can be found as steam form at room temperature, in order to see the effect of the feed composition used in reaction to T-OSC. The structural oxygen storage capacity (OSC) capacities of the catalysts were measured under inert (He) flow rather than reactive feeds (DRF #1 and DRF #2) with the same total volumetric flow and temperature as in the case in T-OSC.

The starting point of the OSC calculation methodology developed is that oxygen derived from the reaction and some surface groups play an active role in the WGS activities of the catalysts. Therefore, in addition to the test involving the reaction over each catalyst, He (inert) experiments under 100% He gas flow were also performed to create a reference base that will enable the ability to discriminate between “structural oxygen” and “effective oxygen”, which is supposed to be related with WGS catalyst activity originating from reaction/reactive media. Experiments involving the reaction test carried out under diluted

Table 3.11. Diluted realistic and inert feed compositions used in OSC analysis.

Feed Name	H ₂ O/CO Feed Ratio	Feed Composition
Diluted Realistic Feed #1 (DRF #1)	6.7	6.5% RF#1 + 93.5% He
Diluted Realistic Feed #1 (DRF #2)	16.2	5.8% RF#2 + 94.2% He
He	-	100% He

Table 3.12. Experiments conducted over catalysts for OSC analysis.

Catalyst	H ₂ O/CO	Temperature (°C)	Exp #
1%Pt-1%Re-1%Na/CeO ₂ _1	6.7	350	1
	16.2	350	2
	He	350	3
1%Pt-1%Re-1%Na/CeO ₂ _2	6.7	350	4
	16.2	350	5
	He	350	6
1%Pt-1%Re-2%Na/CeO ₂	6.7	350	7
	16.2	350	8
	He	350	9
1%Pt-1%Re-1%Na/TiO ₂	6.7	350	10
	16.2	350	11
	He	350	12
1%Pt-1%Re-3%Na/CeO ₂	6.7	350	13
	16.2	350	14
	He	350	15

realistic feed flow and subsequent desorption process up to 800°C, exhibit the "total oxygen storage capacity" (T-OSC), which includes oxygen in the surface groups in the form of lattice and surface formate, carbonate and/or carboxyl-carboxylate, as well as oxygen derived from the H₂O during the WGS reaction and involved in the reaction. However, experiments

carried out under 100% He flow reveal the “structural oxygen capacity” (S-OSC), which includes oxygen in surface groups and in the lattice. By virtue of the methodology, *that enables to use both values*, “Effective oxygen storage capacity” (E-OSC) can be calculated as the difference between the T-OSC obtained in the reaction experiments and the S-OSC obtained in the reference He experiments. Experiments conducted over Na containing catalysts for OSC analysis were given in Tablo 3.12.

The general procedure developed by our group for the T-OSC tests in the IGA-MS system is as follows: A certain amount of catalyst was placed in the IGA chamber and the quartz wool was also placed to prevent dusting under gas flow. While heating the system with atmospheric pressure; the system was degassed with a rate of 50 ml/min until reactor pressure decreased down to 5×10^{-3} mbar in order to remove the air in the IGA reactor and possible adsorbed gases in the pores of the catalyst sample. After that, the sample was reduced under a flow of 15% H₂-He mixture with a total flow rate of 50 ml/min at 375°C and was left under the flow DRF#1 or DRF#2 for 2 hours to allow the WGS reaction to take place. During this time, oxygen molecules stemming from H₂O are also included in the reaction. The reaction gas mixture flow was stopped at the end of two hours. Considering the high volume of the reactor, the sweeping of the reaction gases remaining in the chamber was accomplished by pure He flow lasting for 1 hour. The sample temperature was started to be increased up to 800°C in a controlled manner, following He flush process. During this time, the weight change of the catalyst sample is measured from IGA and the partial pressures of the outlet gases are measured in real time from MS. The only difference between the experiments in which the T-OSC is determined and He experiments performed for the purpose of S-OSC measurement is the step in which the catalyst sample is kept under the flow of DRF#1 and DRF#2 is replaced by the 50 ml/min pure He gas flow in He (inert) experiments in the reaction experiment procedure.

The T-OSC and S-OSC calculations via developed technology are based on the weight change data of the catalyst measured via IGA and the effluent gas composition obtained from MS. Firstly, IGA and MS data are analyzed in detail within the scope of the computational method that allows the OSC data to be obtained precisely. The mismatch between the time-dependent data obtained from the two devices is eliminated on the basis of the moment when the reaction gases are flowing off. Possible instantaneous errors are also corrected in MS

data. In the next step, the minimum signal value for each gas is subtracted from all values for the CO₂ and CO partial pressure data obtained from the MS, and the minimum values for each gas were zeroed. This set of data obtained is called “zeroed data”.

From the zeroed data, the point before the reaction gases are cut off and the signal starts to drop, is selected as the maximum. The data are normalized by dividing the values in the zeroed data set by the selected maximum signal data values and compressed to a range of 0 to 1; this step is called "normalization". For the MS analysis during the experiments, the SEM detector is used, as it provides more sensitive data compared to the Faraday detector with respect to time. Fluctuations in the data set occurred due to very high sensitivity, are corrected by means of the "moving average" method, i.e. by taking the average of 20 previous measurements for each measurement. After smoothing, areas under the graph of "smoothed data vs. time" obtained for CO₂ and CO gases, are determined via OPUS 6.5 Software. Together with the weight change occurring during the temperature increase process; T-OSC and S-OSC calculations are carried out, respectively, depending on the application of the procedure for reactive or inert media. E-OSC of the catalyst sample under the desired reaction condition, for example, under the DRF#1 at 350°C, is calculated by taking the difference of T-OSC determined after reaction under DRF#1 at 350°C and S-OSC determined after He flow at 350°C.

In this thesis, in order to ensure the reliability and sensitivity of the data obtained in the OSC studies, only quartz wool was placed in the chamber and blank tests were performed according to the procedure as described above. It was confirmed that the quartz wool preventing the quartz reactor as well as the catalyst was not reacted and that the sweeping operation provided no reaction gas in the high volume reactor chamber.

3.7. Adsorption Tests

The CO₂ and CH₄ adsorption and desorption isotherms of activated carbon based adsorbents were obtained via combination of gravimetric analyzer and the mass spectrometer system explained in Section 3.2.6. Gravimetric analyzer allows for collecting pressure versus change in the adsorbent weight data in the upstream, whereas and the mass spectrometer

enables to analyze the gases leaving the adsorption unit, i.e., unadsorbed gas streams in the downstream (Figure 3.7).

Adsorption and selective adsorption tests were conducted on AC6 and AC7 samples. The adsorption and desorption isotherms were obtained using 70-75 mg AC-based sample within 0-1000 mbar pressure range for each 100 mbar step, 0-5000 mbar pressure range for each 500 mbar step. In the case of selective adsorption tests, the pressure was increased in 100 mbar increments and the adsorbent weight data collected from the IGA at each pressure level as well as the concentration data of the unadsorbed gas mixture from MS. Four different feed streams were used in the adsorption studies, which are namely; 50 ml/min CO₂ (pure CO₂), 50 ml/min CH₄ (pure CH₄), 5 ml/min CO₂-45 ml/min CH₄ (10% CO₂-90% CH₄) and 25 ml/min CO₂-25 ml/min CH₄ (50% CO₂-50% CH₄). Experiments conducted over each adsorbent for each feed composition, were performed at 3 different temperatures, i.e. RT, 120°C and 200°C. Prior to the adsorption tests, samples were outgassed at RT overnight to eliminate humidity and gases trapped inside the chamber. The adsorption performance of the adsorbents were tested and compared on the basis of their adsorption capacity (mg adsorbed/g adsorbent), mass uptake values (%) and selective adsorption ability of CO₂ over CH₄.

4. RESULTS AND DISCUSSION

The aim of this work is to design and develop efficient catalysts and adsorbents for CO_x elimination to be used in various applications including CO-free hydrogen production from hydrocarbons and CO₂ elimination from natural gas. In this context, the results of this study will be presented and discussed in seven sections:

- WGS performance of Pt-Re-Na/CeO₂ and Pt-Re-Na/TiO₂ catalysts for realistic synthetic feeds
- WGS performance of Pt-Re-Na/CeO₂ and Pt-Re-Na/TiO₂ catalysts under real feed in serial OSR-WGS system
- Characterization of Pt-Re-Na/CeO₂ and Pt-Re-Na/TiO₂ Catalysts
- *In situ* Characterization of Pt-Re-Na/CeO₂ System and *operando* Analysis of WGS Mechanism on Its Sites by FTIR-DRIFTS-MS
- Analysis of “WGS performance-oxygen storage capacity” relation for Pt-Re-Na/CeO₂ and Pt-Re-Na/TiO₂ catalysts
- Combined evaluation of performance, characterization and FTIR-DRIFTS tests results conducted on tri-metallic WGS catalysts
- Selective CO₂ adsorption over activated carbon based adsorbents

4.1. WGS Performance of Pt-Re-Na/CeO₂ and Pt-Re-Na/TiO₂ Catalysts for Realistic Synthetic Feeds

The results of WGS performance tests conducted on trimetallic Pt-Re-Na/CeO₂ and Pt-Re-Na/TiO₂ catalysts were presented in two parts. WGS performance of the catalysts under ideal feed conditions were evaluated in the first part (4.1.1), while the second part involves performance results obtained under realistic feed conditions and their comparative analysis. The effect of Na loading, reaction temperature, feed type and composition (H₂O/CO ratio) on WGS performance of the catalysts were considered as the experimental parameters. Two different H₂O/CO ratios were used for both synthetically prepared ideal and realistic feeds. Performance tests for each feed composition were conducted at three different temperatures (300°C, 350°C, 400°C).

In the performance tests, WGS catalysts were evaluated in terms of their activity, selectivity and stability. Catalytic activity was presented as CO conversion obtained under the ideal and realistic feeds, while net H₂ production was reported as the measure of selectivity for the realistic feed tests. All performance tests were conducted over freshly reduced catalysts and 6h TOS activity data were recorded. 2h TOS data were used to compare the activities of the catalyst samples. TOS activity and stability data of all performance tests are given in Appendix A. It should be noted that, as 1%Pt-1%Re-3%Na/CeO₂ did not show significant activity in the preliminary tests conducted under realistic feed conditions, no further tests were performed on that sample.

Calculation procedures for CO conversion and amount of net H₂ produced are given in Equations (4.1) and (4.2):

$$CO\ Conversion(\%) = \left[\frac{f_{CO,in} - f_{CO,out}}{f_{CO,in}} \right] \times 100 \quad (4.1)$$

$$Net\ H_2\ Production(\%) = \left[\frac{f_{H_2,out} - f_{H_2,in}}{f_{H_2,out}} \right] \times 100 \quad (4.2)$$

where molar flow rates in both feed and product streams were calculated by using Equation (4.3):

$$f_i(\mu\text{mols}^{-1}) = \frac{Pv_{i,gas}}{RT} \quad (4.3)$$

where P is the atmospheric pressure, $v_{i,gas}$ is the volumetric flow rate of the gas, R is the universal gas constant, and T is the absolute temperature.

Activity loss is a measure of stability of the catalysts. It is usually reported as the percent loss of initial activity and were calculated through using Equation (4.4).

$$Activity\ Loss\ (\%) = \left[\frac{CO\ Conversion_{(1h)} - CO\ Conversion_{(6h)}}{CO\ Conversion_{(1h)}} \right] \quad (4.4)$$

4.1.1. WGS performance tests conducted under ideal feeds

The tests were conducted under atmospheric pressure at three different temperatures, i.e. 300°C, 350°C, 400°C for two ideal feed (i.e. feeds having only WGS reactants and inert) conditions, which were presented in Section 3.4.1, Table 3.7. GHSV was kept constant at 120,000 $\text{ml}_{\text{cat}}^{-1}\text{h}^{-1}$ for all tests.

The effect of temperature on the catalyst activity under ideal feed #1 and ideal feed #2 conditions, are given in Figure 4.1 and 4.2, respectively. Equilibrium CO conversions calculated via HSC-Chemistry Software for the specified conditions are also presented in these figures. The highest activities under ideal feed #1 conditions were achieved at 400°C for all the catalysts except 1%Pt-1%Re-2%Na/CeO₂. The activities of sequentially impregnated 1%Pt-1%Re-1%Na/CeO₂ and Re-Na coimpregnated 1%Pt-1%Re-1%Na/CeO₂ catalysts showed an increasing trend in response to increase in temperature. 1%Pt-1%Re-1%Na/TiO₂ catalyst, which was prepared in order to investigate the effect of support type, exhibited the lowest activity at 350°C, in contrast to those of the other catalyst samples. The highest activity under ideal feed #1 conditions, was determined as 81.3% CO conversion over 1%Pt-1%Re-2%Na/CeO₂ at 350°C.

Regarding the performance tests conducted under ideal feed #2, lowering H₂O/CO ratio did not affect the catalyst activities at 400°C, whereas it led to a decrease in catalyst activities at 350°C except Re-Na coimpregnated 1%Pt-1%Re-1%Na/CeO₂ (Figure 4.2). The observed decrease in sequentially impregnated catalyst activities at 350°C may stem from the shift of reaction equilibrium towards reverse WGS under low-H₂O containing ideal feed condition. Under ideal feed #2 condition, the highest conversion level was achieved over sequentially impregnated 1%Pt-1%Re-1%Na/CeO₂ as 74.9% CO conversion at 400°C.

Tests conducted over Pt-Re-Na/CeO₂ and Pt-Re-Na/TiO₂ catalyst samples under ideal feed conditions at different temperatures did not show any significant activity loss with respect to time, meaning that all catalyst samples exhibited high stability throughout 6h TOS. Activity data recorded during 6 h TOS over all catalyst samples under ideal feed conditions are given in Appendix A.

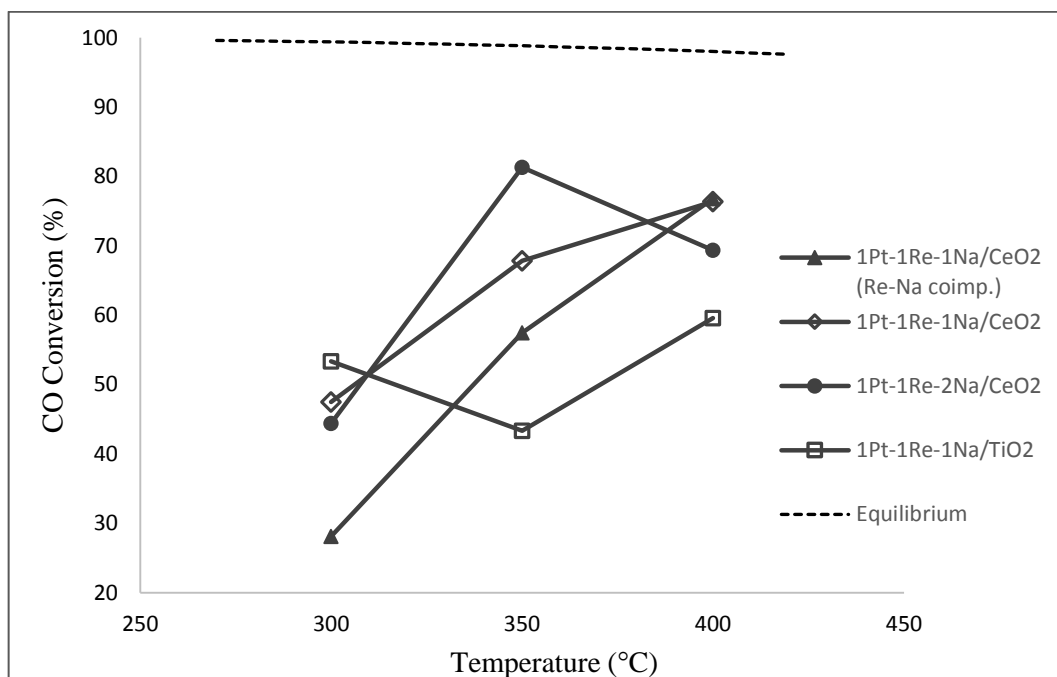


Figure 4.1. Effect of temperature on catalytic activity for ideal feed #1 (3% CO, 15% H₂O, 82% Ar; H₂O/CO=5).

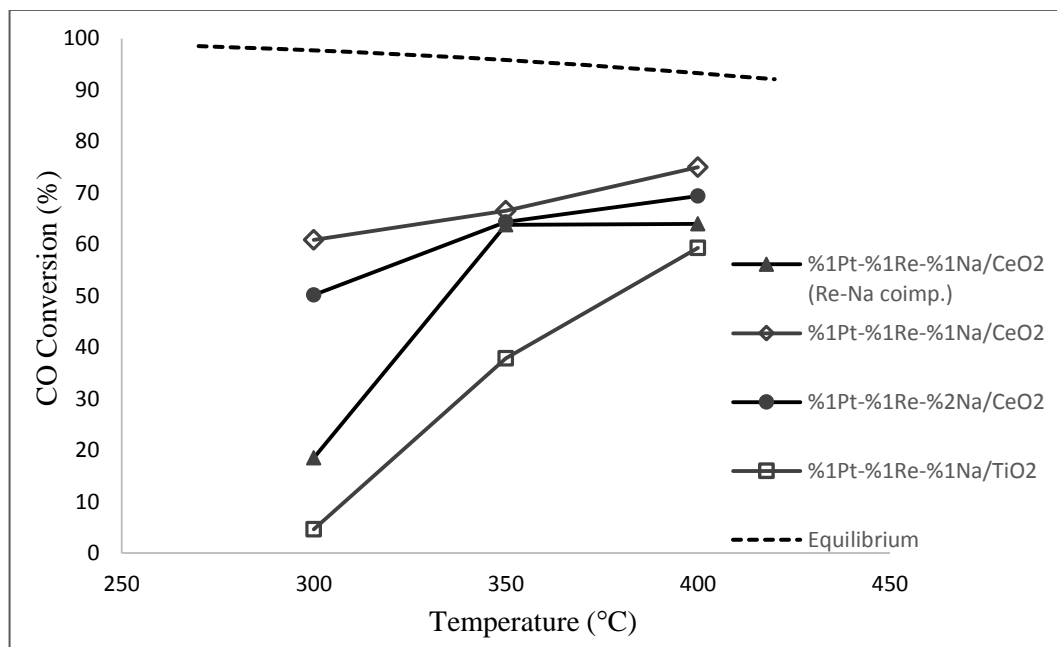


Figure 4.2. Effect of temperature on catalytic activity for ideal feed #2 (3% CO, 6% H₂O, 91% Ar; H₂O/CO=2).

The effect of H₂O/CO feed ratio on the catalytic activity of Re-Na coimpregnated 1%Pt-1%Re-1%Na/CeO₂ catalyst is presented in Figure 4.3 for ideal feed #1 and #2. The results revealed that increasing H₂O/CO feed ratio led to an increase in activities at 300°C and 400°C, whereas a small decrease is observed at 350°C. Changing H₂O/CO ratio in the feed has also an effect on the optimum WGS reaction temperature under specified conditions; i.e. the decrease in H₂O/CO feed ratio to 2 shifts the reaction temperature yielding the highest CO conversion from 350°C to 400°C.

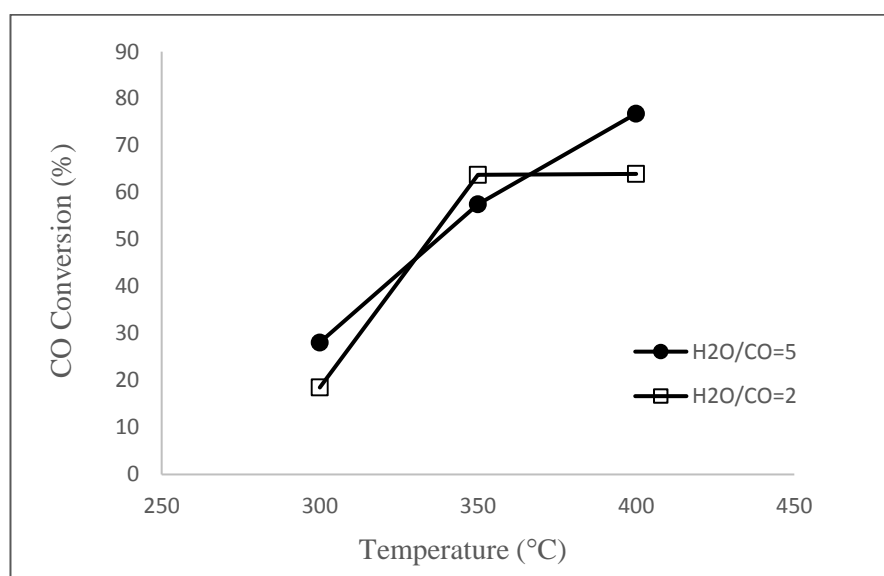


Figure 4.3. Effect of H₂O/CO feed ratio on the catalytic activity of 1%Pt-1%Re-1%Na/CeO₂ (Re-Na coimp.).

The catalytic activities over sequentially impregnated 1%Pt-1%Re-1%Na/CeO₂ under ideal feed #1 and #2 are comparatively analyzed in Figure 4.4. The results show that the activity was not much influenced by H₂O amount at 350°C and 400°C, however reducing H₂O/CO ratio at 300°C make a positive effect on catalyst activity.

The catalytic activity of 1%Pt-1%Re-2%Na/CeO₂ for ideal feeds having two different H₂O/CO ratio is presented in Figure 4.5. Increasing H₂O/CO ratio had a pronounced effect on activity at 350°C for this catalyst. Similar with sequentially impregnated 1%Pt-1%Re-1%Na/CeO₂, activity at 300°C at low H₂O containing feed was found higher than that for the feed with H₂O/CO=5. It can be interpreted that increasing H₂O/CO ratio in the feed leads

to a decrease in catalyst activity at 300°C for sequentially impregnated Pt-Re-Na/CeO₂ catalysts.

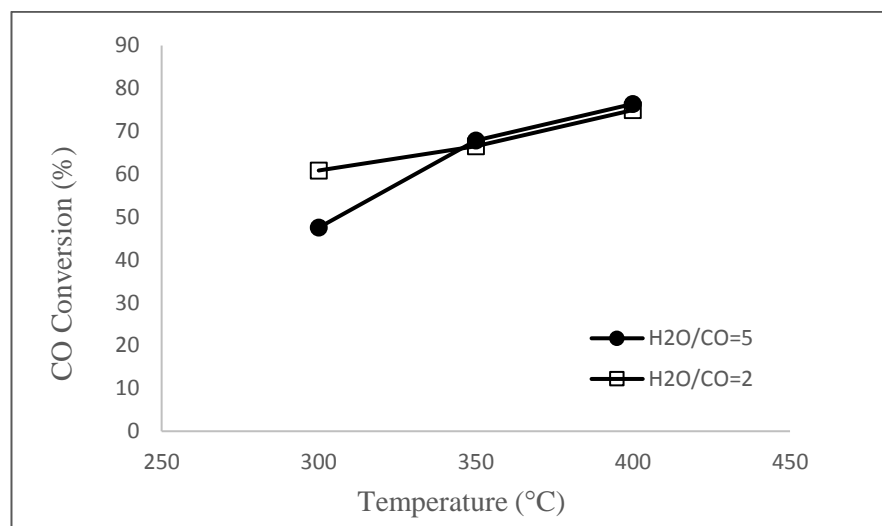


Figure 4.4. Effect of H₂O/CO feed ratio on the catalytic activity of 1%Pt-1%Re-1%Na/CeO₂.

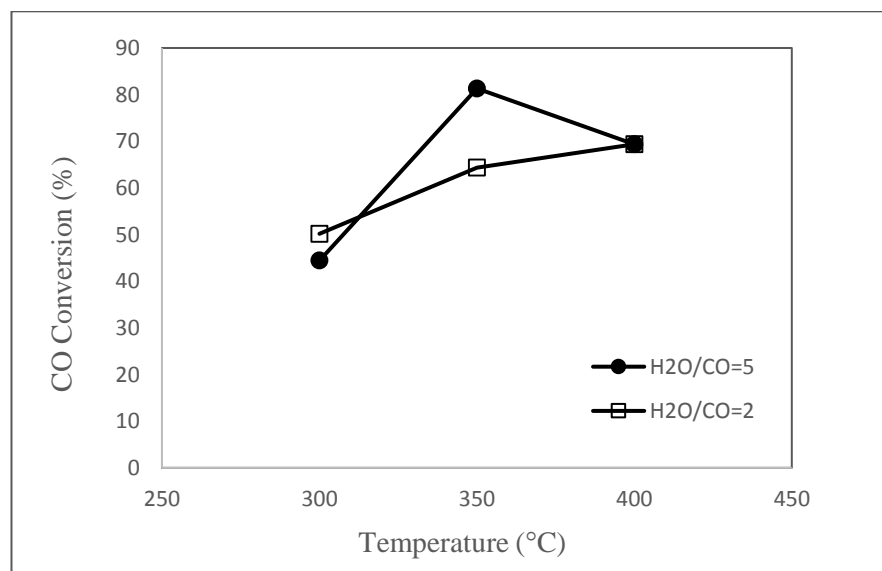


Figure 4.5. Effect of H₂O/CO feed ratio on the catalytic activity of 1%Pt-1%Re-2%Na/CeO₂.

The effect of H₂O/CO feed ratio over 1%Pt-1%Re-1%Na/TiO₂ at different temperatures is exhibited in Figure 4.6. Increasing H₂O/CO ratio has a positive effect for all reaction temperatures, being contrary to the results obtained from CeO₂ supported catalysts. Another point worth to mention is that the lowest activity over 1%Pt-1%Re-1%Na/TiO₂ was achieved at 350°C under the ideal feed condition with H₂O/CO=5.

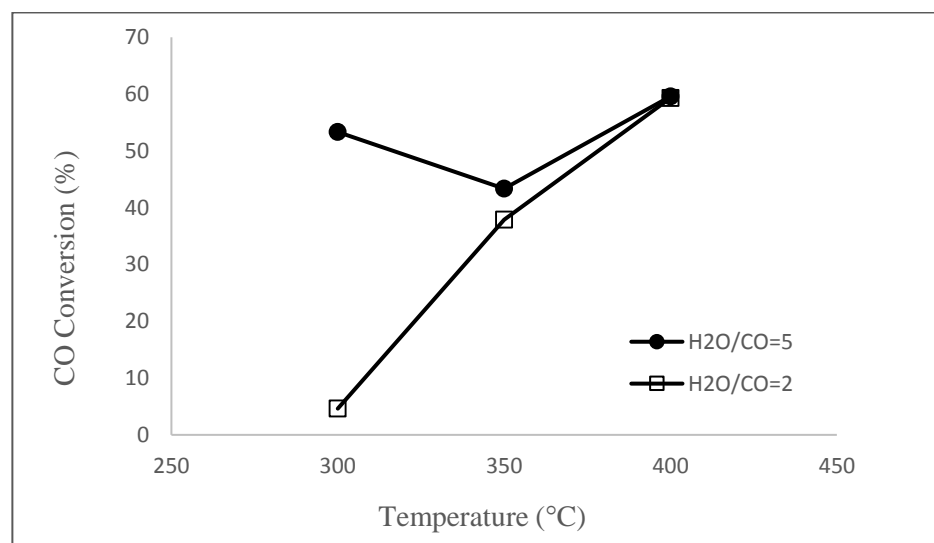


Figure 4.6. Effect of H₂O/CO feed ratio on the catalytic activity of 1%Pt-1%Re-1%Na/TiO₂.

The effect of impregnation procedure on catalyst activity is evaluated based on the results presented in Figures 4.7 and 4.8, for ideal feed #1 and ideal feed #2, respectively. In both cases sequential impregnation was found to enhance the catalytic activity of Pt-Re-Na/CeO₂, although the degree of influence on CO conversion levels at each temperature differs for each ideal feed, i.e. significant enhancement was observed at 300°C and 350°C for the tests conducted under ideal feed #1. Though sequential impregnation almost entirely lost its effect at 350°C in the case of ideal feed #2, it gains importance with the rise in reaction temperature to 400°C.

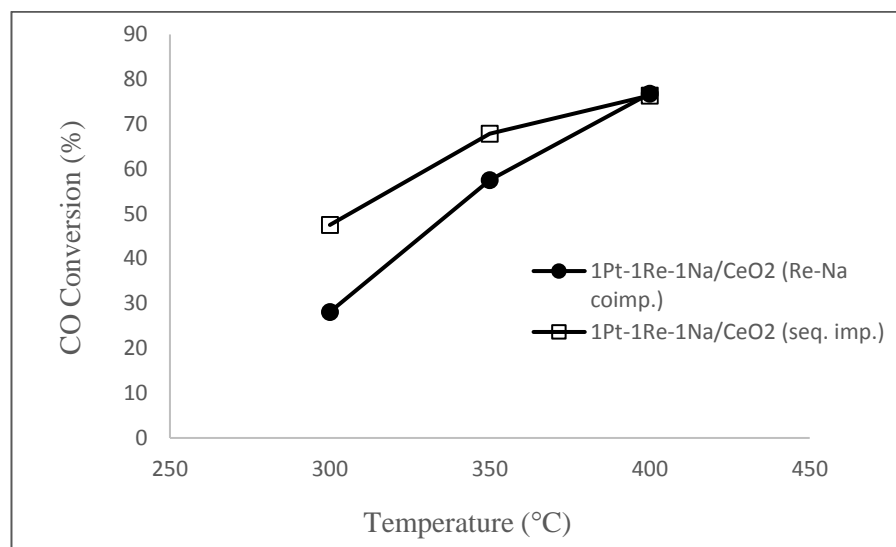


Figure 4.7. Effect of Re-Na impregnation procedure on the catalytic activity of 1%Pt-1%Re-1%Na/CeO₂ under ideal feed #1 (3% CO, 15% H₂O, 82% Ar; H₂O/CO = 5).

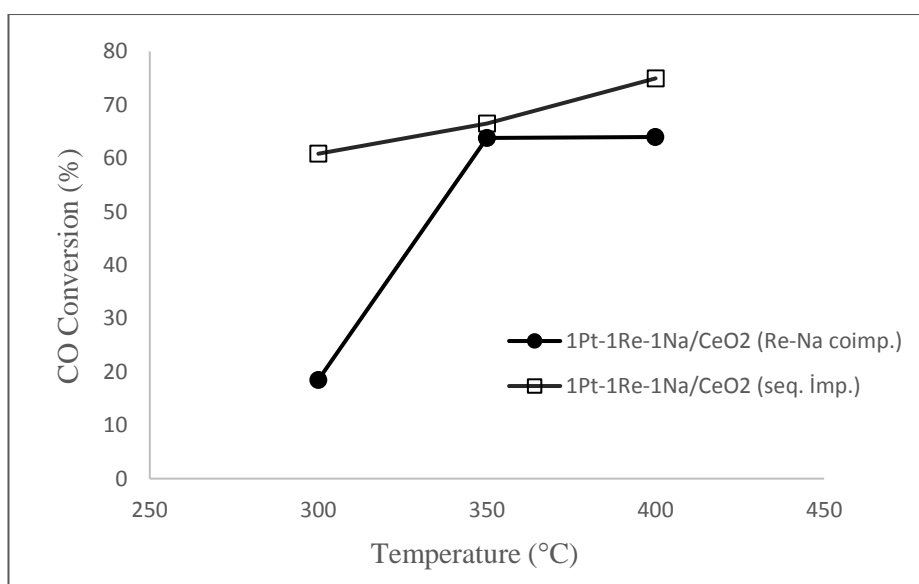


Figure 4.8. Effect of Re-Na impregnation procedure on the catalytic activity of 1%Pt-1%Re-1%Na/CeO₂ under ideal feed #2 (3% CO, 6% H₂O, 91% Ar; H₂O/CO = 2).

The effect of Na loading on the WGS performance of the sequentially impregnated 1%Pt-1%Re-1%Na/CeO₂ and 1%Pt-1%Re-2%Na/CeO₂ tri-metallic samples is analyzed based on the results presented in Figure 4.9 and 4.10, respectively. Due to the negligible activity obtained over 1%Pt-1%Re-3%Na/CeO₂ catalyst, the comparison is made between

the performance of the catalysts with 1% and 2% Na loading. It should be also noted that the WGS activity and stability of bimetallic Pt-Re/CeO₂ catalyst was previously investigated and reported by Özer (Özer, 2016). CO conversion profiles suggest that introducing Na cause a decrease in catalytic activity, however further increase in its loading make an opposite effect under ideal feed #1 condition. Catalytic activity was observed to enhance with increasing Na loading from 1% to 2% under flow of ideal feed #1 at 350°C; however, increasing Na loading did not make any positive effect, even caused a little decrease, on activity under ideal feed #2. On the basis of this evidence, it can be said that the effect of Na loading percent on activity is sensitive to the feed composition used in the performance tests.

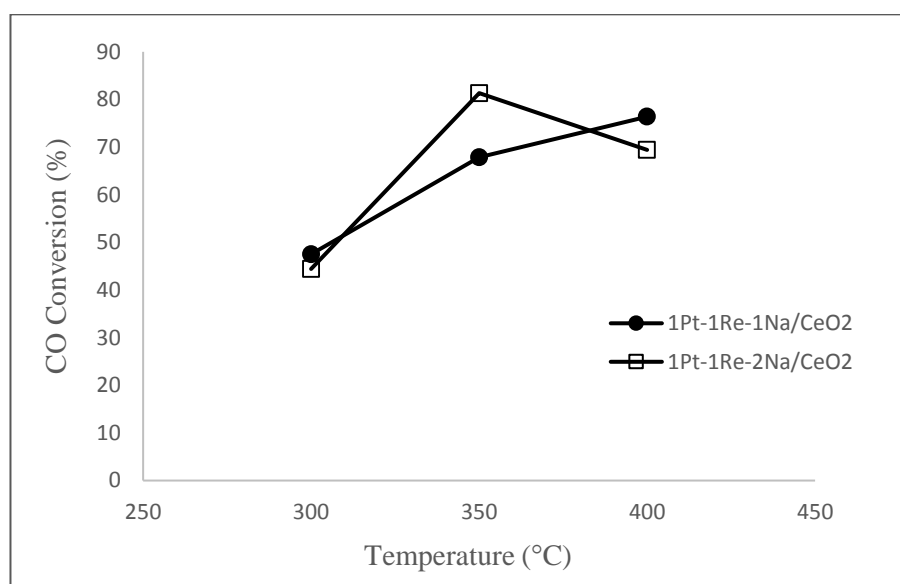


Figure 4.9. Effect of Na loading on the catalytic activity for ideal feed #1 (3% CO, 15% H₂O, 82% Ar; H₂O/CO =5).

The WGS activity data obtained over 1%Pt-1%Re-1%Na/CeO₂ and 1%Pt-1%Re-1%Na/TiO₂ for all temperatures at 2h TOS, which are presented in Figure 4.11 and 4.12, are used to investigate the effect of support type under ideal feed conditions. Catalytic activity of 1%Pt-1%Re-1%Na/CeO₂ was determined to be higher than that of TiO₂ supported catalyst under both ideal feed conditions at all temperatures, except for ideal feed #1 at 300°C.

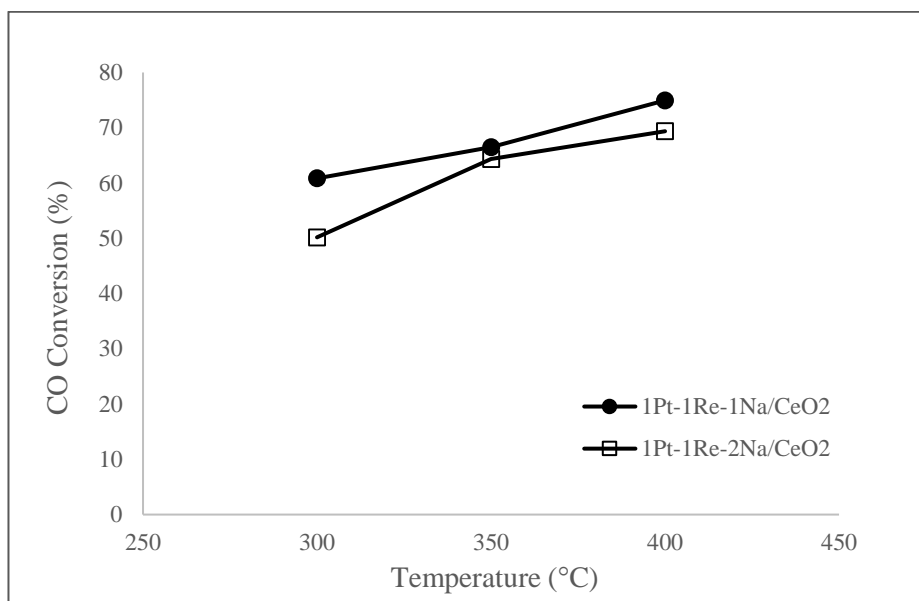


Figure 4.10. Effect of Na loading on the catalytic activity for ideal feed #2 (3% CO, 6% H₂O, 91% Ar; H₂O/CO =2).

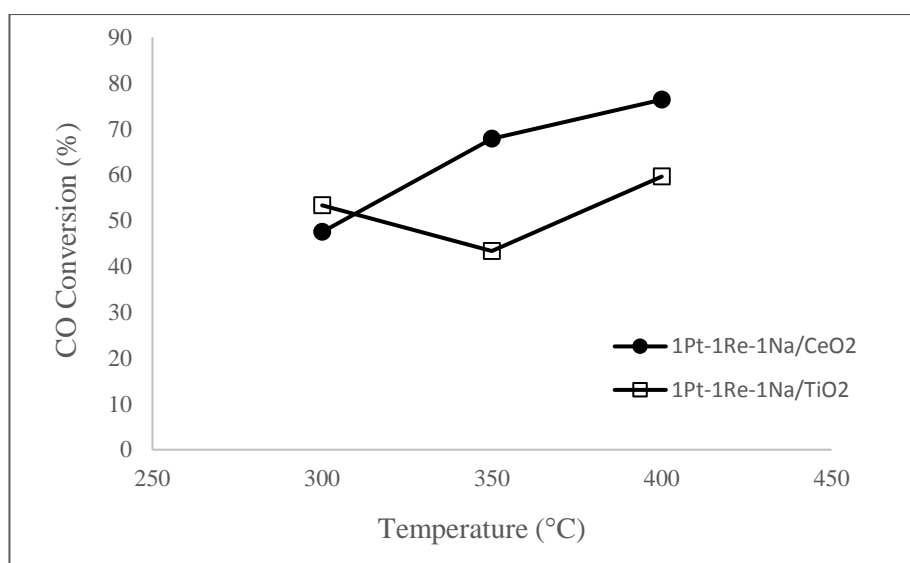


Figure 4.11. Effect of support type on the catalytic activity for ideal feed #1 (3% CO, 15% H₂O, 82% Ar; H₂O/CO =5).

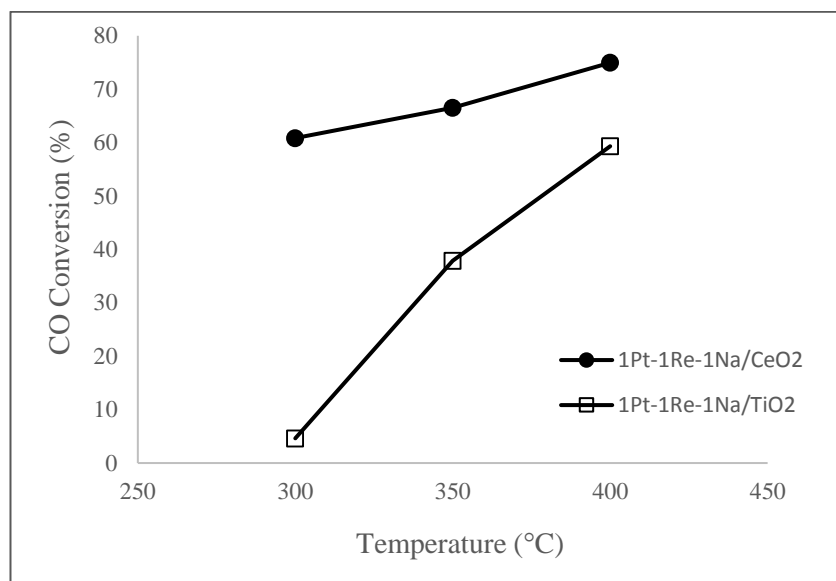


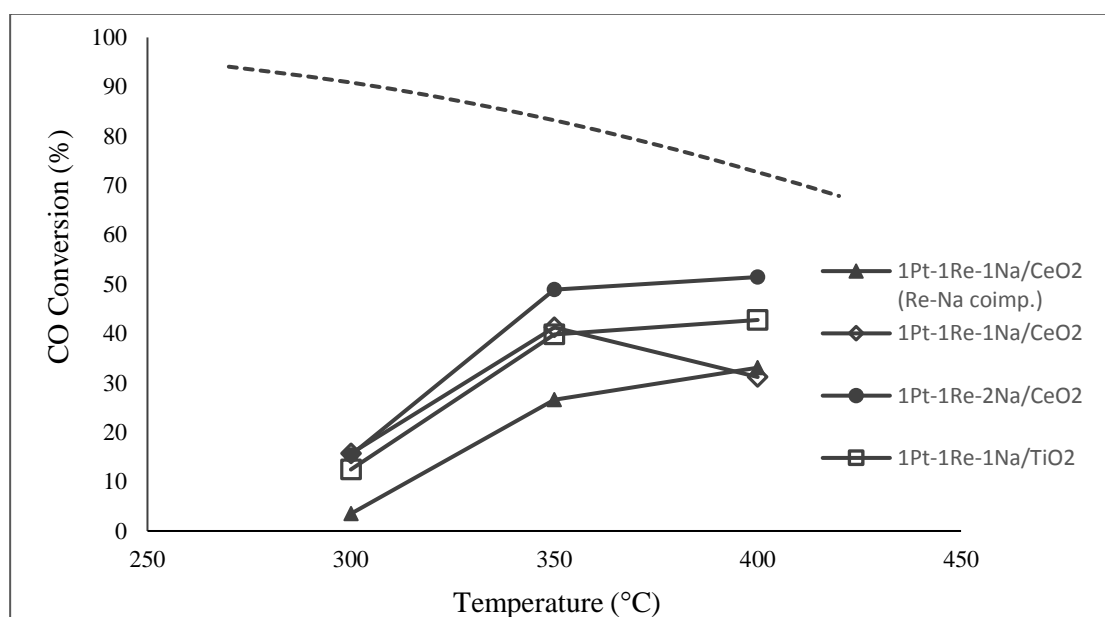
Figure 4.12. Effect of support type on the catalytic activity for ideal feed #2 (3% CO, 6% H₂O, 91% Ar; H₂O/CO =2).

4.1.2. WGS performance tests conducted under realistic feeds

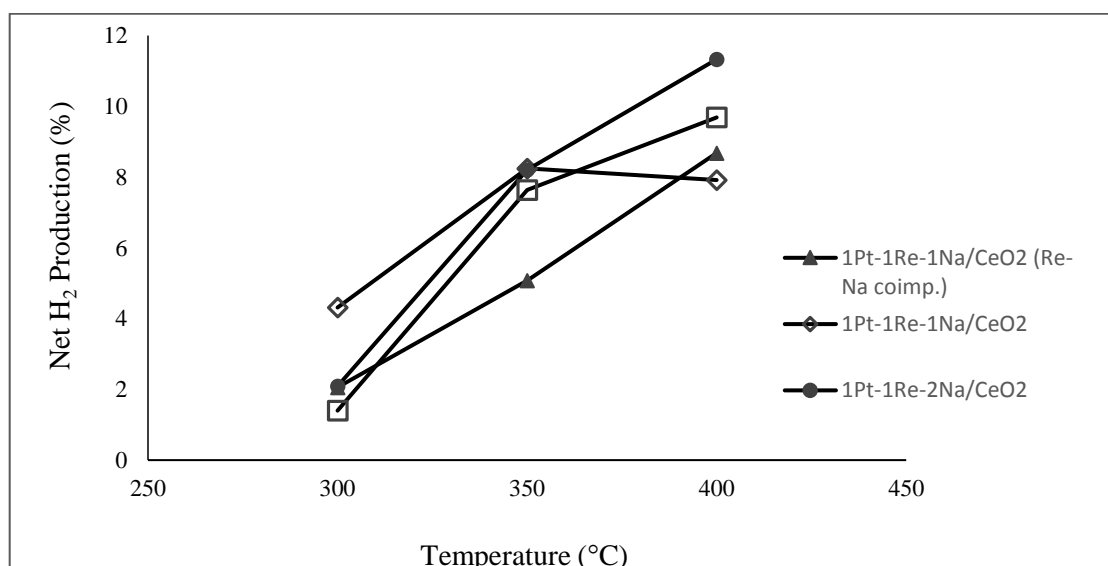
The tests under realistic feed (i.e. synthetically prepared feeds simulating product gas mixture of a typical reformer of a fuel processor) conditions were conducted under atmospheric pressure at three different temperatures, i.e. 300°C, 350°C, 400°C as such in ideal feed conditions. The catalyst weight and total feed flow were kept constant under specified realistic feed conditions having two different H₂O/CO ratios (Section 3.4.1, Table 3.7), which were also used in previous studies (Çağlayan, 2011; Özer, 2016).

The experimentally determined WGS profiles for activity, as CO conversion, and selectivity, as net H₂ production, of the catalyst samples under realistic feed #1 and #2 flows as a function of temperature are shown along with calculated equilibrium CO conversion levels in Figures 4.13a-b and 4.14a-b. The lowest activity under realistic feed conditions was observed over Re-Na coimpregnated 1%Pt-1%Re-1%Na/CeO₂ for both H₂O/CO feed ratios. Catalytic activity data presented in Figures 4.13a and 4.14a collected under realistic feed with H₂O/CO=6.7, were found to be higher than those with H₂O/CO=16.2. It should be noted that, as H₂O, CO₂ and H₂ compositions in both realistic feeds are similar, the main difference between realistic feed compositions arises from their CO concentration levels.

Consequently, the reason of low activity levels measured under realistic feed #2 flow is thought related to its CO concentration, which was less than half of that in realistic feed #1. In other words, low activity originates from relatively limited CO amount *-with respect to H₂O-* available in the WGS feed.

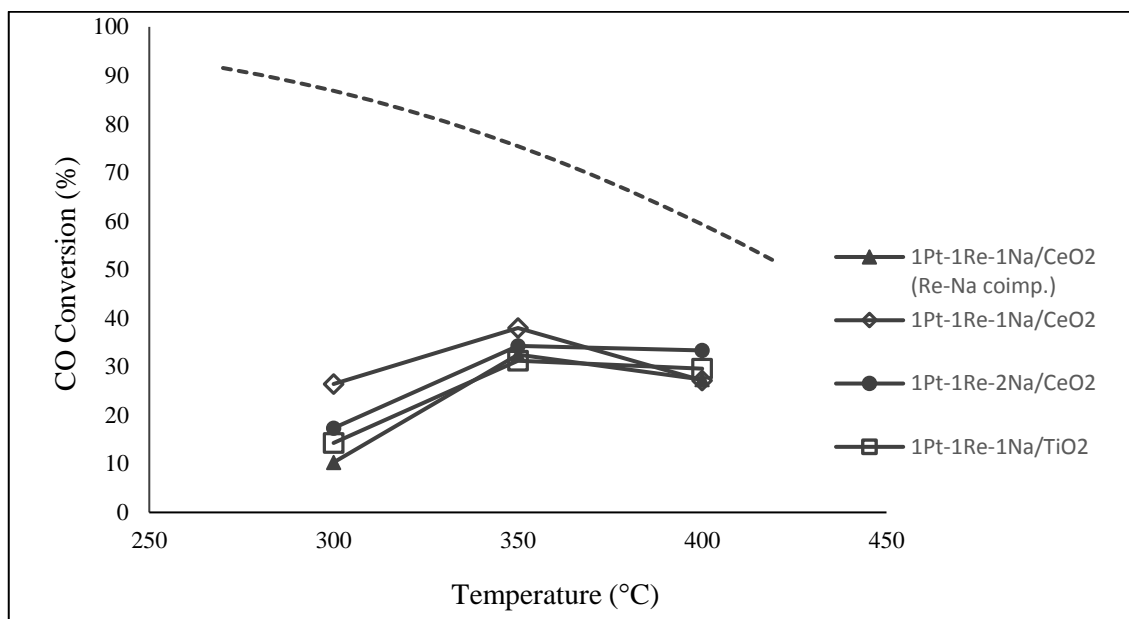


(a)

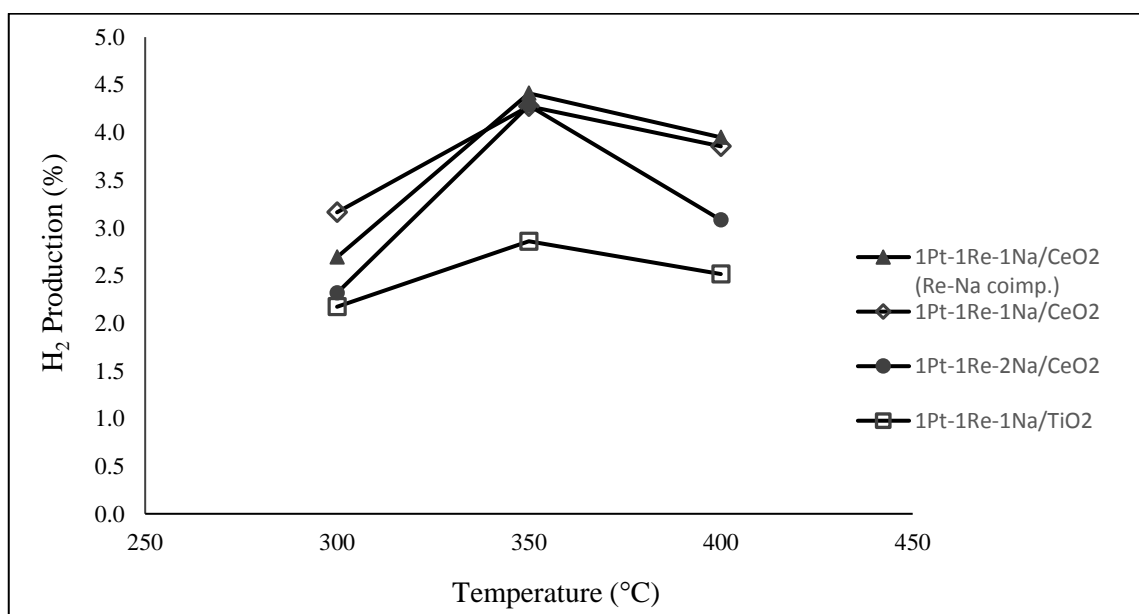


(b)

Figure 4.13. Temperature dependence of (a) catalytic activity and (b) net H₂ production for realistic feed #1 (4.9% CO, 32.7% H₂O, 30% H₂, 10.4% CO₂, 22% Ar, H₂O/CO=6.7).



(a)



(b)

Figure 4.14. Temperature dependence of (a) catalytic activity and (b) net H₂ production for realistic feed #2 (2.1% CO, 34.1% H₂O, 23.7% H₂, 12.3% CO₂, 27.8% Ar, H₂O/CO=16.2).

The highest activity under realistic feed #1 flow was determined as 51.5% over 1%Pt-1%Re-2%Na/CeO₂ at 400°C. It can be also seen that CO conversion values were in accordance with net H₂ production under realistic feed #1. Thus, combined evaluation of

Figures 4.13a and 4.13b indicate that 1%Pt-1%Re-2%Na/CeO₂ was the most active and selective catalyst for the whole temperature range except its inferior selectivity at 300°C. On the other hand, unlike the findings gathered for realistic feed #1, tests performed under realistic feed #2 implied that sequentially impregnated 1%Pt-1%Re-1%Na/CeO₂ showed better activity at both 300°C and 350°C with the highest activity level at 350°C as 38%. It is interesting to note that the net H₂ production for realistic feed #2 did not follow the activity trend. Unexpectedly, net H₂ production obtained over Re-Na coimpregnated 1%Pt-1%Re-1%Na/CeO₂ was measured as high as that obtained over sequentially impregnated 1%Pt-1%Re-1%Na/CeO₂.

The effect of impregnation procedure on WGS activity of the high performance 1%Pt-1%Re-1%Na/CeO₂ catalyst under realistic feed is presented in Figure 4.15 and 4.16, for realistic feed #1 and realistic feed #2, respectively. In both feeds a remarkable enhancement in activity was observed at 300°C and 350°C in favor of catalyst prepared by sequential impregnation. On the other hand, the results indicate that effect of preparation procedure loses its importance when reaction temperature is increased to 400°C.

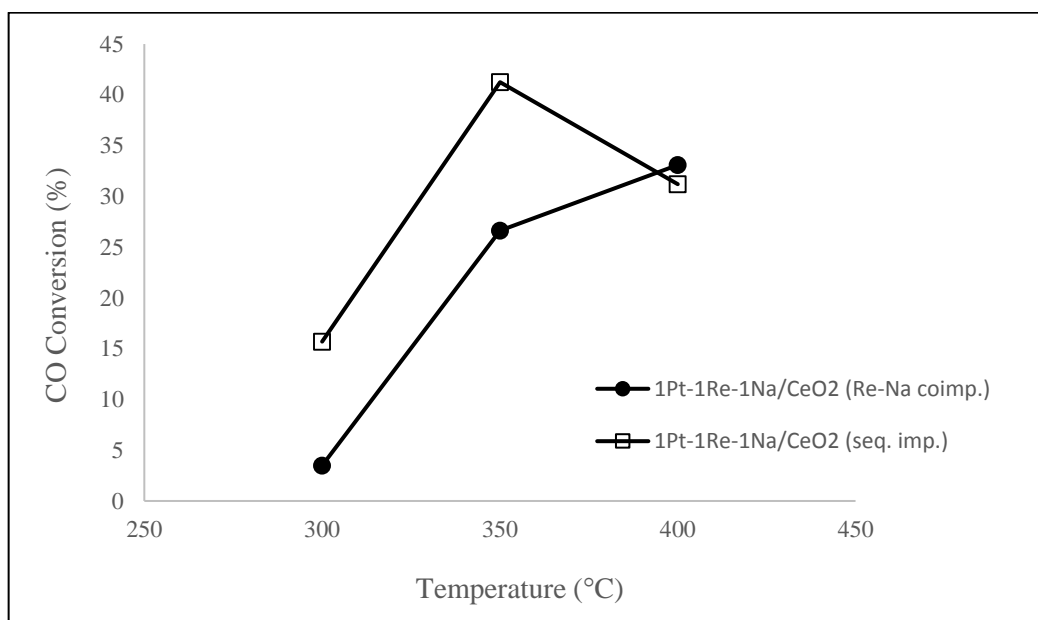


Figure 4.15. Effect of Re-Na impregnation procedure on the catalytic activity of 1%Pt-1%Re-1%Na/CeO₂ under realistic feed #1 conditions (4.9% CO, 32.7% H₂O, 30% H₂, 10.4% CO₂, 22% Ar, H₂O/CO=6.7).

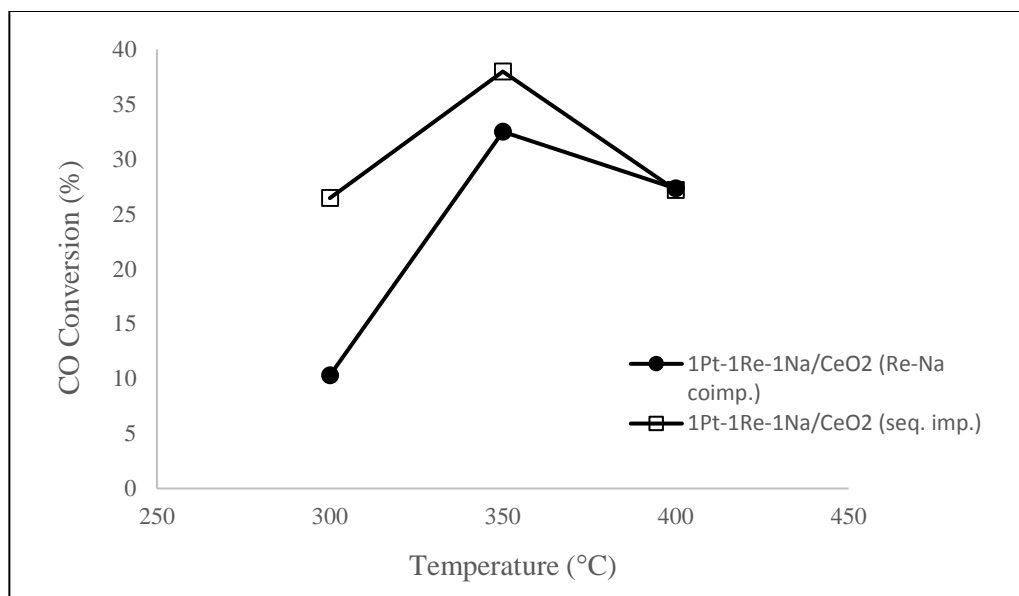


Figure 4.16. Effect of Re-Na impregnation procedure on the catalytic activity of 1%Pt-1%Re-1%Na/CeO₂ under realistic feed #2 conditions (2.1% CO, 34.1% H₂O, 23.7% H₂, 12.3% CO₂, 27.8% Ar, H₂O/CO=16.2).

Figure 4.17 and 4.18 exhibit the effect of Na loading on catalytic activity of 1Pt-1Re/CeO₂ system under realistic feed conditions. As it was indicated before, 1%Pt-1%Re-3%Na/CeO₂ catalyst performance was not included into comparison due to its negligible activity. A decrease in activity was observed in sequentially impregnated 1%Pt-1%Re-1%Na/CeO₂ when compared with that of bimetallic Pt-Re/CeO₂ catalyst, which was previously studied by Özer, however further increase in Na loading provides an enhancement in activity (Özer, 2016). As shown in Figure 4.17, catalytic activity was enhanced in response to the increase in Na loading from 1% to 2% under realistic feed #1, especially for higher temperatures, i.e. at 350°C and 400°C. Contrary to the results reported for realistic feed #1, increasing Na loading made a negative effect on activity under realistic feed #2 (Figure 4.18). A comparative analysis of the activity results obtained under both ideal and realistic feed conditions strongly suggests that “Na loading-feed composition” combination has a pronounced effect on catalyst performance.

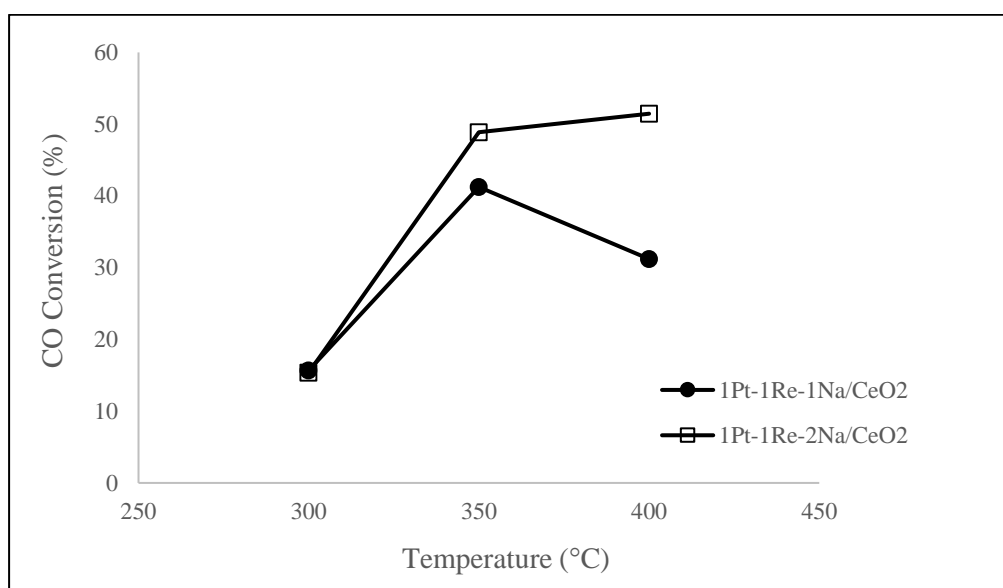


Figure 4.17. Effect of Na loading on the catalytic activity of Pt-Re-Na/CeO₂ under realistic feed #1 conditions (4.9% CO, 32.7% H₂O, 30% H₂, 10.4% CO₂, 22% Ar, H₂O/CO=6.7).

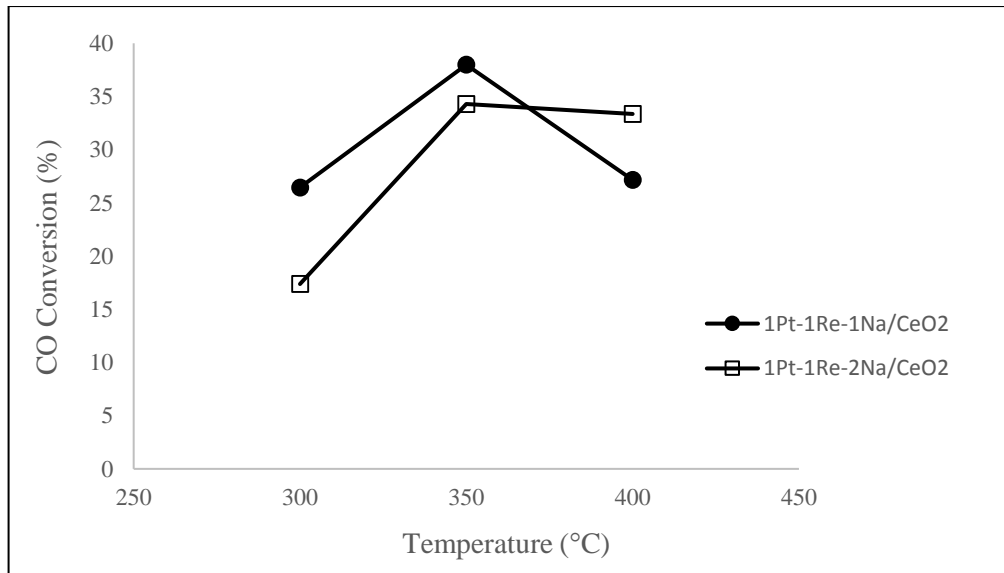


Figure 4.18. Effect of Na loading on the catalytic activity of Pt-Re-Na/CeO₂ under realistic feed #2 conditions (2.1% CO, 34.1% H₂O, 23.7% H₂, 12.3% CO₂, 27.8% Ar, H₂O/CO=16.2).

The effect of support type on WGS activity of 1%Pt-1%Re-1%Na system under realistic feed conditions was also studied (Figure 4.19 and 4.20). In this context, WGS activities of 1%Pt-1%Re-1%Na/CeO₂ and 1%Pt-1%Re-1%Na/TiO₂ were compared for all temperatures. Though 1%Pt-1%Re-1%Na/CeO₂ had somehow slightly higher activity than that of TiO₂ supported one at 300°C and 350°C, the activity measured over 1%Pt-1%Re-1%Na/TiO₂ become significantly higher as the temperature was risen to 400°C.

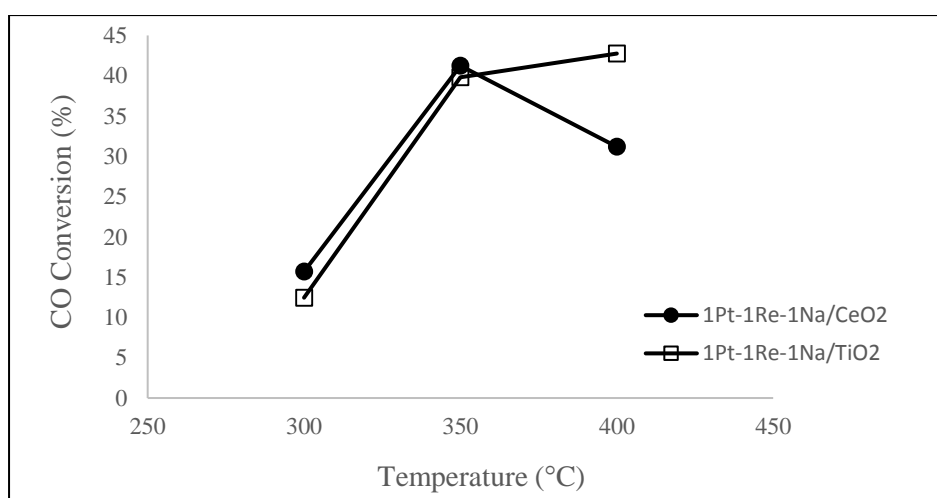


Figure 4.19. Effect of support type on the catalytic activity of Pt-Re-Na catalysts under realistic feed #1 (4.9% CO, 32.7% H₂O, 30% H₂, 10.4% CO₂, 22% Ar, H₂O/CO=6.7).

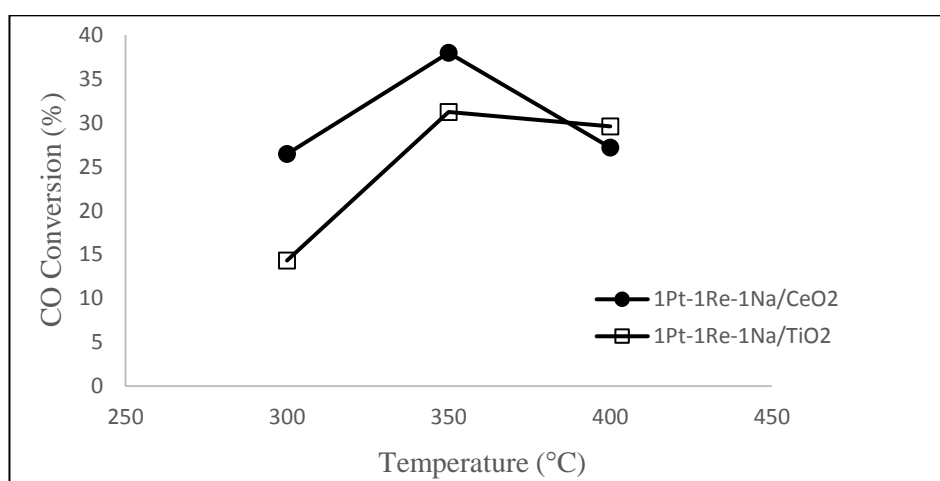


Figure 4.20. Effect of support type on the catalytic activity of Pt-Re-Na catalysts under realistic feed #2 (2.1% CO, 34.1% H₂O, 23.7% H₂, 12.3% CO₂, 27.8% Ar, H₂O/CO=16.2).

The results of the activity tests conducted over all prepared trimetallic Pt-Re-Na catalysts under ideal and realistic feed conditions are combined and presented in Figure 4.21. Under the light of the results obtained under ideal feed conditions, the highest activity was reached over 1%Pt-1%Re-2%Na/CeO₂ at 350°C, besides comparable activities observed over sequentially impregnated 1%Pt-1%Re-1%Na/CeO₂ and 1%Pt-1%Re-2%Na/CeO₂. In general, WGS activities obtained at 350°C and 400°C under realistic feed #1 (H₂O/CO=6.7) were higher than those measured under realistic feed #2 (H₂O/CO=16.2). The highest activity achieved in performance tests over Na promoted catalysts was over 1%Pt-1%Re-2%Na/CeO₂ as 51.5% CO conversion under realistic feed #1.

In the WGS tests conducted under real or realistic feeds, the net H₂ production, which is a measure of selectivity, is a crucial performance feature of a catalyst. The net H₂ production percentages are presented in Figure 4.22 along with the corresponding CO conversion levels. The combined evaluation of activity and selectivity results show that the trends in net H₂ production are in accordance with those observed for activity. The maximum net H₂ production was observed as 11.3% at 400°C under realistic feed #1 over 1%Pt-1%Re-2%Na/CeO₂, which also has the highest CO conversion activity. It should be noted that the increase in temperature had a positive effect on net H₂ production for the catalysts tested under realistic feed #1, however such a trend did not exist when feed was realistic feed #2. It should be kept in mind that high net H₂ production mostly achieved at 350°C.

When all performance data were evaluated together, it was concluded that sequential impregnation method yielded both higher CO conversion and net H₂ production values than Re-Na coimpregnation for all temperatures. Additionally, the performance results indicate that catalyst activity and selectivity was found strongly sensitive to both reaction temperature and feed composition.

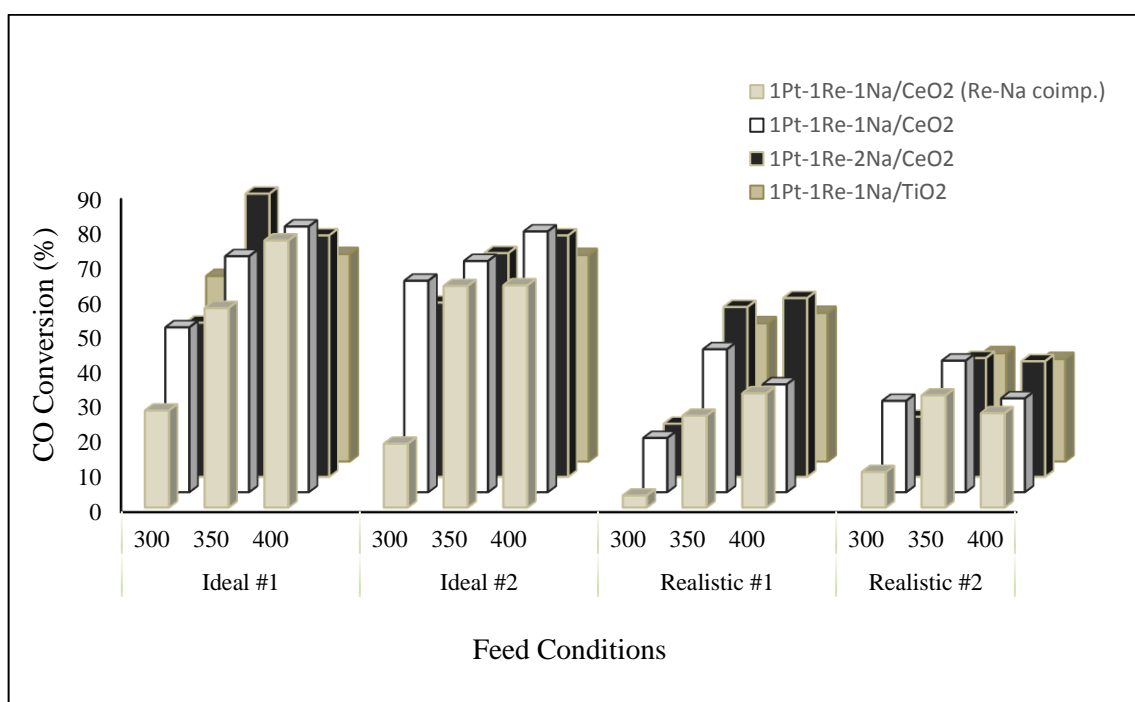


Figure 4.21. Catalyst activities at different feed conditions and temperatures.

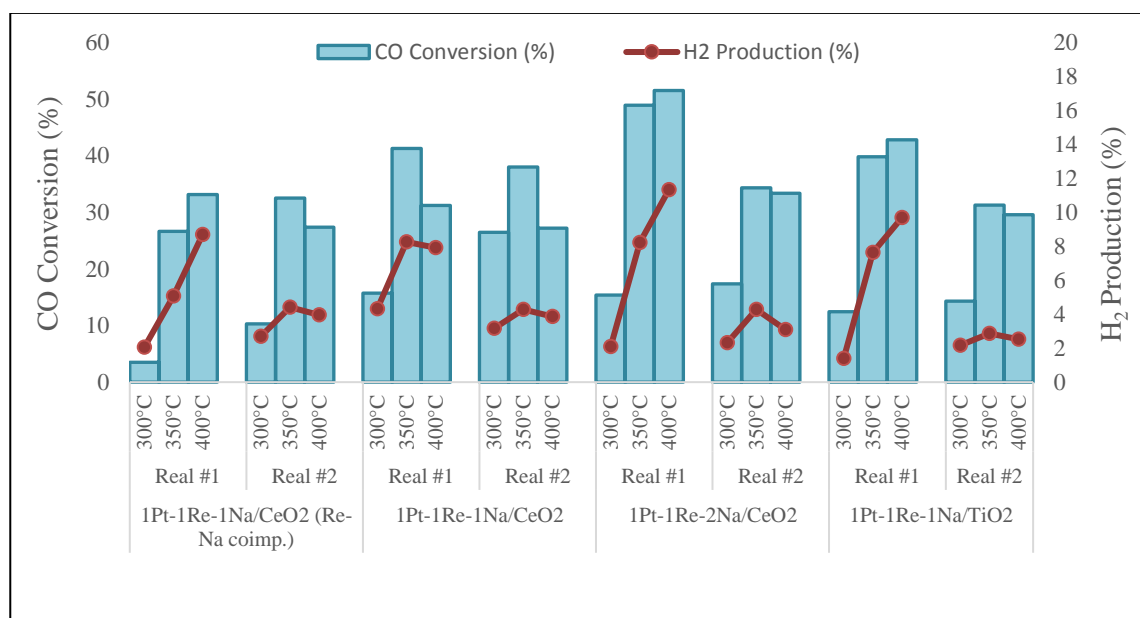


Figure 4.22. CO conversion and net H₂ production percentages for each catalyst at different temperatures under realistic feed #1 and #2 conditions.

4.2. WGS Performance of Pt-Re-Na/CeO₂ And Pt-Re-Na/TiO₂ Catalysts under Real Feed in Serial OSR-WGS System

The WGS catalysts prepared are aimed to be used in a methane Fuel Processor which has an upstream Oxidative Steam Reformer reactor sending its product to WGS reactor. In this section, the performance results of serial oxidative steam reforming (OSR)-WGS tests are presented in order to investigate the real performance of WGS catalysts. The effect of OSR feed composition, WGS catalyst preparation parameters (coimpregnation/sequential impregnation, Na loading, support type) and WGS reaction temperature on serial OSR-WGS performance were examined. Two different feed compositions, resulting in two different real feed mixtures entering WGS reactor, were examined on each catalyst parametrically.

Serial OSR-WGS tests' parameters were based on the results of a previous study on OSR performance of 0.2%Pt-10%Ni/ δ -Al₂O₃ under different conditions (Başar *et al.*, 2018; Öztepe, 2017). As the high performance and hydrogen production had obtained at 450°C over 0.2%Pt-10%Ni/ δ -Al₂O₃, OSR reaction temperature was kept fix at 450°C for all serial OSR-WGS tests in the current study. On the other hand, the effect of WGS reaction temperature was examined parametrically as in the case of individual WGS experiments. Each serial OSR-WGS test took place under the conditions where the exit stream of OSR reactor operates at 450°C enters WGS reactor, which operates at three different temperatures, i.e. 350°C, 350°C and 400°C. Serial experiments were conducted under two different OSR feed compositions, which are presented at Section 3.4.2, Table 3.10. In order to investigate the WGS performance over Pt-Re-Na/CeO₂ in a detailed fashion, the feed compositions of the OSR reactor were chosen such as to yield relatively different carbonmonoxide concentration levels at its product stream. Feed compositions of the OSR reactor along with steam to carbon (S/C) and oxygen to carbon (O/C) feed ratios were given in Table 3.9.

Serial OSR-WGS activity and stability results obtained over sequentially impregnated 1%Pt-1%Re-1%Na/CeO₂ are represented in Figure 4.23 and 4.24 for two different OSR feed compositions. Decrease in CO conversion with respect to WGS reactor temperature became more significant at 400°C in the tests under feed with relatively lower C/O ratio (Figure 4.24) than the one with higher C/O ratio (Figure 4.23). Since OSR reactor temperature in each test was fixed, CH₄ conversion values for the same OSR feed composition measured were almost

identical as expected. Obtaining different CO conversion levels from the ones in single WGS experiments in these serial experiments at each temperature was most likely due to difference between the H_2O/CO ratio produced at the exit of OSR reactor, *which is the WGS feed*, and the H_2O/CO ratios used in the realistic feed compositions during individual WGS tests (see Section 4.2). This considerable difference also confirmed the importance of serial OSR-WGS reaction tests, which actually shows real WGS performance of the catalysts during fuel processing. WGS catalyst activities obtained in serial tests with respect to temperature indicated that operation at low temperature is advantageous for WGS reactor.

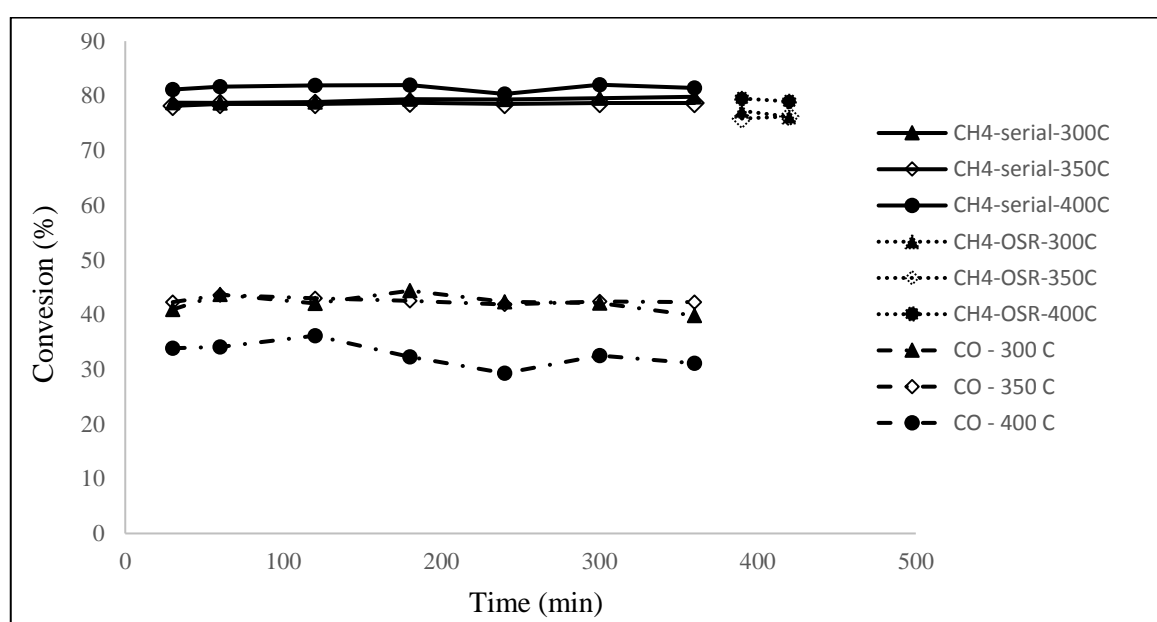


Figure 4.23. 6h TOS OSR and WGS activities over sequentially impregnated 1%Pt-1%Re-1%Na/CeO₂ under 14% CH₄, 9.3% O₂, 56% H₂O, 20.7% Ar ($H_2O/CO=4$, $O/C=1.33$) feed flow at 300°C, 350°C and 400°C.

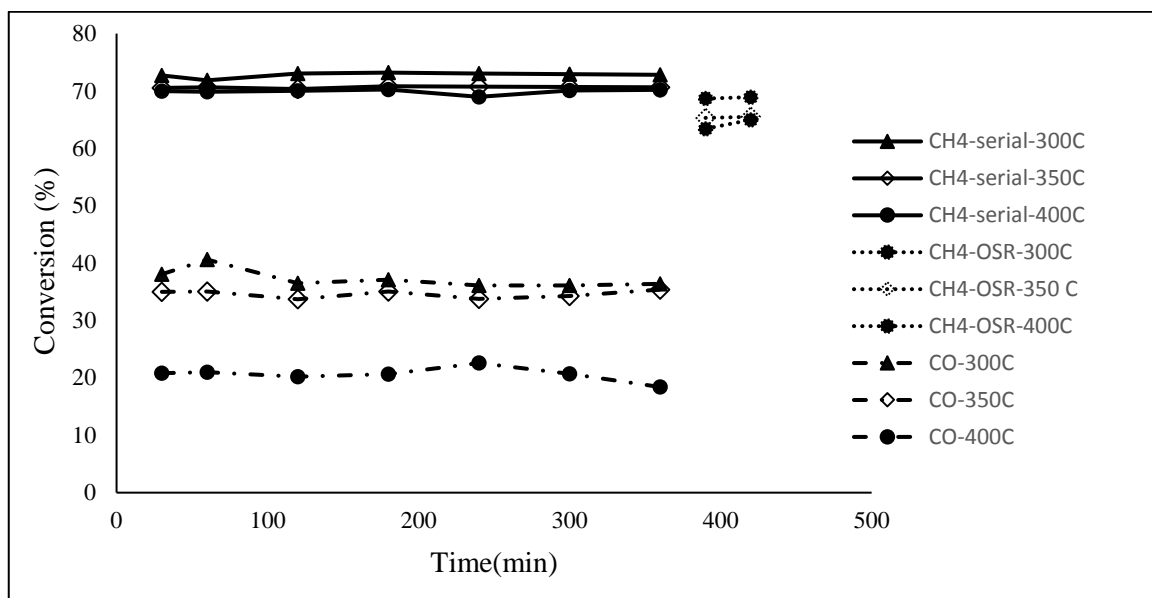


Figure 4.24. 6h TOS OSR and WGS activities over sequentially impregnated 1%Pt-1%Re-1%Na/CeO₂ under 14% CH₄, %6.7 O₂, %56 H₂O, %23.3 Ar (H₂O/CO=4, O/C=0.95 feed flow at 300°C, 350°C and 400°C.

A comparative analysis of the results obtained in serial OSR-WGS and individual WGS tests suggests a strong dependence of overall OSR-WGS system performance not only depends on individual activities of the reactors but also on OSR selectivity, i.e. H₂/CO product ratio, and H₂O concentration in OSR product. CO and CH₄ conversion levels achieved under OSR feed with O/C feed ratios of 1.33 and 0.95 are presented in Figure 4.25 and 4.26, respectively, for serial system utilizing Pt-Re-Na catalysts in WGS reactor. H₂ concentrations measured at the exit of OSR reactor (*which was the feed stream of WGS reactor in serial tests*) and WGS reactor are also exhibited together in Figure 4.25 and 4.26. Note that in serial tests OSR product was directly fed to WGS reactor; all conversion levels (CO and CH₄) and H₂ concentrations presented in these figures were obtained at the end of 2 hour TOS; CH₄ conversions are given for WGS product; and H₂ concentration values are on a dry basis. While individual WGS tests conducted at 300°C gave relatively lower CO conversions, contrary trend was observed in serial tests conducted with O/C=1.33 in OSR feed for all WGS catalysts except 1%Pt-1%Re-2%Na/CeO₂, and increasing temperature led to a decrease in CO conversion values. Interestingly, though serial tests conducted via utilizing 1%Pt-1%Re-1%Na/TiO₂ as the WGS catalyst yielded slightly lower CH₄ and CO conversion values for the whole temperature range, most probably due to its lower oxygen

storage capacity, that will be explained in Section 4.5.1 in detail. Besides, the H₂ concentration (%) at the exit of WGS reactor reached levels obtained at serial tests utilizing the other WGS catalysts.

Among the tests conducted under OSR feed composition with high O/C ratio, the highest serial activity was achieved for the case sequentially impregnated 1%Pt-1%Re-1%Na/CeO₂ was used as the WGS catalyst at 300°C as 42.1% and at 350°C as 43.0% in terms of CO conversion. Decrease in CO conversion can easily be observed over WGS catalysts with increasing WGS reaction temperature for the OSR feed with low O/C ratio (Figure 4.26). Combined evaluation of the serial test results conducted with OSR feeds having different O/C ratios (Figures 4.25 and 4.26 with O/C of 1.33 and 0.95, respectively) indicate that there is a decrease in CH₄ conversion achieved in OSR reactor with a decrease in O/C feed ratio (Figure 4.26). Unlike the results of the individual WGS tests, the highest activity was achieved over Re-Na coimpregnated 1%Pt-1%Re-1%Na/CeO₂ catalyst in serial tests at 350°C as 42.2% under OSR feed having O/C=0.95.

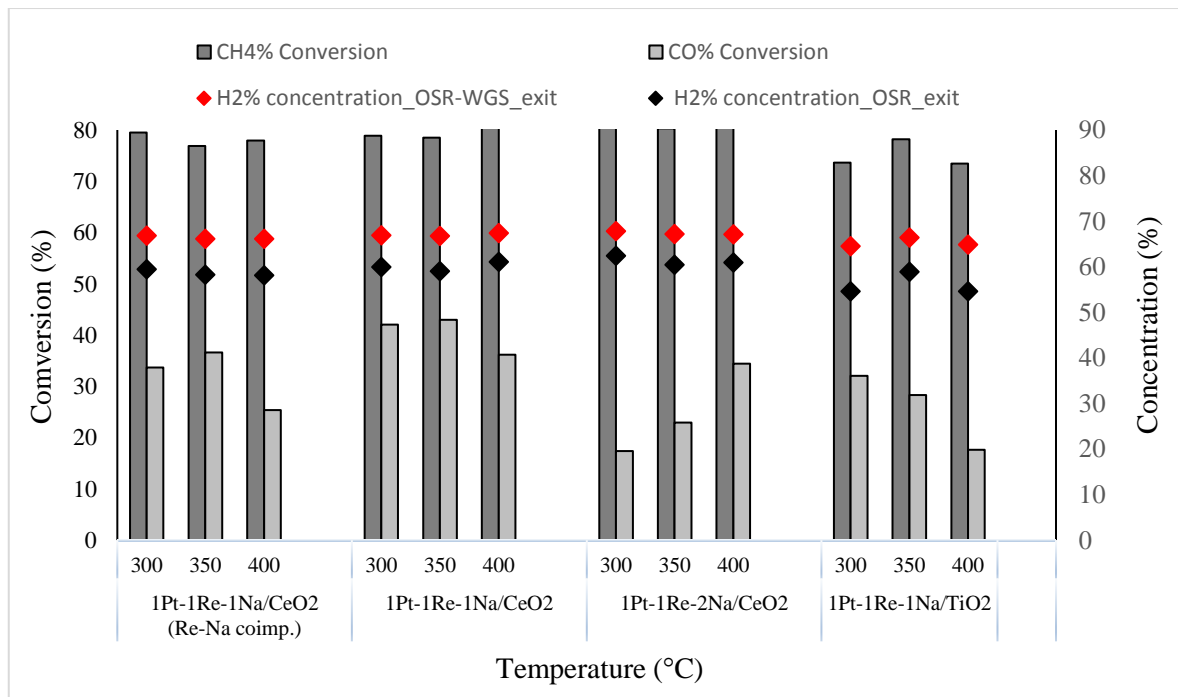


Figure 4.25. OSR activity and real WGS performance data obtained in serial OSR-WGS tests conducted under 14% CH₄, 9.3% O₂, 56% H₂O, 20.7% Ar (H₂O/CO=4, O/C=1.33); WGS temperatures are 300°C, 350°C and 400°C; H₂ concentrations are given on a dry basis.

The overall evaluation of the results indicated that gas composition (and/or composition change) at the exit of OSR reactor affects WGS catalytic activity directly. According to the results of serial tests, even the minute differences, *including those within the limit of experimental error margins*, in OSR product composition may lead to amplified changes in WGS performance. Consequently, stable performance of a fuel processor guaranteeing its product properties stay within the precision limits, which are practically imposed by a PEM fuel cell connected to it, require a sophisticated control system.

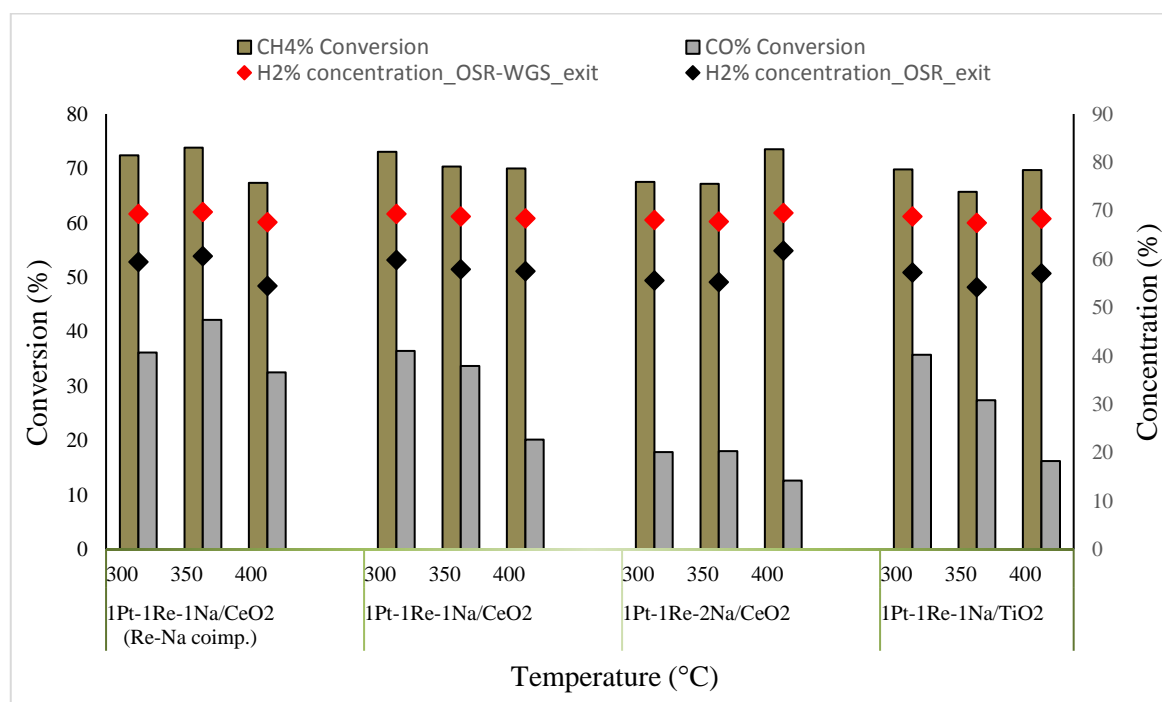


Figure 4.26. OSR activity and real WGS performance data obtained in serial OSR-WGS tests conducted under 14% CH₄, 6.7% O₂, 56% H₂O, 23.3% Ar (H₂O/CO=4, O/C=0.95); WGS temperatures are 300°C, 350°C and 400°C; H₂ concentrations are given on a dry basis.

4.3. Characterization of Pt-Re-Na/CeO₂ and Pt-Re-Na/TiO₂ Catalysts

4.3.1. XRD Analysis:

X-ray diffraction (XRD) patterns of the samples were recorded by using a Cu K_α radiation and continuous scan mode at 2° min⁻¹. XRD spectra of freshly reduced 1%Pt-

1%Re-1%Na/CeO₂, 1%Pt-1%Re-2%Na/CeO₂ and 1%Pt-1%Re-3%Na/CeO₂ catalysts are presented in Figure 4.27.

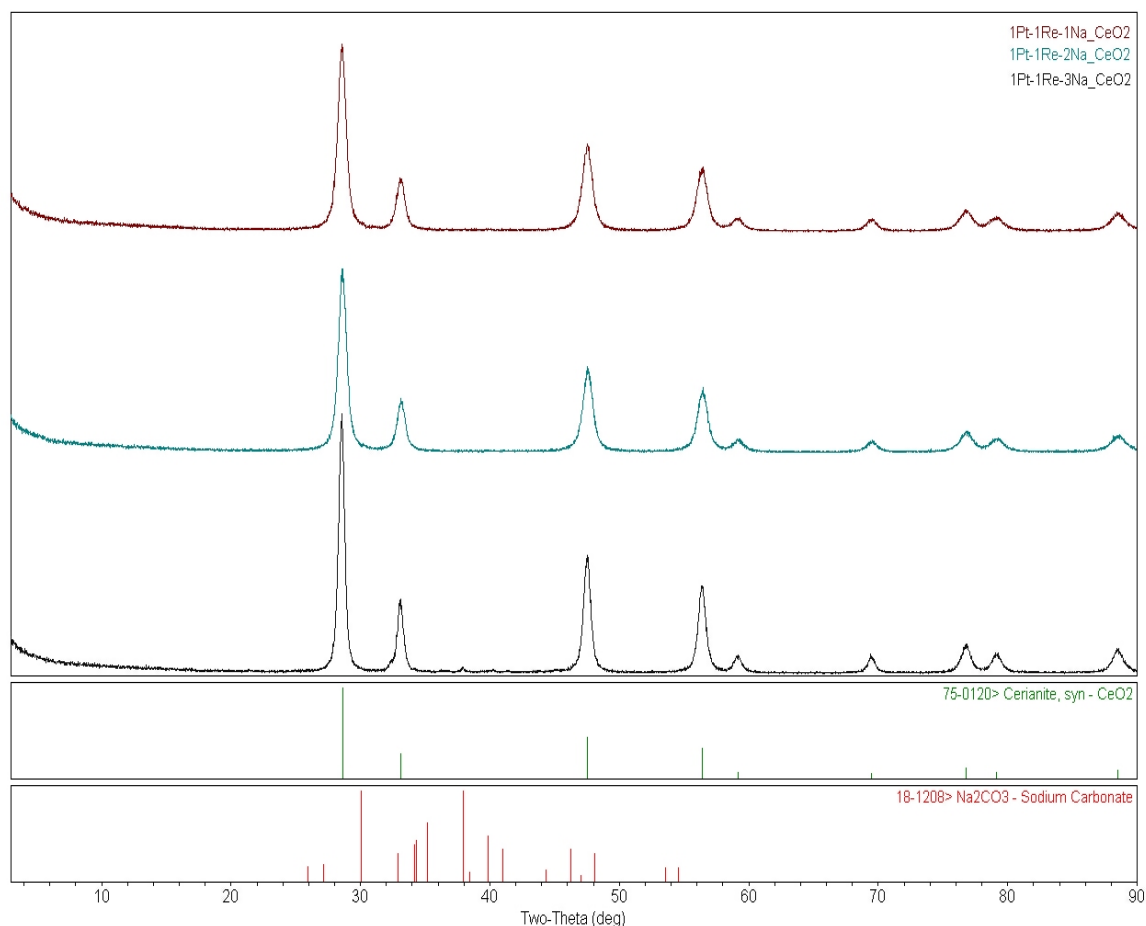


Figure 4.27. XRD Profiles of sequentially impregnated 1%Pt-1%Re-1%Na/CeO₂, 1%Pt-1%Re-2%Na/CeO₂ and 1%Pt-1%Re-3%Na/CeO₂ catalysts.

The CeO₂ support, which was prepared according to the method described in Experimental section, was confirmed having typical characteristics of CeO₂ (*Cerianite*-JCPDS file no. 75-0120) material. No difference was determined among the spectra of 1%Pt-1%Re-1%Na/CeO₂ and 1%Pt-1%Re-2%Na/CeO₂ catalysts and CeO₂ support. The absence of platinum, rhenium or sodium peaks in these catalysts spectra can be seen as the indication of homogeneous distribution of these metals on the surface with crystal sizes smaller than the detection limit of XRD. On the other hand, peaks corresponding to sodium carbonate species were observed in the spectrum of 1%Pt-1%Re-3%Na/CeO₂. The carbonate

formation on this catalyst's surface was also supported by the spectra obtained in FTIR-DRIFTS studies, which is given in Section 4.4. Considering the results obtained in the performance studies, it can be said that sodium carbonate formation causes low catalytic activity for Pt-Re-Na/CeO₂ catalysts.

Figure 4.28 shows the XRD spectra of freshly reduced 1%Pt-1%Re-1%Na/TiO₂ catalyst, which expresses anatase form of TiO₂ (*tetragonal*; JCPDS file no. 99-0008) as the main peak. According to its XRD pattern, the sample has trace amount of rutile TiO₂ and Ti₂O. Unlike the CeO₂ supported Pt-Re-Na systems, formation of ReO₃ is substantiated by XRD pattern. It is reasonable that Re may play a greater role in the redox mechanism over these catalysts via compensating the role of CeO₂, which provide oxygen storage capacity, in CeO₂ supported samples.

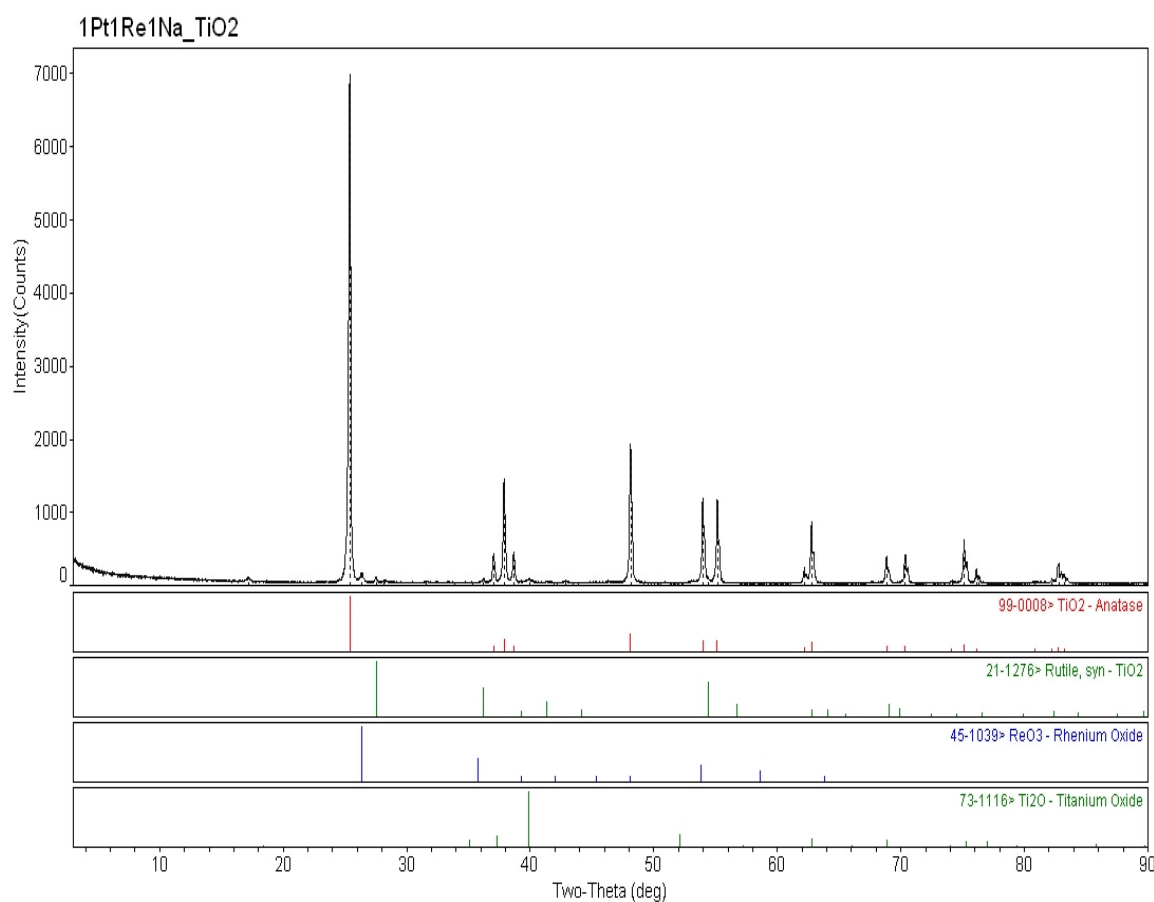


Figure 4.28. XRD Profiles of sequentially impregnated 1%Pt-1%Re-1%Na/TiO₂ catalyst.

The lattice constants of the samples were calculated by applying Bragg's law using Equation (4.5):

$$a = d\sqrt{h^2 + k^2 + l^2} \quad (4.5)$$

where d is the lattice spacing of the cubic crystal, and h , k and l are Miller indices.

Scherrer Equation was used to calculate the mean crystallite sizes of the support and catalysts, as given in Equation (4.6):

$$\tau = \frac{K \lambda}{\beta \cos \theta} \quad (4.6)$$

where K is the shape factor (0.9), λ is the X-ray wavelength (0.154056 nm), β is the line broadening at half the maximum intensity (FWHM) in radians and θ is the Bragg angle in radians.

The lattice constants of CeO₂ and TiO₂ supports, and the reduced catalysts are given in Table 4.1 with the crystallite sizes which were calculated by using diffraction peaks of the plane (1 1 1) and (1 0 1) for CeO₂ supported and TiO₂ supported catalysts, respectively. It was observed that Na, Re and Pt addition did not affect the lattice constants. Crystallite sizes of CeO₂ supported catalysts increased with increased metal loading, however metal loading led to a decrease in support crystallite size in TiO₂ supported catalyst.

The crystallite size of the CeO₂ increased from 10.18 to 13.25 nm in the case of sequentially impregnated 1%Pt-1%Re-1%Na/CeO₂, however crystallite size of the catalyst prepared via coimpregnation with the same amounts of metal loading was less affected. No significant increase in crystallite size was observed in response to the increase in sodium loading to 2%, but further increase in Na loading led to an increase in crystallite size. The relatively high crystallite size obtained for 1% Pt-1% Re-3Na/CeO₂, over which low WGS activity was measured (see section 4.1), indicated that the crystallite size cannot be directly related to the activity. However, there is a significant increase in crystallite size and a pronounced decrease in WGS catalytic activity of the Pt-Na/CeO₂ catalysts in response to

an increase in Na loading 2% to 3%. WGS catalytic activity of 1%Pt-1%Re-3%Na/CeO₂ was found to be considerably low, whereas 1%Pt-1%Re-2%Na/CeO₂ catalyst showed high activity and stability, meaning that the optimum Na loading for Pt-Re/CeO₂ catalysts is in the range of 2-3%. Low catalytic activity of 1%Pt-1%Re-3%Na/CeO₂ catalyst may be related with the significant increase in crystallite size, since sequentially impregnated 1%Pt-1%Re-1%Na/CeO₂ and 1%Pt-1%Re-2%Na/CeO₂ samples, which have similar crystallite sizes, had reached high catalytic activities under the specified reaction conditions. Those result are in accordance with the literature mentioning an optimum value for Na loading used in Pt-Na catalysts to achieve higher WGS catalytic activity under specified conditions (Zhu *et al.*, 2009).

Table 4.1. Lattice constants and crystallite sizes of CeO₂ and reduced samples.

Sample	Lattice Constant, a (nm)	Crystallite size, τ (nm)
CeO ₂	5.41	10.18
1%Pt-1%Re-1%Na/CeO ₂ (coimp.)	5.40	10.66
1%Pt-1%Re-1%Na/CeO ₂	5.40	13.25
1%Pt-1%Re-2%Na/CeO ₂	5.41	13.46
1%Pt-1%Re-3%Na/CeO ₂	5.41	17.15
TiO ₂	4.96	44.51
1%Pt-1%Re-1%Na/TiO ₂	4.95	44.28

4.3.2. SEM Analysis

SEM images of co-impregnated 1%Pt-1%Re-1%Na/CeO₂, sequentially impregnated 1%Pt-1%Re-1%Na/CeO₂, 1%Pt-1%Re-2%Na/CeO₂, 1%Pt-1%Re-1%Na/TiO₂ and 1%Pt-1%Re-3%Na/CeO₂ catalysts are given in Figures 4.29-4.34. Although there was no significant difference between zoomed SEM images of CeO₂-supported catalysts, bright spots, which were circled, were found on the sequentially impregnated 1%Pt-1%Re-1%Na/CeO₂ and 1%Pt-1%Re-2%Na/CeO₂ catalysts were shown on Figure 4.31.

SEM images were obtained by using MIX detector type and combination of SEM and BSE property enable brightening of Pt particles, which have high molecular weight. The size of these bright particles coincided with the Pt metal dimensions previously determined on the SEM image of 1% Pt-1%Re-1% V/CeO₂ catalyst (Özer, 2016). Since EDX device was

not operating properly, it was not possible to confirm this result with EDX. The striped structure seen in all of the catalysts supported by CeO_2 showed that this structure had formed due to nature of CeO_2 support. The absence of clear Pt particles on the Na impregnated surfaces in the SEM images can be explained by the lower Pt particle size formed during catalyst preparation.

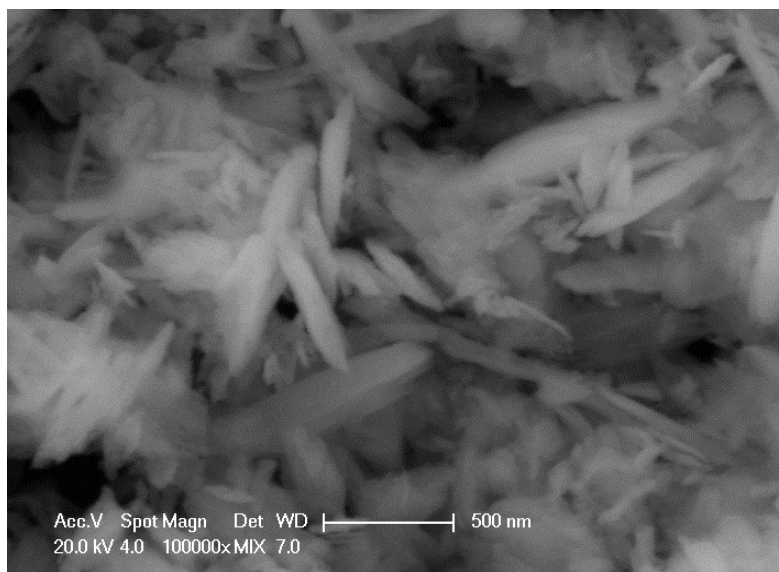


Figure 4.29. SEM image of coimpregnated %1Pt-%1Re-%1Na/ CeO_2 catalyst (x100000).

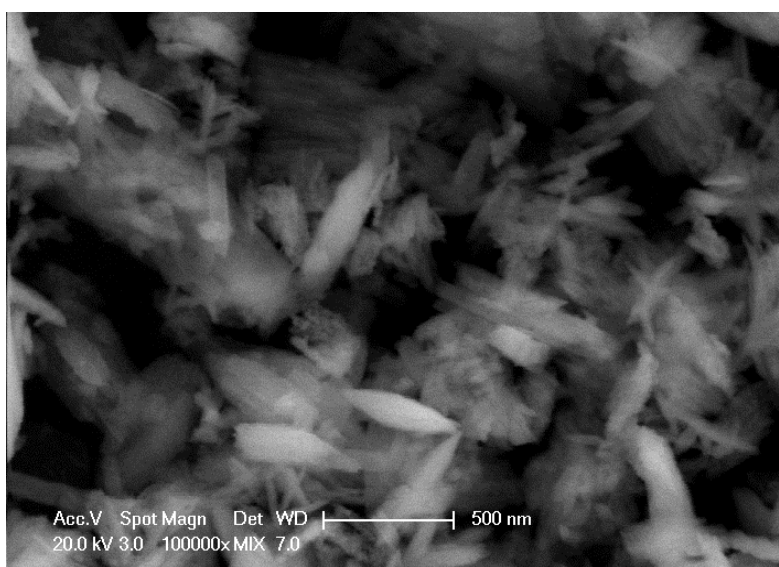


Figure 4.30. SEM image of sequentially impregnated %1Pt-%1Re-%1Na/ CeO_2 catalyst (x100000).

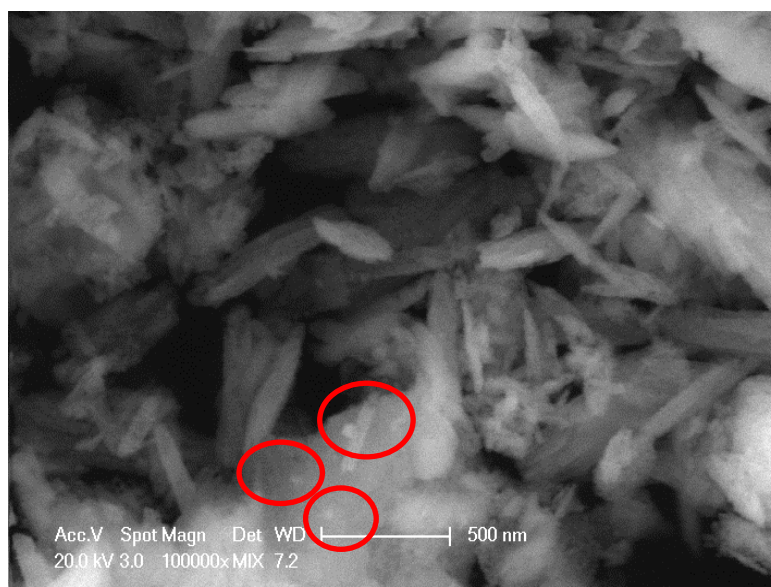


Figure 4.31. SEM image of sequentially impregnated %1Pt-%1Re-%2Na/CeO₂ catalyst (x100000).

In the SEM image of 1% Pt-1% Re-1%Na/TiO₂ catalyst, which is presented in Figure 4.32, circular structured particles, which were attributed to TiO₂ support, were noticed instead of the striped structure as in the case of CeO₂ supported catalysts. Pt metal particles on this surface can be distinguished more clearly than that of on CeO₂ supported surface. It was thought that the absence of Pt particles in lighter areas can be resulted from use of MIX detector, and the reason cannot be defined precisely due to lack of EDX analysis.

The SEM image of the 1%Pt-1%Re-3%Na/CeO₂ catalyst is given in Figure 4.33. Agglomerated structures, which were not observed on the catalyst surfaces with less Na loadings, were recognized in the catalyst surface with 3% Na loading. Similar structures were found in the SEM image of the used 1%Pt-1%Re-1%Na/CeO₂ catalyst given in Figure 4.34. Referring to the results of FTIR-DRIFTS studies carried out under reaction conditions in Section 4.4, carbonate formation was observed on Na-containing catalysts and these clusters were thought to belong to carbonate groups. The presence of Na₂CO₃ in the XRD analysis on 1% Pt-1%Re-3% Na/CeO₂ also supported this deduction.

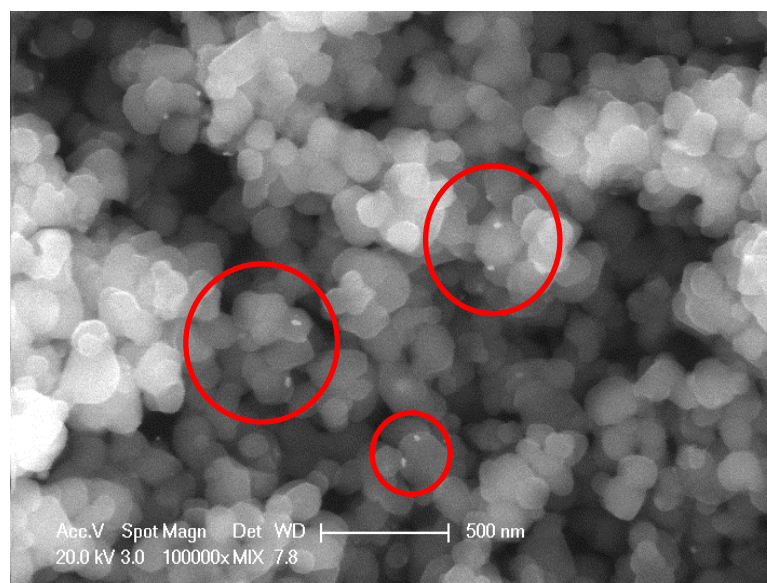


Figure 4.32. SEM image of sequentially impregnated %1Pt-%1Re-%1Na/TiO₂ catalyst (x100000).

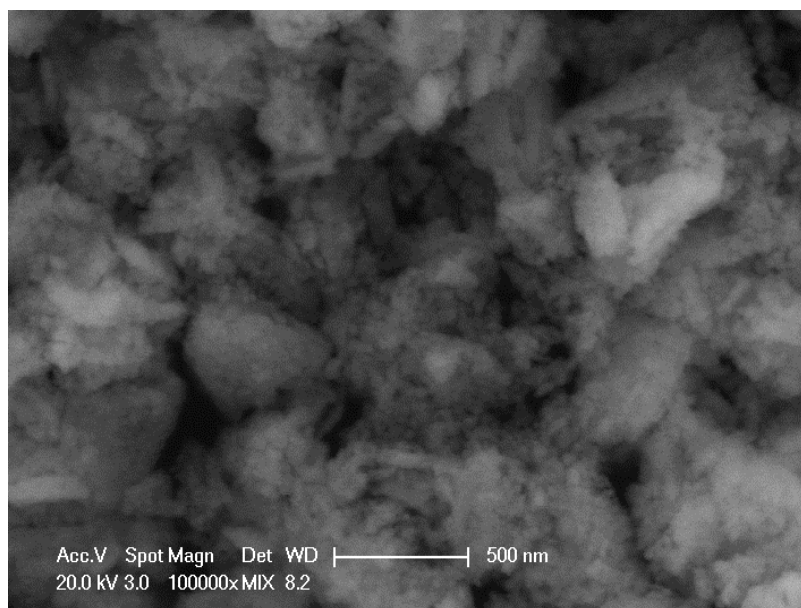


Figure 4.33. SEM image of sequentially impregnated %1Pt-%1Re-%3Na/CeO₂ catalyst (x100000).

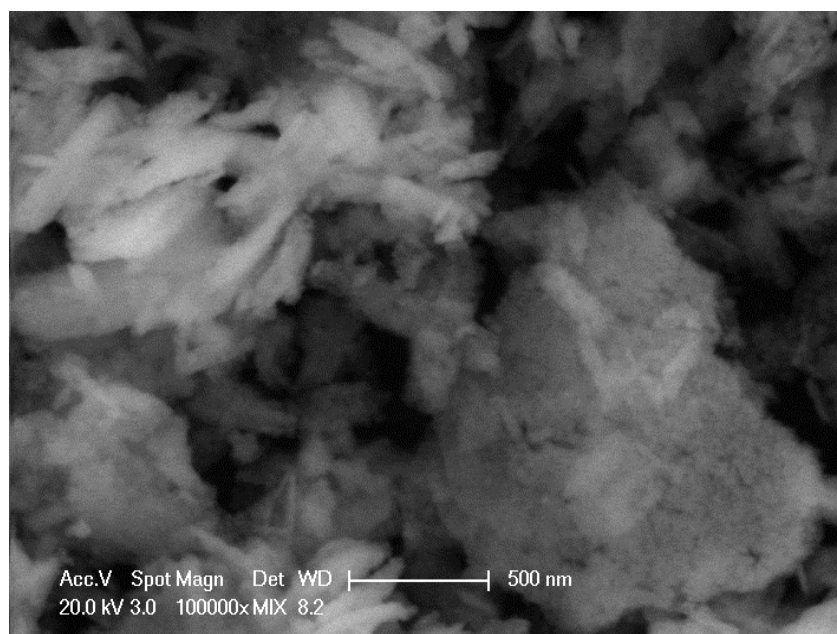


Figure 4.34. SEM image of sequentially impregnated 1%Pt-1%Re-2%Na/CeO₂ catalyst after reaction (x100000).

4.3.3. XPS Analysis:

Elemental composition of the catalyst surface and oxidation states of the metallic species present were investigated by X-ray photoelectron spectroscopy. Due to the redox step of the WGS reaction mechanism affecting oxidation states of the metal oxides; XPS is an important tool for assessing the changes occurred during reaction through analyzing the differences of the metallic species on the spent catalysts from those on freshly reduced ones. Characteristic oxidation states of Ce, Na, O, Pt, Re and Ti atoms were observed in the XP spectra of the samples.

Figure 4.35 displays the XP spectra of Ce 3d core level electrons of the freshly reduced and spent catalysts, which were subjected to WGS reaction conditions under the flow of realistic feed #1. The spectra includes two principal energy spin-orbit states: Ce3d_{3/2} and Ce3d_{5/2}. Ce atoms have two oxidation states in those spin orbits, namely Ce³⁺, which is labeled as u and Ce⁴⁺, which is labeled as v, respectively.

Ce 3d region of the XPS spectra were evaluated and relative amount of Ce^{3+} compound was estimated using the following formula:

$$[Ce^{3+}] = I - Ce^{3+} / (I - Ce^{3+} + I - Ce^{4+}) \quad (4.7)$$

where $I - Ce^{3+}$ and $I - Ce^{4+}$ represent the sum of the intensities of two doublets resulting from Ce_2O_3 and three doublets resulting from CeO_2 , respectively.

Table 4.2 illustrates the Ce^{3+} content of the freshly reduced and spent catalysts studied in this work. The formation of active OH groups participated in WGS reaction had been reported to occur on Ce^{3+} defect sites (Vignatti *et al.*, 2011; Hwang *et al.*, 2011). The highest Ce^{3+} content was not observed on the most active catalyst, as in the case of previous studies performed over CeO_2 supported catalysts (Çağlayan, 2011; Özer, 2016). The absence of a direct relationship between activity and Ce^{3+} sites for Na containing catalysts, which is in contrast to that observed for Na-free catalysts used in previous studies, may have occurred due to the presence of Na and the amount of Na loading as well. When the spectra of freshly reduced and spent forms were compared for each catalyst, there observed a change in the distribution of the peaks of Ce^{3+} and Ce^{4+} regions in an unexpected way in spent catalysts. Ce^{3+} percentage was observed to be increased in sequentially impregnated 1%Pt-1%Re-1%Na/ CeO_2 and 1%Pt-1%Re-2%Na/ CeO_2 samples, which exhibited high activity in the performance tests, after being exposed to realistic feed conditions. Coimpregnated 1%Pt-1%Re-1%Na/ CeO_2 catalyst was determined as the only catalyst on which the Ce^{3+} content reduced after reaction conditions. From this point of view, NaO_x groups formed during catalyst preparation, rather than Ce^{3+} content, can be related with catalytic activity for these catalysts. Although the Ce 3d peak distribution of 1%Pt-1%Re-3%Na/ CeO_2 show similarity with other sequentially impregnated samples, its low activity was in accordance with the low peak intensities of both Ce^{3+} and Ce^{4+} regions compared to those observed on all freshly reduced forms of CeO_2 supported samples.

Table 4.2. Ce^{3+} contents (%) of freshly reduced and spent catalysts under realistic feed #1 and realistic feed #2 conditions.

Catalyst	Ce^{3+} (%)		
	Freshly Reduced	Spent in RF#1	Spent in RF#2
1%Pt-1%Re-1%Na/CeO ₂ (coimp.)	21.14	19.22	16.01
1%Pt-1%Re-1%Na/CeO ₂	15.91	17.65	18.02
1%Pt-1%Re-2%Na/CeO ₂	18.96	20.34	18.80
1%Pt-1%Re-3%Na/CeO ₂	15.97	20.52	-

The Na1s spectra of the freshly reduced and spent catalysts are shown in Figure 4.36. There are peak formations observed in Na1s region at 1071.85-1071.44 eV, which corresponds to metallic Na, Na₂O, NaOH (Dongil *et al.*, 2015). The peak in the region near 1070.5 eV, which is also reported as an indication of presence of Na₂O, was observed intensified in the freshly reduced form of sequentially impregnated 1%Pt-1%Re-1%Na/CeO₂ and 1%Pt-1%Re-2%Na/CeO₂, which are the most catalytically active samples. The peak intensity decreases in 1%Pt-1%Re-3%Na/CeO₂ sample, and it was also not dominant in TiO₂ supported catalyst. Peaks located in the region of 1071.1–1071.5 eV are attributed to the presence of NaHCO₃ and Na₂CO₃, and the ones in the region 1072.3–1072.5 eV are corresponding to Na and Na₂O (Ma *et al.*, 2018; Guerrero *et al.*, 2012). Peaks around 1070.5 eV was observed to be less significant, and a shift towards 1071.5 eV region was observed after being exposed to realistic feed #1, which indicates the utilization of oxygen reducing the oxides during the reaction. The most significant shift was seen in the spectra of 1%Pt-1%Re-2%Na/CeO₂ sample, which is in accordance with its high activity under realistic feed #1 conditions at 350°C.

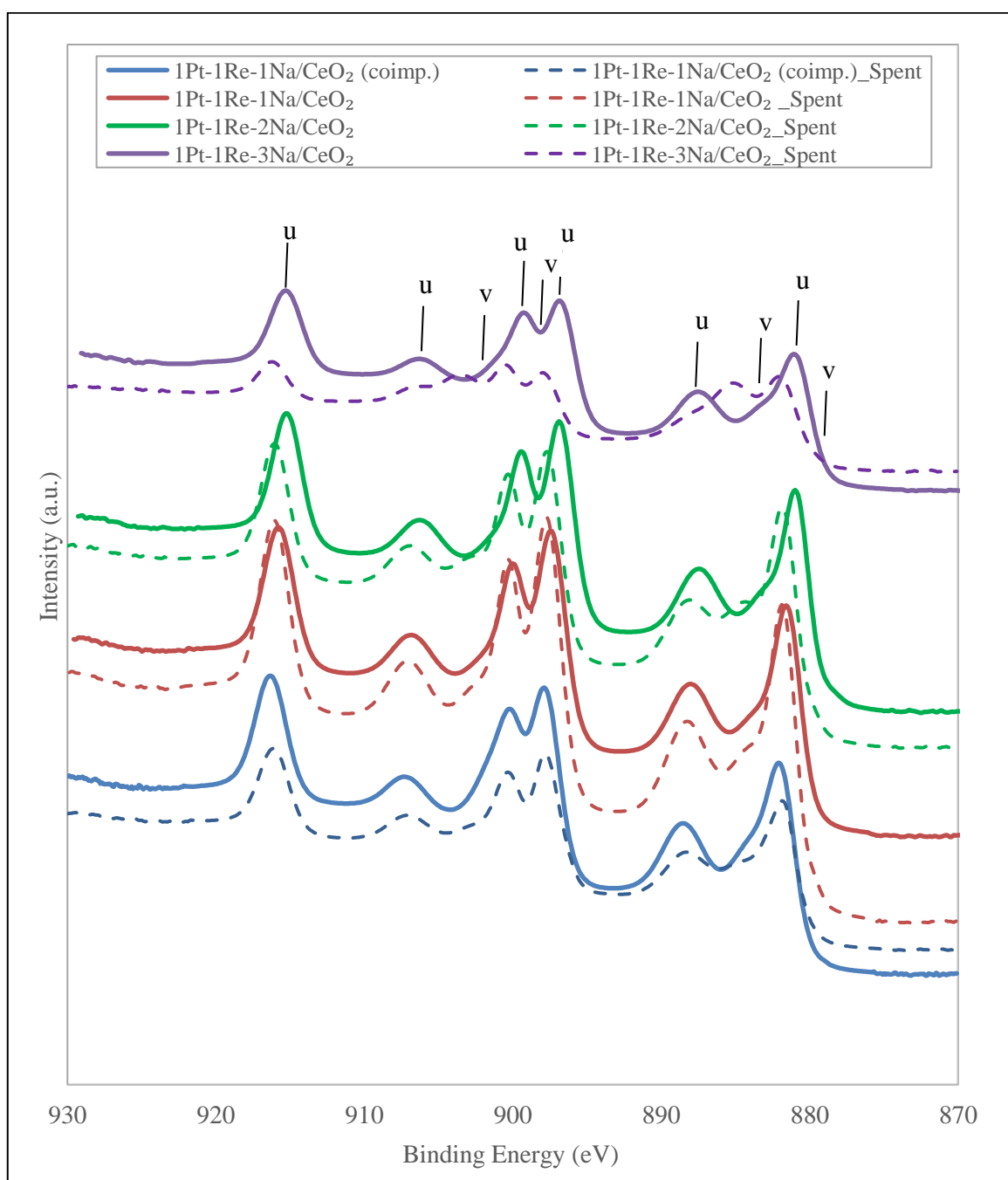


Figure 4.35. XP Spectra showing the Ce3d region of freshly reduced and spent (realistic feed #1, 350°C) catalyst samples (v: Ce³⁺, u: Ce⁴⁺).

Figure 4.37 displays the XP spectra of the O1s region of freshly reduced and spent catalyst samples. The O1s spectra mainly consist of three regions; 528.6-529.9 eV, 531.1-531.6 eV, 532.3-533.0 eV. Among those, the first region is referred to lattice oxygen in CeO₂ and/or NaO_x, while the second one is attributed to surface chemisorbed oxygen (O₂²⁻ and O⁻) (Ma *et al.*, 2018; Dongil *et al.*, 2015), and the last one is an indication of O species associated with Na such as O in NaO_x, -OH and carbonates (Zhu *et al.*, 2011). The peak showing the lattice oxygen in freshly reduced catalysts was observed to be shifted towards 528 eV with the increase in Na loading for CeO₂ supported catalysts, implying that lattice oxygen in CeO₂ and/or NaO_x plays an important role on the activity of these catalysts. It was observed that the peak referring to lattice oxygen in 1%Pt-1%Re-3%Na/CeO₂ sample was decreased more regarding the change in other peaks' intensities. Although this peak was still significant in spectra of the other spent catalysts, relatively lower peak intensity for 3%Na loaded one can be explained by the absence of its surface oxygen, stored as oxides, participating to redox mechanism. The peak position referring to lattice oxygen in TiO₂ supported catalysts is reported to be in the range of 529.7-530 eV region, in accordance with the results obtained for 1%Pt-1%Re-1%Na/TiO₂ sample. Another peak obtained at the binding energy range 530.8–531.5 eV is attributed to Ti–OH (Li *et al.*, 2016). The peak showing the lattice oxygen in this catalyst's spectrum was not affected by Na addition in contrast to what observed for CeO₂ supported catalysts, i.e. the interaction between Na and CeO₂ support is thought more significant than that between Na and TiO₂ support. The distribution of peaks of TiO₂ supported catalyst after reaction was found to be different from that of the CeO₂ supported catalysts. This may be the indication of different WGS reaction mechanisms on the surface of the TiO₂ and CeO₂ supported catalysts.

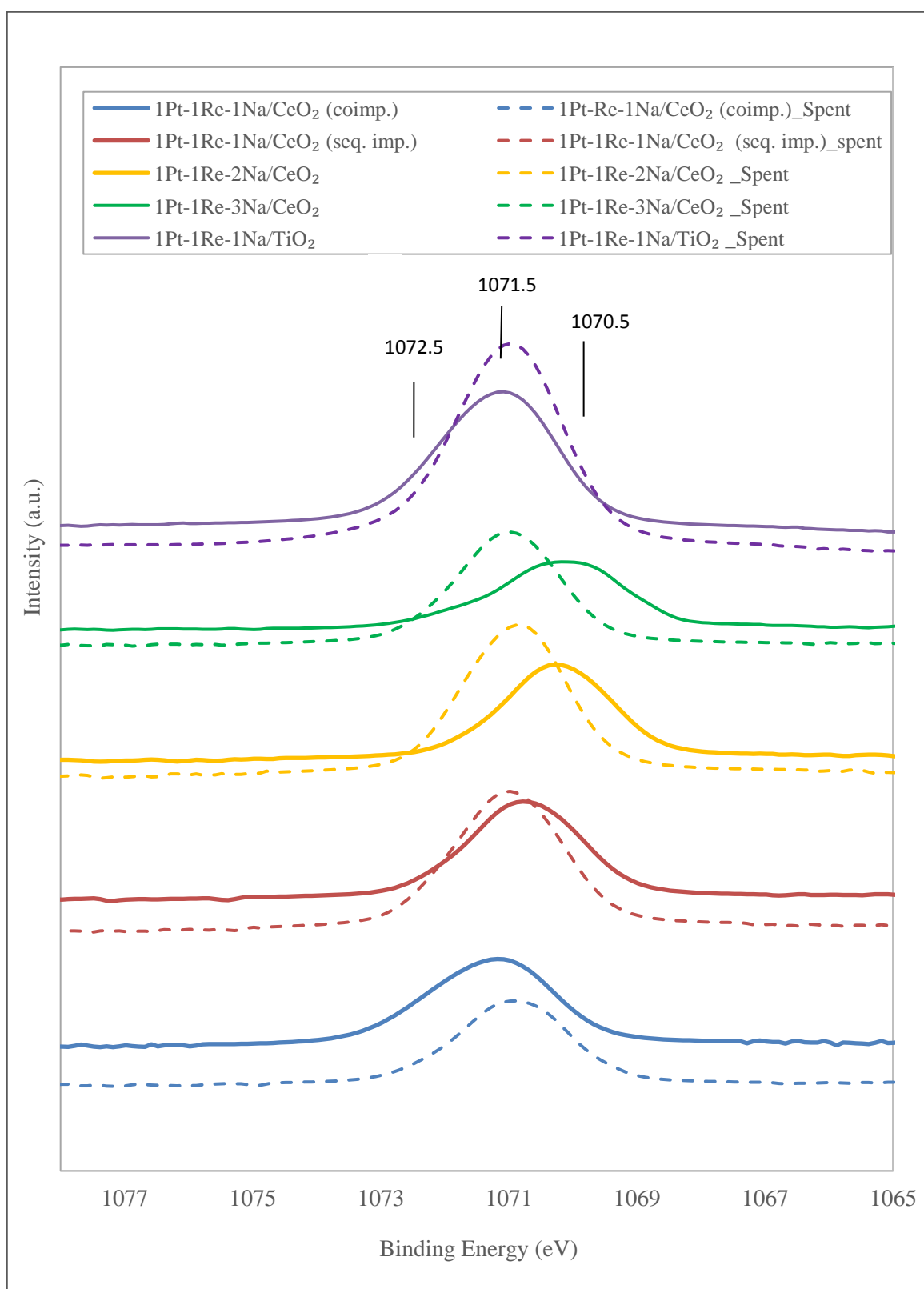


Figure 4.36. XP Spectra showing the Na 1s region of freshly reduced and spent (realistic feed #1, 350°C) catalyst samples.

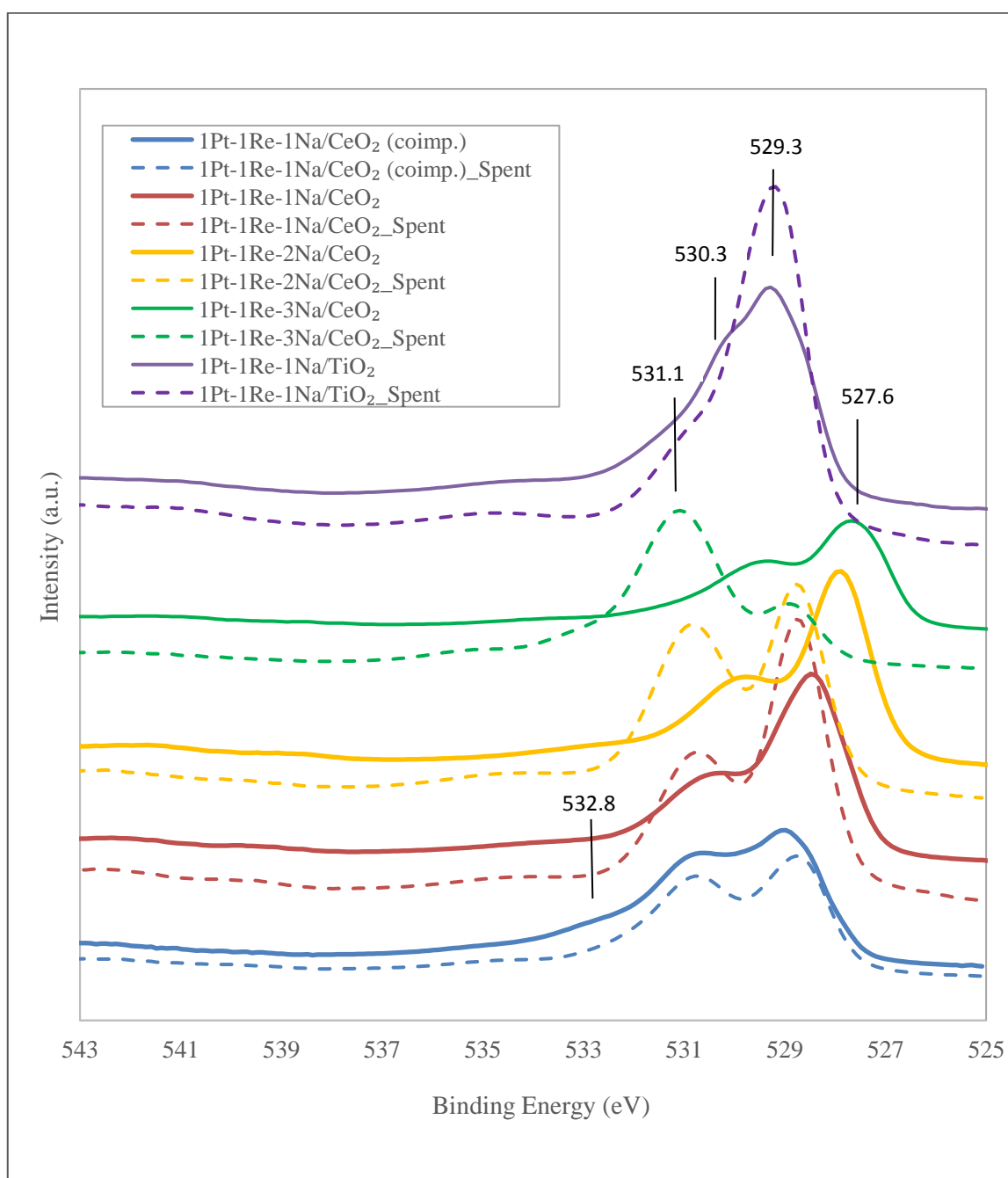


Figure 4.37. XP Spectra showing the O1s region of freshly reduced and spent (realistic feed #1, 350°C) catalyst samples.

Figure 4.38 presents the XPS spectra of Pt 4f region of the fresh and spent catalysts. The Pt 4f_{7/2} peak at 71.0 eV and the Pt 4f_{5/2} peak at 74.2 eV are assigned to Pt⁰; the peaks at 71.9 and 75.1 eV are assigned to Pt²⁺, whereas the peaks at 74.3 and 77.5 eV are assigned to Pt⁴⁺ species (Pierre *et al.*, 2007; Yu *et al.*, 2010; Wang *et al.*, 2018). Spectra of freshly

reduced form of sequentially impregnated 1%Pt-1%Re-1%Na/CeO₂ and 1%Pt-1%Re-2%Na/CeO₂ samples yielded higher intensity peaks attributed to Pt²⁺ species, which are known to be active species for WGS reaction (Roh *et al.*, 2012; Zhu *et al.*, 2011). Higher intensity Pt²⁺ peaks observed are in accordance with the high catalytic activity of these catalysts.

Additionally, presence of higher intensity of Pt²⁺ peaks in spectra of sequentially impregnated sample is in agreement with Pt4f spectra of coimpregnated 1%Pt-1%Re-1%Na/CeO₂ sample, which exhibits the presence of Pt⁴⁺ species rather than Pt²⁺. The results furtherly indicated possible blockage of the active Pt sites at higher Na loadings leading to a very limited Pt²⁺ and Pt⁴⁺ presence, as in the case of 3% Na loaded sample.

XPS results of the Re 4f region of all catalysts (Figure 4.39) exhibit that Re exists as Re⁴⁺, Re⁶⁺, and Re⁷⁺ species on all catalysts' surface with different ratios. The spectra obtained on each sample was found to be in accordance with the literature data revealing the presence of two Re 4f_{7/2} contributions with binding energies of 45.9 ± 0.3 eV and 47.5 ± 0.2 eV, which were assigned to Re oxide species with minor oxygen atoms in its environment (ReO_x) and Re⁷⁺ (Re₂O₇ or ReO₄⁻) species, respectively (Toledo *et al.*, 2019). A peak around 50 eV binding energy, which cannot be specified from literature, was obtained in spectra of coimpregnated 1%Pt-1%Re-1%Na/CeO₂ and sequentially impregnated 1%Pt-1%Re-1%Na/TiO₂ samples most probably due to the ReO_x formed during coaddition of Na-Re precursors on CeO₂ in the first case, and addition of Na precursor in TiO₂. This peak disappeared from the spectrum of coimpregnated 1%Pt-1%Re-1%Na/CeO₂ after subjected to reaction conditions, however no significant change was observed in the spectrum of sequentially impregnated 1%Pt-1%Re-1%Na/TiO₂ upon reaction. This difference strongly suggests the occurrence of different WGS reaction mechanisms on the surface of CeO₂ and TiO₂ supported catalysts.

The Ti2p spectra of the freshly reduced and spent 1%Pt-1%Re-1%Na/TiO₂ catalysts are shown in Figure 4.40. In the literature, Ti2p peaks having binding energies of 458.8, 457.5, 455.1 and 454.1 eV are attributed to TiO₂, Ti₂O₃, TiO and Ti, respectively (Lu *et al.*, 2000; Li *et al.*, 2016). TiO₂ species, indicated by a shoulder type peak at 458.6 eV, were observed on freshly reduced 1%Pt-1%Re-1%Na/TiO₂ catalyst, whereas this peak disappears

after reaction in the spent sample. The intensification of peaks upon reaction, which gets more significant for the peaks belong to species with higher Ti:O ratio, suggests the participation of oxygen in WGS reaction.

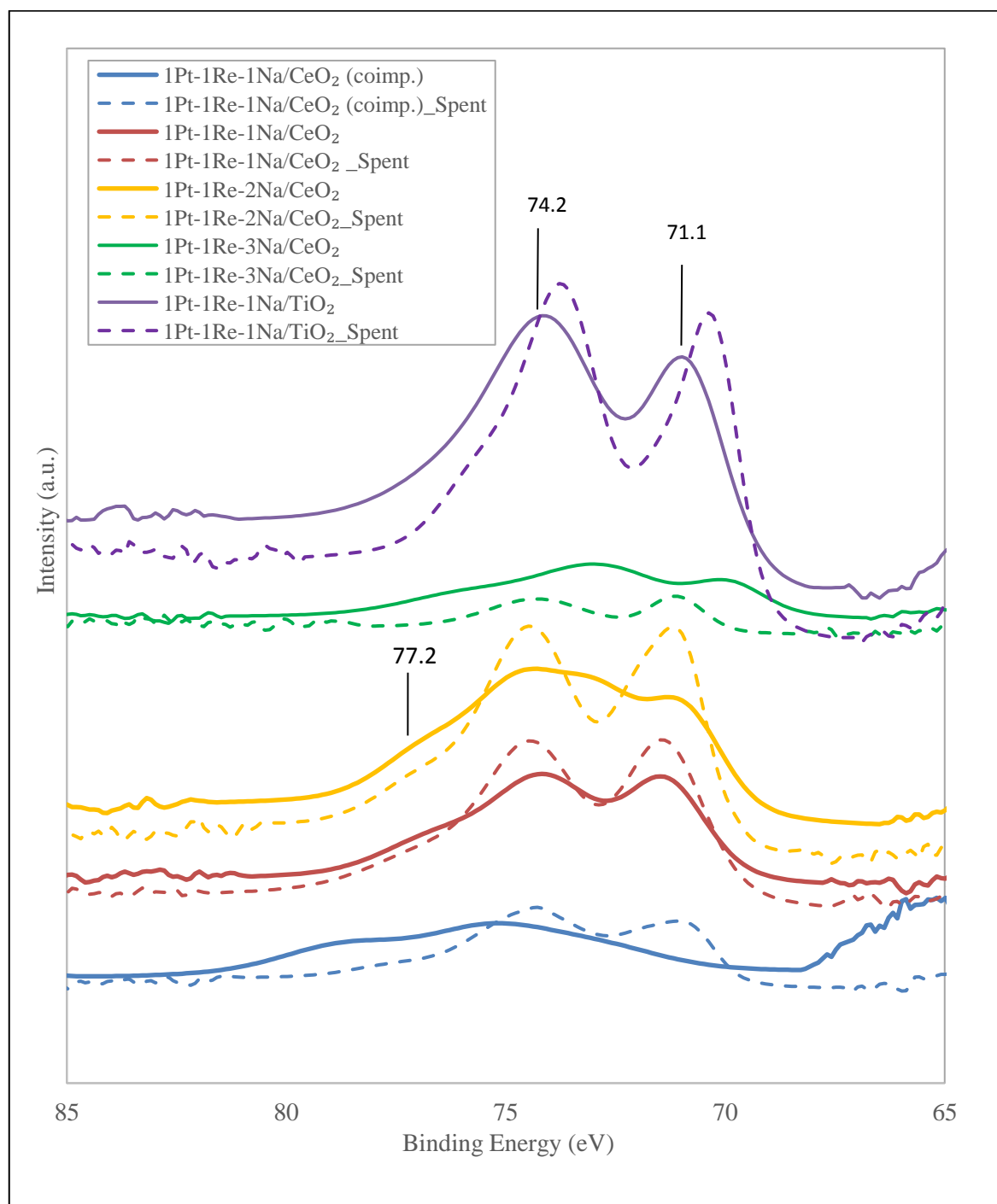


Figure 4.38. XP Spectra showing the Pt4f region of freshly reduced and spent (realistic feed #1, 350°C) catalyst samples.

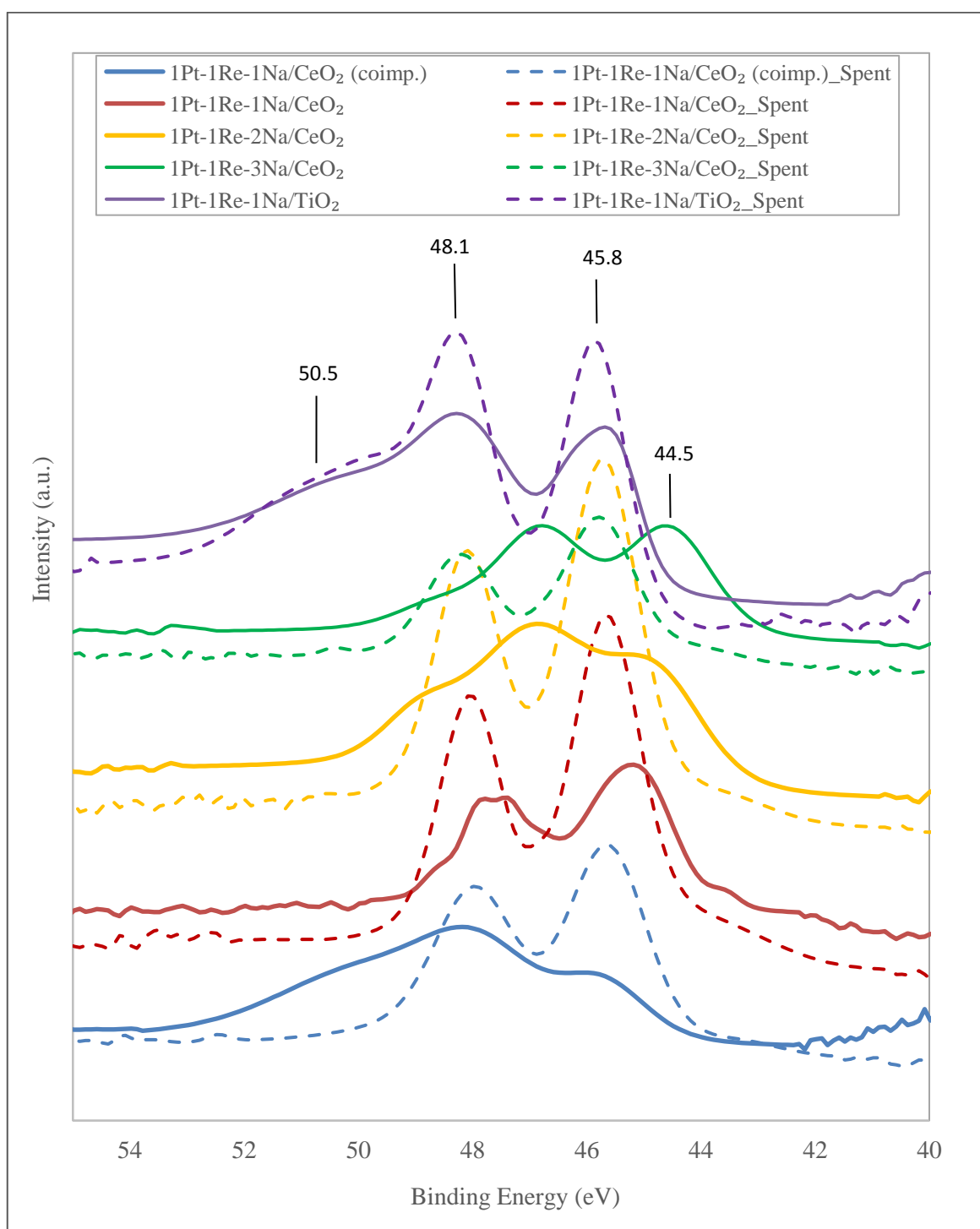


Figure 4.39. XP Spectra showing the Re4f region of freshly reduced and spent (realistic feed #1, 350°C) catalyst samples.

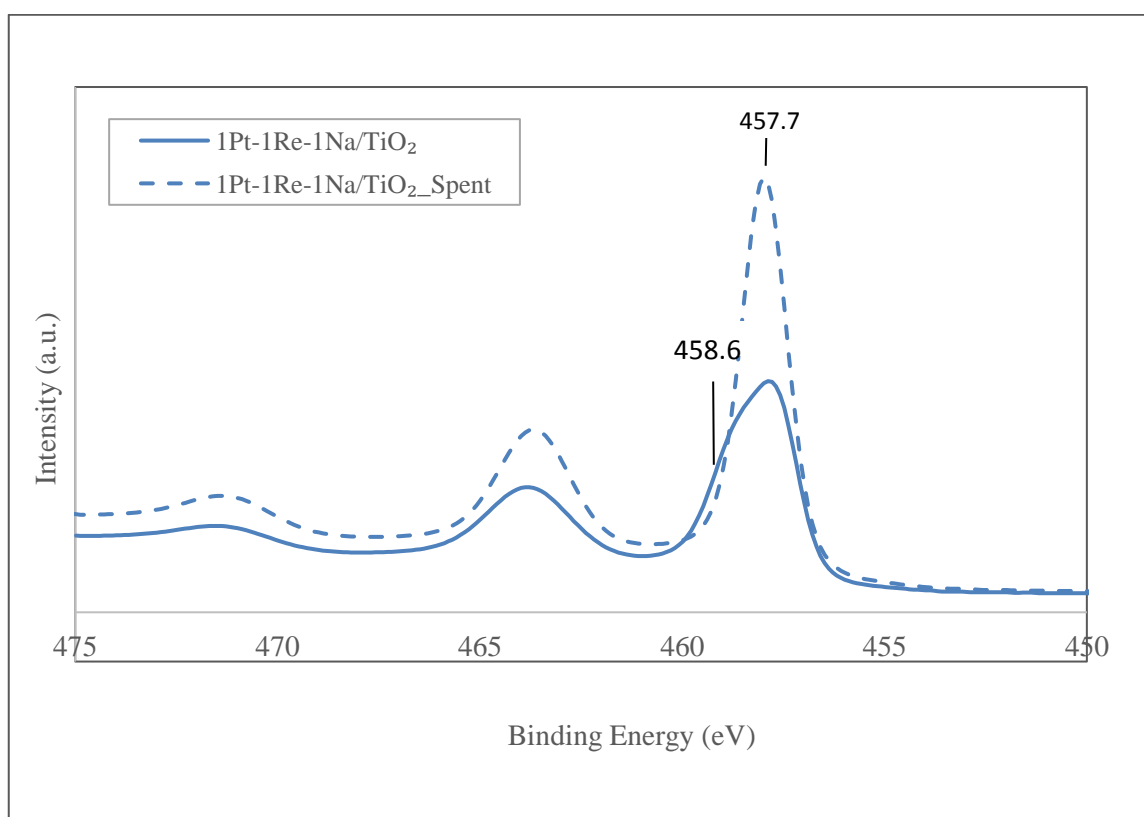


Figure 4.40. XP Spectra showing the Ti2p region of freshly reduced and spent (realistic feed #1, 350°C) 1%Pt-1%Re-1%Na/TiO₂ sample.

4.3.4. Raman Spectroscopy Analysis

Raman spectroscopy is a technique used to detect vibrational, rotational, and other states in a molecular system, capable of probing the chemical composition of materials. It is considered to be the most powerful technique for characterization of surface metal oxide species (Wu *et al.*, 2011).

Figure 4.41 shows the Raman spectra of freshly reduced CeO₂ supported catalyst samples with the spent ones exposed to performance test conditions for 6h TOS under RF#1 and RF#2 at 350°C. Raman spectra was found dominated by CeO₂ bands, in accordance with the studies in the literature reporting CeO₂ bands are stronger in terms of signal compared to other oxide bands (Wu *et al.*, 2011). The sharpest peak, which was observed at around 460 cm⁻¹ in all freshly reduced and spent samples, belongs to CeO₂ band. Along with the main

peak, the samples exhibited CeO_2 peaks at 250, 590 and 1175 cm^{-1} , which were also in accordance with the literature values (Martinez-Huerta *et al.*, 2004; Wu *et al.*, 2011).

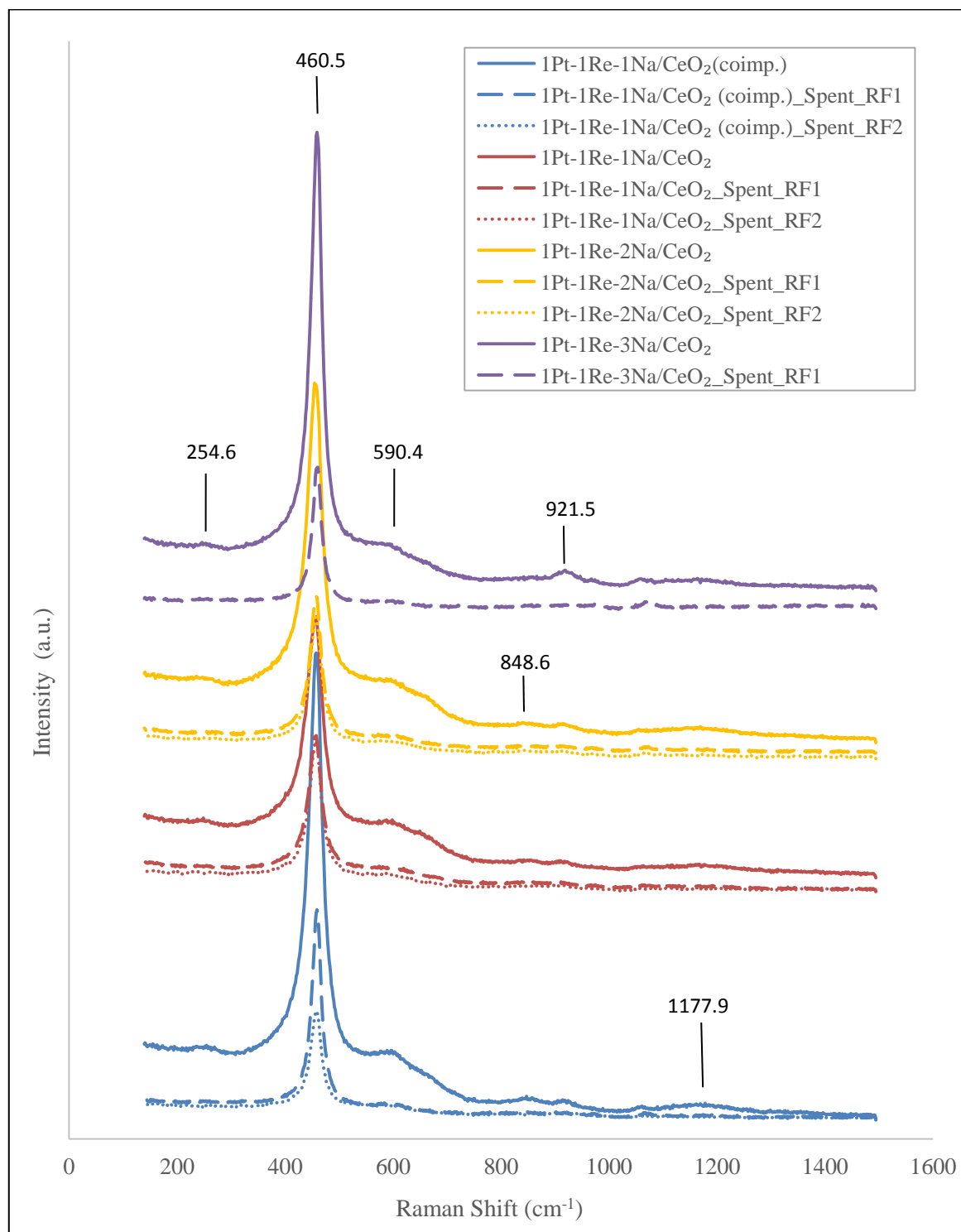


Figure 4.41. Raman spectra of freshly reduced and spent forms of CeO_2 supported catalyst samples subjected to RF #1 and RF#2 at 350°C .

The band, which was observed at around 1065 cm^{-1} , especially for the spent samples, is associated with the carbonate ions (Tripathy *et al.*, 2014; Liu *et al.*, 2010). 800-1400 cm^{-1} region of the spectra of 1%Pt-1%Re-2%Na/CeO₂ sample were expanded as an example in Figure 4.42. As can be seen from the figure, there is a clearly distinguishable peak at 1065 cm^{-1} , which can be associated with sodium carbonate species, in the spectra of the spent catalysts subjected to RF#1 and RF#2 at 350°C . In the literature, the region around 1160 cm^{-1} or 1050 cm^{-1} has been associated with the degree of superoxide and carbonate contamination (Eysel *et al.*, 1975). The peaks observed at around 850 and 920 cm^{-1} correspond with the peaks associated with Re species, which were reported at 855 and 910 cm^{-1} in the literature (Poulakis *et al.*, 1999; Kichanov *et al.*, 2009). The fact that these peaks become smaller in the spectrum of both spent catalysts subjected to RF#1 and RF#2 strongly suggests that those species participate in the WGS reaction mechanism and are utilized of during reaction.

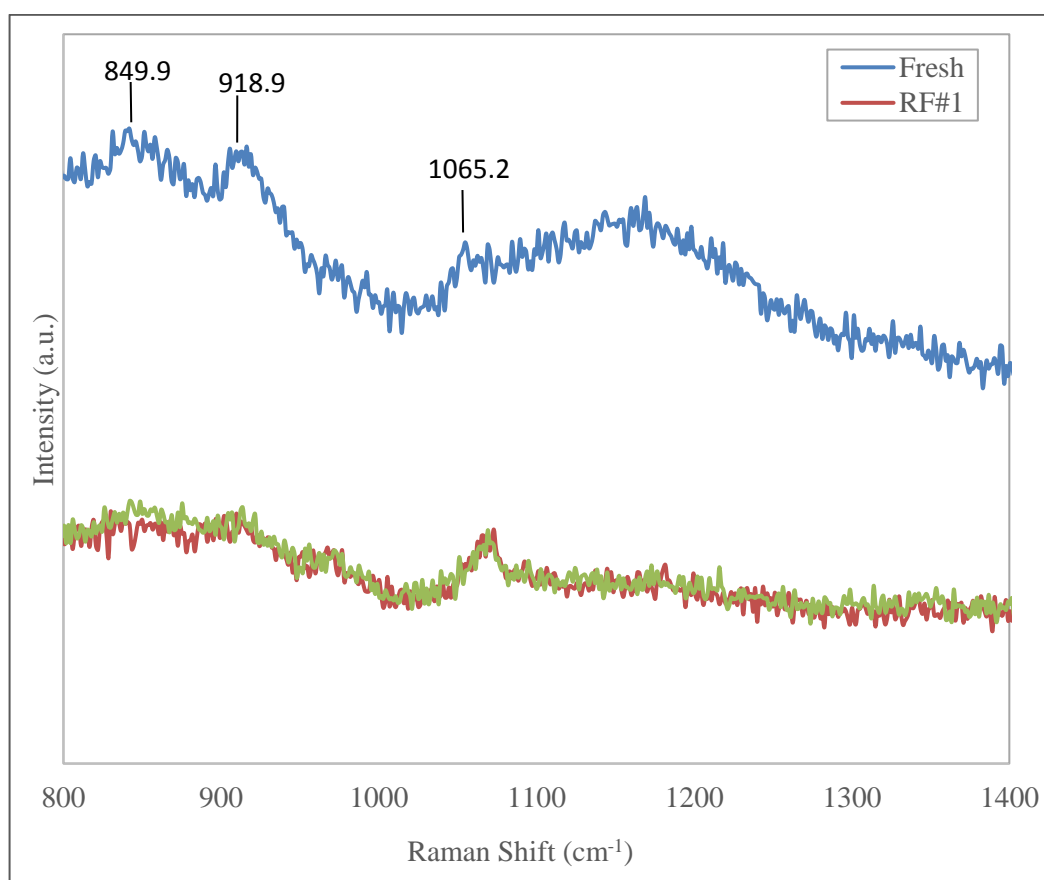


Figure 4.42. The expanded Raman spectra of freshly reduced and spent 1%Pt-1%Re-2%Na/CeO₂ supported catalyst samples subjected to RF #1 and RF#2 at 350°C .

The Raman spectra of the freshly reduced and spent 1%Pt-1%Re-1%Na/TiO₂ catalysts (Figure 4.43) have characteristic peaks coming from titania support, which are confirmed with the literature (Rico-Frances *et al.*, 2016). Band at 144cm⁻¹, which was obtained as the most intense band, is attributed to O-Ti-O bonding type vibration for anatase titania. The bands at 399, 513, 519 and 639 cm⁻¹ were also associated with titania support in accordance with the information of anatase features. 795 and 965 cm⁻¹ bands were detected in TiO₂ supported catalyst, more noticeably in freshly reduced sample. In order to examine these peaks in detail, 700-1000 cm⁻¹ region of the spectra of 1%Pt-1%Re-1%Na/TiO₂ catalyst were expanded in Figure 4.44. The peak at ca. 965 cm⁻¹ is attributed to the surface Re species, as the peak at 969 cm⁻¹ was reported corresponding to ReO₄ species (Petrov *et al.*, 1968) in the literature.

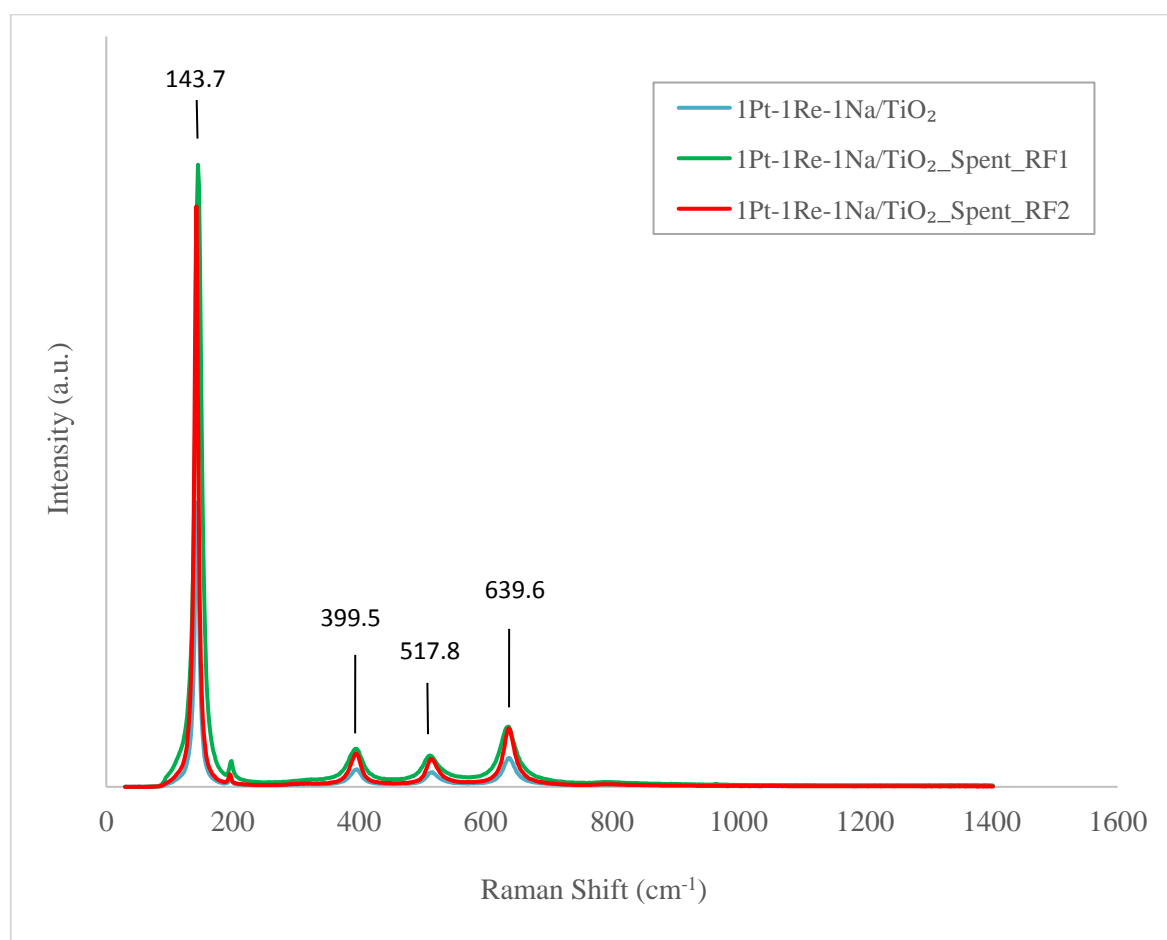


Figure 4.43. Raman spectra of freshly reduced and spent 1%Pt-1%Re-1%Na/CeO₂ catalyst samples subjected to RF #1 and RF #2 at 350°C.

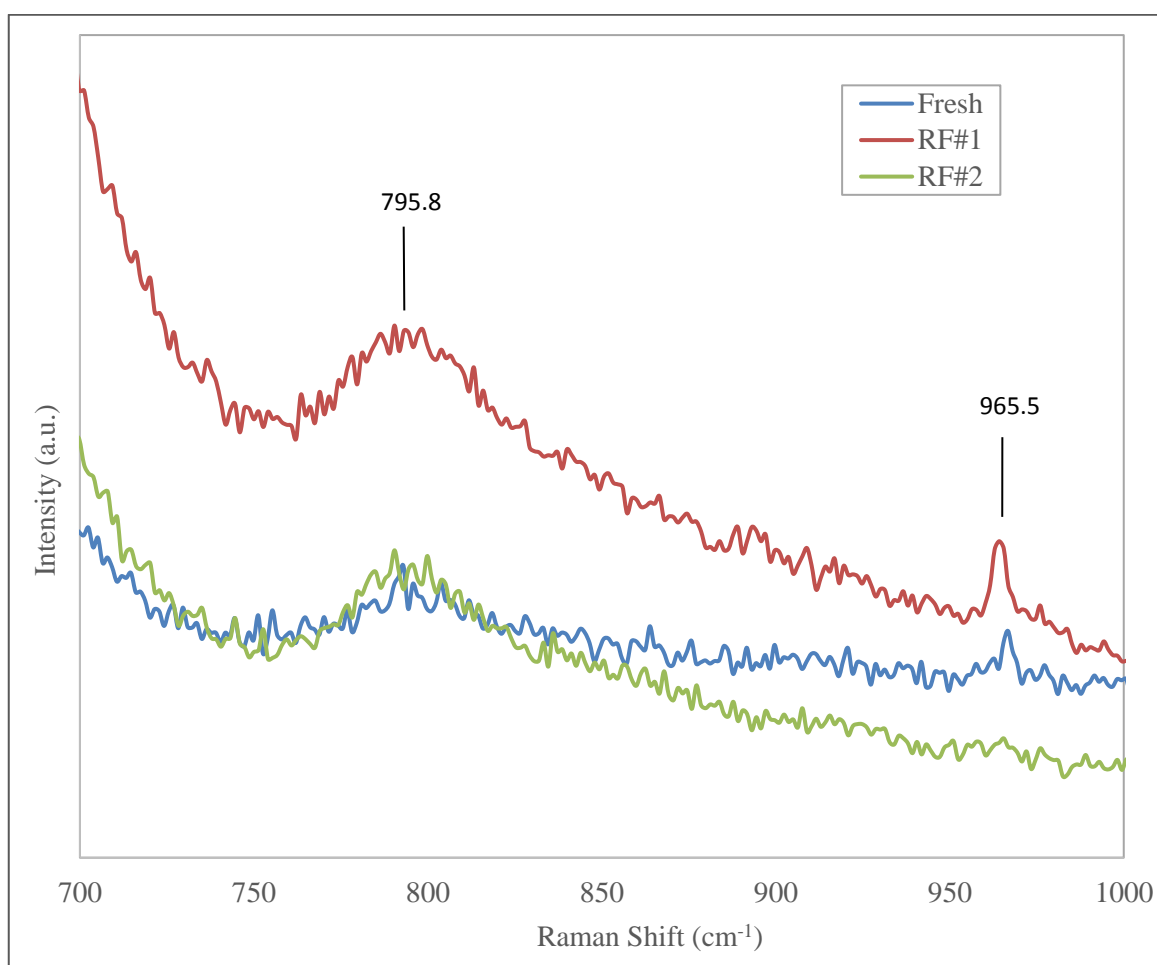


Figure 4.44. The expanded Raman spectra of freshly reduced and spent 1%Pt-1%Re-1%Na/TiO₂ supported catalyst samples subjected to RF #1 and RF #2 at 350°C.

4.3.5. CO Chemisorption as a Measure of Dispersion

CO chemisorption studies were conducted over all catalysts in order to determine the number of exposed metal atoms, which is a measure of metal dispersion. The studies were performed over 75 mg catalyst sample. An *in situ* reduction procedure, which is the same as the one used prior to the activity tests except the adapted total flow as 60 ml/min for being compatible with CATLAB rig, was used in the measurements. 0.1 ml of pulses containing 5% CO in balance inert was used during CO uptake analysis. CO was assumed to be adsorbed only on Pt at room T and “metal atom to adsorbed gas” stoichiometry (CO:Pt) was assumed as 1 in accordance of the literature (Bo *et al.*, 2018; Kugai *et al.*, 2015; Lenarda *et al.*, 2018).

Pt dispersion values obtained for all catalyst samples are presented in Table 4.3. The highest Pt dispersion values were achieved over sequentially impregnated 1%Pt-1%Re-1%Na/CeO₂ and 1%Pt-1%Re-2%Na/CeO₂ samples, which are in complete agreement with their high WGS activity. Na loading higher than this range, i.e. 1-2%, lowers the Pt dispersion, perhaps due to coverage of the active sites by Na species; nearly zero percent Pt dispersion calculated for the 1%Pt-1%Re-3%Na/CeO₂ sample is a strong indication of Na blockage. The results furtherly indicate that sequential impregnation enhances Pt dispersion.

It should be noted that as the above mentioned assumptions used in dispersion calculations may involve error margins coming from the possible adsorption of CO on Re sites and/or the effect of metal-metal interaction affecting the stoichiometry of adsorption, etc., the results presented in Table 4.3 were not used in calculating Turnover Frequency (TOF) values of the active Pt sites. However, that error margin should not be so high considering the significantly low CO uptake of 1%Pt-1%Re-3%Na/CeO₂ anyhow.

Table 4.3. The Pt dispersion values of catalyst samples.

Catalysts	Pt Dispersion (%)
1%Pt-1%Re-1%Na/CeO ₂ (coimp.)	5.52
1%Pt-1%Re-1%Na/CeO ₂	10.09
1%Pt-1%Re-2%Na/CeO ₂	9.60
1%Pt-1%Re-3%Na/CeO ₂	0.09
1%Pt-1%Re-1%Na/TiO ₂	5.44

4.4. *In situ* Characterization of Pt-Re-Na/CeO₂ System and *Operando* Analysis of WGS Mechanism on Its Sites by FTIR-DRIFTS-MS

In this section, the results of the detailed *in-situ* and *operando* FTIR-DRIFTS-MS studies conducted on CeO₂, 1%Pt-1%Re-1%Na/CeO₂ and 1%Pt-1%Re-3%Na/CeO₂ are presented and discussed. In the tests, throughout which both the FTIR-DRIFT spectra and MS data were obtained simultaneously; CO adsorption at 300°C was followed by WGS reaction at the same temperature. In *operando* reaction tests, FTIR-DRIFTs spectra were used in determination of reaction steps occurring on the surface, while MS data were used

in evaluation of catalytic activity and selectivity. Structure-mechanism-performance relation for WGS reaction over Pt-Re-Na/CeO₂ system was tried to be established via comparative analysis of both FTIR-DRIFTS and MS data collected under *operando* conditions.

A characteristic FTIR-DRIFTS spectrum is shown in Figure 4.45. In general, the peaks in; 3900-3000 cm⁻¹ range are assigned to O-H bonds, 3000-2700 cm⁻¹ range are assigned to formate groups having C-H bond, 2350 cm⁻¹ to gas phase CO₂, 2200-1800 cm⁻¹ range are assigned to gas phase or adsorbed/coordinated CO molecule, 1800-800 cm⁻¹ range are assigned to carbonate/formate groups having symmetric and asymmetric O-C-O bonds.

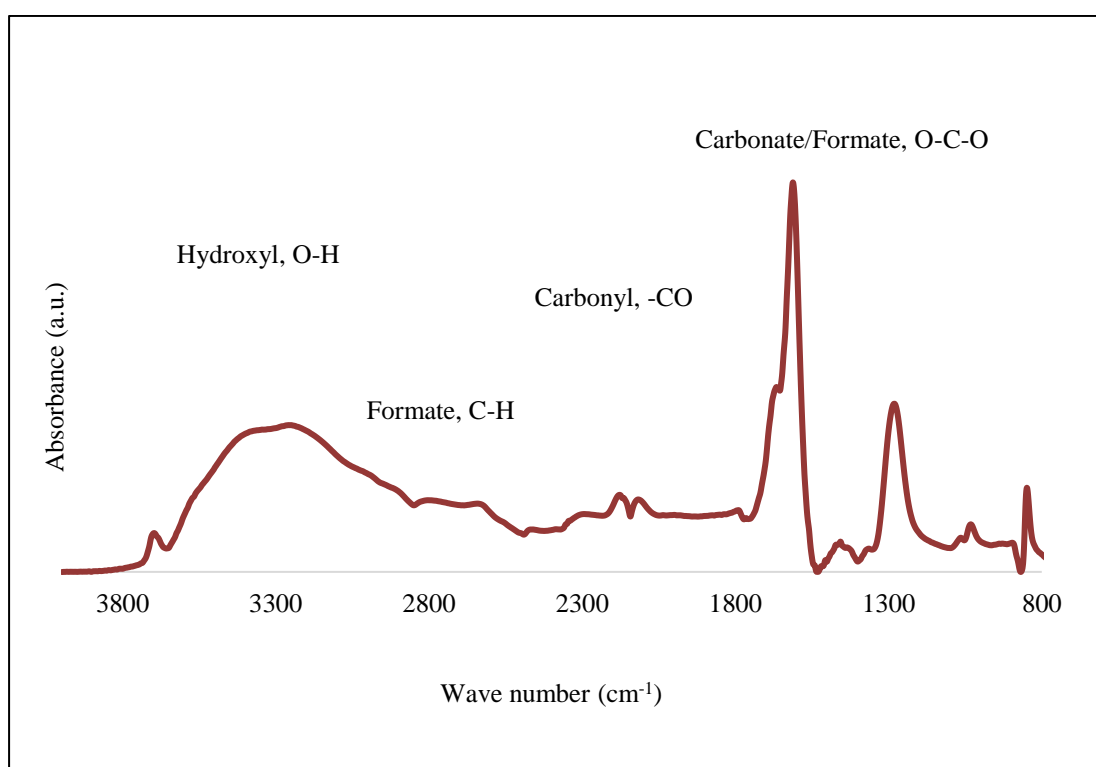


Figure 4.45. Characteristic FTIR-DRIFT spectrum.

At the start of the tests on CeO₂ support, it was reduced *in-situ* and the background spectrum was recorded. Then, at the end of 30th minute TOS of each of the following steps, a spectrum was acquired; (i) He flow before CO adsorption, (ii) CO adsorption under He-CO (1%) mixture, (iii) He flush after CO adsorption, (iv) under WGS reaction conditions for ideal feed flow (1.36% CO-2.72% H₂O-balance He), and (v) He flush after WGS reaction. All the spectra obtained are presented in Figure 4.46.

Peaks at 3654 cm^{-1} wave number and $3600\text{--}3270\text{ cm}^{-1}$ wave number ranges correspond to bridged and multi bonded OH groups (type II and III) on CeO_2 surface, respectively (Li *et al.*, 1989; Holmgren *et al.*, 1999; Jacobs *et al.*, 2007). The observed downfalls in hydroxyl band peaks when ‘1% CO-balance He’ mixture was sent to the surface indicated the use of these groups. Extensive studies on Au-Re/ CeO_2 catalysts performed by our group (Çağlayan, 2011) show that these OH groups on the CeO_2 surface are OH molecules that were formed during reduction with H_2 . Under the flow of 1.36% CO-2.72% H_2O containing ideal WGS feed, a significant increase was observed for the peaks at 3683 , 3654 and 3623 cm^{-1} wave numbers depending on the H_2O dissociation. Peak 3683 cm^{-1} indicates the linearly adsorbed OH groups on CeO_2 surface (Holmgren *et al.*, 1999; Jacobs *et al.*, 2007), whereas wide peaks at 3254 and 3140 cm^{-1} were associated with symmetric and asymmetric free OH groups (Armaroli *et al.*, 2004). OH groups were swept out by He flush after reaction step under ideal feed.

Peaks at 2944 , 2826 and 2700 cm^{-1} in the $3000\text{--}2700\text{ cm}^{-1}$ wave number range, which were formed under 1% CO flow, belong to the monodentate and bidentate formate groups (Jacobs *et al.*, 2007; Goguet *et al.*, 2004; Meunier *et al.*, 2007a). The fact that these peaks did not change after He flush indicates that these groups are strongly attached to the surface. Further, no observed change in these peaks under ideal feed flow indicate that the formate groups do not participate in the reaction. The 2350 cm^{-1} peak of the gas phase CO_2 molecule was found to be hardly visible under CO and the ideal feed stream flows, indicating that the WGS reaction was limited over CeO_2 , which is confirmed by the MS data presented in Figures 4.47 and 4.48.

An enlarged presentation of $2000\text{--}2300\text{ cm}^{-1}$ region of FTIR-DRIFT spectra obtained over CeO_2 at 300°C were represented for the same steps in Figure 4.49. The peaks at 2180 and 2120 cm^{-1} , which can be seen in the spectra taken under CO adsorption and reaction conditions, belong to the gas phase CO molecule, and become invisible after the He flush. 2178 and 2127 cm^{-1} peaks seen in the spectra of the He flush step show the interaction of Ce^{4+} and Ce^{3+} , respectively, with CO (Saw *et al.*, 2014; Holmgren *et al.*, 1999). These peaks cannot be observed under CO adsorption and reaction conditions, as they remain under the peaks of the gas phase CO molecule.

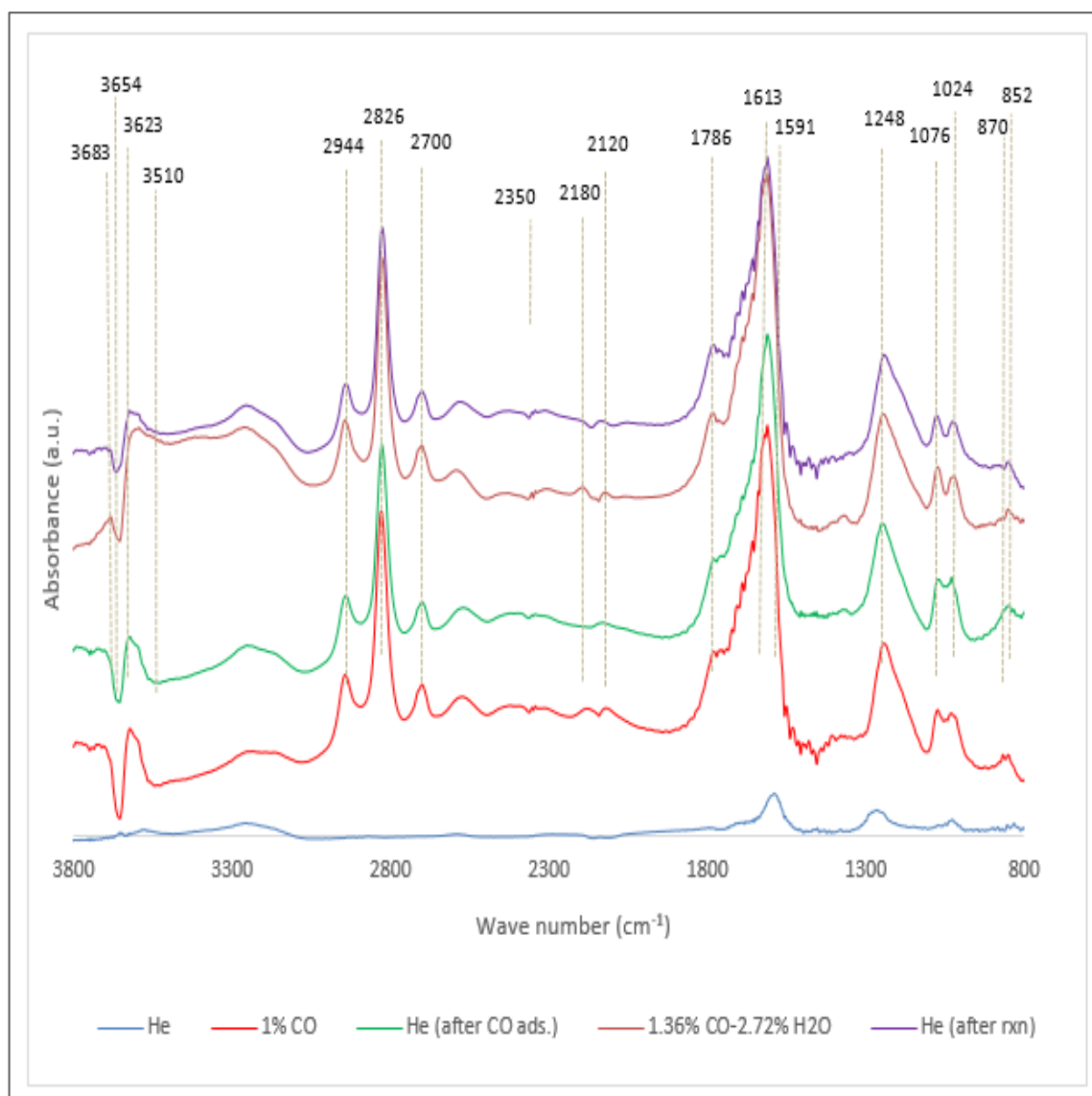


Figure 4.46. FTIR-DRIFT spectra obtained over CeO₂ at 300°C under various feed flows.

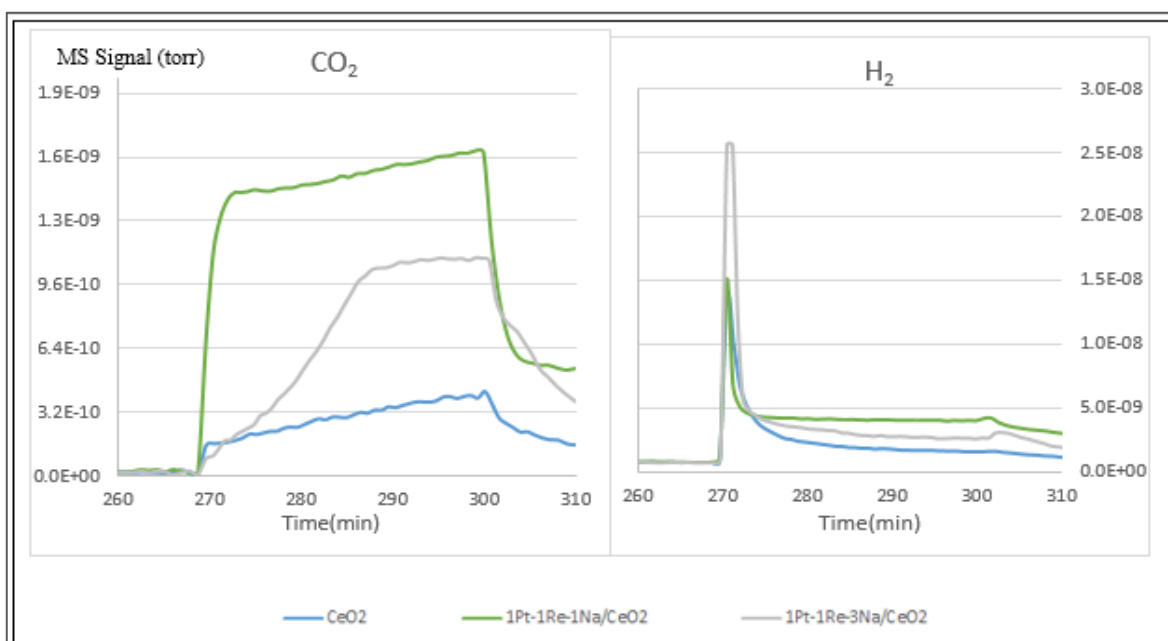


Figure 4.47. MS signals of CO_2 and H_2 molecules in the exit stream of FTIR-DRIFTS system during 1% CO adsorption at 300°C over in-situ reduced support and catalyst samples.

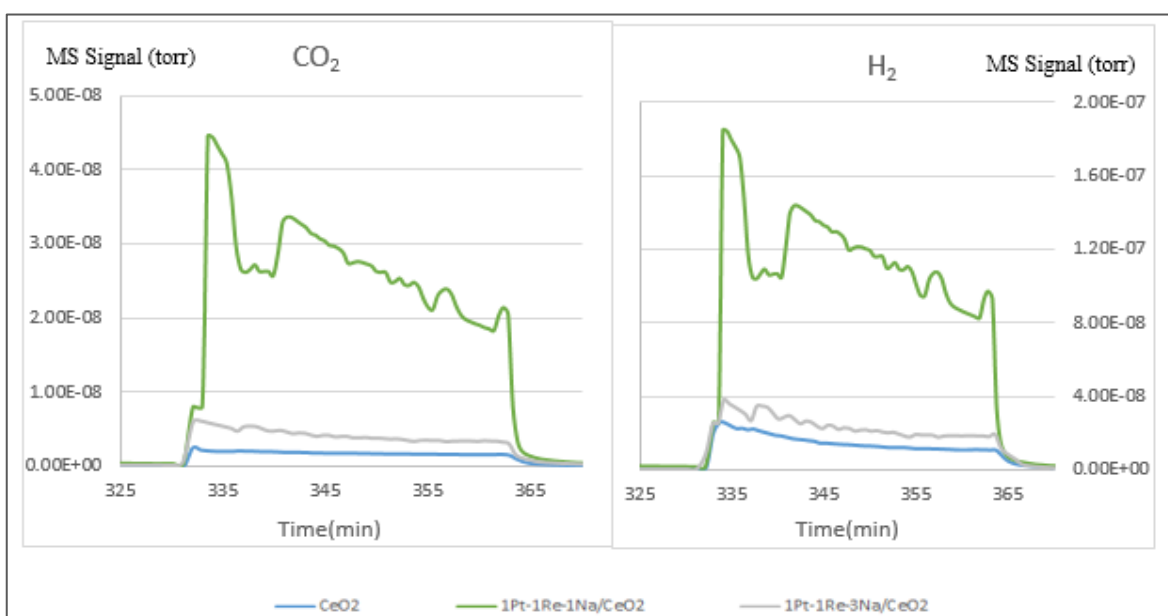


Figure 4.48. MS signals of CO_2 and H_2 molecules in the exit stream of FTIR-DRIFTS system under 1.36%CO-2.72% H_2O feed flow at 300°C over in-situ reduced support and catalyst samples.

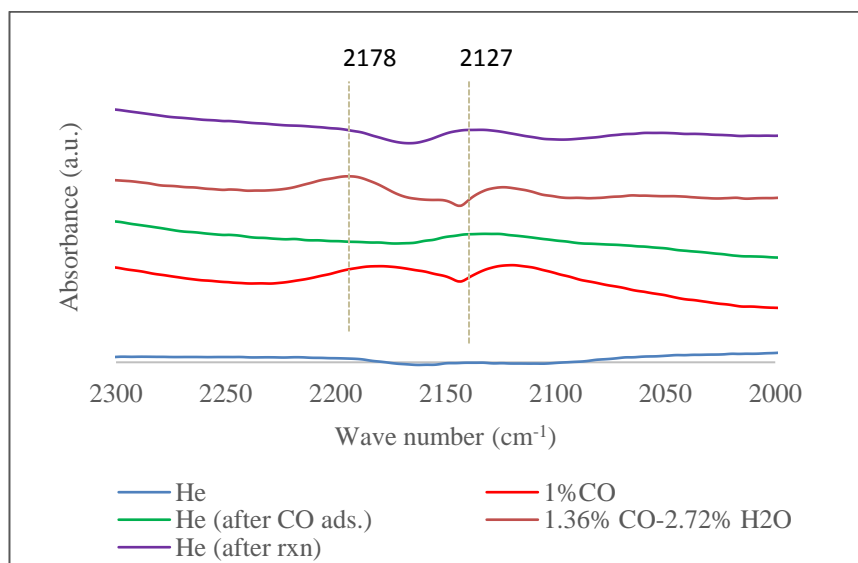


Figure 4.49. 2000-2300 cm^{-1} region of the FTIR-DRIFT spectra obtained over CeO_2 at 300°C under various feed flows.

Prominent peaks of carbonate, formate and carboxyl groups were obtained during CO adsorption in the 1700-800 cm^{-1} wave number range (Figure 4.46). In accordance with the literature, the wave number range between 1700-1650 cm^{-1} corresponds to carboxyl groups; 1591 and 1248 cm^{-1} peaks refer to unidentate formate groups, 1548 and 1360 cm^{-1} peaks belong to bidentate formate groups (Jacobs *et al.*, 2007; Jacobs *et al.*, 2003; Holmgren *et al.*, 1999). Peaks, which are at 1786, 1613, 1076, 1024, 870 and 852 cm^{-1} wave numbers, belong to carbonate groups; and the peaks at 1613 and 1024 cm^{-1} indicate hydrogen carbonate formation (Holmgren *et al.*, 1999; Jacobs *et al.*, 2007; Meunier *et al.*, 2007b). The peaks, which belong to these surface groups, did not undergo any change under varying conditions after CO adsorption, such as peaks in the range 3000-2700 cm^{-1} . This finding shows that all surface groups formed by CO adsorption on the surface of CeO_2 are stable and strongly attached to the surface.

As the first step of FTIR-DRIFTS study on 1%Pt-1%Re-1%Na/ CeO_2 , the sample was reduced *in-situ* and the background spectrum was recorded. Then, at the end of 30th minute TOS of each of the following steps, a spectrum was acquired; (i) He flow before CO adsorption, (ii) CO adsorption under He-CO (1%) mixture, (iii) He flush after CO adsorption, (iv) under WGS reaction conditions for ideal feed flow (1.36% CO-2.72% H_2O -

balance He) and (v) He flush after WGS reaction. All the spectra obtained are presented in Figure 4.50.

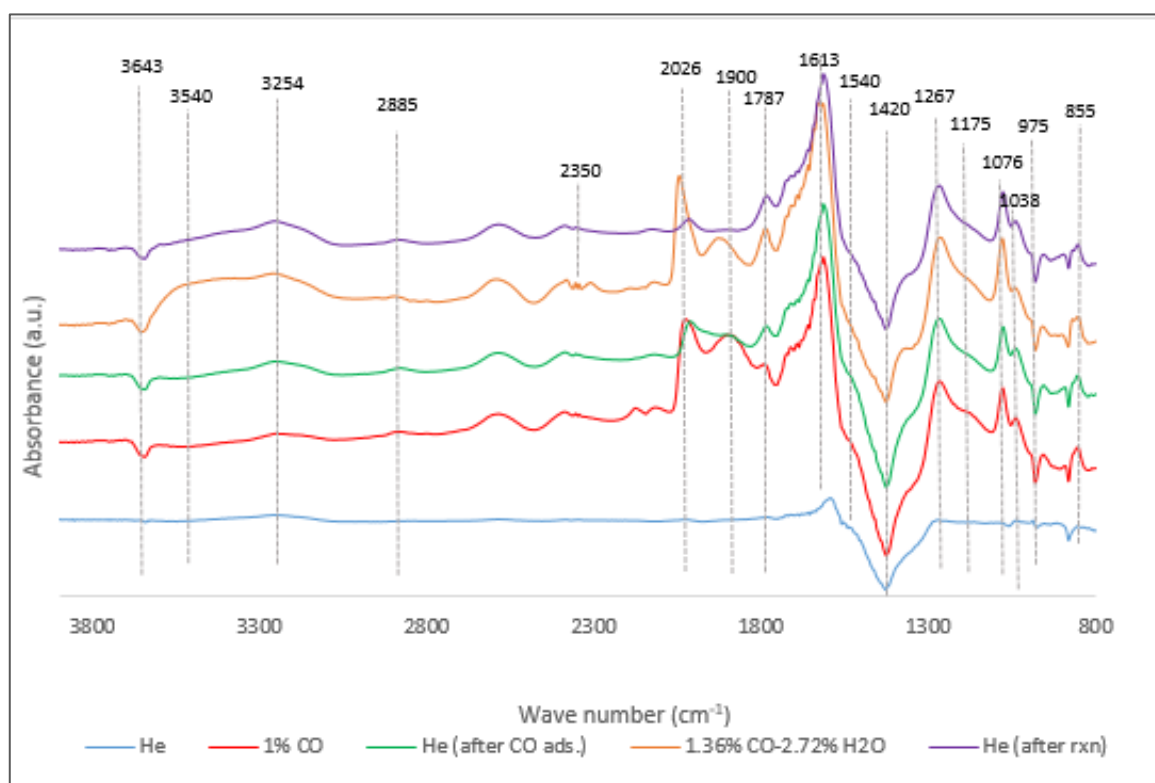


Figure 4.50. FTIR-DRIFT spectra obtained over 1%Pt-1%Re-1%Na/CeO₂ at 300°C under various feed flows.

During CO adsorption, a reduction in the wave number of 3643 cm⁻¹ was observed, but the significant reduction in the hydroxyl band around the 3540 cm⁻¹ wave number, like in the case of CeO₂ support, attributed to the type III OH group was not observed, indicating other OH groups were used in product formation (Li *et al.*, 1989; Holmgren *et al.*, 1999; Jacobs *et al.*, 2007). A slight increase observed in this area during the He flush after CO adsorption should be noted. A general increase was observed in the 3683-3254 cm⁻¹ wave number range during WGS reaction condition under diluted ideal feed flow due to decomposition of H₂O. It was observed that some of the formed OH groups were swept, but a noticeable amount of these groups were observed to be remained on the surface compared to that acquired for He-flush step following CO adsorption.

The subsequent peaks corresponding to the unidentate and bidentate formate groups (3000-2700 cm^{-1}) seen over the CeO_2 support surface were not observed on 1%Pt-1%Re-1%Na/ CeO_2 ; only a peak at 2885 cm^{-1} was obtained in this region (Jacobs *et al.*, 2007; Holmgren *et al.*, 1999; Meunier *et al.*, 2007a). This peak, which indicates the formation in small during CO adsorption, did not disappear with He flush, and did not show any change under ideal feed conditions as well. The absence of these formate groups in C-H band can point out either the formate groups are not formed over Na containing catalysts or formate groups which are generated, are used very rapidly.

The gas phase CO_2 peak (2350 cm^{-1}) was formed under both CO adsorption and reaction conditions, in accordance with the MS data of the CO_2 and H_2 gases (Figures 4.47 and 4.48), with a more pronounced amount under ideal feed WGS reaction condition. It was seen that this peak disappeared after He flush in both cases. Enlarged version of 1700-2300 cm^{-1} region of the FTIR-DRIFT spectra obtained over 1%Pt-1%Re-1%Na/ CeO_2 sample at 300°C were shown in Figure 4.51. The gas phase CO peaks were acquired at 2180 and 2120 cm^{-1} wave numbers under 1% CO flow, and the peak at 2127 cm^{-1} , which indicates the interaction of Ce^{+3} with CO, has become visible after He flush in the spectrum of 1%Pt-1%Re-1%Na/ CeO_2 catalyst (Saw *et al.*, 2014; Holmgren *et al.*, 1999). In accordance with the MS data, the gas phase CO peaks observed under ideal feed condition were less prominent than those observed under 1% CO flow condition confirming WGS reaction. According to the literature, linearly adsorbed CO on Pt yields peaks in 2100-1950 cm^{-1} wave number range, while bridge and trifold bonded CO is indicated by peaks in 1700-1900 cm^{-1} region (Riguetto *et al.*, 2004; Vignatti *et al.*, 2010). Under the light of this information, 2026 cm^{-1} peak formed alongside of gas phase CO peaks during CO adsorption, shows linearly bonded CO molecule on Pt, and the peak at 2006 cm^{-1} wave number on the crest of this peak is thought belonging to the linearly bonded CO molecule on Re (Nguyen *et al.*, 2015; Azzam *et al.*, 2008). The peak at 1924 cm^{-1} is assigned to the CO molecule bridged to Pt, while peak at 1787 cm^{-1} is attributed to trifold bonded CO molecule. Linear and bridge bonded CO molecules were swept via He flush following CO adsorption, but the trifold bonded CO molecules remained on the surface indicating their stronger adsorption on the catalyst. Under the ideal feed containing reaction conditions, the peak referring to linearly adsorbed CO on Pt shifted to 2045 cm^{-1} , and the Pt-CO peak corresponding to the bridge bonded CO was shifted to 1900 cm^{-1} . The ratio between bridge bonded and linearly bonded species were

changed; it was observed that linearly bonded groups were formed more than bridged bonded ones under these conditions. A large proportion of linearly bonded CO and all bridged CO species were swept under He flush step following reaction conditions, however, there was no change in the peak belongs the trifold bonded CO molecule, as in the previous case. The addition of Na to Pt-containing catalysts has been shown to enable formation of multiple and strongly bonded CO molecules, yielding peaks in the range of 1770-1690 cm^{-1} wave numbers (Cybulskis *et al.*, 2016). The decrease of 1540 cm^{-1} peak corresponding to bidentate formate groups (Jacobs *et al.*, 2007; Jacobs *et al.*, 2003; Holmgren *et al.*, 1999) became more pronounced with Na addition; *it should be noted that 1540 cm^{-1} peak was not observed in another study conducted concurrently on Pt-Re-V/CeO₂ catalysts by our group members.* An increase was observed in peaks at 1787, 1613, 1267, 1076, 1038 and 855 cm^{-1} , which are assigned to carbonates. In addition, the decrease in the hydrogen carbonate peak at ca. 1420 cm^{-1} wave number is thought be specific to Na containing catalysts, and may stem from interaction with Na (Holmgren *et al.*, 1999; Jacobs *et al.*, 2007; Meunier *et al.*, 2007b; Guerrero *et al.*, 2012). The significant decrease in intensity of hydrogen carbonate peak in anhydrous media during CO adsorption indicates its active use of in WGS reaction. No increase or decrease were observed in intensity of these peaks upon He flush applied following CO adsorption. A slight increase in carbonate peaks at 1787, 1613, 1267, 1076, 1038 and 855 cm^{-1} , was observed reaction conditions with ideal feed confirming that they were resilient to He flush.

After analyzing a member of Pt-Re-Na/CeO₂ system having high WGS performance, the formulation that have shown the poorest performance, 1%Pt-1%Re-3%Na/CeO₂, was studied under identical conditions aiming to form a comparison basis. As the first step of FTIR-DRIFTS study, 1%Pt-1%Re-3%Na/CeO₂ was reduced *in-situ* and the background spectrum was recorded. Then, at the end of 30th minute TOS of each of the following steps, a spectrum was acquired; (i) He flow before CO adsorption, (ii) CO adsorption under He-CO (1%) mixture, (iii) He flush after CO adsorption, (iv) under WGS reaction conditions for ideal feed flow (1.36% CO-2.72% H₂O-balance He) and (v) He flush after WGS reaction. All the spectra obtained are presented in Figure 4.52.

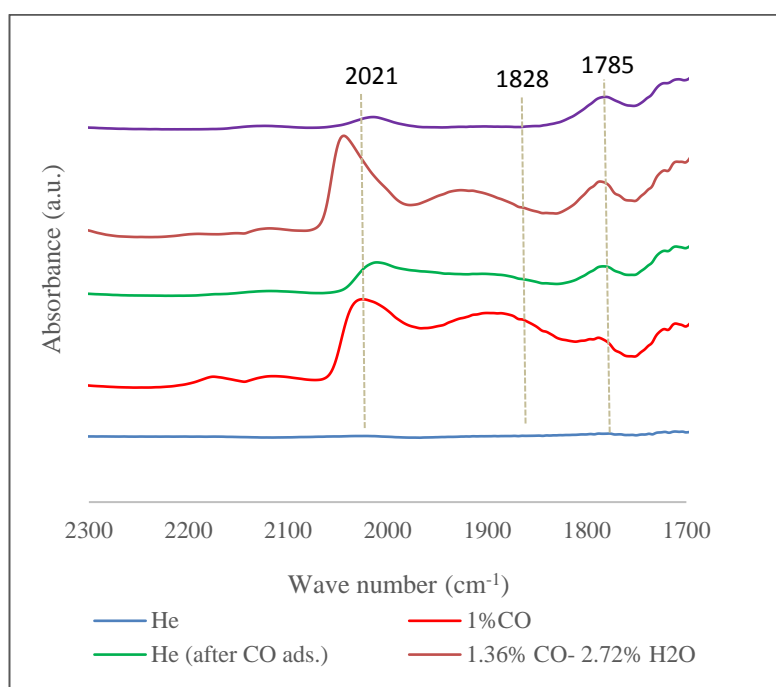


Figure 4.51. 1700-2300 cm^{-1} region of the FTIR-DRIFT spectra obtained over 1%Pt-1%Re- 1%Na/CeO₂ at 300°C under various feed flows.

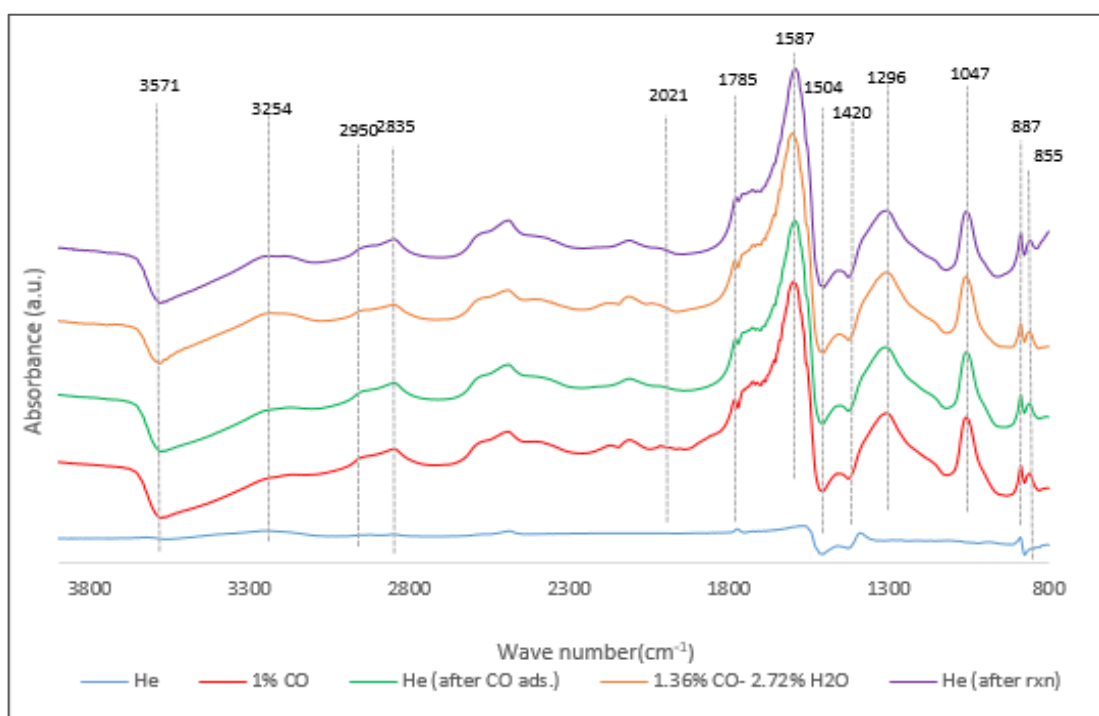


Figure 4.52. FTIR-DRIFT spectra obtained over 1%Pt-1%Re-3%Na/CeO₂ at 300°C under various feed flows.

During CO adsorption over 1%Pt -1% Re-3%Na/CeO₂, a downfall was observed in the OH band, compared to that recorded over 1%Pt -1%Re-1%Na/CeO₂, it shifted to the wave number 3571 cm⁻¹, and a general decrease was shown in the 3600-3250 cm⁻¹ wave number range. There is no change in the profile for that range upon He flush, and there was a slight increase under ideal feed conditions. Additionally, no change was observed during He flush following the reactive conditions. Though the only peak acquired in C-H band of the formate groups over %Pt-1%Re-1%Na /CeO₂ was at 2885 cm⁻¹, other formate peaks were shown at 2950 and 2835 cm⁻¹ over 1%Pt-1%Re-3%Na/CeO₂ (Jacobs *et al.*, 2007; Holmgren *et al.*, 1999; Meunier *et al.*, 2007a). These peaks did not show any change during CO adsorption, reaction and He flush stages of the analysis. Gas phase CO₂ peak at 2350 cm⁻¹, which was clearly visible for 1%Pt -1%Re-1%Na/CeO₂, was not observed. This result, indicating that the reaction was practically not occurred on 1%Pt -1% Re-3%Na/CeO₂ surface at 300°C, also confirmed by the MS data of the CO₂ and H₂ signals, given in Figures 4.47 and 4.48, respectively. The peaks at 2180 and 2120 cm⁻¹ wave numbers corresponding to the gas phase CO molecule were formed during CO adsorption and disappeared after sweeping. The peak at 2127 cm⁻¹, showing the interaction of Ce⁺³ with CO, and smaller ones in vicinity, also became visible after sweeping (Saw *et al.*, 2014; Holmgren *et al.*, 1999). The peaks at 2021, 1785 cm⁻¹ and a shoulder at 1828 cm⁻¹ are attributed to linearly, bridged and trifold adsorbed CO molecules on the metal, respectively. These peaks were formed during CO adsorption and could not be swept via He flush. Gas phase CO peak was reappeared during the ideal feed condition, and it was observed that the peak at 2021 cm⁻¹ wave number, which indicates linearly adsorbed Pt-CO and/or Re-CO interaction (Riguetto *et al.*, 2004), became apparent and did not change during the following He flush. It has been found that 1587, 1296, 1047, 887 and 855 cm⁻¹ wave numbers corresponding to carbonate groups, were formed during CO adsorption. Considering the related literature, the peaks at 1587, 1296 cm⁻¹ and crest at 1008 cm⁻¹ refers to bidentate carbonates; 1504 cm⁻¹ peak corresponds to unidentate carbonates; 1420 and 1047 cm⁻¹ peaks belongs to hydrogen carbonates, and peaks at 870 and 855 cm⁻¹ refers to polydentate carbonates (Holmgren *et al.*, 1999; Jacobs *et al.*, 2007; Meunier *et al.*, 2007b; Guerrero *et al.*, 2012). There were no noticeable changes in the 1504 and 1420 cm⁻¹ peaks during CO adsorption and under reaction conditions, compared to those in the initial spectrum of the catalyst. The decrease in 1420 cm⁻¹ peak during reaction over 1%Pt-1%Re-1%Na/CeO₂, while no observed change under the same conditions for essentially inactive 1%Pt -1% Re-3%Na/CeO₂ strongly indicates

that these groups are used during reaction. No decrease or increase was observed in the intensities of all carbonate peaks with He flush or under reaction conditions, indicating no new carbonate groups were formed on the surface over 3%Na loaded Pt-Re-Na sample. In complete accordance with the WGS performance test results that showed very low WGS activity of 1%Pt -1% Re-3%Na/CeO₂; the surface remains completely the same under the reaction conditions suggested by FTIR-DRIFTS, and the reaction is very limited on the surface, based on the MS data of CO₂ and H₂ signals given, in Figures 4.47 and 4.48. The peaks, which had been formed successively in the 2600-2400 cm⁻¹ wave number range during CO adsorption and could not be swept, were also formed in the spectra of 1%Pt-1%Re-3%Na/CeO₂ differentiating in intensities and number of peaks. Although a peak at ca. 2560 cm⁻¹ in this range also appears in the spectra of CeO₂ support, the difference in 1%Pt-1%Re-3%Na/CeO₂ spectra may indicate Na-support interaction.

4.5. Analysis of “WGS Performance-Oxygen Storage Capacity” Relation for Pt-Re-Na/CeO₂ and Pt-Re-Na/TiO₂ Catalysts

The oxygen storage capacities (OSCs) of the catalysts *whose performances were tested*, (Section 4.1-4.2) were calculated through using a methodology developed by our group (see Section 3.6 for detailed description) which utilizes IGA-MS system. Based on the results collected, three different oxygen storage capacity types defined in the methodology, namely total oxygen storage capacity (T-OSC), structural oxygen storage capacity (S-OSC) and effective oxygen storage capacity (E-OSC), were calculated. As a general approach, the calculation method of OSCs was based on the number of moles of CO₂ and CO gases leaving the catalyst surface during temperature increase up to 800°C upon the application of either reactive or inert environments. Calculation procedure was applied on both reaction and inert tests' data in order to determine three types of OSCs. The *operando* OSC measurements were performed under the flow of diluted forms of Realistic Feed #1 and #2, which were used in WGS performance tests; those diluted feed mixtures are named as DRF#1 and DRF#2, respectively. The compositions of DRF#1 and DRF#2, and the experimental conditions of OSC measurement tests were tabulated in Table 3.11 and Table 3.12, respectively.

OSC is generally categorized into two groups in the literature, namely total OSC and dynamic OSC (Li *et al.*, 2019). Total OSC, which is related to the overall amount of transferable oxygen including surface and bulk oxygen, is also called as thermodynamic OSC or oxygen storage capacity complete (OSCC). On the other hand, dynamic OSC represents the most reactive oxygen containing species and readily available oxygen, both of which are associated with the high mobility of the oxygen (Li *et al.*, 2019; Aneggi *et al.*, 2006).

In a similar manner, in the current study, structural OSC (S-OSC) was defined as the capacity of the oxygen in the lattice and also in the formate, carbonate or carboxyl-carboxylate like species on the surface. Effective OSC (E-OSC), which is defined as the difference between T-OSC and S-OSC, was used to describe oxygen playing a role in the WGS reaction mechanism, *i.e.* oxygen formed, used and renewed during reaction, specific to reaction conditions, *i.e.* at given temperature and for a specified feed composition. In the OSC tests, it was assumed that oxygen leaves the surface as CO₂ and CO during temperature increase. This assumption was validated via IGA-MS experiment setup with no detection of oxygen or water during temperature increase up to 800°C.

The OSC calculation methodology combines the weight change of the sample, which is obtained via IGA measurements (Section 3.6) during the temperature increase from reaction or inert treatment temperature up to 800°C, and the CO₂/CO volume ratio leaving the surface during that time, which can be determined from MS data (see Section 3.6). The equations used for evaluating the oxygen storage capacities of the samples are given below (Equations 4.8- 4.13). Ideal gas assumption was made for CO₂ and CO gases to obtain molar ratio of CO₂ and CO:

$$P_{CO_2}V_{CO_2} = \dot{n}_{CO_2}RT_{CO_2} \quad (4.8)$$

$$P_{CO}V_{CO} = \dot{n}_{CO}RT_{CO} \quad (4.9)$$

where \dot{n}_{gas} represents the molar flow rate of the gas, P_{gas} is the atmospheric pressure, V_{gas} is the volume of the gas, R is the universal gas constant and T_{gas} is the absolute temperature. By using these equations, following relation can be obtained:

$$\frac{V_{\text{CO}_2}}{V_{\text{CO}}} = \frac{\dot{n}_{\text{CO}_2}}{\dot{n}_{\text{CO}}} = \left(\frac{n_{\text{CO}_2}}{n_{\text{CO}}} \right) \quad (4.10)$$

The change in sample weight during the temperature increase from reaction temperature to 800°C, was used to determine the moles of CO₂ and CO gases by combining the Eqns (4.10) and (4.11).

$$\text{Weight Change} = MW_{\text{CO}} \times n_{\text{CO}} + MW_{\text{CO}_2} \times n_{\text{CO}_2} \quad (4.11)$$

where MW_{gas} and n_{gas} denote the molecular weight of the gas, and the moles of gas leaving the sample, respectively. Subsequently, OSCs of the samples were determined in mmol O/g_{cat} by using Equations (4.12) and (4.13).

$$\text{Total moles of O} = 1 \times n_{\text{CO}} + 2 \times n_{\text{CO}_2} \quad (4.12)$$

$$\text{OSC (mmol/g}_{\text{cat}}) = \text{Total moles of O (mmol)}/w_{\text{cat}} \quad (4.13)$$

where OSC signifies total oxygen storage capacity (T-OSC) or structural oxygen storage capacity (S-OSC) based on the experimental procedure, and w_{cat} is the sample weight.

4.5.1. Oxygen Storage Capacity Tests

The reaction step of the oxygen storage capacity tests were performed over all catalyst samples at 350°C, the temperature at which –in general- the highest CO conversion values achieved in the activity tests. After the period of *operando* reaction, inert treatment was applied at 350°C. Subsequently the temperature was increased up to 800°C with a ramp rate of 7°C/min in order to observe the O containing species leaving the surface. The reaction feed compositions were given previously in Table 3.11.

Three types of OSCs, which were explained in detail in Section 3.6 were determined for all catalyst samples. Total OSC (T-OSC) and structural OSC (S-OSC) were obtained by following the procedure mentioned in the previous paragraph with only a difference in feed composition, such that the former one includes the diluted reaction feed given in Table 3.11 and the latter includes only inert gas flow. Effective OSC was predefined as the difference between T-OSC and S-OSC. Figure 4.53 and 4.54 present three types of OSCs of each sample subjected to DRF #1 and DRF #2 at 350°C, respectively.

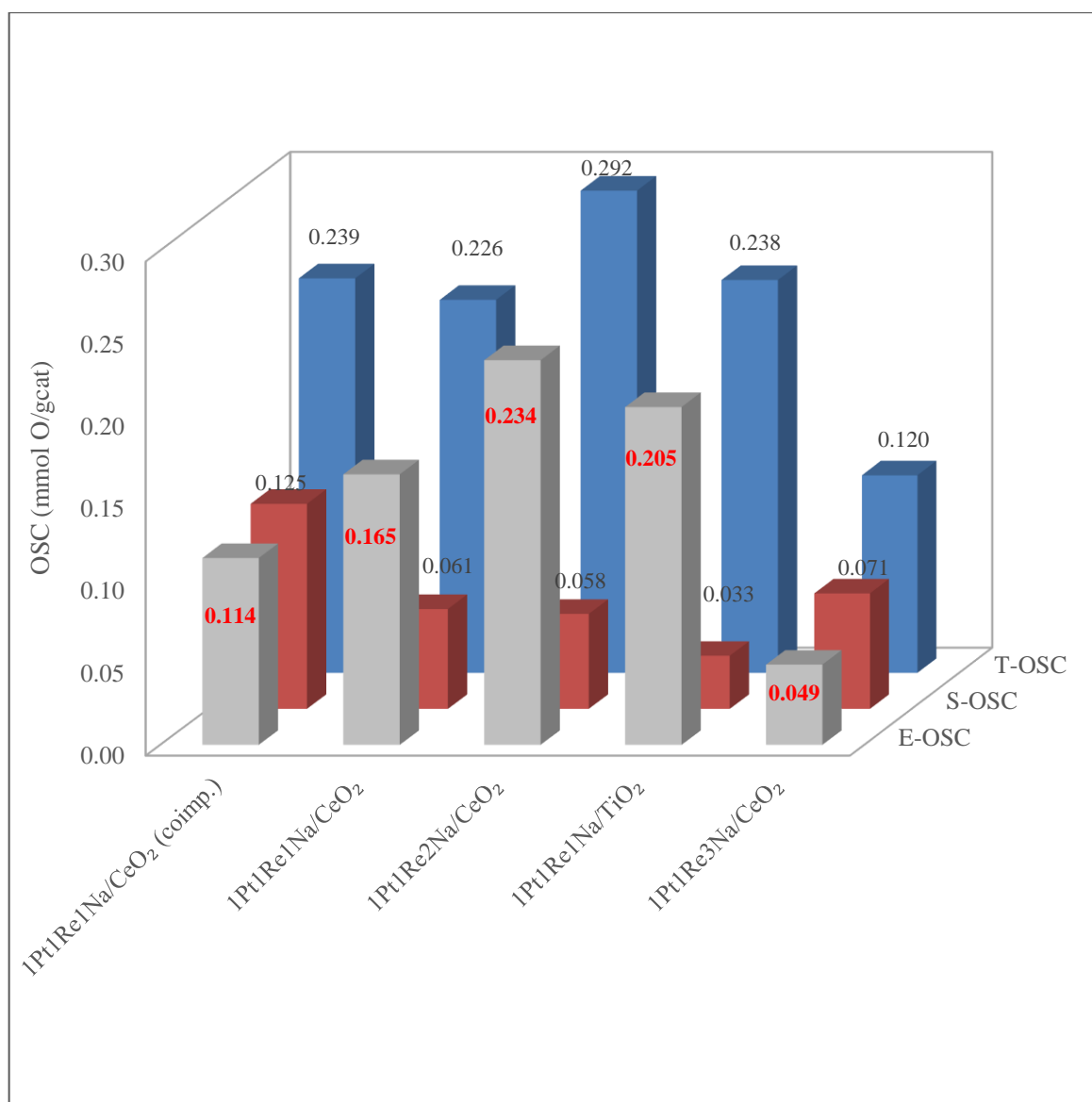


Figure 4.53. Oxygen Storage Capacities of catalysts tested at 350°C under DRF #1

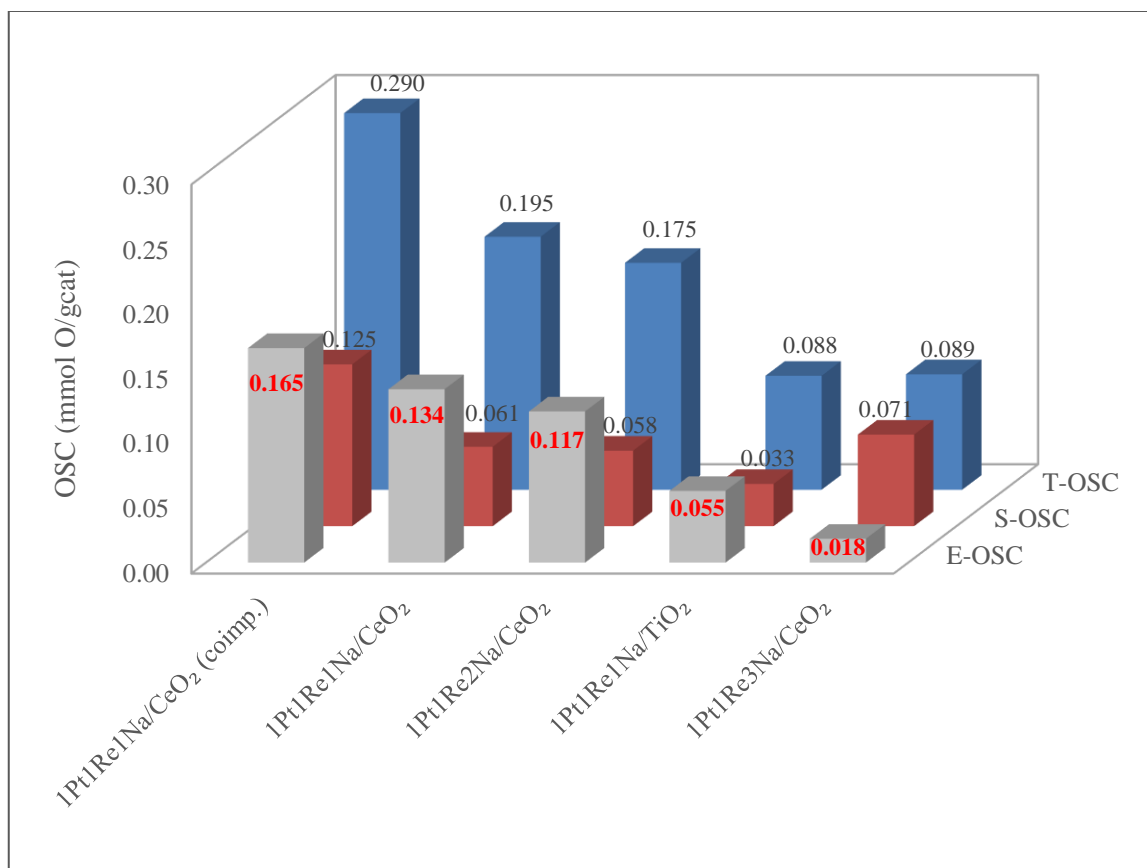
(H₂O/CO=6.7).

Figure 4.54. Oxygen Storage Capacities of catalysts tested at 350°C under DRF #2 (H₂O/CO=16.2).

Figure 4.53 shows that E-OSCs and T-OSCs of the catalyst samples do not follow the same trend, which emphasizes the importance and the necessity of E-OSC calculation. The ranges of the T-OSCs, S-OSCs, and E-OSCs of the samples subjected to DRF#1 were found as 0.120-0.292, 0.033-0.125 and 0.049-0.234 mmol O/g_{cat}, respectively. Though the highest T-OSC and E-OSC were determined for 1%Pt-1%Re-2%Na/CeO₂ catalyst, the highest S-OSC was calculated for coimpregnated 1%Pt-1%Re-1%Na/CeO₂. 1%Pt-1%Re-1%Na/CeO₂ and 1%Pt-1%Re-2%Na/CeO₂ samples were found to have higher T-OSC and E-OSCs, which is not the case for all catalysts samples, i.e., low E-OSC was encountered in coimpregnated 1%Pt-1%Re-1%Na/CeO₂ due to its relatively high S-OSC despite of its high T-OSC. Coimpregnation of Re and Na brought along a high S-OSC along with catalyst's T-OSC, since both metals occur in oxide forms on the surface. It should be worth mentioning that the S-OSC of the TiO₂ supported catalyst was lower than that of the CeO₂ supported

catalysts. S-OSCs were also affected by Na loading of CeO₂ supported catalysts, however not linearly. This result can imply that Na loading may have a significant influence on Na-CeO₂ interaction. Considering the carbonate peaks, which formed under reaction conditions and did not disappear with He flush in the FTIR-DRIFTS spectra of 1%Pt-1%Re-3%Na/CeO₂ catalyst; consistently, coming up with a low E-OSC, which refers to the renewed oxygen on the surface after used in the reaction.

Similar relations were elucidated utilizing the data presented in Figure 4.54 for the samples subjected to DRF#2 at 350°C. Note that the same S-OSC values were used in E-OSC determination under both DRF#1 & 2, as S-OSCs were obtained after the sample was subjected to only inert flow being independent of the reaction conditions. As a general remark, T-OSCs, S-OSCs, and E-OSC values of the samples changed between 0.089-0.290, 0.033-0.125 to, and 0.018-0.165 mmol O/g_{cat}, respectively. Coimpregnated 1%Pt-1%Re-1%Na/CeO₂ sample was determined to have the highest OSC values of all types. The lowest E-OSC was calculated for 1%Pt-1%Re-3%Na/CeO₂ sample in the case of DRF#2 flow. E-OSCs of the samples calculated for DRF#2, which is a feed with higher H₂O/CO ratio as 16.2, are lower in general compared to those calculated for DRF#1 flow (H₂O/CO=6.7), except the coimpregnated 1%Pt-1%Re-1%Na/CeO₂ sample. Since the H₂O flow was kept constant for both DRF flows, as presented in Table 3.11, it was the H₂O/CO ratio in the feed that dominantly affects the T-OSC and E-OSC of the catalysts. The results, in general, implies that low H₂O/CO ratio *-depending on higher CO concentration in the feed-* leads to an enhanced E-OSC and consequently favors WGS reaction over Pt-Re-Na system. It should be noted that decreasing H₂O concentration as keeping CO concentration constant most probably do not affect E-OSC in the same manner. On the basis of the FTIR-DRIFTS spectra obtained under 1%CO and ideal feed flow conditions, introducing H₂O into the feed gave broad peaks in the OH band providing renewable oxygens for maintaining the occurrence of reaction. Presence of H₂O contributes to the T-OSC, and thereby E-OSC of the catalyst. However, effect of H₂O concentration cannot be examined in the FTIR-DRIFTS-MS studies due to the limitation caused by H₂O condensation. It should be noted that increasing CO composition up to 8% in the feed flow while keeping H₂O concentration constant was also found to enhance the WGS activity in the *operando* FTIR-DRIFTS-MS studies conducted by our group member Ali Uzun. Therefore, it was thought that the catalysts' surfaces were

not saturated under ideal feed conditions used in FTIR-DRIFTS-MS tests, and there exists an optimum CO concentration for WGS activity when H₂O concentration remains the same.

E-OSC and CO conversion values of all catalysts, subjected to both feed flow conditions, are presented in Figure 4.55 and Figure 4.56. A prominent relation between E-OSC and WGS activity was confirmed with the compatible results obtained under DRF#1 and RF#1, as presented in Figure 4.55. The highest E-OSC for DRF#1 feed was calculated over 1%Pt-1%Re-2%Na/CeO₂, which also exhibited the highest WGS activity under RF#1. Similarly, the lowest E-OSC was obtained over essentially inactive %1Pt-1%Re-3%Na/CeO₂ sample as expected. Figure 4.56 shows the relation between performance results and E-OSCs of the catalysts subjected to DRF#2 and RF#2 flow. Although the results were generally compatible, one exception was that the coimpregnated 1%Pt-1%Re-1%Na/CeO₂ sample was found to be have the highest E-OSC, although it does not show the highest WGS activity.

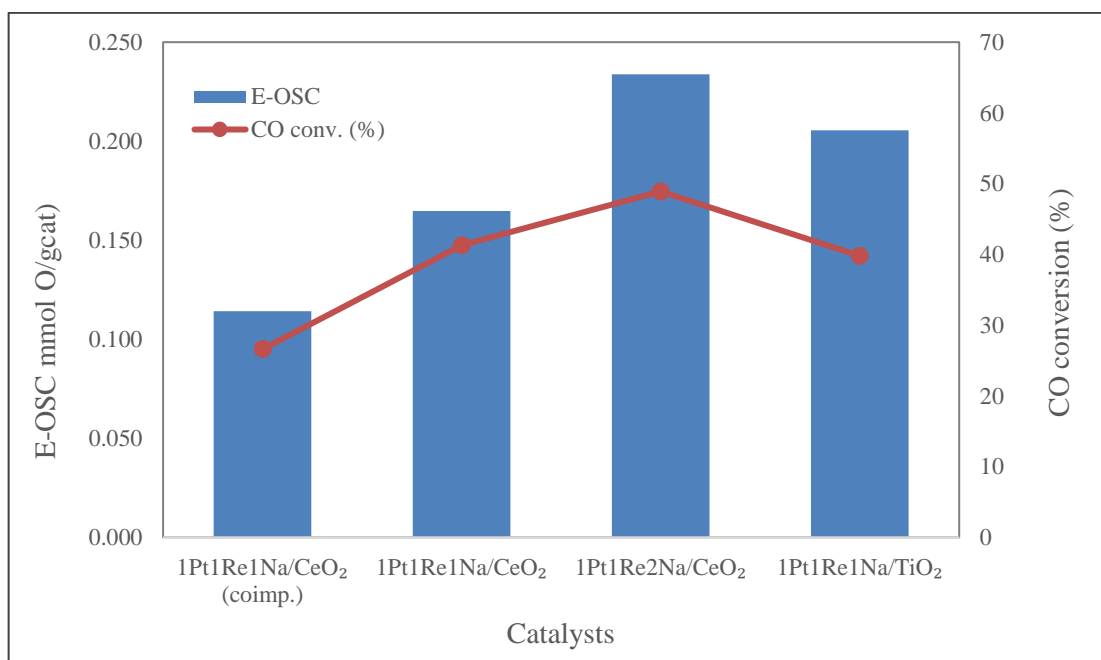


Figure 4.55. Effective OSCs and CO conversions of the samples obtained at 350°C under DRF #1 (H₂O/CO=6.7).

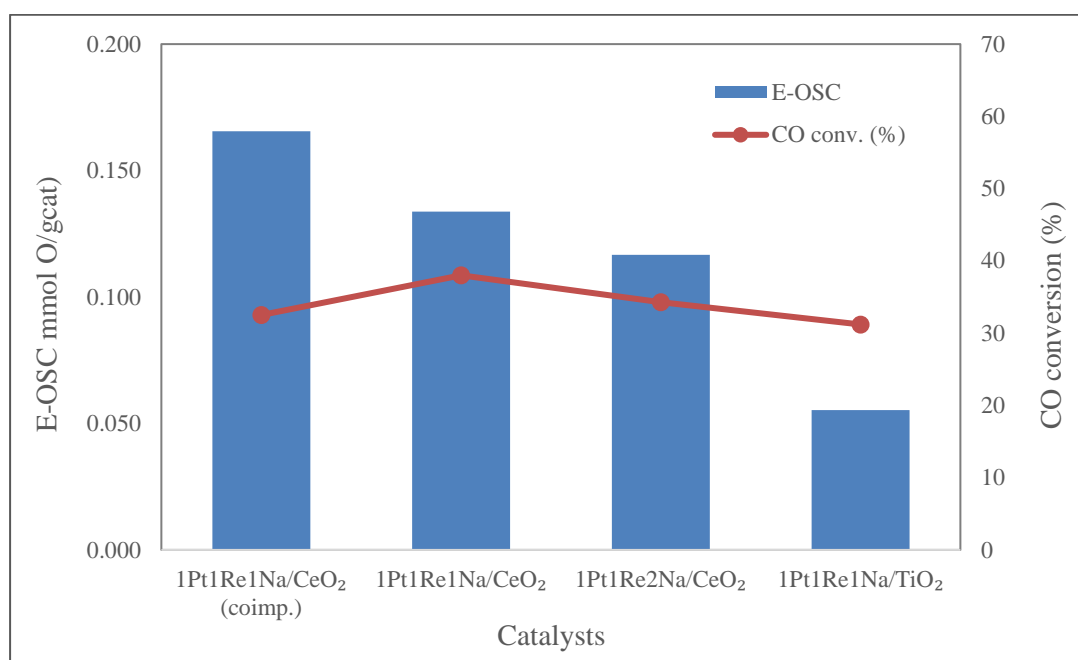


Figure 4.56. Effective OSCs and CO conversions of the samples obtained at 350°C under DRF #2 (H₂O/CO=16.2).

4.6. Combined Evaluation of Performance, Characterization and FTIR-DRIFTS Tests Results Conducted on Tri-Metallic WGS Catalysts

The results of WGS catalytic activity tests of the Na containing catalysts were analyzed and the performance sequence of the catalysts at 350°C under Realistic Feed #1 (RF#1) were found as 1%Pt-1%Re-2%Na/CeO₂ > 1%Pt-1%Re-1%Na/CeO₂ > 1%Pt-1%Re-1%Na/TiO₂ > 1%Pt-1%Re-1%Na/CeO₂ (coimp.) > 1%Pt-1%Re-3%Na/CeO₂. Under Realistic Feed #2 (RF#2), WGS performance results of these catalysts, with the exception of 1%Pt-1%Re-3%Na/CeO₂, were approached to each other within the range of 30-35% conversion, which indicates a relatively lower WGS performance compared to the results obtained under RF #1 due to lower CO concentration in the feed. Although WGS catalytic activities at 300°C were not very promising under realistic feed conditions, the catalysts showed high performance under real feed flow in the tests conducted in serial OSR-WGS system. Operating the WGS reactor at lower temperatures was found not to be unreasonable under real conditions, which has a higher H₂O concentration in the WGS reactor feed stream compared to that of realistic feed composition used in the realistic feed tests.

The sequence of the catalysts in terms of WGS catalytic activity was interpreted via characterization techniques, FTIR-DRIFTS-MS studies and OSC tests. In the XPS analysis, Na1s spectra of the Na containing samples showed that the peak corresponding to Na₂O species (1070.5 eV) (Figure 4.36) were more intense for the freshly reduced forms of 1%Pt-1%Re-1%Na/CeO₂ and 1%Pt-1%Re-2%Na/CeO₂ samples. Owing to the oxygen utilization, this peak became less evident in the spectra of used samples, which were subjected to RF#1 conditions. The most significant example of this change in the peak intensity was observed in the Na1s spectra of 1%Pt-1%Re-2%Na/CeO₂, which also gave the highest WGS activity at 350°C under RF#1 conditions. The distributions of the peaks corresponding to Ce³⁺ and Ce⁴⁺ species in Ce3d spectra of the fresh and spent catalysts have indicated that Ce³⁺/Ce⁴⁺ ratio for the spectra of the highly active spent catalysts have increased, even though Ce³⁺ sites were known as active sites for WGS reaction (Vignatti *et al.*, 2011; Hwang *et al.*, 2011). Combining the findings of the Na1s and Ce3d spectra of the highly active catalysts, 1%Pt-1%Re-1%Na/CeO₂ and 1%Pt-1%Re-2%Na/CeO₂, suggests the NaO_x species should be more influential than CeO_x species in the WGS reaction mechanisms of the Na containing catalysts.

The high intensity in Pt²⁺ peaks, which corresponds to active sites (Roh *et al.*, 2012; Zhu *et al.*, 2011), in Pt4f XPS spectra of the catalysts confirms high WGS activity achieved over sequentially impregnated 1%Pt-1%Re-1%Na/CeO₂ and 1%Pt-1%Re-2%Na/CeO₂ samples. On the other hand, relatively low WGS activity observed over coimpregnated 1%Pt-1%Re-1%Na/CeO₂ is in accordance with its more significant Pt⁴⁺ peak in its spectrum. Additionally, limited Pt²⁺ and Pt⁴⁺ presence was observed in the spectrum of 1%Pt-1%Re-3%Na/CeO₂ sample, due to the blockage of Pt sites at higher Na loadings. Metal dispersion results were also correlated with the activity results, i.e. essentially zero dispersion was measured for 1%Pt-1%Re-3%Na/CeO₂ sample which essentially inactive, whereas sequentially impregnated 1%Pt-1%Re-1%Na/CeO₂ and 1%Pt-1%Re-2%Na/CeO₂ samples have high and similar metal dispersions.

Re4f region of XPS spectra belonging to less active samples have a ReO_x peak at 50 eV, which was only observed in the spectra of coimpregnated 1%Pt-1%Re-1%Na/CeO₂ and 1%Pt-1%Re-1%Na/TiO₂. This peak disappeared from the spectrum of coimpregnated 1%Pt-1%Re-1%Na/CeO₂ upon subjecting to RF#1 reaction conditions, indicating that these

groups are participated in the reaction; however it remained in the spectrum of 1%Re-1%Na/TiO₂ catalyst under same conditions, supporting the idea that the reaction proceeds through different mechanisms over CeO₂ and TiO₂ supported samples.

The correlation between the WGS catalytic activity and Effective Oxygen Storage Capacity (E-OSC) concept has been explained Section 4.5. E-OSC values of the catalysts were found to be in accordance with their performance results. On the other hand, S-OSC of the catalyst can be related with the oxygen that cannot be renewed under reaction conditions. It was determined that coimpregnated 1%Pt-1%Re-1%Na/CeO₂ sample has higher S-OSC compared to those of sequentially impregnated ones most probably due to the simultaneous formations of Na and Re oxides on the surface. Lowest values of both catalytic activity and E-OSC were obtained for 1%Pt-1%Re-3%Na/CeO₂ sample. In the O1s spectra of this sample subjected to RF#1 conditions, the decrease in the intensity of the peak corresponding to lattice oxygen (528 eV) was observed to be more significant in comparison with other catalysts' (Ma *et al.*, 2018; Dongil *et al.*, 2015). This decrease most likely originates from the lack of surface oxygen leading to low E-OSC.

The importance of E-OSC on catalytic activity can also be understood by comparing the spectra of spent CeO₂ and TiO₂ supported catalysts. After subjecting to RF#1 conditions, oxygen utilization from catalyst surface was found not similar for CeO₂ and TiO₂ supported catalysts, indicated by the difference in distributions of the peaks in O1s spectra of each sample. Low E-OSC when TiO₂ was used as support was thought lead to participation of different oxygen groups to reaction mechanism, thereby different reaction path on the catalyst surface.

WGS reaction mechanism over Pt-Re-Na/CeO₂ catalysts can be interpreted through the associated changes in formate and carbonate groups observed during the tests conducted in FTIR-DRIFTS-MS. Regarding the spectra of CeO₂, 1%Pt-1%Re-1%Na/CeO₂ and 1%Pt-1%Re-3%Na/CeO₂ samples, formate groups were detected in the range of 3000-2700 cm⁻¹ wavenumber as 3 subsequent peaks in the spectra of CeO₂ and 1%Pt-1%Re-3%Na/CeO₂ after subjecting to feed flow containing 1% CO and also ideal feed #2 conditions. On the contrary, only one formate peak at 2885 cm⁻¹ was observed in the spectra of 1%Pt-1%Re-1%Na/CeO₂ sample, which has high WGS activity. The formation of only one formate peak

in the spectra of this catalyst indicates that either formate groups corresponding to other two peaks (2950, 2835 cm^{-1}) did not form at all under reaction conditions or were consumed very rapidly. Formate peaks shown after CO adsorption and ideal feed steps were observed not been swept during He flush conducted after each step indicates that these groups were strongly attached to the surface. Additionally, no change was observed at 1420 cm^{-1} wavenumber of 1%Pt-1%Re-3%Na/CeO₂ spectra corresponding to hydrogen carbonate, whereas consumption of hydrogen carbonate species was seen clearly for the case of 1%Pt-1%Re-1%Na/CeO₂ sample. In the spectrum obtained under reaction conditions (IF#2) also showed that number of bridge bonded CO molecules were more than linearly bonded ones considering the CO adsorption step. High activity of 1%Pt-1%Re-1%Na/CeO₂ sample can also be explained by the use of different OH groups (giving peaks at 3643 cm^{-1}) than those used by 1%Pt-1%Re-3%Na/CeO₂ and the CeO₂ while subjecting to IF#2 conditions from support. The peaks, which were observed in the range of 1700-800 cm^{-1} , corresponds to carbonate groups, and carbonate formation was also confirmed by 1065 cm^{-1} peak of Raman spectra obtained for spent samples.

4.7. Selective CO₂ Adsorption over Activated Carbon Based Adsorbents

In this part of the current study, AC based adsorbents were modified such as to enhance their surface basicity with the aim of improving both their CO₂ adsorption capacity and CO₂ adsorption selectivity. In this context, first AC6 and AC7 series samples, which are NaOH impregnated and calcined versions of air oxidized (AC2) and HNO₃ oxidized (AC3) forms of a commercial activated carbon, Norit ROX, were prepared (Section 3.3.3). In preparation of the adsorbent series, calcination temperature were used as the experimental parameter, and three different adsorbents were prepared for each of AC6 and AC7 series (Table 3.6). In the second step, CO₂ and CH₄ adsorption capacities of each sample were determined under pure CO₂ and pure CH₄ flows in 0-1000 mbar total pressure (P_T) range. Then, the selective adsorption ability all those samples were measured under CO₂-CH₄ gas mixture flow at room temperature (RT), 120°C and 200°C for the same pressure range. The adsorption performance of the adsorbents were tested and measured by using IGA-DSMS system, and comparatively analyzed on the basis of their adsorption capacity, in terms of mg adsorbed/g adsorbent or percentage mass uptake, and of their selective CO₂ adsorption ability from CO₂-CH₄ mixtures having two different CO₂:CH₄ ratios; CO₂:CH₄= 1:1 and 1:9. Additionally,

high pressure adsorption and selective adsorption tests for P_T range of 0-5000 mbar were conducted on a sample showed superior overall performance. The microstructural properties of the adsorbents were characterized by Scanning Electron Microscopy/Electron dispersive X-Ray (SEM-EDX). N_2 -He adsorption was used in microphysical characterization of the adsorbents by their Total Surface Area (TSA), Total Pore Volume (TPV) and Pore Size Distribution (PSD).

In the current work, a novel methodology, which was first developed and introduced by our group for the determination of selective adsorption capacity of the adsorbent under multicomponent gas mixture atmosphere/flow (Acar *et al.*, 2018), was used. The methodology utilizes IGA-DSMS data in order to calculate adsorption/selective adsorption capacities and adsorption kinetics parameters of an adsorbent for each component of a binary, tertiary and multicomponent gas mixtures.

4.7.1. Determination of Selective Adsorption Capacities of an Adsorbent under Flow of Multicomponent Gas Mixtures

The integrated gravimetric analyzer-mass spectrometer (IGA-MS) system is designed in such a way that; (i) in the feeding block, gas mixtures having specified composition, flow rate and total pressure are prepared through utilizing a homemade system involving automatic mass flow controllers and valving/piping for mixing of gasses, (ii) changes in total adsorbent weight are acquired by the gas sorption analyzer in real time with respect to the ramp type changes in pressure followed by data acquisition at the specified pressure set point, and (iii) the composition of the unadsorbed gas stream leaving the adsorption chamber is analyzed via dynamic sampling mass spectrometer. The combined use of gravimetric sorption measurements and unadsorbed/effluent gas mixture analysis results is the basis of our novel methodology that can be used in determination of the adsorption capacity of the adsorbent *and parameters of adsorption kinetics* for each species in multicomponent sorption studies.

As the first step of the calculation procedure, blank experiments are carried out at RT for the multicomponent gas mixtures to be tested, i.e. 50% CO_2 -50% CH_4 and 10% CO_2 -90% CH_4 mixtures in the current study, without using any adsorbent material in the sample

container. Blank tests are conducted in order to observe the effect of ramp type pressure increase by the gas sorption analyzer and corresponding partial pressure signals of the studied gases for each set pressure level on the mass spectrometer analysis. The output data of mass spectrometer resemble S-shaped curve between each successive pressure set points, e.g. 500-600 mbar as given in Figure 4.57. The partial pressure signal at time t_1 , which belongs to the former set point, i.e. 500 mbar, is subtracted from all the partial pressure signals in the current pressure range studied. Then, these data are divided by the steady state pressure signal belonging to the latter set point, i.e. 600 mbar, which results in normalized partial pressure levels for each species. Finally, time vs. normalized pressures are used to approximate the area under the solid curve from t_1 to t_3 via trapezoidal rule (Figure 4.57).

As the second step of the calculation procedure, S-shaped curve obtained in adsorption tests is investigated as two consecutive regions; in Region (*i*), pressure is ramp-wise increased, and adsorption of both species occur on the adsorbent material from t_1 to t_2 ; and in Region (*ii*), pressure set point is reached in the adsorption chamber, however the adsorption process continues at constant pressure till adsorbent surface is saturated with related species from t_2 to t_3 (Figure 4.57). The slight decrease in partial pressure signal in the mass spectrometer and the increase in the weight of the adsorbent with respect to time due to ongoing adsorption in gas sorption analyzer can be clearly seen in Figure 4.57 and Figure 4.58, respectively. Therefore, normalization procedure for the adsorption tests is based on the partial pressure signal corresponding to time t_2 (the time at which the pressure set point is reached) instead of steady state partial pressure signal used in the blank tests. Then, the area under the dashed curve in normalized pressure vs time graph is approximated from t_1 to t_3 by using trapezoidal rule.

As the next step, the area under the adsorption curve (dashed) is subtracted from the area under the blank curve (solid), which is related to the amount of adsorption (Figure 4.57). Volume of each gas sent is calculated by using the volumetric flow rate of each species (v_j) in the feed stream and the time range (t_1 - t_3). The area, which corresponds to the amount of the sent gas that has reached mass spectrometer shown as rectangular area in Figure 4.57, is used to relate the volume of each gas sent to the volume of the adsorbed gas, i.e. the ratio of areas are related to the ratio of the volume of the gases as given in Equation (4.14). Since

$P_{b,1}^*$ and $P_{b,3}^*$ are lower and upper limits of the normalized partial pressure data of blank tests, Equation (4.14) can be simplified into Equation (4.15).

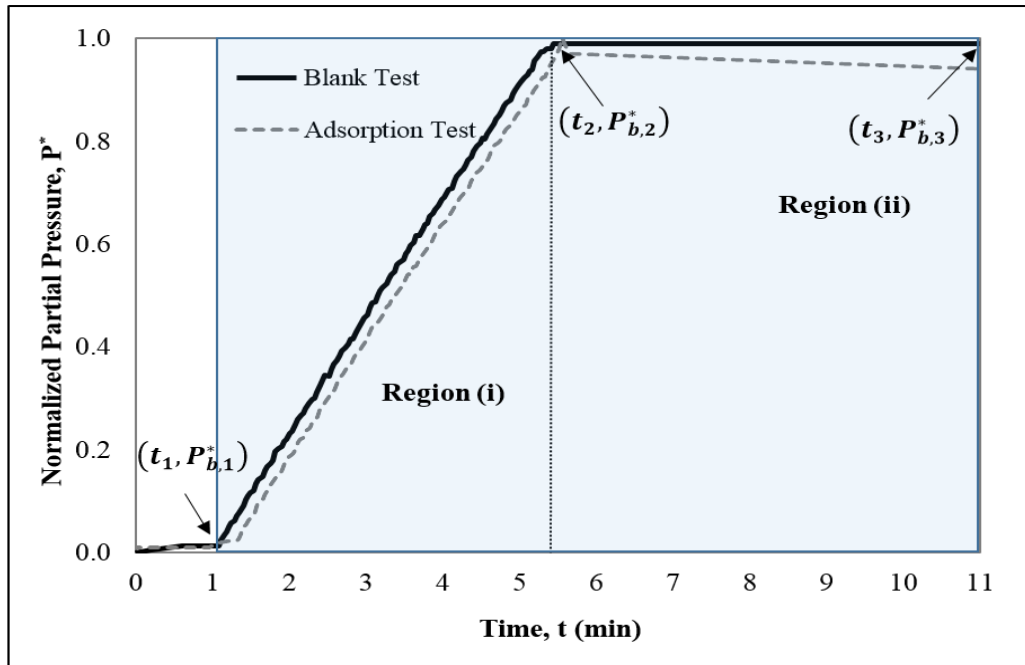


Figure 4.57. Comparison of normalized MS partial pressures in blank and adsorption tests at RT for 500-600 mbar pressure range with 50% CO₂-50% CH₄ mixture.

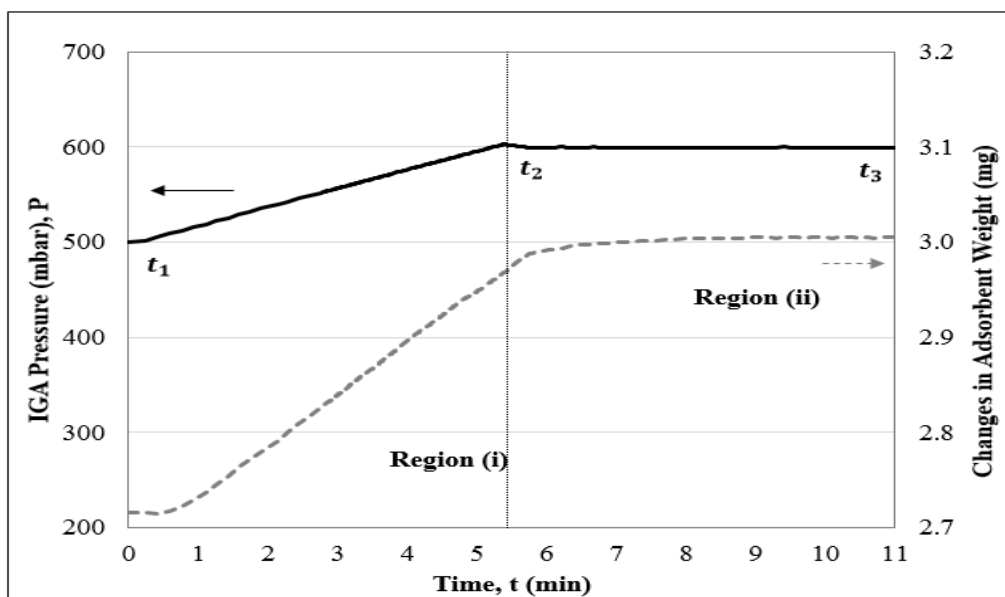


Figure 4.58. Change of IGA pressure and adsorbent weight with respect to time for the adsorption test conducted at RT for 500-600 mbar pressure range with 50% CO₂-50% CH₄ mixture.

$$\frac{\int_{t_1}^{t_3} P_{blank}^*(t)dt - \int_{t_1}^{t_3} P_{ads}^*(t)dt}{(t_3 - t_1) \times (P_{b,3}^* - P_{b,1}^*)} = \frac{V_{adsorbed\ gas}}{v_j \times (t_3 - t_1)} \quad (4.14)$$

$$v_j \times \left[\int_{t_1}^{t_3} P_{blank}^*(t)dt - \int_{t_1}^{t_3} P_{ads}^*(t)dt \right] = V_{adsorbed\ gas} \quad (4.15)$$

By using the information of the molar volume of an ideal gas at atmospheric conditions (1 atm and 25 °C) as 24.5 liters; adsorbed volumes, moles and weights of each species in the multicomponent mixture are calculated successively. The total weight change data due to adsorption directly acquired from the gas sorption analyzer and those calculated by using the current methodology differ due to the purge of a big portion of the feed gas in Region (*ii*), i.e. at constant pressure region, by the vacuum pump before and after the adsorption chamber. Thereby, this methodology combines total weight change and MS data, i.e. weight ratio of the adsorbed species. Finally, by using this weight ratio, the calculated adsorbed amounts are normalized with respect to the total weight change measured in gas sorption analyzer.

4.7.2. Pure Carbon Dioxide and Methane Adsorption Studies

The CO₂ and CH₄ adsorption/desorption isotherms were obtained for gas mixtures having different CO₂:CH₄ ratios in order to investigate the changes in adsorption behavior, i.e. *adsorption capacity and adsorption selectivity*, of the activated carbon based adsorbents upon modifications, heat/chemical treatments and/or alkali impregnations applied. Adsorption and desorption isotherms obtained under pure 50 ml/min CO₂ flow over AC6-200 at different temperatures are presented in Figure 4.59. A comparative analysis of the adsorption profiles obtained in experiments conducted at different temperatures showed that there is a decrease in mass uptake percentage with the increase in temperature. Data showed that the adsorption capacity at room temperature was 5-folds of what obtained in the experiments performed at 120°C and 200°C. Overlap of adsorption and desorption profiles indicates that the adsorption of CO₂ on the adsorbent is reversible. Mass uptake data at high temperatures shows that the surface reach saturation at relatively low pressures in comparison to that determined at RT. Similar to adsorption capacity-temperature relation of the sample observed under pure CO₂ flow, adsorbed CH₄ amount under pure 50 ml/min CH₄

flow at RT was found to be approximately 4-folds the capacity observed at 120°C and 200°C (Figure 4.60); likewise, the surface saturation under pure CH₄ flow was reached at lower pressures compared to that observed at RT: *for instance, the adsorbent surface was saturated at ca. 400 mbar in the adsorption tests performed at 200°C*. As a general remark, the saturation pressure level decreases as the temperature increases. The marked difference between the adsorption behavior of the sample for pure CO₂ and pure CH₄ is the observed mismatch of adsorption and desorption isotherms under CH₄ atmosphere indicating CH₄ molecules cannot be completely flushed from the adsorbent surface during desorption.

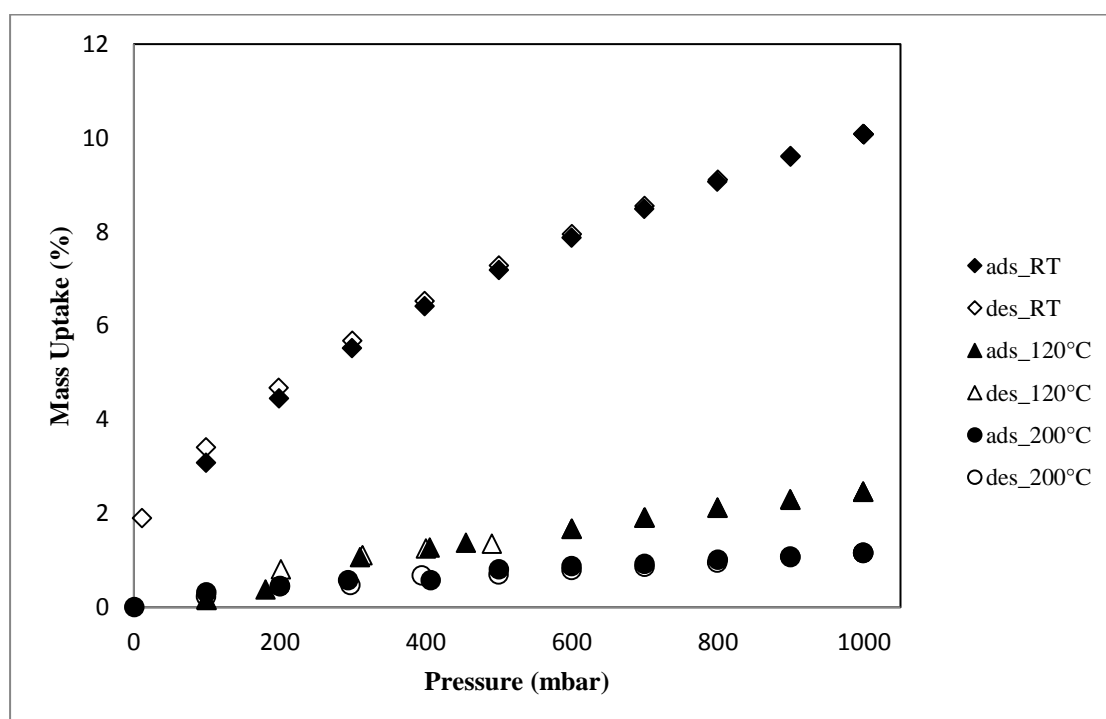


Figure 4.59. Mass uptake (%) of AC6-200 under pure 50 ml/min CO₂ flow.

The mass uptakes (%) obtained at 1000 mbar pressure for AC6-200 samples of equal weight under pure CO₂ and pure CH₄ flows were compared in Figure 4.61. For instance, the mass uptake (%) obtained under 50 ml/min CO₂ flow at 1000 mbar was measured as 10.1% at RT, whereas it was 1.6% under 50 ml/min CH₄ flow for the same conditions. When the similar analysis was performed on molar basis *aiming to eliminate effect of molecular weight difference*; CO₂/CH₄ molar uptake ratio at RT was calculated as 2.2 and a decrease was observed with the increase in temperature, meaning that CO₂ adsorption capacity of the sample is more sensitive to temperature increase than its CH₄ adsorption capacity.

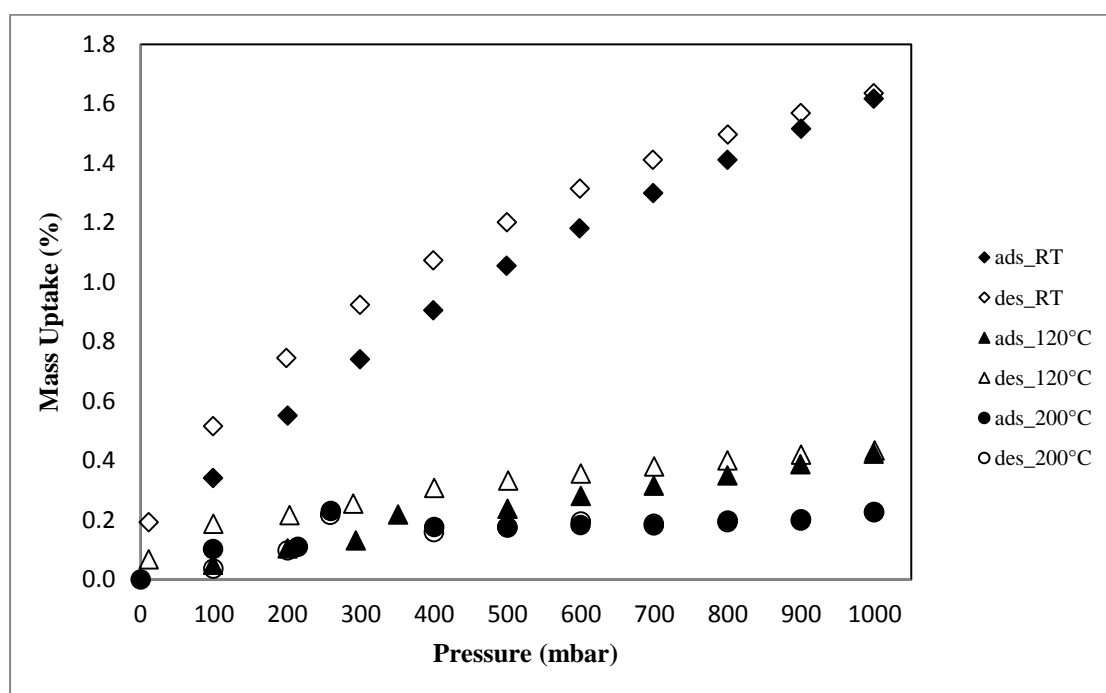


Figure 4.60. Mass uptake (%) of AC6-200 under pure 50 ml/min CH₄ flow.

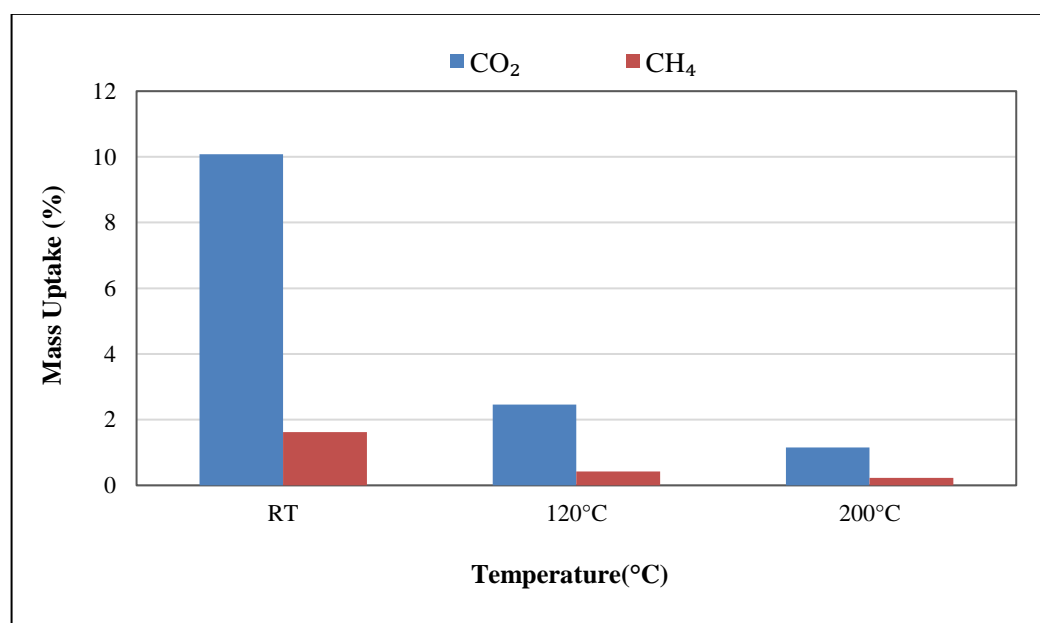


Figure 4.61. Mass uptake (%) comparison of AC6-200 under pure 50 ml/min CO₂ flow and 50 ml/min CH₄ flow (1000 mbar data).

The adsorption behavior of AC6-250 as a function of pressure at RT, 120°C and 200°C are presented for pure CO₂ and pure CH₄ flows in Figures 4.62 and 4.63, respectively, and the adsorption capacities of AC6-250 at 1000 mbar for pure CO₂ and pure CH₄ flows are comparatively shown in Figure 4.64.

Compared with the results obtained for AC6-200, CO₂ adsorption capacity results presented in Figure 4.64 for AC6-250 revealed that the adsorption capacity decreased from 10.1% to 9.2% at RT, from 2.5% to 0.4% at 120°C, from 1.2% to 0.2% at 200°C in. Similarly, CH₄ adsorption capacity results presented in Figure 4.64 for AC6-250 indicated that, compared with the results obtained for AC6-200, CH₄ adsorption capacity decreased from 1.6% to 1.2% at RT, from 0.4% to 0.3% at 120°C. The comparison of two adsorbents also indicated that no change in their mass uptake was observed at 200°C (Figure 4.61 and 4.64).

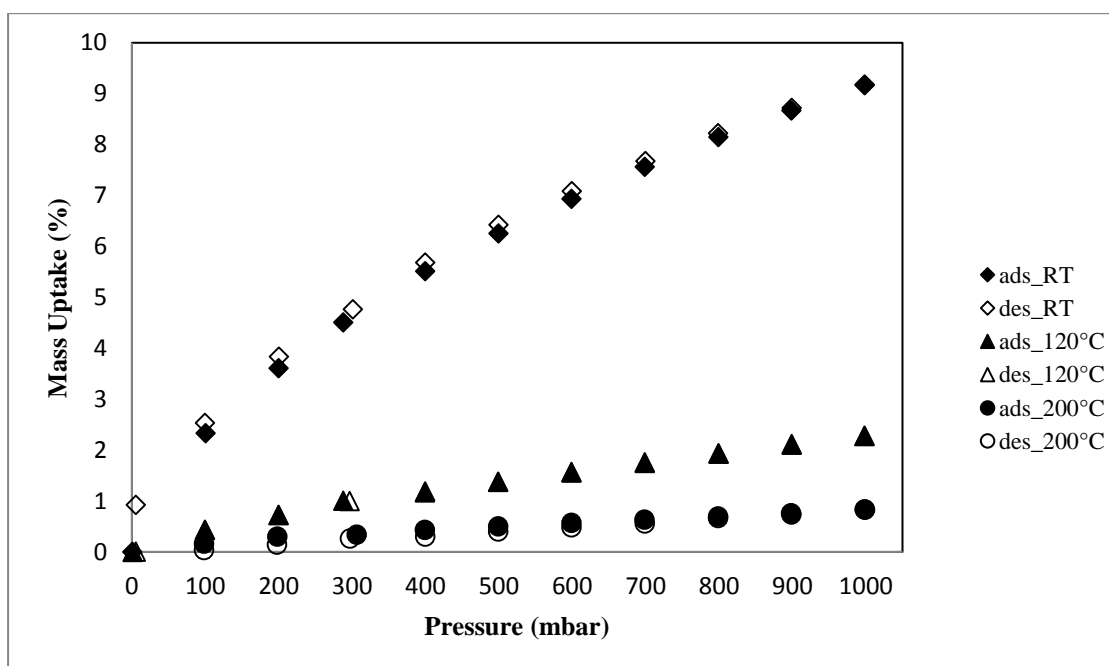


Figure 4.62. Mass uptake (%) of AC6-250 under pure 50 ml/min CO₂ flow.

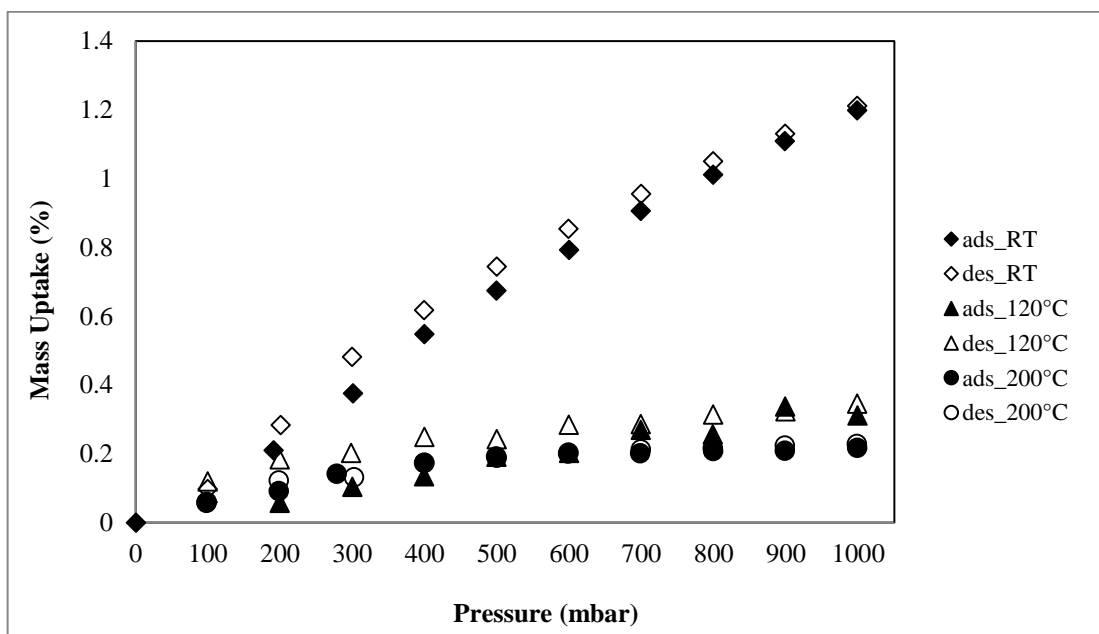


Figure 4.63. Mass uptake (%) of AC6-250 under pure 50 ml/min CH₄ flow.

In the experiments carried out at a flow rate of 50 ml/min, adsorbed amount of CO₂ at a pressure of 1000 mbar at room temperature on AC6-250 was determined as 9.2%, while 1.2% mass uptake was measured under pure CH₄ flow (Figure 4.64). As CO₂ adsorption capacity is more sensitive to temperature compared to that for CH₄, the ratio of adsorbed amount of CO₂ to CH₄ decreases with increasing temperature.

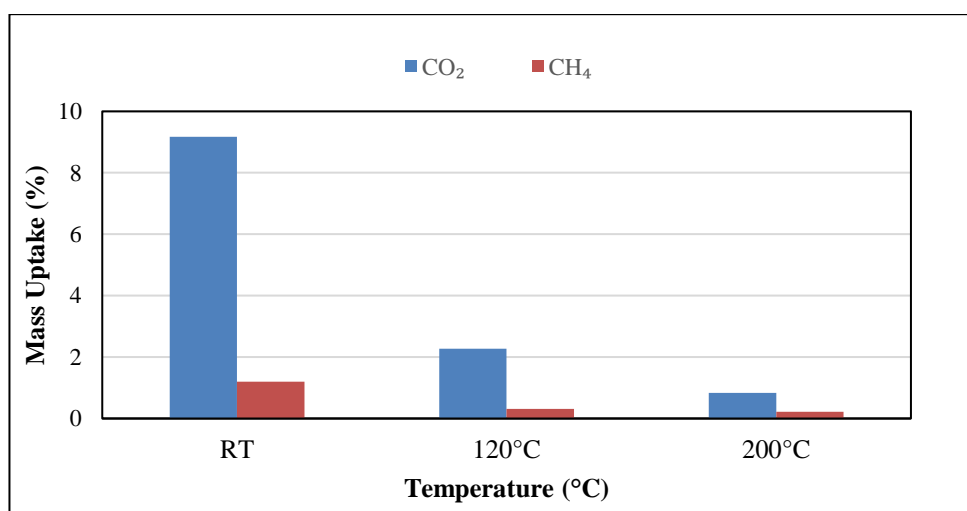


Figure 4.64. Mass uptake (%) comparison of AC6-250 under pure 50 ml/min CO₂ flow and 50 ml/min CH₄ flow (1000 mbar data).

The results of adsorption tests of AC6-300 conducted under pure 50 ml/min CO₂ and pure 50 ml/min CH₄ feed flow are presented in Figures 4.65 and 4.66, respectively. The comparison of results of the adsorption tests performed at different temperatures revealed that mass uptake percentage of the adsorbent was observed to decrease significantly with the temperature increase for both adsorbates, expectedly. When the mass uptake percentage values measured at RT and 120°C were compared, the increase in adsorbent weight at RT was determined to be 5 times and 4 times of that obtained at 120°C for CO₂ and CH₄, respectively.

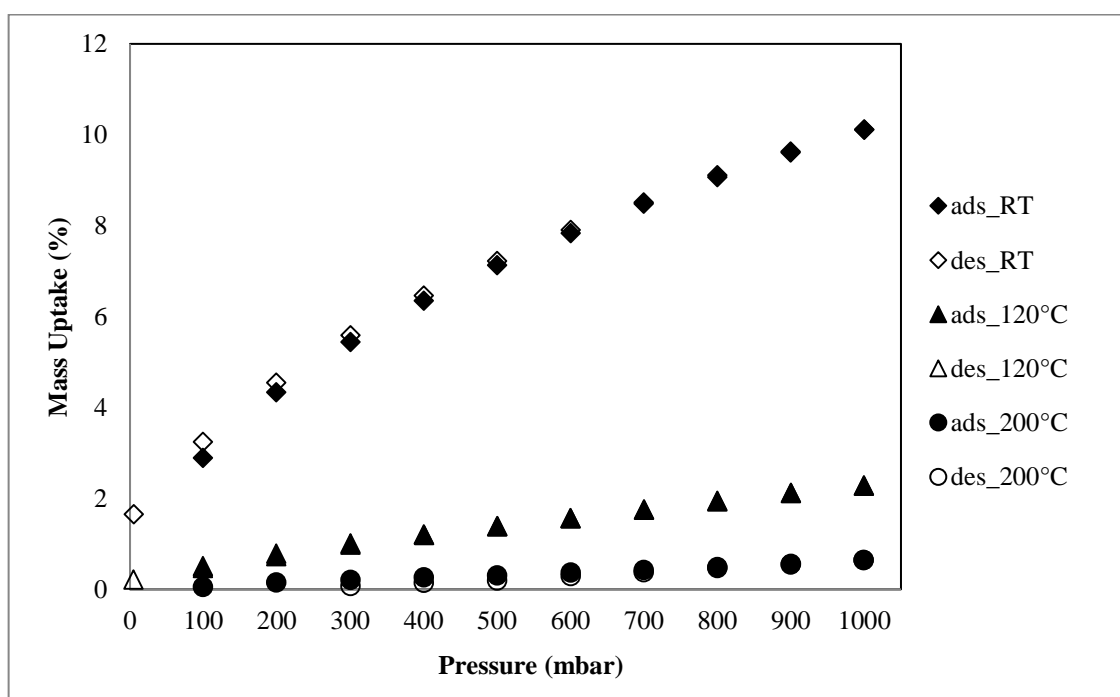


Figure 4.65. Mass uptake (%) of AC6-300 under pure 50 ml/min CO₂ flow.

Adsorption tests of AC6-300 performed at RT under 50 ml/min CO₂ flow exhibited 10.1% increase in adsorbent weight, while 1.3% weight increase was observed under 50 ml/min CH₄ flow. Comparison of the results of the experiments on AC6-300 under pure flows clearly shows that CO₂ adsorption capacity at 1000 mbar pressure level is 8 times that of CH₄ under same conditions (Figure 4.67).

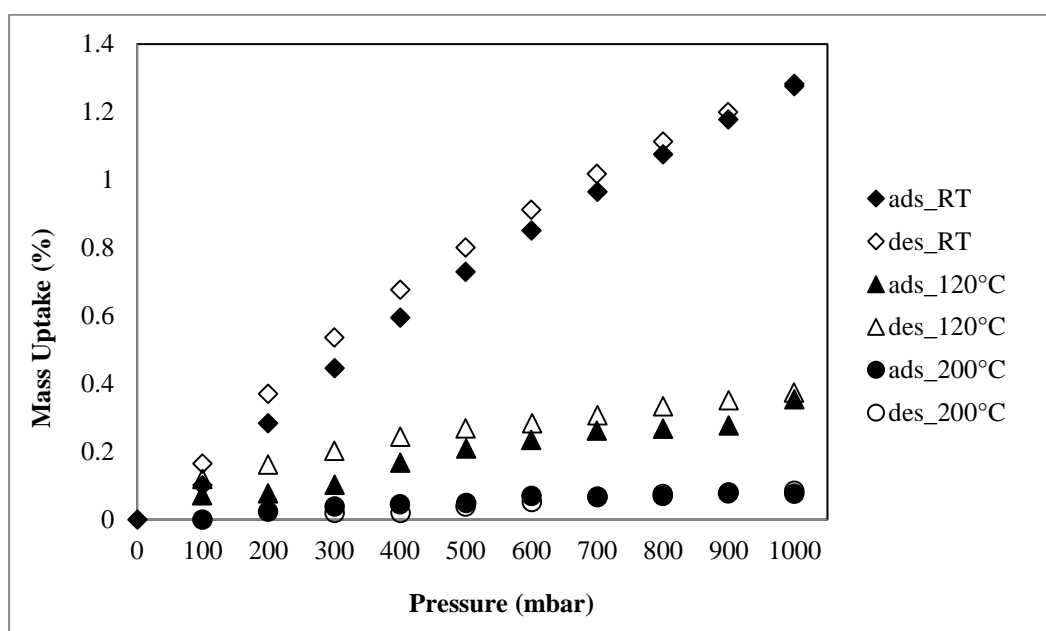


Figure 4.66. Mass uptake (%) of AC6-300 under pure 50 ml/min CH₄ flow.

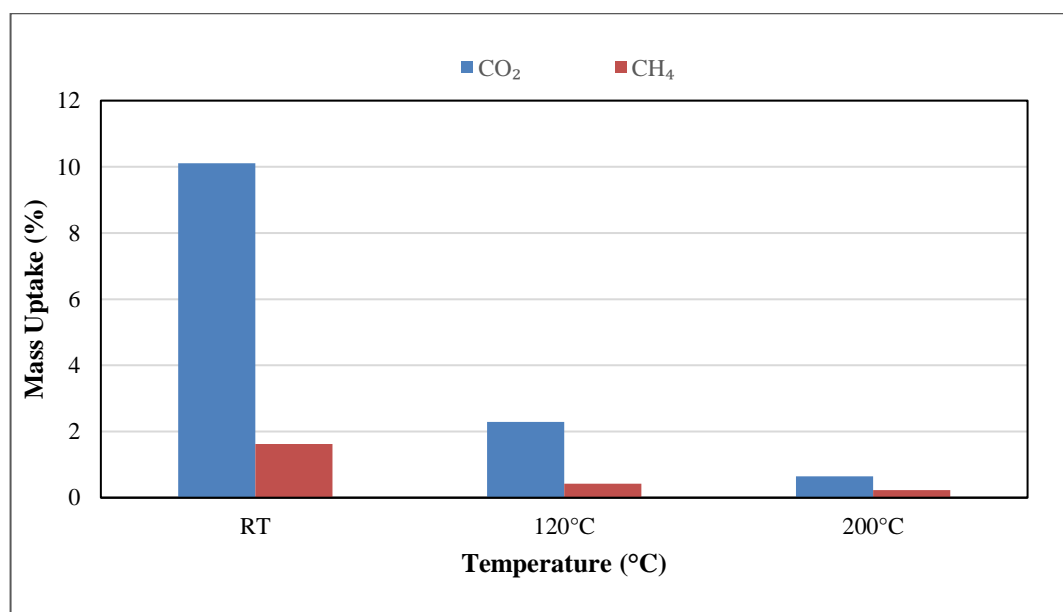


Figure 4.67. Mass uptake (%) comparison of AC6-300 under pure 50 ml/min CO₂ flow and 50 ml/min CH₄ flow (1000 mbar data).

CO₂ and CH₄ adsorption capacities of AC6 adsorbents prepared with different calcination temperatures are compared in Figure 4.68. It was observed that adsorbed amount of CO₂ is higher for AC6-200 and AC6-300 adsorbents compared to that on AC6-250. It should be noted that though amount of CH₄ adsorption on AC6-300 was less than the mass uptake of CH₄ on AC6-200, CO₂ adsorption capacity of these adsorbents were very close to each other.

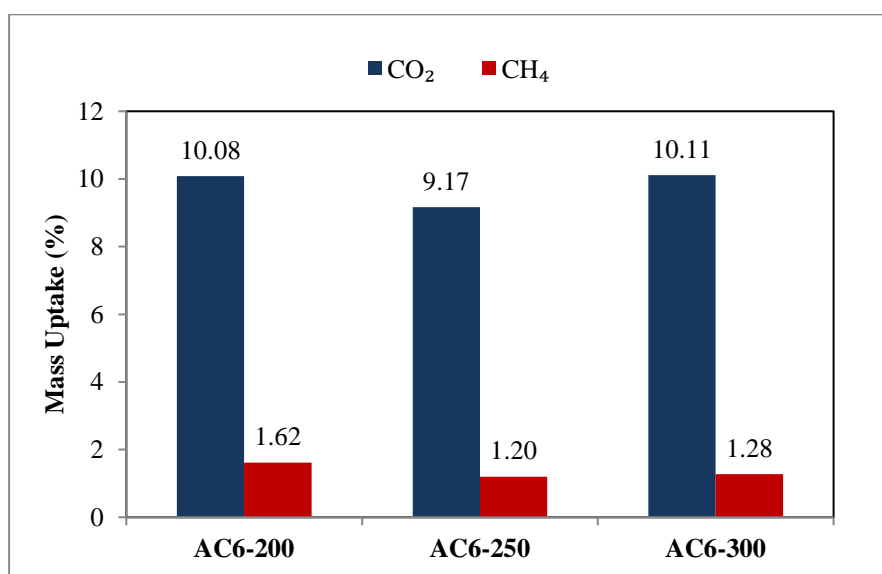


Figure 4.68. Adsorbed amounts of CO₂ and CH₄ on AC6-200, AC6-250 and AC6-300 under pure 50 ml/min CO₂ flow and 50 ml/min CH₄ flow at RT (1000 mbar data).

CO₂ and CH₄ adsorption capacities of AC7 adsorbents prepared at different calcination temperatures are shown in Figure 4.69. The highest CO₂ mass uptake among AC7 adsorbents was observed on AC7-200 as 7.83%. The lowest CH₄ mass uptake was also observed on the same adsorbent as desired. It was noticed that there was no dependence of CO₂ and CH₄ mass uptake values on the adsorbent calcination temperature. When all AC7 adsorbents were considered generally, it was obviously seen that CO₂ mass uptake values on AC7 adsorbents were lower than those on AC6 adsorbents, i.e. AC7 adsorbents were relatively inexpedient. When the results of the tests performed under pure CO₂ and CH₄ flows were compared, the ratios of adsorbed amounts of CO₂ to CH₄ were observed higher for AC7 adsorbents, however their performance under CO₂-CH₄ mixture flows should be examined in order to make an accurate comment on their selectivity towards CO₂.

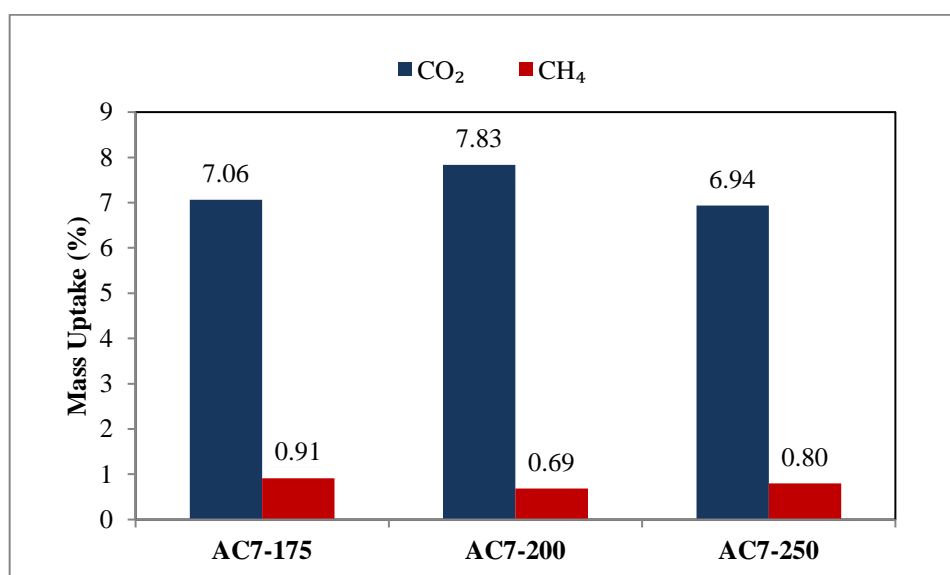


Figure 4.69. Adsorbed amounts of CO₂ and CH₄ on AC7-175, AC7-200 and AC7-250 under pure 50 ml/min CO₂ flow and 50 ml/min CH₄ flow at RT (1000 mbar data).

4.7.3. Selective Adsorption Tests

Results of the adsorption studies conducted on AC6-200 under flow of different compositions are compared in Figure 4.70. The weight change of the sample showing total adsorption (CO₂+CH₄), which was determined by IGA, was observed to decrease when CO₂ amount in the feed mixture was reduced. While total mass uptake on AC6-200 was observed as 10.1% under 100% CO₂ flow (50 ml/min CO₂) at 1000 mbar, it decreased to 6.16% under 50% CO₂-50% CH₄ flow (25 ml/min CO₂-25 ml/min CH₄) and 3.66% under 10% CO₂-90% CH₄ flow (5 ml/min CO₂-45 ml/min CH₄). This decrease in the total mass uptake may be thought either stem from the decrease in CO₂ amount and/or CO₂ selectivity of the adsorbent and/or due to adsorption of CH₄ molecules, which have lower mass than CO₂ molecules. In order to make a definite conclusion, the importance of selective adsorption analysis becomes crucial.

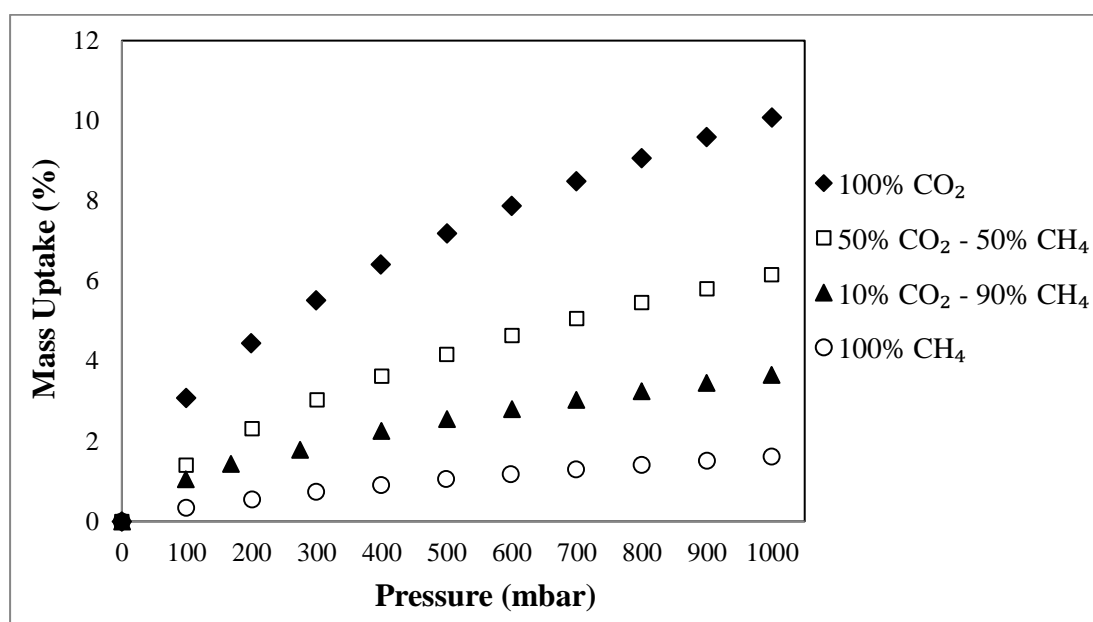


Figure 4.70. Mass uptake (%) of AC6-200 at different flow compositions.

CH₄ adsorption, respectively. The average CO₂:CH₄ mass ratio, i.e. the adsorption selectivity was calculated as 3.7, while CO₂:CH₄ mass ratio in the feedstream was 2.75. CO₂:CH₄ ratio of the adsorbed amounts at each pressure level are presented in Figure 4.72. Selective CO₂ and CH₄ adsorption capacities of AC6-200 calculated by using IGA-MS data obtained under 5ml/min CO₂- 45 ml/min CH₄ feed flow are given in Figure 4.73. 36.6 mg/g total mass uptake was obtained via IGA under these conditions and selectivity calculations showed that adsorbed amounts of CO₂ and CH₄ were 11.3 mg/g and 25.1 mg/g, respectively at 1000 mbar total pressure. While the mass ratio of CO₂: CH₄ in the feed mixture was 0.3, the selectivity of CO₂: CH₄ adsorption on the AC6-200 was calculated as 0.6. The change in CO₂:CH₄ adsorption ratio as a function of total pressure is presented in Figure 4.74. The decrease in CO₂:CH₄ ratio as a function of pressure can be explained through the relatively higher increase in the interaction between the adsorbent surface-CH₄ being more than that of the adsorbent surface-CO₂ over AC6-200 with the increase in total pressure, leading the increase in the surface concentration of CH₄. The data of the experiments performed on AC6-200 with different flow compositions indicated that CO₂:CH₄ ratio of the adsorbed gas was higher than the CO₂:CH₄ ratio of the feed gas mixture, meaning that CO₂ adsorption on AC6-200 can be performed selectively.

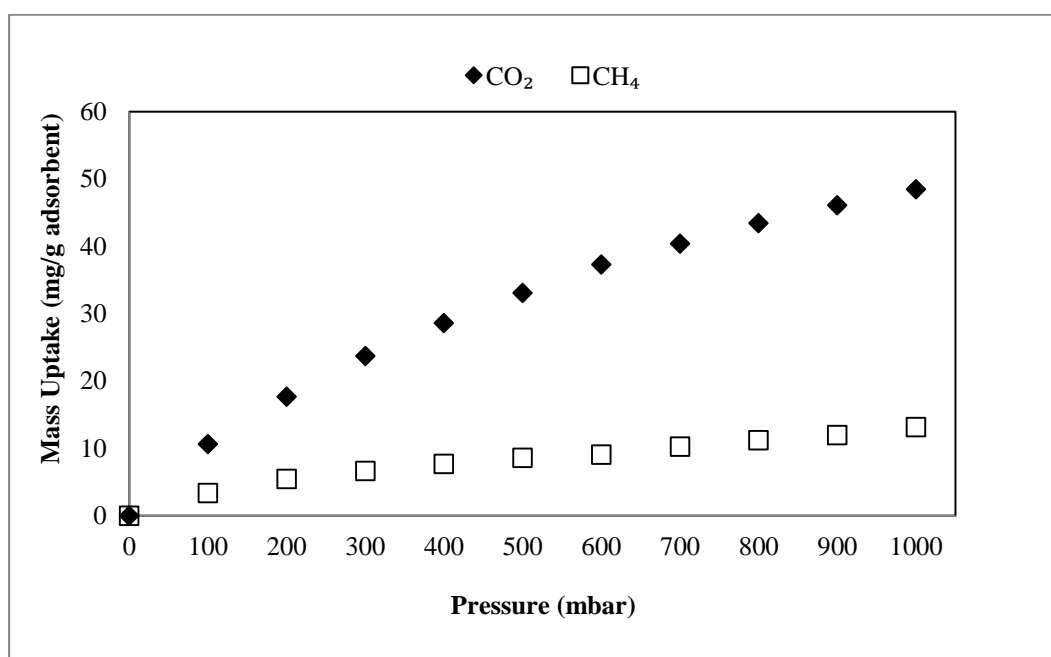


Figure 4.71. Mass uptake (mg/g adsorbent) of AC6-200 at RT under 25 ml/min CO₂- 25 ml/min CH₄ flow.

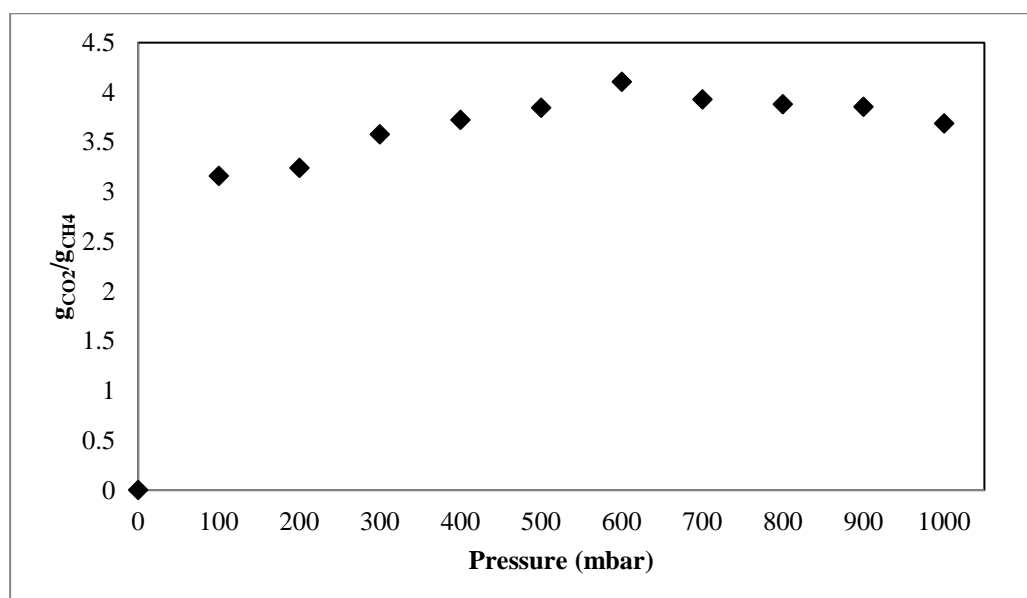


Figure 4.72. Adsorbed CO₂/CH₄ ratio on AC6-200 at RT and 0-1000 mbar under 25 ml/min CO₂- 25 ml/min CH₄ flow.

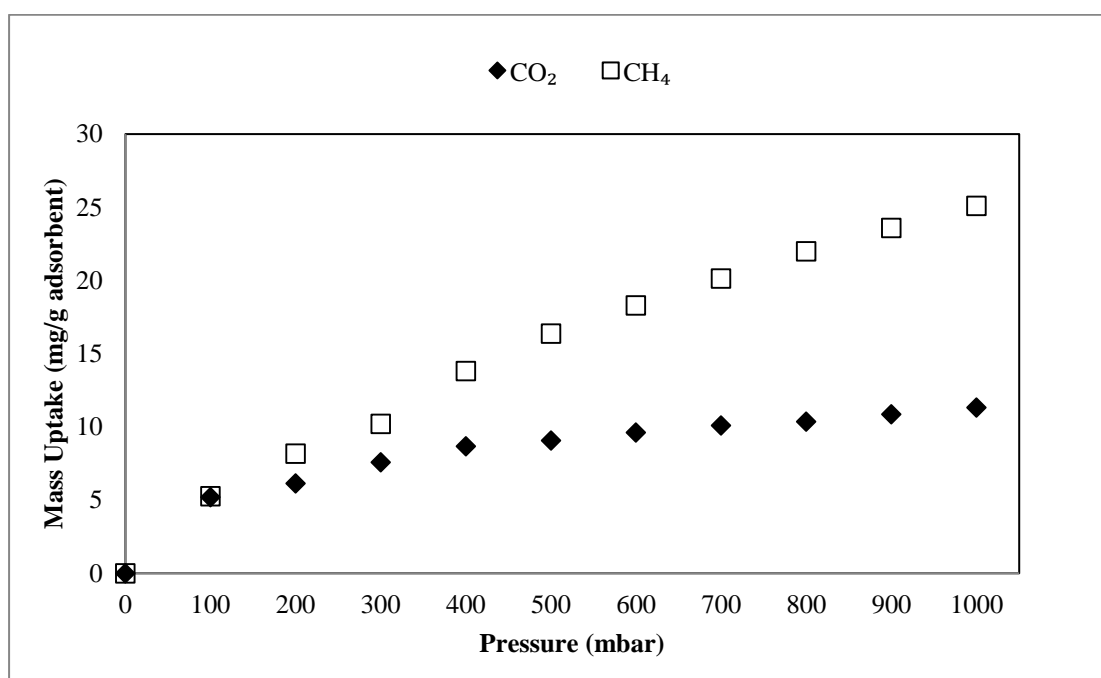


Figure 4.73. Mass uptake (mg/g adsorbent) of AC6-200 at RT under 5 ml/min CO₂- 45 ml/min CH₄ flow.

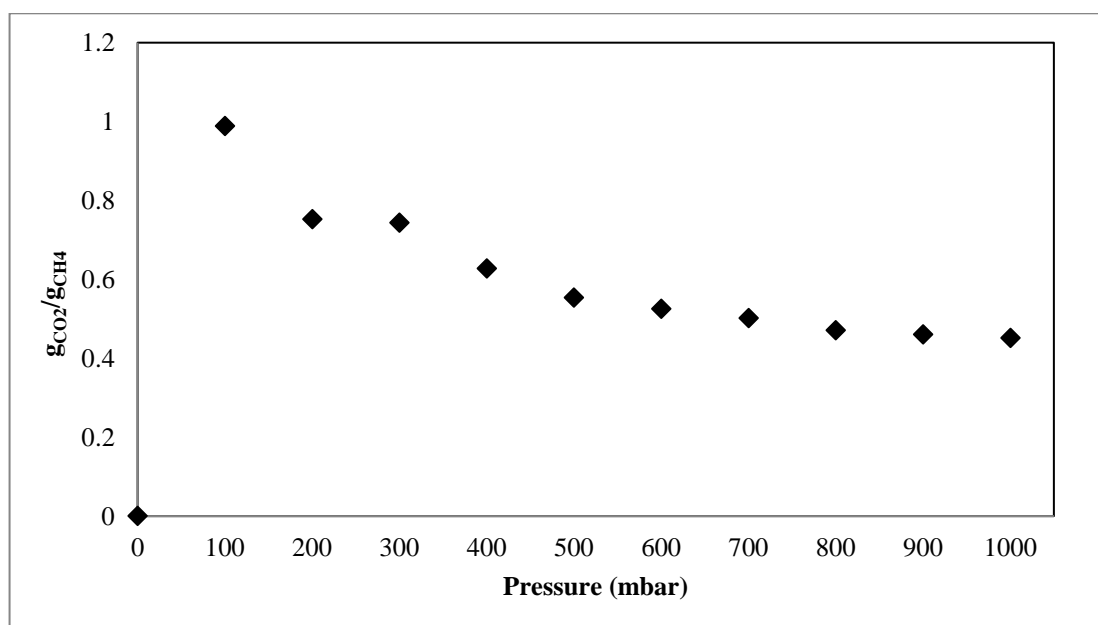


Figure 4.74. Adsorbed CO₂/ CH₄ ratio on AC6-200 at RT and 0-1000mbar under 5 ml/min CO₂- 45 ml/min CH₄ flow.

Selective adsorption capacity calculation procedure was also applied to the data obtained for AC6-250, AC6-300 and AC7-200 at RT. When the data of these experiments and related calculations were analyzed comparatively; the best performing adsorbent in terms of CO₂ selective adsorption under 25 ml/min CO₂- 25 ml/min CH₄ flow, was determined as AC6-200 with adsorption capacities of 48.47 mg/g and 13.14 mg/g for CO₂ and CH₄, respectively at 1000 mbar. The most selective adsorption performance under 5ml/min CO₂ - 45 ml/min CH₄ was also belongs to AC6-200; the adsorbed amount of CO₂ and CH₄ calculated under this flow composition was calculated as 11.33 mg/g and 25.10 mg/g, respectively. In analyzing the selective adsorption ability of the adsorbents, not only the adsorbed amounts of the gases, but also the ratio of the adsorbate gases (in the current case CO₂:CH₄) fed has great importance. Selective adsorption performances of adsorbents under 25 ml/min CO₂-25 ml/min CH₄ and 5 ml/min CO₂-45 ml/min CH₄, are compared and presented in Figures 4.75 and 4.76, respectively. The highest selectivity for CO₂:CH₄ was observed on AC6-200 under both feed gas mixtures. The adsorption ratio of CO₂: CH₄ under 25 ml/min CO₂-25 ml/min CH₄ flow was calculated as 3.7, while the same ratio under 5 ml/min CO₂-5 ml/min CH₄ was determined as 0.45.

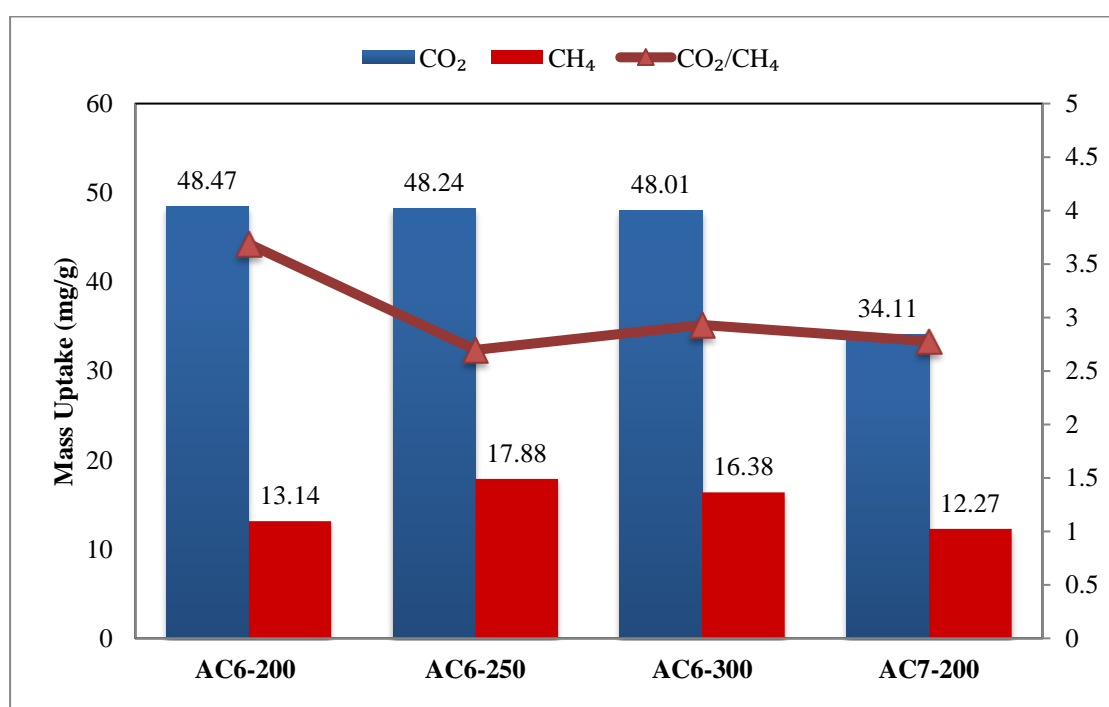


Figure 4.75. Adsorbed amounts of CO₂ and CH₄ on AC6-200 at RT under 25 ml/min CO₂- 25 ml/min CH₄ flow.

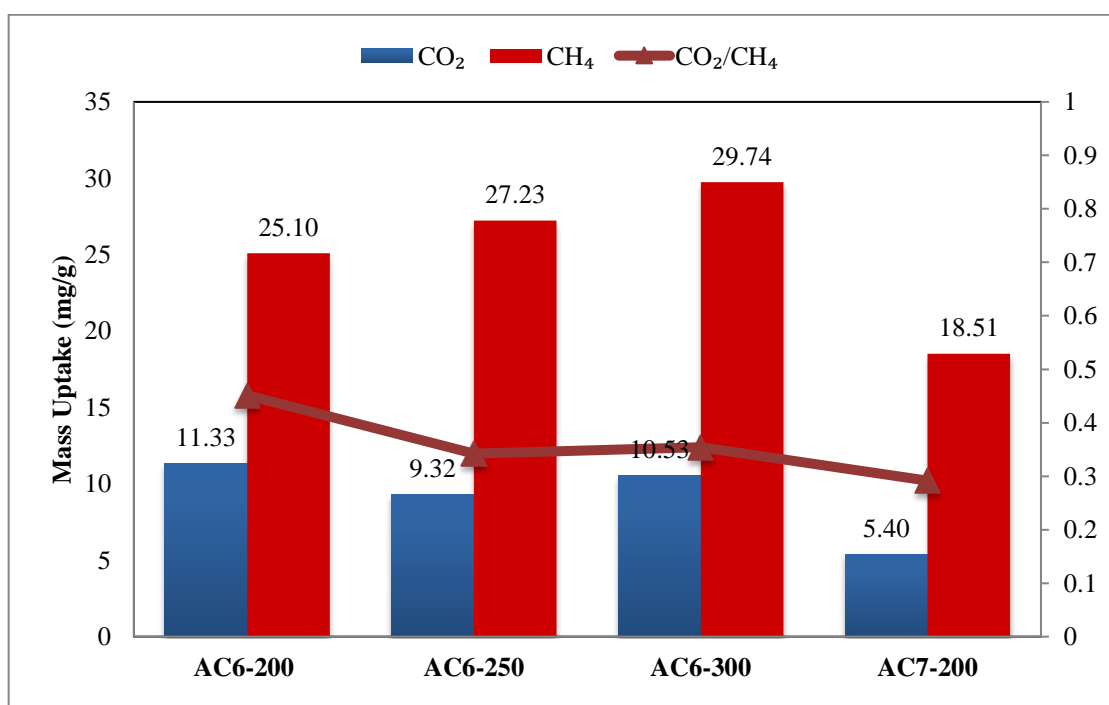


Figure 4.76. Adsorbed amounts of CO₂ and CH₄ on AC6-200 at RT under 5 ml/min CO₂- 45 ml/min CH₄ flow.

In the studies performed under different feed compositions including CO₂ and CH₄, the selective adsorption capacities of NaOH impregnated AC samples pretreated by nitric acid oxidation were also examined. As can be followed from Figure 4.76 and 4.77 as an example, significantly lower mass uptake and CO₂:CH₄ adsorption selectivity were observed on nitric acid oxidized AC7-200 compared to those of its counterpart air oxidized sample AC6-200. The results indicate that air oxidized AC adsorbents were considered as more favorable adsorbents among NaOH impregnated samples. When the performances of AC6 adsorbents calcined at different temperatures were compared, calcination temperature was found not to show any specific trend on adsorption performance as observed under pure CO₂ and pure CH₄ flows; the highest performance in selective adsorption tests was achieved on AC6-200.

4.7.4. High Pressure Adsorption Tests

The results of the high pressure adsorption studies conducted on AC6-200, *which had showed the highest performance among the adsorbents tested*, under different feed

compositions for 0-5000 mbar pressure range, were comparatively analyzed in Figure 4.77 and Figures 4.78-4.80 for its total and selective adsorption capacities, respectively. It was observed that total adsorption ($\text{CO}_2 + \text{CH}_4$) amount, determined by the mass uptake measured by IGA, showed a decreasing trend with the decrease in CO_2 concentration in the feed mixture, which is similar to those observed in studies conducted for 0-1000 mbar pressure.

As can be seen in Figure 4.77; mass uptakes on AC6-200 at the total pressure of 5000 mbar were found to be 16.7% under pure CO_2 flow; 13.5% under 45 CO_2 ml/min-45 ml/min CH_4 (50% CO_2 -50% CH_4) flow; 4.8% under 5 ml/min CO_2 -45 ml/min CH_4 (10% CO_2 -90% CH_4) flow and 3.8% under pure CH_4 flow.

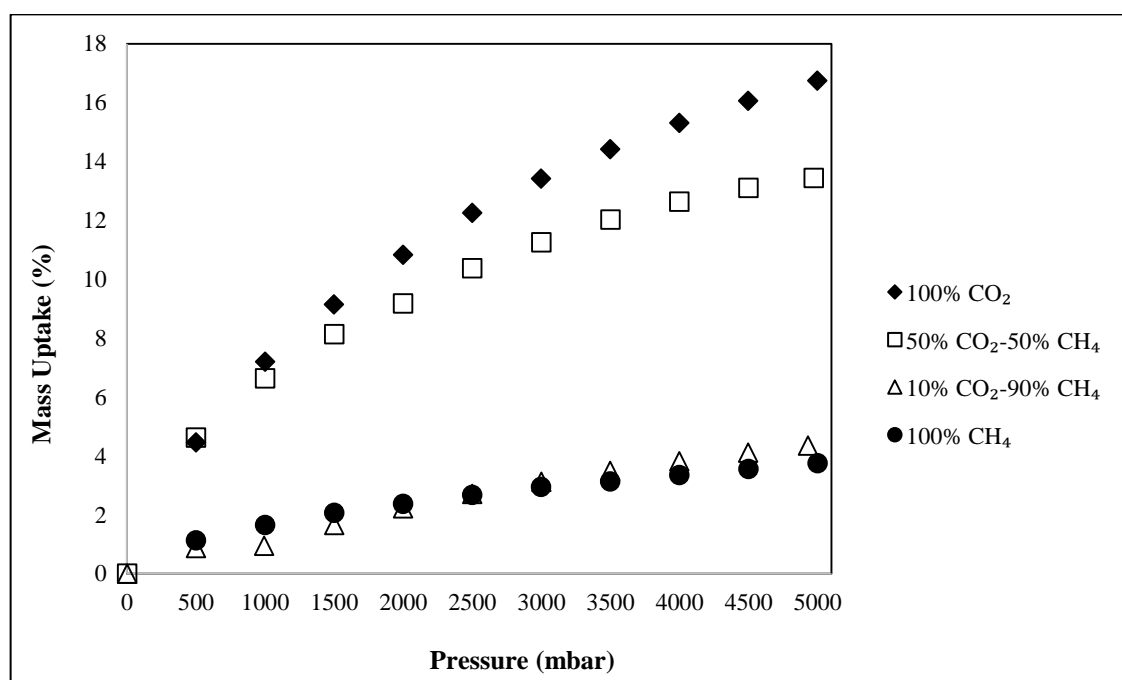


Figure 4.77. Mass uptake (%) on AC6-200 under different feed compositions in the 0-5000 mbar pressure range.

The adsorbed amounts of CO₂ and CH₄ on AC6-200 under 45 ml/min CO₂- 45 ml/min CH₄ feed flow with respect to pressure are presented in Figure 4.78. Selectivity analysis through using IGA-MS data revealed that out of 131.1 mg/g total (CO₂ + CH₄) adsorption; 99.5 mg/g was CO₂ and 31.6 mg/g was CH₄. While the mass ratio of CO₂: CH₄ in the feedstream was 2.75, CO₂: CH₄ mass ratio, i.e. the adsorption selectivity, at 5000 mbar was calculated as 3.15.

Similarly, the adsorbed amounts of CO₂ and CH₄ on AC6-200 under 9 ml/min CO₂ - 81 ml/min CH₄ feed flow with respect to pressure are presented in Figure 4.78. Selectivity analysis through using IGA-MS data revealed that out of 41.1 mg/g total (CO₂ + CH₄) adsorption; 14.4 mg/g was CO₂ and 26.2 mg/g was CH₄. Average CO₂:CH₄ adsorption selectivity on AC6-200 was calculated as 1.1 , while the mass ratio of CO₂:CH₄ in the feed mixture was 0.3.

The CO₂:CH₄ mass uptake ratio data with respect to pressure are shown in Figure 4.80 for two different feed flows, *which had different CO₂:CH₄ ratio (CO₂: CH₄ = 1: 1 and 1: 9 on a flow basis)* in the range 0-5000 mbar. CO₂:CH₄ adsorption ratio profiles, which were obtained under 9 ml/min CO₂-81 ml/min CH₄ feed flow in the range of 0-5000 mbar, were found to be in agreement with the ones obtained in the range of 0-1000 mbar, i.e. there was a decrease in the adsorbed CO₂:CH₄ ratio in comparison to experiments conducted under 50% CO₂-50% CH₄ flow. On the other hand, as it can be followed from Figure 4.80, when the CO₂:CH₄ ratio in the feed was 1, the increase in pressure up to 2000 mbar yielded a fairly constant CO₂:CH₄ adsorption ratio, but made a jump at 2500 mbar then reached a plateau between 2500-5000 mbar. These results indicated that increase in pressure led to an increase in adsorbent-CH₄ interaction more than adsorbent-CO₂ interaction for the tests performed under low CO₂ concentration feeds; while increase in total pressure strengthened adsorbent-CO₂ interaction under the flow of feed having higher CO₂:CH₄ ratio, i.e. high CO₂ concentration favors adsorbent-CO₂ interaction than that between adsorbent-CH₄, leading enhanced, *in the current case fairly stable*, CO₂ adsorption selectivity.

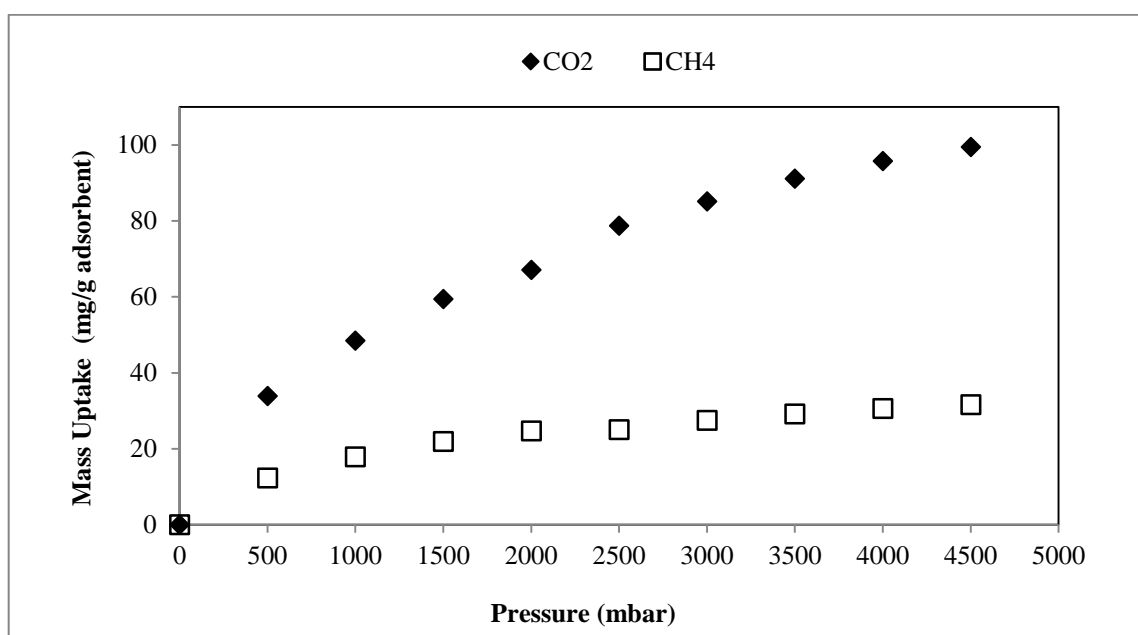


Figure 4.78. Mass uptakes (mg/g adsorbent) of CO₂ and CH₄ on AC6-200 under 45 ml/min CO₂-45 ml/min CH₄ flow (50% CO₂-50% CH₄).

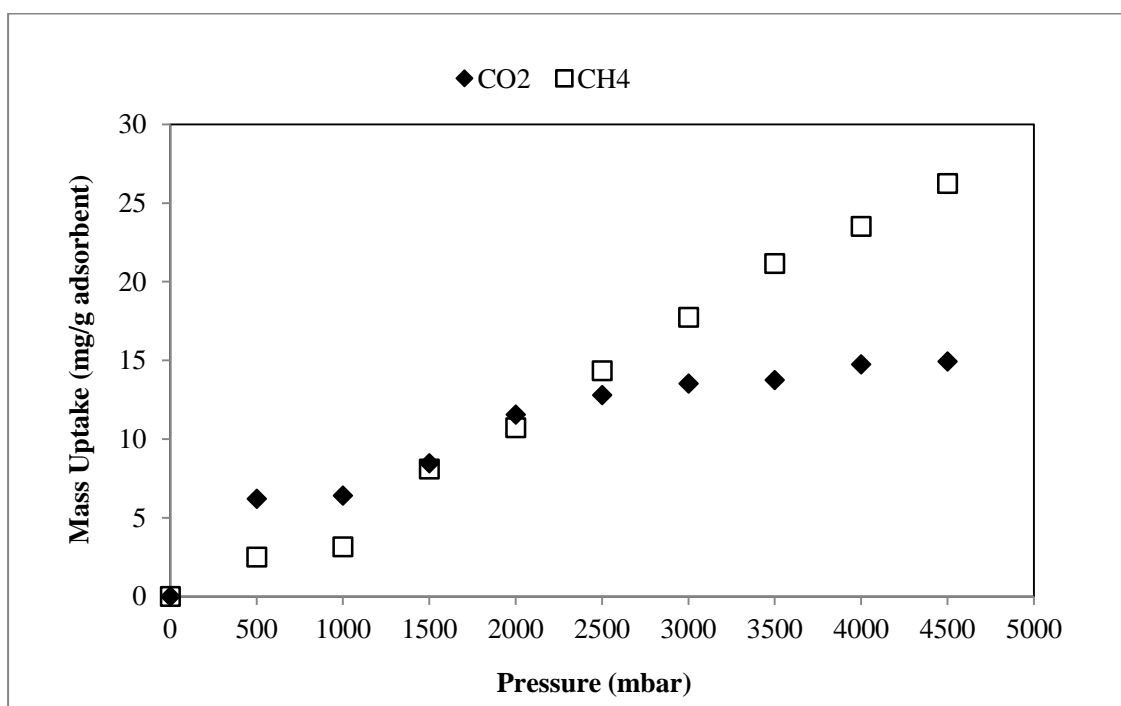


Figure 4.79. Mass uptakes (mg/g adsorbent) of CO₂ and CH₄ on AC6-200 under 9 ml/min CO₂-81 ml/min CH₄ flow (10% CO₂-90% CH₄).

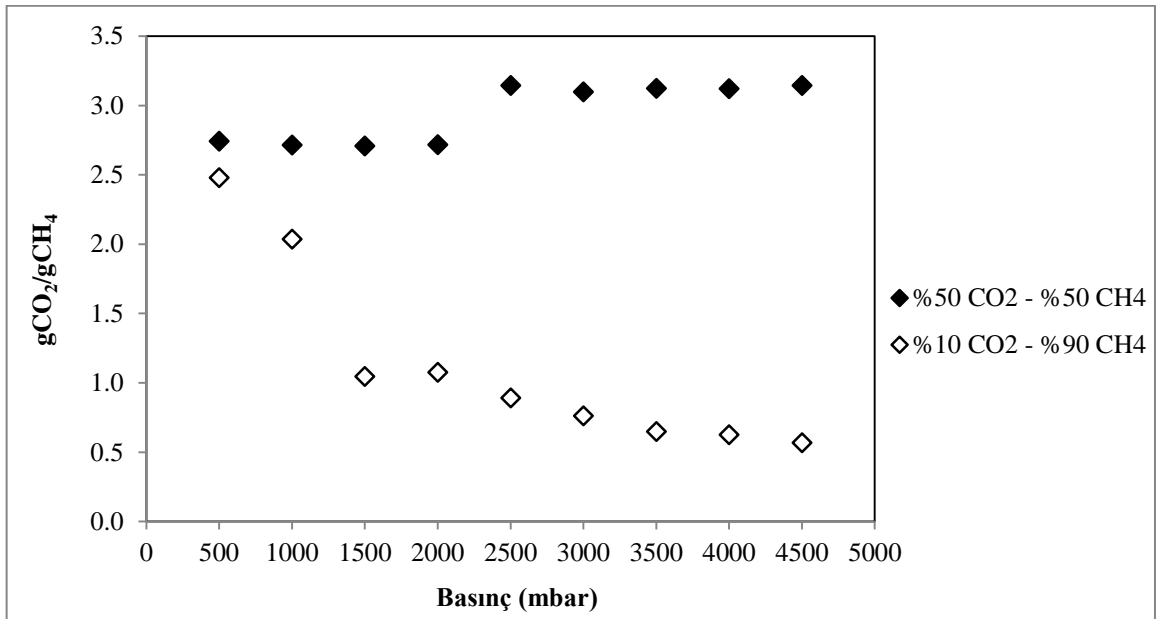


Figure 4.80. The adsorbed mass ratio of CO₂:CH₄ under CO₂-CH₄ mixture feed flows in the pressure range of 0-5000 mbar.

4.7.5. Adsorption Modelling Studies on AC6 and AC7 Adsorbents

As a part of the adsorption modelling studies has been conducted in our group, CO₂ and CH₄ isotherms on AC6 and AC7 samples, which were obtained at RT, 120°C and 200°C under pure CO₂/CH₄ atmosphere, were fitted to Langmuir, Freundlich and Dubinin-Radushkevich (D-R) models as in our previous study (Çağlayan and Aksoylu, 2016) to obtain information on the adsorption mechanism, strength of adsorption and surface properties of the adsorbent.

The simplest theoretical model that can be used to describe monolayer adsorption quantitatively is the Langmuir equation, which assumes a uniform surface, a single layer of adsorbed material and constant temperature. The Langmuir equation may be written as follows:

$$\frac{P}{Q} = \frac{1}{Q_m} P + \frac{1}{bQ_m} \quad (4.16)$$

where Q is the amount adsorbed (mmol/g adsorbent), P is the pressure (mmHg), Q_m is the theoretical monolayer saturation capacity and b is the Langmuir isotherm constant.

The Freundlich equation is an empirical formula which provides a very reasonable description of non-linear adsorption isotherms involving heterogeneous surfaces (multilayer adsorption) can be written in the form:

$$Q = kP^{1/n} \quad (4.17)$$

where k and n are Freundlich constants, which represent adsorption capacity and adsorption intensity, respectively.

Dubinin and Radushkevich describes the adsorption of gases and vapors on microporous adsorbents such as carbons. The Dubinin-Radushkevich (D-R) equation may be written as:

$$\frac{W}{W_0} = \exp \left[- \left(\frac{RT}{E} \ln \left(\frac{P}{P_0} \right) \right)^2 \right] \quad (4.18)$$

where W is the amount of gas adsorbed per unit mass of adsorbent (cm^3/g catalyst), W_0 is micropore capacity (cm^3/g catalyst), R is the universal gas constant (8.315 J/mol K), T is the temperature (K), E is the characteristic energy (J/mol) and P_0 is the saturation pressure (mmHg).

According to the data obtained from regression analysis, Freundlich and D-R models were found more suitable to explain CO_2 adsorption behavior; as expected, it was determined that the Langmuir model based on monolayer adsorption did not explain adsorption behavior on modified activated carbon adsorbents, which are heavily populated with heterogeneous sites. CH_4 adsorption behavior of adsorbents for all the pressure and temperature ranges tested were not well fitted, hence it was determined that they cannot be modeled by using these equations. As examples, Freundlich isotherms ($\log Q$ vs. $\log P$) and D-R isotherms (\ln

W vs. $(\ln P_{\text{sat}}/P)^2$ for CO_2 and CH_4 adsorption over AC6-200 are given in Figures 4.81-4.84.

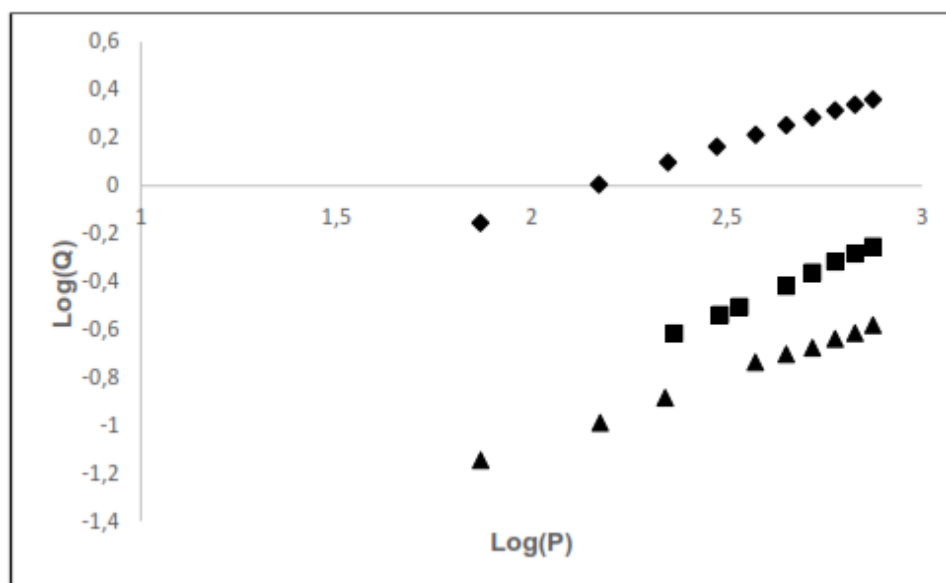


Figure 4.81. Freundlich isotherms for CO_2 adsorption over AC6-200 under different temperatures (\blacklozenge) 25°C, (\blacksquare) 120°C, and (\blacktriangle) 200°C.

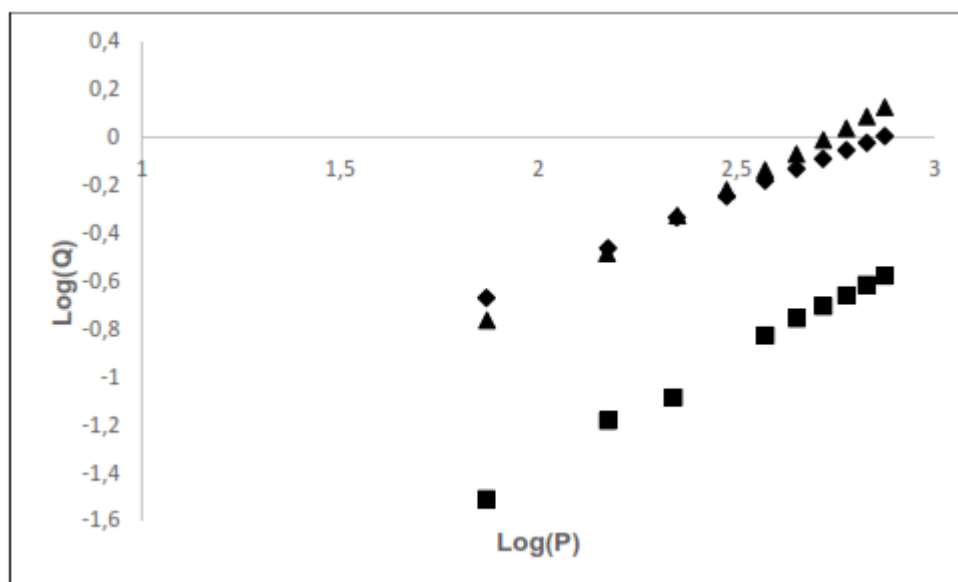


Figure 4.82. Freundlich isotherms for CH_4 adsorption over AC6-200 under different temperatures (\blacklozenge) 25°C, (\blacksquare) 120°C, and (\blacktriangle) 200°C.

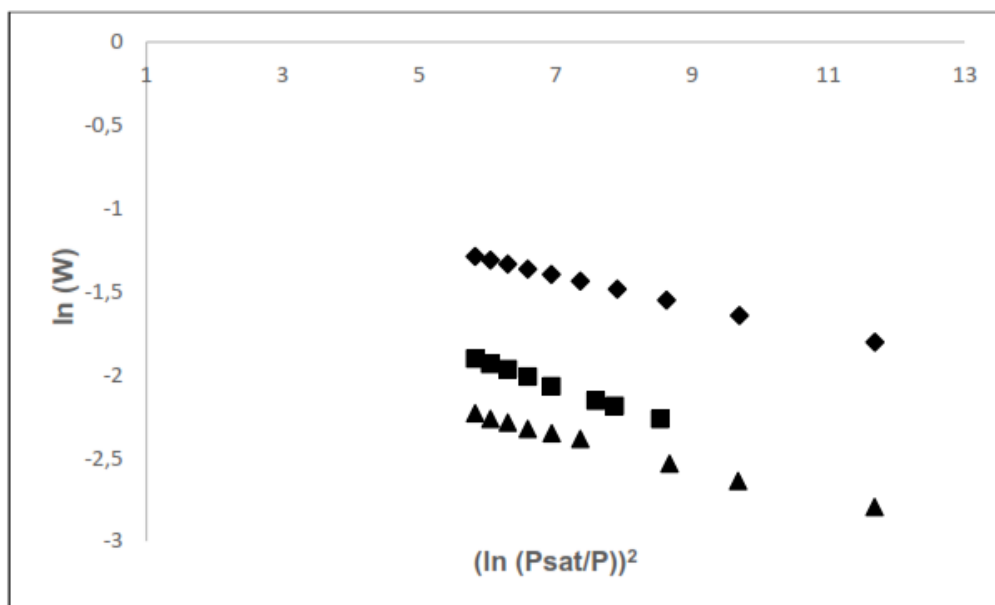


Figure 4.83. D-R isotherms for CO₂ adsorption over AC6-200 under different temperatures (◆) 25°C, (■) 120°C, and (▲) 200°C.

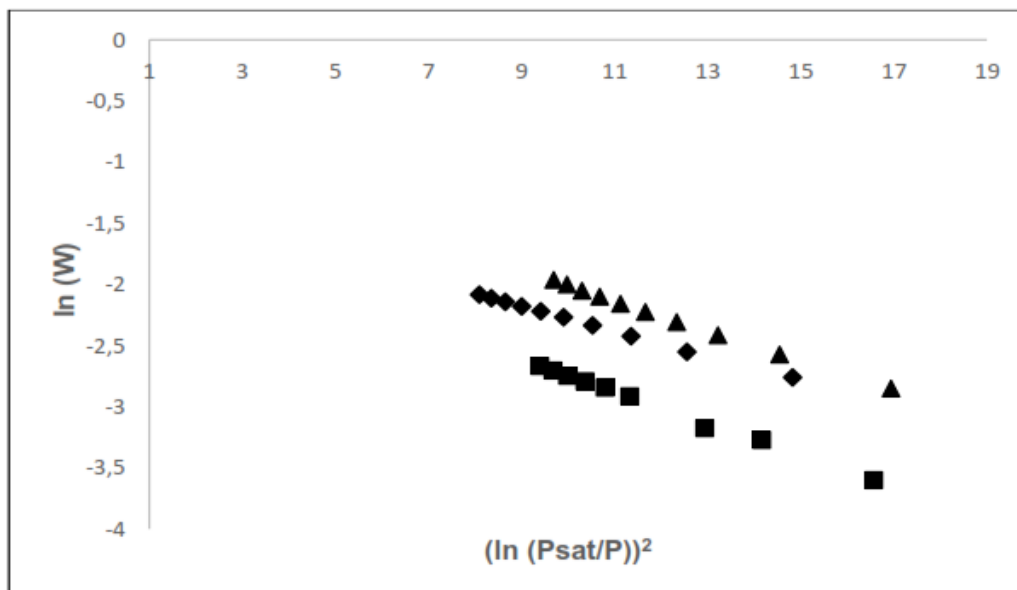


Figure 4.84. D-R isotherms for CH₄ adsorption over AC6-200 under different temperatures (◆) 25°C, (■) 120°C, and (▲) 200°C.

The CO₂ and CH₄ adsorption parameters obtained for identifying the suitability of Langmuir, Freundlich and D-R models to the adsorption behaviour of AC6 and AC7 adsorbents, are presented in Tables 4.4-4.5, Tables 4.6-4.7 and Tables 4.8-4.9, respectively.

Regression analysis results showed that the Langmuir adsorption model can only be used to calculate CO₂ adsorption parameters at room temperature. This result points out the heterogeneous structure of the surfaces of AC6 and AC7 adsorbents, which is consistent with the results of SEM and EDS studies that will be given in the next section.

Theoretical monolayer saturation capacities of the adsorbents, which were obtained via Langmuir model, varied between 2.11-3.50 mmol/g adsorbent range at RT. Langmuir isotherm constants were in the range of 0.0019-0.0060 mmHg⁻¹. In all calculations, the correlation coefficients were greater than 0.99 for the tests conducted at RT. In accordance with the fact that the adsorption rate is negatively affected by temperature rise, the increase in temperature led to a drastic decrease in both Langmuir model parameters calculated (Table 4.4). The validity of the Langmuir isotherm was observed to be broken down easily as the temperature increased.

Table 4.4. Langmuir isotherm parameters for CO₂ adsorption.

Adsorbent	Langmuir Constants (RT)			Langmuir Constants (120°C)			Langmuir Constants (200°C)		
	Q _m	b	R ²	Q _m	b	R ²	Q _m	b	R ²
AC6-200	3.3979	0.0026	0.9916	1.4501	0.0008	0.9732	0.3995	0.0022	0.9050
AC6-250	3.4447	0.0019	0.9915	0.9965	0.0013	0.9549	0.4964	0.0008	0.9765
AC6-300	3.5014	0.0024	0.9915	1.1331	0.0011	0.9638	0.8330	0.0003	0.4628
AC7-200	2.1142	0.0060	0.9919	0.6832	0.0031	0.9944			

Table 4.5. Langmuir isotherm parameters for CH₄ adsorption.

Adsorbent	Langmuir Constants (RT)			Langmuir Constants (120°C)			Langmuir Constants (200°C)		
	Q _m	b	R ²	Q _m	b	R ²	Q _m	b	R ²
AC6-200	1.9646	0.0014	0.9946	1.2026	0.0004	0.4806	0.1511	0.0086	0.9469
AC6-250	6.5488	0.0002	0.4253	2.7609	0.0001	0.0569	0.1886	0.0038	0.9677
AC6-300	3.7064	0.0004	0.9716	0.5438	0.0008	0.4726	-0.1482	-0.0011	0.0096
AC7-200	8.1367	0.0001	0.3442	0.3787	0.0029	0.9863			

The parameters of Freundlich equation obtained for CO₂ adsorption over AC based adsorbents, k and $1/n$, are given in Table 4.6 for different temperatures. All specified parameter values were obtained from graphs of $\log(Q)$ vs. $\log(P)$. An example of this type of graph was given in Figure 4.81 in the case for the CO₂ adsorption over AC6-200 adsorbent. Freundlich model assumes multilayered adsorption and irregular adsorption heat dissipation on the heterogeneous surface (Ma *et al.*, 2011; Shi *et al.*, 2013). As the temperature rose from 25°C to 120°C, the decrease in the k values, which could be considered as the criterion of the adsorption capacity in the specified conditions, showed that the CO₂ adsorption rate on the samples decreased (Mourao *et al.*, 2006; Kilduff and King, 1997). As can be seen in Table 4.6, $1/n$ values stay within the range of 0-1 for all adsorbents, indicating that Freundlich isotherm is suitable for modeling CO₂ adsorption on tabulated samples. In the view of the fact that high $1/n$ values are indication of relatively regular surfaces, it can be said that among the NaOH-impregnated samples, air oxidized adsorbents (AC6 series) have a more regular surface than that of HNO₃-oxidized adsorbents (AC7 series) (Shi *et al.*, 2013).

As the adsorption temperature increases from 25°C to 120°C, the increase in $1/n$ values can be associated with the decrease in surface heterogeneity. As can be seen in Table 4.7, the $1/n$ parameter at all temperature values was in the range of 0-1 only for the AC6-200 adsorbent, even if the regression coefficient values at RT were 0.99 for all the adsorbents. This suggests that the Freundlich isotherm can only be used to model CH₄ adsorption on AC6-200. Using this table, it can be said that the temperature increase from 25°C to 120°C led to a decrease in adsorption rate of CH₄ on AC6-200 as well as a decrease in the surface heterogeneity.

Table 4.6. Freundlich isotherm parameters for CO₂ adsorption.

Adsorbent	Freundlich Constants (RT)			Freundlich Constants (120°C)			Freundlich Constants (200°C)		
	k	1/n	R ²	k	1/n	R ²	k	1/n	R ²
AC6-200	0.0778	0.5126	0.9997	0.0045	0.7279	0.9989	0.0062	0.5643	0.9981
AC6-250	0.0414	0.5946	0.9990	0.0047	0.7097	0.9977	0.0019	0.6887	0.9922
AC6-300	0.0653	0.5401	0.9991	0.0053	0.6914	0.9996	0.0004	0.8876	0.9924
AC7-200	0.1737	0.3527	0.9996	0.0211	0.4752	0.9988			

Table 4.7. Freundlich isotherm parameters for CH₄ adsorption.

Adsorbent	Freundlich Constants (RT)			Freundlich Constants (120°C)			Freundlich Constants (200°C)		
	k	1/n	R ²	k	1/n	R ²	k	1/n	R ²
AC6-200	0.0119	0.6741	0.9990	0.0006	0.9254	0.9967	0.0040	0.8795	0.9997
AC6-250	0.0015	0.9414	0.9901	0.0002	1.0666	0.9747	0.0040	0.5532	0.9226
AC6-300	0.0019	0.9207	0.9952	0.0005	0.9141	0.9644	0.0000	1.0263	0.6989
AC7-200	0.0004	1.0690	0.9906	0.0115	0.4741	0.9997			

Adsorption parameters in D-R equation for each sample were obtained through regression analysis of data fitted to D-R form, as $\ln(W)$ vs. $(\ln(P_{\text{sat}}/P))^2$. The CO₂ and CH₄ adsorption graphs of the AC6-200 sample are presented as an example in Figure 4.83 and 4.84, respectively. The characteristic energy and micropore capacity (W_0) values calculated for each adsorbent based on the adsorption of CO₂ and CH₄ are also listed in Tables 4.8 and 4.9, respectively.

While CO₂ micropore capacity values for all adsorbents were observed to be decreased with temperature, the calculations also showed that air oxidized adsorbents (AC6) had higher micropore adsorption capacities than those prepared with HNO₃ oxidation (AC7), and this finding is in accordance with experimental data. The calculated results revealed that the characteristic energy for the AC7-200 adsorbent was higher than that of the AC6 adsorbents. The value of E is important in terms of providing information about the adsorption mechanism. E values of 8 kJ/mol and below indicate physical adsorption, while E values

between 8-16 kJ/mol indicate ion exchange (Yu and Luo, 2014). Accordingly, the evaluation of available CO₂ adsorption data referred to both validity of physical adsorption mechanisms for all adsorbents in the specified temperature range, and the possibility of simultaneous ion exchange mechanism for the AC7-200 sample. The calculated parameters indicated that the D-R isotherms consisted of one part for all adsorbents examined, i.e., only one micropore size was dominant for each sample (Gil and Grange, 1996).

While evaluating CH₄ adsorption data according to the D-R equation, only the ones with 0.99 regression coefficient in Table 4.9 were taken into account. Accordingly, it was clearly noticed that the micropore capacity of the AC6-200 adsorbent at room temperature for CH₄ gas was very low compared to that of other adsorbents. The high CO₂ selectivity of AC6-200 revealed by the experimental data can be explained by the fact that AC6-200 had a higher microporous capacity calculated for CO₂ than that for CH₄ gas based on the D-R equation.

Table 4.8. Dubinin-Radushkevich (D-R) isotherm parameters for CO₂ adsorption.

Adsorbent	D-R Constants (RT)			D-R Constants (120°C)			D-R Constants (200°C)		
	W ₀ (cc/g)	E (J/mol)	R ²	W ₀ (cc/g)	E (J/mol)	R ²	W ₀ (cc/g)	E (J/mol)	R ²
AC6-200	0.1655	8.3355	0.9988	0.0775	6.7077	0.9974	0.0210	7.9476	0.9959
AC6-250	0.1834	7.7322	0.9996	0.0579	7.0803	0.9974	0.0197	7.1957	0.9897
AC6-300	0.1779	8.1163	0.9995	0.0548	7.1836	0.9950	0.0339	5.8777	0.9879
AC7-200	0.0893	10.0459	0.9989	0.0323	8.6575	0.9982			

Table 4.9. Dubinin-Radushkevich (D-R) isotherm parameters for CH₄ adsorption.

Adsorbent	D-R Constants (RT)			D-R Constants (120°C)			D-R Constants (200°C)		
	W ₀ (cc/g)	E (J/mol)	R ²	W ₀ (cc/g)	E (J/mol)	R ²	W ₀ (cc/g)	E (J/mol)	R ²
AC6-200	0.0540	7.7892	0.9993	0.0359	6.8653	0.9970	0.1615	7.0890	0.9991
AC6-250	0.1335	6.1443	0.9937	0.0530	6.2547	0.9801	0.0070	8.8995	0.9397
AC6-300	0.1376	6.1920	0.9923	0.0320	6.7573	0.9694	0.0035	6.2271	0.6931
AC7-200	0.3671	5.0892	0.9383	0.0096	9.4174	0.9977			

4.7.6. SEM Analysis of Adsorbents

SEM images of AC6-200 and AC6-300, as examples of adsorbents prepared by NaOH impregnation on air oxidized AC, are exhibited in Figure 4.85. Images with an approximate uniformity of NaOH on these adsorbents, which were prepared by using 10% NaOH, were also supported by EDX results giving an average of 5-6% Na⁺. Thin layers were observed over AC6-200 and AC6-300 adsorbents, but became relatively less pronounced with the increase of the heat treatment to 300°C.

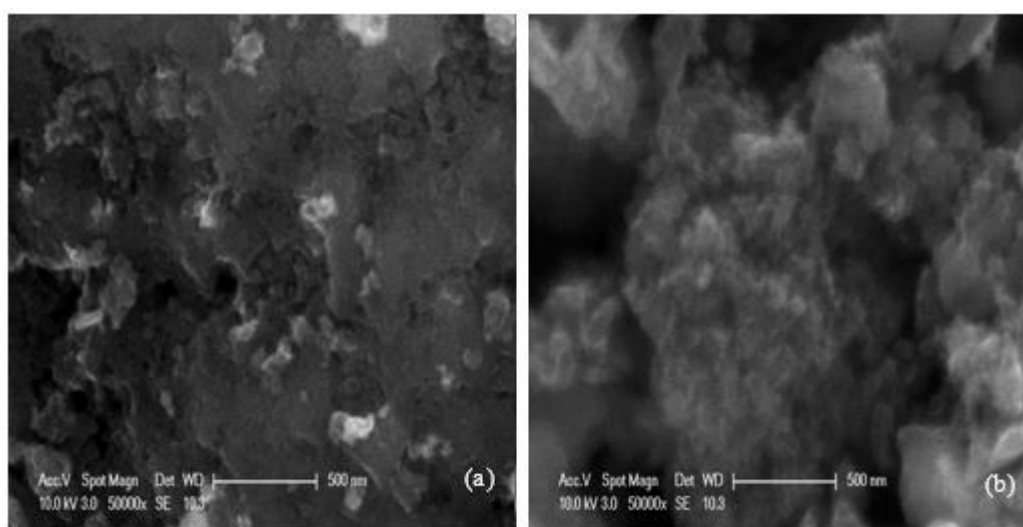


Figure 4.85. SEM images of (a) AC6-200 and (b) AC6-300 adsorbents (x50000).

Back scattering electron images (BSEs) of AC6-200, AC6-250 and AC6-300 adsorbents are presented in Figure 4.86a-c, respectively. As can be seen from the images, NaOH distribution on the surface of AC6-200 was observed to be more homogeneous than that on surfaces of the other adsorbents tested. Significant Na⁺ clusters observed on the surfaces of AC6-250 and AC6-300 were thought as a result of the increase in calcination temperature. In EDX studies performed on these adsorbents, 8-9% Na⁺ concentration obtained in some regions confirms the Na clusters observed in Figure 4.86b-c.

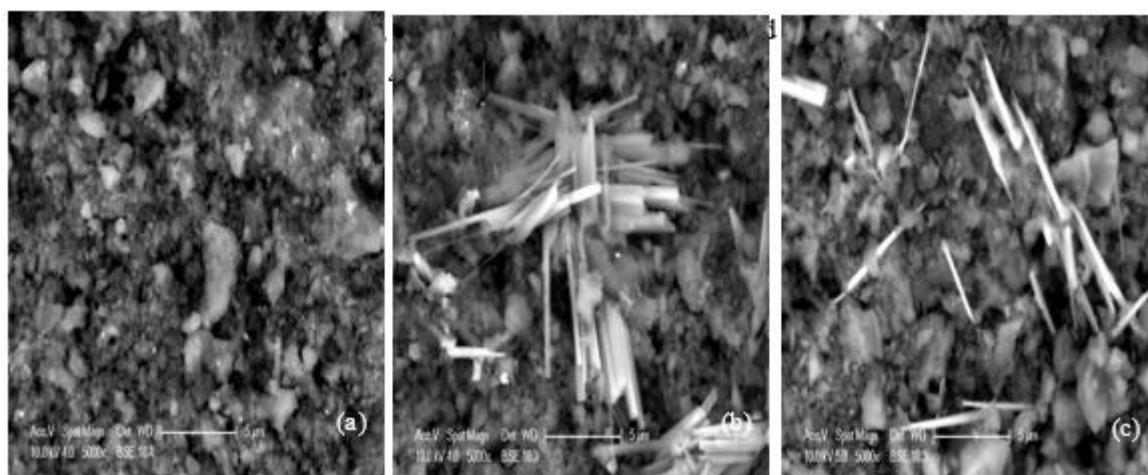


Figure 4.86. BSEs of (a) AC6-200 (b) AC6-250 and (c) AC6-300 adsorbents (x50000).

In Figure 4.87, images of air oxidized AC6-200 adsorbent (Secondary Electron Image *SE*, and Back Scattering Electron Image *BSE*, Figure 4.86a-b) and nitric acid oxidized AC7-200 adsorbent (*SE* and *BSE*, Figure 4.86c-d) are presented. Although they were calcined at the same temperature, the images reveal AC6-200 and AC7-200 have significantly different pore structures and most probably average pore sizes. In the EDX analysis, Na^+ surface loadings on AC6-200 and AC7-200 were determined as 6.24% and 6.05%, respectively.

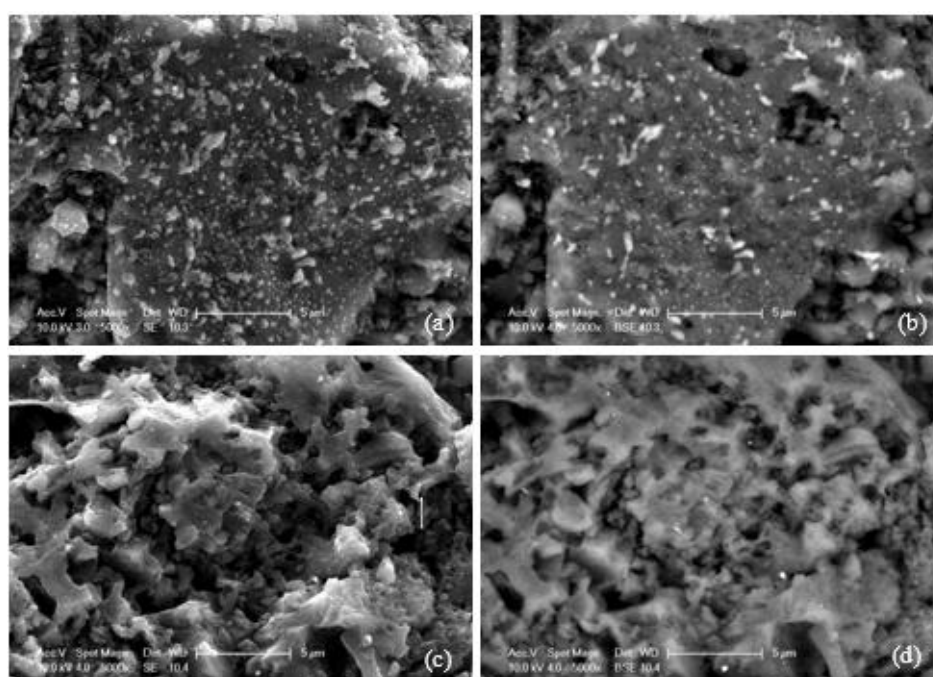


Figure 4.87. SE (a,c) and BSE (b,d) images of AC6-200 and AC7-200 adsorbents (x5000).

4.7.7. BET Surface Area and Total Pore Volume Analysis

Total surface area (TSA) and total pore volume (TPV) of the AC adsorbents were calculated by using BET and Dubinin-Raduskevich methods, respectively. BET surface area and total pore volumes of all alkali modified adsorbents *as well as AC2 and AC3 as reference bases*, are presented in Table 4.10. BET areas and TPVs of AC6 samples were observed to be approximately 2 folds of those of AC7 adsorbents. It was observed that BET areas of NaOH impregnated and calcined AC2 samples (AC6s) have not decreased significantly compared to that of reference AC2. The decrease in the surface areas and also pore volumes after the modification of AC2 adsorbents, are due to the impregnation procedure followed by a calcination period. When AC6 and AC7 adsorbents were compared in their own groups, calcination temperature was found affecting the surface area and pore volume slightly, however results have not shown any trend with increasing temperature. It was also observed that the NaOH impregnation followed by calcination step had a more significant effect on the physical properties of the AC3 samples, leading approximately halved BET area and total pore volume values.

Table 4.10. BET surface areas and total pore volumes of modified AC adsorbents.

Adsorbent	BET Area (m ² /g)	TPV (cm ³ /g)
AC2	1047	0.420
AC3	795.2	0.294
AC6-200	931.6	0.368
AC6-250	882.5	0.353
AC6-300	922.8	0.370
AC7-175	406	0.152
AC7-200	428	0.160
AC7-250	459.5	0.172

Pore size distributions (PSD) of the modified adsorbents are presented in Figure 4.88. The majority of the pores of all adsorbents were found having size between 1-2 nm width range, confirming the microporous character of AC adsorbents. Although all the samples showed similar profiles, AC6 samples have greater number of micropores within the 1-2nm

pore width range. The PSD profiles presented in Figure 4.88 also emphasizes the significant effect of NaOH impregnation and calcination combination on microphysical structure of AC3 samples.

It should be kept in mind that the reason for the difference between TSAs and TPVs of AC2 and AC3 is the different pretreatment procedures applied on the pristine activated carbon during their preparation. In this context, the results show that HNO_3 oxidation pretreatment causes a more significant loss in surface area and pore volume compared to air oxidation.

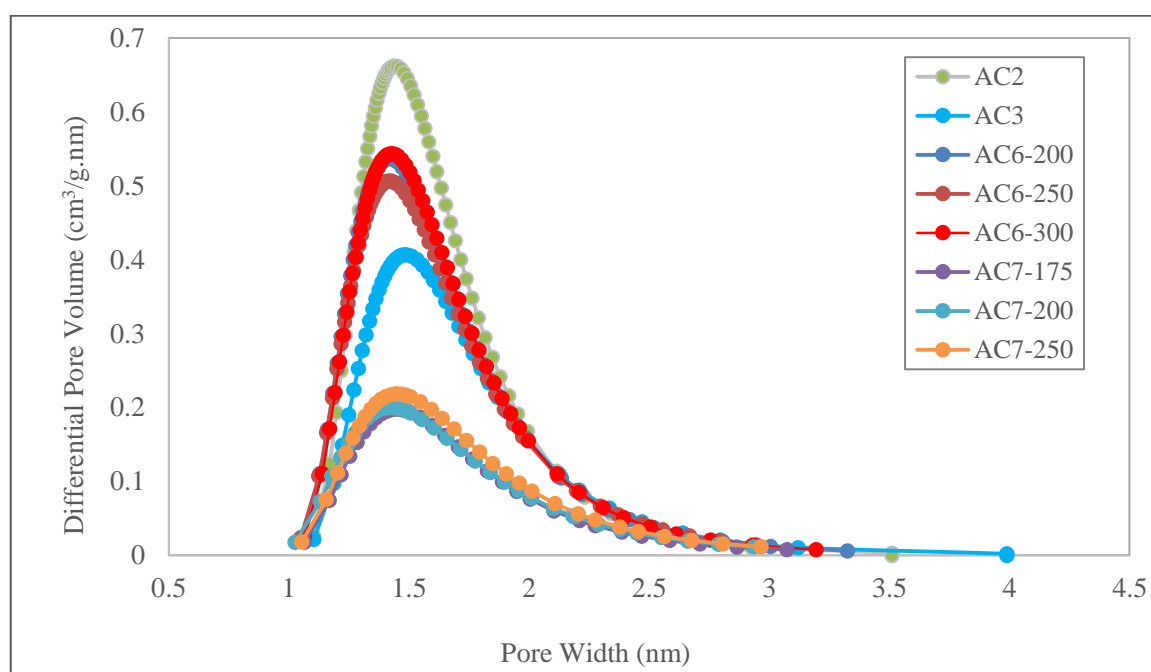


Figure 4.88. Pore size distributions of AC adsorbents.

5. CONCLUSION

5.1. Conclusions

The goal of this research study is to design and develop active, stable and selective alkali promoted Pt-based catalysts and activated carbon-based adsorbents for CO_x elimination to be used in various applications including CO-free hydrogen production via fuel processing and CO₂ removal through pre-combustion technologies.

In this context, individual WGS and serial OSR-WGS reaction performance tests were carried out over the tri-metallic WGS catalyst series, Pt-Re-Na/CeO₂ and Pt-Re-Na/TiO₂. Characterization studies of these catalysts were also carried out via SEM, XPS, XRD and Raman spectroscopy. Metal dispersions of these catalysts were also evaluated via CO pulse experiments. *Operando* FTIR-DRIFTS-MS tests were conducted over selected Pt-Re-Na/CeO₂ catalysts, which gave relatively high and low performance results. Additionally, oxygen storage capacity (OSC) tests were performed over each catalyst in order to obtain a relation between activities and OSCs of the catalysts. Apart from analysis of WGS catalysts, adsorption studies of modified AC based adsorbents were carried out under feed flows with two different compositions at RT, 120°C, and 200°C. The conclusions drawn will be presented in six sections.

In the first part of the study, the purpose was to investigate the WGS performances of trimetallic Pt-Re-Na/CeO₂ and Pt-Re-Na/TiO₂ catalysts under ideal and realistic conditions. The major conclusions obtained from this part are as follows:

- The highest activities under ideal feed #1 ($H_2O/CO=5$) conditions were achieved at 400°C for all the catalysts except 1%Pt-1%Re-2%Na/CeO₂.
- The highest activity under ideal feed #1 conditions, was determined as 81.3% CO conversion over 1%Pt-1%Re-2%Na/CeO₂ at 350°C.

- Under ideal feed #2 ($H_2O/CO=2$) condition, the highest conversion level was achieved over sequentially impregnated 1%Pt-1%Re-1%Na/CeO₂ as 74.9% CO conversion at 400°C.
- Sequential impregnation was found to enhance the catalytic activity of Pt-Re-Na/CeO₂ under both ideal and realistic conditions.
- The effect of Na loading on performance altered with respect to the feed composition used in the performance tests, *i.e. there is an interaction between the effects of Na loading and feed composition.*
- 1%Pt-1%Re-3%Na/CeO₂ catalyst exhibited negligible activity, therefore it was inferred that Na loading has an optimum value in terms of high WGS catalytic activity.
- Catalytic activity of 1%Pt-1%Re-1%Na/CeO₂ was generally determined to be higher than that of TiO₂ supported catalyst under ideal and realistic feed conditions except the condition that the reaction taking place under realistic feed at 400°C.
- Catalytic activities obtained under realistic feed with $H_2O/CO=6.7$, were found to be higher than realistic feed with $H_2O/CO=16.2$, largely affected by CO concentration in the feed stream. The highest activity was found to be achieved over 1%Pt-1%Re-2%Na/CeO₂ as 51.5% CO conversion among performance tests of the catalysts under realistic feed.
- Net H₂ production trends corresponding to each reaction temperature and catalyst composition, were determined to be in accordance with activity results. Maximum net H₂ production was observed as 11.3% at 400°C under realistic feed #1 over 1%Pt-1%Re-2%Na/CeO₂, in accordance with the activity results.
- Sequential impregnation method provided higher CO conversion levels and also net H₂ production values than Re-Na coimpregnation for all temperatures.
- Catalyst activity and selectivity was found to be very sensitive to feed composition, besides reaction temperature.

Secondly, the performance results obtained under real feed conditions are presented. Real conditions were provided by carrying out serial oxidative steam reforming (OSR)-WGS reactions, in which 0.2%Pt-10%Ni/ δ -Al₂O₃ was used as the OSR catalyst and OSR reaction temperature was fixed at 450°C. The following conclusions can be drawn according to the obtained results:

- CO conversion levels obtained in these serial experiments at each temperature were found to be different from the ones in single WGS experiments. This was thought to be most likely due to difference between the H₂O/CO ratio produced at the exit of OSR reactor and the H₂O/CO ratio used in the realistic feed composition in single WGS reactor inlet. This considerable difference also confirmed the importance of serial OSR-WGS reaction tests, which revealed real WGS performance.
- CO conversion values were observed to decrease with temperature increase. Decrease in CO conversion with respect to temperature became more significant at 400°C in the tests conducted under OSR feed composition having relatively lower O/C ratio ($O/C=0.95$) than the one with higher O/C ratio ($O/C=1.33$).
- While single WGS tests conducted at 300°C gave relatively lower CO conversions, contrary trend was observed in serial tests over all catalysts except 1%Pt-1%Re-2%Na/CeO₂. WGS catalyst activities obtained in serial tests with respect to temperature indicated that operation at low temperature was found beneficial for WGS reactor.
- Among the serial OSR-WGS tests carried out, the highest WGS activity was achieved over sequentially impregnated 1%Pt-1%Re-1%Na/CeO₂ at 300°C as 42.1% and at 350°C as 43.0% in terms of CO conversion under OSR feed composition with high O/C ratio ($O/C=1.33$).

In the third part, the freshly reduced and spent forms of Na promoted catalysts were characterized. The major conclusions that can be drawn from this part can be given as follows:

- The absence of platinum, rhenium or sodium peaks in XRD spectra of the catalysts indicates homogeneous distribution of these metals on the surface. On the other hand, peaks corresponding to sodium carbonate species were observed in the spectrum of 1%Pt-1%Re-3%Na/CeO₂. Considering the results obtained in the performance studies, it can be said that sodium carbonate formation causes low catalytic activity for Pt-Re-Na/CeO₂ catalysts.

- In the SEM image of 1% Pt-1% Re-1%Na/TiO₂ catalyst, circular structured particles were observed, whereas the striped structure was encountered in the SEM image of CeO₂ supported catalysts. On the contrary to the catalysts with less Na loading, agglomerated structures were observed on in the catalyst surface with 3% Na loading. Similar structures were also found in the SEM image of the spent catalysts.
- Combining the findings of the Na1s and Ce3d XP spectra of the highly active 1%Pt-1%Re-1%Na/CeO₂ and 1%Pt-1%Re-2%Na/CeO₂ catalysts, it can be suggested that NaO_x species are more influential than CeO_x species in the WGS reaction mechanisms. The interaction of Na and CeO₂ support was thought to be more significant than that between Na and TiO₂ support, indicated by the change in lattice oxygen peak in the spectrum of CeO₂ supported catalysts in contrast to no change observed in case of TiO₂ supported catalyst. Considering the XP spectra of Pt 4f region of the samples, sequential impregnation was thought to provide the formation of active species, however 3% Na loading may have blocked the active Pt sites.
- Sodium carbonate species were also observed in the Raman spectra of spent catalysts which were subjected to RF#1 ($H_2O/CO=6.7$) and RF#2 ($H_2O/CO=16.2$) at 350°C. Re species were thought to be used during reaction, since the peaks associated with these species became smaller in the spectrum of both spent catalysts subjected to RF#1 and RF#2.
- The highest Pt dispersion values were achieved over sequentially impregnated 1%Pt-1%Re-1%Na/CeO₂ and 1%Pt-1%Re-2%Na/CeO₂ catalyst samples, compatible with their higher WGS activity obtained. The results indicated that Na loading higher than 1-2% range lowers the Pt dispersion, probably due to Na species coverage.

Regarding the extreme *-high and low-* WGS performance of the 1%Pt-1%Re-1%Na/CeO₂ and 1%Pt-1%Re-3%Na/CeO₂, those catalysts were characterized *in-situ* and subjected to *operando* WGS tests in FTIR-DRIFTS-MS. The conclusions of this section are as follows:

- Limited WGS activity was observed over CeO₂ support depending on the combined results of the hardly visible peak of the gas phase CO₂ molecule in the spectrum and MS data.

- Prominent peaks of carbonate, formate and carboxyl groups were observed in the spectra of CeO₂ support during CO adsorption. This finding shows that all surface groups formed by CO adsorption on CeO₂ are stable and strongly attached to the surface.
- Formate groups in C-H band, which were observed in the spectra of CeO₂, are not formed over Na containing catalysts. This can point out either the formate groups are not formed over these catalysts or the formate groups generated are used very rapidly.
- Trifold bonded CO molecules were observed having stronger adsorption on the catalyst than linear and bridge bonded CO, as trifold bonded CO remained on the surface after He flush.
- Bidentate formate group formation was determined to become more pronounced with Na addition.
- The significant decrease in intensity of hydrogen carbonate peak in anhydrous media during CO adsorption indicates its active use of in WGS reaction.
- In the spectra of 1%Pt -1% Re-3%Na/CeO₂, formate and carbonate peaks occurred after CO adsorption step did not show any change during He flush and ideal feed condition. While this result is combined with the negligible WGS activity observed via MS, formate and carbonate groups can be pronounced to have contribution to WGS reaction mechanism on Pt-Re-Na/CeO₂ catalysts.

In the fifth section of the results, oxygen storage capacity (OSC) measurements of the samples were performed under *operando* reaction conditions, and a relation between WGS performance and OSCs were tried to be established. The major conclusions of this study can be summarized as follows:

- The highest T-OSC and E-OSC were determined for 1%Pt-1%Re-2%Na/CeO₂ catalyst subjected to DRF#1 ($H_2O/CO=6.7$), however the highest S-OSC was measured for coimpregnated 1%Pt-1%Re-1%Na/CeO₂ sample.
- S-OSC of the TiO₂ supported catalyst was found to be lower than that of the CeO₂ supported catalysts.
- S-OSCs were found to be affected by Na loading of CeO₂ supported catalysts, however not linearly. This result can imply that Na loading has a significant influence on Na-CeO₂ interaction.

- Low E-OSC value of 1%Pt-1%Re-3%Na/CeO₂ catalyst, which refers to low number of renewed oxygen on the surface after used in the reaction is consistent with results of the FTIR-DRIFTS spectra of 1%Pt-1%Re-3%Na/CeO₂ catalyst, over which the carbonate peaks formed during reaction conditions did not disappear with He flush.
- Considering the compatible results obtained in OSC tests conducted under DRF#1 and performance tests conducted under RF#1 conditions; there exists a significant relation between E-OSC and activity. The highest E-OSC was determined over 1%Pt-1%Re-2%Na/CeO₂ sample, which also exhibited the highest WGS activity under these conditions. Similarly, the lowest E-OSC was obtained over 1%Pt-1%Re-3%Na/CeO₂ sample as expected. Catalytic activity and E-OSC relation was also confirmed with the compatible results obtained under DRF#2 and RF#2 ($H_2O/CO=16.2$) except in the case of coimpregnated 1%Pt-1%Re-1%Na/CeO₂ sample.

The last part of the research consists of pure (CO_2 and CH_4) and selective (*for CO_2 - CH_4 mixtures*) adsorption studies over modified activated carbon based adsorbents prepared by subjecting commercial activated carbon to different oxidative, alkali and thermal treatments. Adsorption test results were analyzed through using a new methodology, which was developed for determination of selective adsorption properties of adsorbents under multicomponent mixtures. The following conclusions were drawn:

- A comparative analysis of the adsorption profiles obtained in experiments conducted at different temperatures showed that mass uptake percentage decreased as the temperature increased.
- CO_2 adsorption and desorption profiles indicate that the adsorption of CO_2 on the AC adsorbents is reversible, whereas CH_4 molecules cannot be completely flushed from the adsorbent surface during desorption process.
- Based on the comparative analysis of the mass uptakes (%) of AC6-200 samples under pure CO_2 and pure CH_4 flows, it was concluded that CO_2 adsorption capacity of a sample is more sensitive to temperature increase than its CH_4 adsorption capacity.
- The effect of calcination temperature applied on CO_2 and CH_4 mass uptake values was observed to be insignificant.

- Based on the pure CO₂ and CH₄ adsorption tests; CO₂ mass uptake values on AC7 adsorbents were determined to be lower than that on AC6 adsorbents, i.e. AC7 adsorbents were relatively inexpedient.
- The best performing adsorbent in terms of CO₂ selective adsorption under 25 ml/min CO₂- 25 ml/min CH₄ and 5ml/min CO₂ - 45 ml/min CH₄ flows, was determined as AC6-200.
- Among NaOH impregnated samples, the ones prepared on air oxidized AC were found more favorable adsorbents than those prepared on nitric acid oxidized AC.
- Based on the results of the high pressure range experiments conducted under low CO₂ concentration *including mixture flow*, the increase in adsorbent-CH₄ interaction as a function of pressure was observed more significant than adsorbent-CO₂ interaction. However, under the flow of mixture with higher CO₂:CH₄ ratio, the increase in total pressure strengthened adsorbent-CO₂ interaction relatively more, *i.e. adsorbent-CO₂ interaction was balanced with adsorbent-CH₄ interaction.*
- Based on the D-R equation, air oxidized adsorbents (AC6) were determined to have higher micropore adsorption capacities than those prepared with HNO₃ oxidation (AC7).
- Adsorption performance of the AC adsorbents were found directly related with the BET surface area of the samples.
- Regarding the total surface area and total pore volume analysis of the adsorbents, HNO₃ oxidation pretreatment was determined to cause a more significant loss in surface area and pore volume compared to air oxidation.

5.2. Recommendations

Considering the results of the present study, the following points are thought to be beneficial for the future studies:

- Pt-Na/CeO₂, Na/CeO₂ and Pt/CeO₂ catalysts can be prepared and tested in order to see the role of Re and Na precisely.
- Different real feed conditions obtained in OSR studies can be used in the performance tests of the catalaysts.

- Kinetic studies can be performed over Pt-Re-Na/CeO₂ and Pt-Re-Na/TiO₂ catalysts in order to obtain a reliable power-law type rate expression.
- *Operando* FTIR-DRIFTS-MS studies over coimpregnated 1%Pt-1%Re-1%Na/CeO₂, and sequentially impregnated 1%Pt-1%Re-2%Na/CeO₂ and 1%Pt-1%Re-1%Na/TiO₂ can be carried out, in order to see the effect of impregnation sequence, Na loading and support type on the reaction mechanism.
- Consecutive CO-H₂O pulses can be included in the FTIR-DRIFTS-MS experiments in order to observe the formation of the surface groups clearly.
- Additional OSC tests can be performed for reference systems, like Pt/CeO₂, Re/CeO₂, Na/CeO₂, Pt-Re/CeO₂, Pt-Na/CeO₂ and Re-Na/CeO₂, to form a reliable reference basis/benchmarks in investigating the effect of adding metal or promoter on OSC.
- H₂O vapour can also be introduced to the adsorption system in the selective adsorption tests, as CO₂ selectivity of the adsorbents have crucial importance for wet effluents of the processes.

REFERENCES

- Acar, B., M. S. Başar, B. M. Eropak, B. S. Çağlayan, and A. E. Aksoylu, 2018, “CO₂ Adsorption over Modified AC Samples: A New Methodology for Determining Selectivity”, *Catalysis Today*, Vol. 301, pp. 112-124.
- Ahmed, S., R. Ahluwalia, S. H. D. Lee, and S. Lottes, 2006, “A Gasoline Fuel Processor Designed to Study Quick-Start Performance”, *Journal of Power Sources*, Vol. 154, pp. 214-222.
- Ahmed, S., and M. Krumpelt, 2001, “Hydrogen from Hydrocarbon Fuels for Fuel Cells”, *International Journal of Hydrogen Energy*, Vol. 26, pp. 291–301.
- Andreeva, D., V. Idakiev, T. Tabakova, L. Ilieva, P. Falaras, A. Bourlinos, and A. Travlos, 2002, “Low-Temperature Water-Gas Shift Reaction over Au/CeO₂ Catalysts”, *Catalysis Today*, Vol. 72, pp. 51–57.
- Aneggi, E., M. Boaro, C. Leitenburg, G. Dolcetti, and A. Trovarelli, 2006, “Insights into the Redox Properties of Ceria-Based Oxides and Their Implications in Catalysis”, *Journal of Alloys and Compounds*, Vol. 408–412, pp. 1096–1102.
- Arenillas, A., T. C. Drage, K. Smith, and C. E. Snape, 2005, “CO₂ Removal Potential of Carbons Prepared by Co-pyrolysis of Sugar and Nitrogen Containing Compounds”, *Journal of Analytical and Applied Pyrolysis*, Vol. 74, pp. 298–306.
- Armaroli, T., T. Bécue, and S. Gautier, 2004, “Diffuse Reflection Infrared Spectroscopy (DRIFTS): Application to the in situ Analysis of Catalysts”, *Oil&Gas Science and Technology*, Vol. 59, pp. 215-237.
- Auer, E., A. Freund, J. Pietsch, and T. Tacke, 1998, “Carbons as Supports for Industrial Precious Metal Catalysts”, *Applied Catalysis A: General*, Vol.173, pp. 259-271.

- Avcı, A. K., D. L. Trimm, and Z. I. Önsan, 2002, “Quantitative Investigation of Catalytic Natural Gas Conversion for Hydrogen Fuel Cell Applications”, *Chemical Engineering Journal*, Vol. 90, pp. 77–87.
- Azzam, K. G., I. V. Babich, K. Seshan, and L. Lefferts, 2007, “A Bifunctional Catalyst for the Single-Stage Water–Gas Shift Reaction in Fuel Cell Applications. Part 2. Roles of the Support and Promoter on Catalyst Activity and Stability”, *Journal of Catalysis*, Vol. 251, pp. 163–171.
- Azzam, K. G., I. V. Babich, K. Seshan, and L. Lefferts, 2008 “Role of Re in Pt–Re/TiO₂ Catalyst for Water Gas Shift Reaction: A Mechanistic and Kinetic Study”, *Applied Catalysis B: Environmental*, Vol. 80, pp. 129–140.
- Balsamo, M., T. Budinova, A. Ertoa, A. Lancia, B. Petrova, N. Petrov, and B. Tsyntsarski, 2013, “CO₂ Adsorption onto Synthetic Activated Carbon: Kinetic, Thermodynamic and Regeneration Studies”, *Separation and Purification Technology*, Vol. 116, pp. 214–221.
- Başar, M. S., 2016, *A Study on CO-Free Hydrogen Production and Adsorbent Design for Selective Carbon Dioxide Removal*, Ph.D. Thesis, Boğaziçi University.
- Başar, M. S., B. S. Çağlayan, and A. E. Aksoylu, 2018, “A Study on Catalytic Hydrogen Production: Thermodynamic and Experimental Analysis of Serial OSR-PROX System”, *Fuel Processing Technology*, Vol. 178, pp. 301–311.
- Başar, M. S., H. Bedir, and A. E. Aksoylu, 2016, “Steady state performance analysis of OSR and serial OSR-WGS reactors”, *Fuel Processing Technology*, Vol. 152, pp. 240–249.
- Beaver, M. G., H. S. Caram, and S. Sircar, 2009, “Selection of CO₂ Chemisorbent for Fuel-cell Grade H₂ Production by Sorption-Enhanced Water Gas Shift Reaction”, *International Journal of Hydrogen Energy*, Vol. 34, pp. 2972–2978.

- Belmabkhout, Y., G. D. Weireld, and M. Frere, 2004, “High-Pressure Adsorption Isotherms of N₂, CH₄, O₂, and Ar on Different Carbonaceous Adsorbents”, *Journal of Chemical & Engineering Data*, Vol. 49, pp. 1379-1391.
- Bi, Y., H. Xu, W. Li, and A. Goldbach, 2009, “Water–Gas Shift Reaction in a Pd Membrane Reactor over Pt/Ce_{0.6}Zr_{0.4}O₂ Catalyst”, *International Journal of Hydrogen Energy*, Vol.34, pp. 2965–2971.
- Biniak, S., G. Szymanski, J. Siedlewski, and A. Swiatkowski, 1997, “The Characterization of Activated Carbons with Oxygen and Nitrogen Surface Groups”, *Carbon*, Vol. 35, No. 12, pp. 1799-1810.
- Bo, Z., S. Ahn, M.A. Ardagh, N.M Schweitzer, C. P. Canlas, O. K. Farha, and J. M. Notestein, 2018, “Synthesis and Stabilization of Small Pt Nanoparticles on TiO₂ Partially Masked by SiO₂”, *Applied Catalysis A: General*, Vol. 551, pp. 122-128.
- Boaro, M., M. Vicario, J. Llorca, C. Leitenburg, G. Dolcetti, and A. Trovarelli, 2009, “A Comparative Study of Water Gas Shift Reaction over Gold and Platinum Supported on ZrO₂ and CeO₂–ZrO₂”, *Applied Catalysis B: Environmental*, Vol. 88, pp. 272–282.
- Cai, X., Y. Cai, and W. Lin, 2008, “Autothermal Reforming of Methane over Ni Catalysts Supported over ZrO₂-CeO₂-Al₂O₃”, *Journal of Natural Gas Chemistry*, Vol. 17, pp. 201-207.
- Cameron, D., R. Holliday, and D. Thompson, 2003, “Gold’s Future Role in Fuel Cell Systems”, *Journal of Power Sources*, Vol.118, pp. 298–303.
- Cargnello, M., V. Doan-Nguyen, T. R. Gordon, R. E. Diaz, E. A. Stach, R. J. Gorte, P. Fornasiero, and C. B. Murray, 2013, “Control of Metal Nanocrystal Size Reveals Metal-Support Interface Role for Ceria Catalysts”, *Science*, Vol. 341, pp. 771-773.

- Chen, Y., J. Cheng, P. Hu, H. Wang, 2008, "Examining the Redox and Formate Mechanisms for Water–Gas Shift Reaction on Au/CeO₂ using density functional theory", *Surface Science*, Vol. 602, pp. 2828–2834.
- Choung S. Y., M. Ferrandon, and T. Krause, 2005, "Pt-Re Bimetallic Supported on CeO₂-ZrO₂ Mixed Oxides as Water–Gas Shift Catalysts", *Catalysis Today*, Vol. 99, pp. 257–262.
- Colussi, S., L. Katta, F. Amoroso, R. J. Farrauto, and A. Trovarelli, 2014, "Ceria-Based Palladium Zinc Catalysts as Promising Materials for Water Gas Shift Reaction", *Catalysis Communications*, Vol. 47, pp. 63-66.
- Cormos C. C., 2011, "Hydrogen Production from Fossil Fuels with Carbon Capture and Storage Based on Chemical Looping Systems", *International Journal of Hydrogen Energy*, Vol. 36, pp. 5960-5971.
- Cornaglia, C. A., J. F. Múnera, L. M. Cornaglia, E. A. Lombardo, P. Ruiz, and A. Karelavic, 2012, "Effect of the Support on the Catalytic Stability of Rh Formulations for the Water–Gas Shift Reaction", *Applied Catalysis A: General*, Vol. 435–436, pp. 99–106.
- Corti, C. W., R. J. Holliday, and D. T. Thompson, 2005, "Commercial Aspects of Gold Catalysis", *Applied Catalysis A: General*, Vol. 291, pp. 253–261.
- Cybulskis, V. J., J. Wang, J. H. Pazmino, F. H. Ribeiro, and N. Delgass, 2016, "Isotopic Transient Studies of Sodium Promotion of Pt/Al₂O₃ for the Water-Gas Shift Reaction", *Journal of Catalysis*, Vol. 339, pp. 163-172.
- Çağlayan, B. S., 2011, *Design and Development of Catalysts & Adsorbents for CO_x free H₂ Production*, Ph.D. Thesis, Boğaziçi University.
- Çağlayan, B.S., and A. E. Aksoylu, 2009, "Water-Gas Shift Reaction over Bimetallic Pt-Ni/Al₂O₃ Catalysts", *Turkish Journal of Chemistry*, Vol.33, pp. 249–256.

- Çağlayan, B. S., and A. E. Aksoylu, 2011, “Water–Gas Shift Activity of Ceria Supported Au–Re Catalysts”, *Catalysis Communications*, Vol.12, pp. 1206–1211.
- Çağlayan, B. S., and A. E. Aksoylu, 2013, “CO₂ Adsorption on Chemically Modified Activated Carbon”, *Journal of Hazardous Materials*, Vol. 252– 253, pp. 19– 28.
- Çağlayan, B. S., and A. E. Aksoylu, 2016, “CO₂ Adsorption Behavior and Kinetics on Chemically Modified Activated Carbons”, *Turkish Journal of Chemistry*, Vol. 40, pp. 576-587.
- Çağlayan, B. S., A. K. Avcı, Z. İ. Önsan, and A. E. Aksoylu, 2005, “Production of Hydrogen over Bimetallic Pt–Ni/ δ -Al₂O₃: I. Indirect Partial Oxidation of Propane”, *Applied Catalysis A: General*, Vol. 280, pp. 181–188.
- Dali, A. M., A. S. Ibrahim, and A. Hadi, 2012, “General Study about Activated Carbon for Adsorption Carbon Dioxide”, *Journal of Purity, Utility Reaction and Environment*, Vol. 1 No. 5, pp. 206-221.
- Dandekar, A., R. T. K. Baker, and M. A. Vannice, 1998, “Characterization of Activated Carbon, Graphitized Carbon Fibers and Synthetic Diamond Powder Using TPD and DRIFTS”, *Carbon* Vol. 36, pp. 1821–1831.
- Darmstadt, H., and C. Roy, 2003, “Surface Spectroscopic Study of Basic Sites on Carbon Blacks”, *Carbon*, Vol. 41, pp. 2662–2665.
- Dongil, A.B., L. Pastor-Pérez, A. Sepúlveda-Escribano, and P. Reyes, 2015, “Promoter Effect of Sodium in Graphene-Supported Ni and Ni–CeO₂ Catalyst for the Low-Temperature WGS Reaction”, *Applied Catalysis A: General*, Vol. 505, pp. 98–104.
- Duarte de Farias, A. M., P. Bargiela, M.C. Rocha, and M. A. Fraga, 2008, “Vanadium-Promoted Pt/CeO₂ Catalyst for Water–Gas Shift Reaction”, *Journal of Catalysis*, Vol. 260, pp. 93–102.

- Duprez, D., C. Descorme, T. Birchem, and E. Rohart, 2001, "Oxygen Storage and Mobility on Model Three-Way Catalysts", *Topics in Catalysis*, Vol. 16-17, pp. 1–4.
- El-Moemen, A. A., A. Karpenko, Y. Denkwitz, and R. J. Behm, 2009, "Activity, Stability and Deactivation Behavior of Au/CeO₂ Catalysts in the Water Gas Shift Reaction at Increased Reaction Temperature (300 °C)", *Journal of Power Sources*, Vol. 190, pp. 64–75.
- Ersöz, A., H. Olgun, and S. Özdoğan, 2006, "Reforming Options for Hydrogen Production from Fossil Fuels for PEM fuel cells", *Journal of Power Sources*, Vol. 154, pp. 67-73.
- Eysel, H. H., and S. Thym, 1975, "Raman Spectra of Peroxides", *Zeitschrift für anorganische und allgemeine Chemie*, Vol. 411, pp. 97-192.
- Ghenciu, A.F., 2002, "Review of Fuel Processing Catalysts for Hydrogen Production in PEM Fuel Cell Systems", *Current Opinion in Solid State and Materials Science*, Vol. 6, pp. 389-399.
- García, S., M. V. Gil, C. F. Martín, J. J. Pis, F. Rubiera, and C. Pevida, 2011, "Breakthrough Adsorption Study of a Commercial Activated Carbon for Pre-combustion CO₂ Capture", *Chemical Engineering Journal*, Vol.171, pp. 549–556.
- Gil, A., and P. Grange, 1996, "Application of the Dubinin-Radushkevich and Dubinin-Astakhov Equations in the Characterization of Microporous Solids", *Colloids and Surfaces A*, Vol. 113, pp. 39-50.
- Goguet, A., D. Tibiletti, F. Meunier, J. Breen, and R. Burch, 2004, "Spectrokinetic Investigation of Reverse Water-Gas Shift Reaction Intermediates over a Pt/CeO₂ Catalyst", *Journal of Physical Chemistry B*, Vol. 108, pp. 20240-20246.
- Gomes, V.G., and K. W. K. Yee, 2002, "Pressure Swing Adsorption for Carbon Dioxide Sequestration from Exhaust Gases", *Separation and Purification Technology*, Vol. 28, pp. 161–171.

- Gonzalez Castaño, M., T. R. Reina, S. Ivanova, M. A. Centeno, and J. A. Odriozola, 2014, “Pt vs. Au in Water–Gas Shift Reaction”, *Journal of Catalysis*, Vol. 314, pp. 1-9.
- Gökaliler, F., 2012, *Characterization and Performance Analysis of Fuel Flexible OSR-WGS Catalysts*, Ph.D. Thesis, Boğaziçi University.
- Gökaliler, F., B. A. Göçmen, and A. E. Aksoylu, 2008, “The effect of Ni:Pt ratio on oxidative steam reforming performance of Pt–Ni/Al₂O₃ catalyst”, *International Journal of Hydrogen Energy*, Vol. 33, pp. 4358 – 4366.
- Gökaliler, F., Z. I. Önsan, and A. E. Aksoylu, 2013, “Power-law Type Rate Expression for WGS Reaction over Au–Re/CeO₂ Catalyst under Realistic Fuel Processor Conditions”, *Catalysis Communications*, Vol.39, pp.70–73.
- Grande, C. A., R. Blom, A. Möller, and J. Möllmer, 2013, “High-Pressure Separation of CH₄/CO₂ Using Activated Carbon”, *Chemical Engineering Science*, Vol.89, pp.10–20.
- Guerrero, S., I. Guzmán, G. Aguila, B. Chornik, and P. Araya, 2012, “Study of Na/Cu/TiO₂ Catalysts for the Storage and Reduction of NO”, *Applied Catalysis B: Environmental*, Vol. 123– 124, pp. 282– 295.
- Gupta, R. B., 2009, *Hydrogen Fuel: Production, Transport, and Storage*, CRC Press, Florida.
- Hagh, B. F., 2004, “Stoichiometric Analysis of Autothermal Fuel Processing”, *Journal of Power Sources*, Vol. 130, pp. 85-94.
- Haruta, M., 1997, “Size and Support Dependency in the Catalysis of Gold”, *Catalysis Today*, Vol. 36, pp.153-166.

- Holmgren, A., B. Andersson, and D. Duprez, 1999, "Interactions of CO with Pt/Ceria Catalysts", *Applied Catalysis B: Environmental*, Vol. 22, pp. 215–230.
- Hsiao, H. Y., C. M. Huang, M. Y. Hsu, and H. Chen, 2011, "Preparation of High-Surface-Area PAN-based Activated Carbon by Solution-Blowing Process for CO₂ Adsorption", *Separation and Purification Technology*, Vol. 82, pp. 19–27.
- Hu, Y., and E. Ruckenstein, 2004, "Catalytic Conversion of Methane to Synthesis Gas by Partial Oxidation and CO₂ Reforming", *Advances in Catalysis*, Vol. 48, pp. 297-345.
- Hwang, K., J. Park, and S. Ihm, 2011, "Si-Modified Pt/CeO₂ Catalyst for a Single-Stage Water-Gas Shift Reaction", *International Journal of Hydrogen Energy*, Vol. 36, pp. 9685-9693.
- Jacobs, G., R. A. Keogh, and B. H. Davis, 2007, "Steam Reforming of Ethanol over Pt/Ceria with CO-Fed Hydrogen", *Journal of Catalysis*, Vol. 245, pp. 326-337.
- Jacobs, G., L. Williams, U. Graham, G. A. Thomas, D. E. Sparks, and B. H. Davis, 2003, "Low Temperature Water–Gas Shift: in-situ DRIFTS-Reaction Study of Ceria Surface Area on The Evolution of Formats on Pt/CeO₂ Fuel Processing Catalysts for Fuel Cell Applications", *Applied Catalysis A: General*, Vol. 252, pp. 107–118.
- Jang, D. I., and S. J. Park, 2012, "Influence of Nickel Oxide on Carbon Dioxide Adsorption Behaviors of Activated Carbons", *Fuel*, Vol. 102, pp. 439–444.
- Kai, L., W. Xuezhong, Z. Zexing, W. Xiaodong, and W. Duan, 2007, "Oxygen Storage Capacity of Pt-, Pd-, Rh/CeO₂-Based Oxide Catalyst", *Journal of Rare Earths*, Vol. 25, pp. 6-10.
- Kakuta, N., N. Morishima, M. Kotobuki, T. Iwase, T. Mizushima, Y. Sato, and S. Matsuura, 1997, "Oxygen Storage Capacity (OSC) of Aged Pt/CeO₂/Al₂O₃ Catalysts: Roles of Pt and CeO₂ Supported on Al₂O₃", *Applied Surface Science*, Vol. 121-122, pp. 408-412.

- Kalamaras, C. M., G. G. Olympiou, and A. M. Efstathiou, 2008, “The Water-Gas Shift Reaction on Pt/ γ -Al₂O₃ Catalyst: Operando SSITKA-DRIFTS-Mass Spectroscopy Studies”, *Catalysis Today*, Vol.138, pp. 228–234.
- Kalamaras, C. M., S. Americanou, and A. M. Efstathiou, 2011, “Redox vs Associative Formate with –OH Group Regeneration, WGS Reaction Mechanism on Pt/CeO₂: Effect of Platinum Particle Size”, *Journal of Catalysis*, Vol. 279, pp. 287–300.
- Kalamaras, C. M., D. D. Dionysiou, and A. M. Efstathiou, 2012, “Mechanistic Studies of the Water–Gas Shift Reaction over Pt/Ce_xZr_{1-x}O₂ Catalysts: The Effect of Pt Particle Size and Zr Dopant”, *ACS Catalysis*, Vol. 2, pp. 2729–2742.
- Kichanov, S.E., D.P. Kozlenko, J. Wasicki, L.S. Dubrovinsky, P. Czarnecki, W. Nawrocik, B.N. Savenko, D.K. Pogoreliy, and K.M. Podurets, 2009, “Structural Phase Transitions and Raman Spectra of Pyridinium Perrhenate at High Pressures”, *Journal of Molecular Structure*, Vol. 921, pp. 68–71.
- Kilduff, J. E., and C. J. King, 1997, “Effect of Carbon Adsorbent Surface Properties on the Uptake and Solvent Regeneration of Phenol”, *Industrial and Engineering Chemistry Research*, Vol. 36, pp. 1603-1613.
- Kim, B. J., K. S. Cho, and S. J. Park, 2010, “Copper Oxide-Decorated Porous Carbons for Carbon Dioxide Adsorption Behaviors”, *Journal of Colloid and Interface Science*, Vol. 342, pp. 575–578.
- Kugai, J., E. B. Fox, and C. Song, 2015, “Kinetic Characteristics of Oxygen-Enhanced Water Gas Shift on CeO₂-Supported Pt-Cu and Pd-Cu Bimetallic Catalysts”, *Applied Catalysis A: General*, Vol. 497, pp. 31-41.
- Lee, S. Y., and S. J. Park, 2013, “Determination of the Optimal Pore Size for Improved CO₂ Adsorption in Activated Carbon Fibers”, *Journal of Colloid and Interface Science*, Vol. 389, pp. 230–235.

- Lenarda, A., M. Bellini, A. Marchionni, H. A. Miller, T. Montini, M. Melchionna, F. Vizza, M. Prato, and P. Fornasiero, 2018, “Nanostructured Carbon Supported Pd-Ceria as Anode Catalysts for Anion Exchange Membrane Fuel Cells Fed with Polyalcohols”, *Inorganica Chimica Acta*, Vol. 470, pp. 213-220.
- Leppelt, R., B. Schumacher, V. Plzak, M. Kinne, and R. J. Behm, 2006, “Kinetics and Mechanism of the Low-Temperature Water–Gas Shift Reaction on Au/CeO₂ Catalysts in an Idealized Reaction Atmosphere”, *Journal of Catalysis*, Vol. 244, pp. 137–152.
- Li, C., K. Sivaranjani, and J. M. Kim, 2016, “Synthesis of Alkali Promoted Mesoporous, Nanocrystalline Pd/TiO₂ Catalyst for Water Gas Shift Reaction”, *Catalysis Today*, Vol. 265, pp. 45–51.
- Li, C., S. Yoshihisa, A. Toru, K. Domen, M. Ken-ichi, and O. Takaharu, 1989, “Carbon Monoxide and Carbon Dioxide Adsorption on Cerium Oxide Studied by Fourier-Transform Infrared Spectroscopy”, *Journal of Chemical Society*, Vol. 85, pp. 929-943.
- Li, H., Y. Bi, J. Yan, L. Zhang, and X. Yin, 2013, “Bulk Oxygen Promoted Water–Gas Shift Reaction Activity over Pt/Ce_{0.6}Zr_{0.4}O₂ catalyst”, *Catalysis Communications*, Vol. 42, pp. 45–49.
- Li, J., Y. Han, Y. Zhu, and R. Zhou, 2011, “Purification of Hydrogen from Carbon Monoxide for Fuel Cell Application over Modified Mesoporous CuO–CeO₂ Catalysts”, *Applied Catalysis B: Environmental*, Vol. 108-109, pp. 72-80.
- Li, L., P. A. Quinlivan, and D. R. U. Knappe, 2002, “Effects of Activated Carbon Surface Chemistry and Pore Structure on the Adsorption of Organic Contaminants from Aqueous Solution”, *Carbon*, Vol. 40, pp. 2085–2100.

- Li, P., X. Chen, Y. Li, and J. W. Schwank, 2019, “A Review on Oxygen Storage Capacity of CeO₂-Based Materials: Influence Factors, Measurement Techniques, and Applications in Reactions Related to Catalytic Automotive Emissions Control”, *Catalysis Today*, Vol. 327, pp. 90–115.
- Liu, H., D. Yang, Z. Zheng, X. Ke, E. Waclawik, H. Zhu, and R. L. Frost, 2010, “A Raman Spectroscopic and TEM Study on the Structural Evolution of Na₂Ti₃O₇ during the Transition to Na₂Ti₆O₁₃”, *Journal of Raman Spectroscopy*, Vol. 41, pp. 1331-1337.
- Lozano-Castello, D., D. Cazorla-Amorós, A. Linares-Solano, and D. F. Quinn, 2002, “Micropore Size Distributions of Activated Carbons and Carbon Molecular Sieves Assessed by High-Pressure Methane and Carbon Dioxide Adsorption Isotherms”, *Journal of Physical Chemistry B*, Vol. 106, pp. 9372-9379.
- Lu, G., S. L. Bernasek, and J. Schwartz, 2000, “Oxidation of a Polycrystalline Titanium Surface by Oxygen and Water”, *Surface Science*, Vol. 458, pp. 80–90.
- Ma, L., C. Y. Seo, X. Chen, J. Li, and J. W. Schwank, 2018, “Sodium-Promoted Ag/CeO₂ Nanospheres for Catalytic Oxidation of Formaldehyde”, *Chemical Engineering Journal*, Vol. 350, pp. 419–428.
- Ma, Z. H., Q. Li, Q. Y. Yue, B. Y. Gao, W. H. Li, and X. Xu, 2011, “Adsorption Removal of Ammonium and Phosphate from Water by Fertilizer Controlled Release Agent Prepared from Wheat Straw”, *Chemical Engineering Journal*, Vol. 171, pp. 1209–1217.
- Maroto-Valer, M. M., Z. Tang, and Y. Zhang, 2005, “CO₂ Capture by Activated and Impregnated Anthracites”, *Fuel Processing Technology*, Vol. 86, pp. 1487 – 1502.
- Martin, C. F., M. G. Plaza, J. J. Pis, F. Rubiera, C. Pevida, and T. A. Centeno, 2010, “On the Limits of CO₂ Capture Capacity of Carbons”, *Separation and Purification Technology* Vol. 74, pp. 225–229.

- Martínez-Huerta, M. V., J. M. Coronado, M. Fernández-García, A. Iglesias-Juez, G. Deo, J. L. G. Fierro, and M. A. Bañares, 2004, “Nature of the Vanadia–Ceria Interface in V^{5+}/CeO_2 Catalysts and Its Relevance for the Solid-State Reaction toward $CeVO_4$ and Catalytic Properties”, *Journal of Catalysis*, Vol. 225, pp. 240-248.
- Meunier, F.C., A. Goguet, C. Hardacre, R. Burch, and D. Thompsett, 2007, “Quantitative DRIFTS Investigation of Possible Reaction Mechanisms for the Water–Gas Shift Reaction on High-Activity Pt- and Au-based Catalysts”, *Journal of Catalysis*, Vol. 252, pp. 18–22.
- Meunier, F.C., D. Reid, A. Goguet, S. Shekhtman, C. Hardacre, R. Burch, W. Deng, and M. Flytzani-Stephanopoulos, 2007, “Quantitative Analysis of the Reactivity of Formate Species Seen by DRIFTS over a $Au/Ce(La)O_2$ Water-Gas Shift Catalyst: First Unambiguous Evidence of the Minority Role of Formates as Reaction Intermediates”, *Journal of Catalysis*, Vol. 247, pp. 277-287.
- Mhadeshwar, A.B., and D.G. Vlachos, 2005, “Is the Water–Gas Shift Reaction on Pt Simple? Computer-Aided Microkinetic Model Reduction, Lumped Rate Expression, and Rate-Determining Step”, *Catalysis Today*, Vol.105, pp. 162.
- Min, P., S. Zhang, Y. Xu, and R. Li, 2018, “Enhanced Oxygen Storage Capacity of CeO_2 with Doping-Induced Unstable Crystal Structure”, *Applied Surface Science*, Vol. 448, pp. 435–443.
- Moraes, T. S., R. C. R. Neto, M. C. Ribeiro, L. V. Mattos, M. Kourtelesis, S. Ladas, X. Verykios, F. B. Noronha, 2016, “Ethanol conversion at low temperature over CeO_2 —Supported Ni-based catalysts. Effect of Pt addition to Ni catalyst”, *Applied Catalysis B: Environmental*, Vol. 181, pp. 754–768.
- Moreno, M., G. T. Baronetti, M. A. Laborde, and F. J. Mariño, 2008, “Kinetics of Preferential CO Oxidation in H_2 Excess (COPROX) over CuO/CeO_2 Catalysts”, *International Journal of Hydrogen Energy*, Vol.33, pp. 3538-3542.

- Morikawa, A., K. Kikuta, A. Suda, and H. Shinjo, 2009, "Enhancement of Oxygen Storage Capacity by Reductive Treatment of Al_2O_3 and $\text{CeO}_2\text{-ZrO}_2$ Solid Solution Nanocomposite", *Applied Catalysis B: Environmental*, Vol. 88, pp. 542–549.
- Mourao, P. A. M., P. J. M. Carrott, and M. M. L. R. Carrott, 2006, "Application of Different Equations to Adsorption Isotherms of Phenolic Compounds on Activated Carbons Prepared from Cork", *Carbon*, Vol. 44, pp. 2422–2429.
- Natesakhawat, S., X. Wang, L. Zhang, and U. S. Ozkan, 2006, "Development of Chromium-Free Iron-based Catalysts for High-Temperature Water-Gas Shift Reaction", *Journal of Molecular Catalysis A: Chemical*, Vol. 260, pp. 82–94.
- Nguyen, T.S., F. Morfin, M. Aouine, F. Bosselet, J. L. Rousset, and L. Piccolo, 2015, "Trends in the CO Oxidation and PROX Performances of the Platinum-Group Metals Supported on Ceria", *Catalysis Today*, Vol. 253, pp.106–114.
- Olympiou, G. G., C. M. Kalamaras, C. D. Zeinalipour-Yazdi, and A. M. Efstathiou, 2007, "Mechanistic Aspects of the Water–Gas Shift Reaction on Alumina -supported Noble Metal Catalysts: In situ DRIFTS and SSITKA-Mass Spectrometry Studies", *Catalysis Today*, Vol. 127, pp. 304–318.
- Otake, Y., and R. G. Jenkins, 1993, "Characterization of Oxygen-Containing Surface Complexes Created on a Microporous Carbon by Air and Nitric Acid Treatment", *Carbon*, Vol. 31, pp. 109–121.
- Özer, Ö., 2016, *Design and Development of Pt-Based Trimetallic WGS Catalysts*, M.Sc. Thesis, Boğaziçi University.
- Öztepe, C., 2017, *An Experimental Study Aiming to Enhance the Performance of OSR of a Fuel Processor*, M.Sc. Thesis, Boğaziçi University.
- Öztürk, G., 2018, *An Experimental Study on WGS Catalysts: Relating Performance under Realistic Feed with Oxygen Holding Capacity*, M.Sc. Thesis, Boğaziçi University.

- Panagiotopoulou, P., and D. I. Kondarides, 2004, “Effect of Morphological Characteristics of TiO₂-supported Noble Metal Catalysts on their Activity for the Water–Gas Shift Reaction”, *Journal of Catalysis*, Vol.225, pp. 327–336.
- Panagiotopoulou, and P., D. I. Kondarides, 2006, “Effect of the Nature of the Support on the Catalytic Performance of Noble Metal Catalysts for the Water–Gas Shift Reaction”, *Catalysis Today*, Vol. 112, pp. 49–52.
- Papirer, E., S. Li, and J. B. Donnet, 1987, “Contribution to the Study of Basic Surface Groups on Carbons”, *Carbon*, Vol. 25, pp. 243–247.
- Pasel, J., R. C. Samsun, A. Tschauer, R. Peters, and D. Stolten, 2018, “Water-gas Shift Reactor for Fuel Cell Systems: Stable operation for 5000 hours”, *International Journal of Hydrogen Energy*, Vol.43, pp. 19222-19230.
- Petrov, K. I., V. G. Pervykh, M. B. Varfolomeev, and V. E. Plyushchev, 1968, “Infrared Absorption Spectra and Raman Spectra of the Perrhenate Tetrahydrates of the Rare Earth Elements, Lanthanum, and Yttrium”, *Zhurnal Prikladnoi Spektroskopii*, Vol. 8, pp. 660-666.
- Pevida, C., M. G. Plaza, B. Arias, J. Feroso, F. Rubiera, and J. J. Pis, 2008, “Surface Modification of Activated Carbons for CO₂ Capture”, *Applied Surface Science*, Vol. 254, pp.7165–7172.
- Pierre, D., W. Deng, and M. F. Stephanopoulos, 2007, “The Importance of Strongly Bound Pt-CeO_x Species for the Water-gas Shift Reaction: Catalyst Activity and Stability Evaluation”, *Topics in Catalysis*, Vol. 46, pp. 363-373.
- Pilasombat, R., H. Daly, A. Goguet, J. P. Breen, R. Burch, C. Hardacre, and D. Thompsett, 2012, “Investigation of the Effect of the Preparation Method on the Activity and Stability of Au/CeZrO₄ Catalysts for the Low Temperature Water Gas Shift Reaction”, *Catalysis Today*, Vol. 180, pp.131–138.

- Plaza, M. G., C. Pevida, C. F. Martín, J. Feroso, J. J. Pis, and F. Rubiera, 2010, “Developing Almond Shell-Derived Activated Carbons as CO₂ Adsorbents”, *Separation and Purification Technology*, Vol. 71, pp. 102–106.
- Plaza, M. G., S. García, F. Rubiera, J. J. Pis, and C. Pevida, 2011, “Evaluation of Ammonia Modified and Conventionally Activated Biomass Based Carbons as CO₂ Adsorbents in Post-combustion Conditions”, *Separation and Purification Technology*, Vol. 80, pp. 96–104.
- Poulakis, N., D. Lampakis, and E. Liarokapis, 1999, “Re-induced Raman active modes in HgBa₂Ca_{n-1}Cu_nO_{2n+2+δ} compounds”, *The American Physical Society*, Vol.60, pp.3244-3251.
- Radhakrishnan, R., R. R. Willigan, Z. Dardas, and T. H. Vanderspurt, 2006 “Water Gas Shift Activity and Kinetics of Pt/Re Catalysts Supported on Ceria-Zirconia Oxides”, *Applied Catalysis B: Environmental*, Vol. 66, pp. 23–28.
- Ratnasamy, P., D. Srinivas, C.V.V. Satyanarayana, P. Manikandan, R. S. Senthil Kumaran, M. Sachin, and V. N. Shetti, 2004, "Influence of the Support on the Preferential Oxidation of CO in Hydrogen-Rich Steam Reformates over the CuO–CeO₂–ZrO₂ System", *Journal of Catalysis*, Vol. 221 pp. 455–465.
- Reina, T. R., S. Ivanova, M. A. Centeno, and J. A. Odriozola, 2015, “Boosting the Activity of a Au/CeO₂/Al₂O₃ Catalyst for the WGS Reaction”, *Catalysis Today*, Vol.253, pp. 149-154.
- Reuse, P., A. Renken, K. Haas-Santo, O. Görke, and K. Schubert, 2004, “Hydrogen Production for Fuel Cell Application in an Autothermal Microchannel Reactor”, *Chemical Engineering Journal*, Vol. 101, pp. 133-141.
- Rhodes, C., B. Peter Williams, F. King, and G.J. Hutchings, 2002, “Promotion of Fe₃O₄-Cr₂O₃ High Temperature Water Gas Shift Catalyst”, *Catalysis Communications*, Vol.3, pp. 381.

- Ribeiro, A., C. Grande, F. Lopes, M. Loureiro, and A. Rodrigues, 2009, “Four Beds Pressure Swing Adsorption for Hydrogen Purification: Case of Humid Feed and Activated Carbon Beds”, *AIChE Journal*, Vol. 55, pp.12-14.
- Rico-Francés, S., E.O. Jardim, T.A. Wezendonk, F. Kapteijn, J. Gascon, A. Sepúlveda-Escribano, and E. V. Ramos-Fernandez, 2016, “Highly Dispersed Pt^{δ+} on Ti_xCe_(1-x)O₂ as an Active Phase in Preferential Oxidation of CO”, *Applied Catalysis B: Environmental*, Vol. 180, pp.169–178.
- Riguetto, B. A. R., S. Damyanova, G. Gouliev, C. M. P. Marques, L. Petrov, and J. M. C. Bueno, 2004, “Surface Behavior of Alumina-Supported Pt Catalysts Modified with Cerium as Revealed by X-ray Diffraction, X-ray Photoelectron Spectroscopy, and Fourier Transform Infrared Spectroscopy of CO Adsorption”, *Journal of Physical Chemistry B*, Vol. 108, pp. 5349-5358.
- Rodriguez, J. A., 2011, “Gold-based Catalysts for the Water–Gas Shift Reaction: Active Sites and Reaction Mechanism”, *Catalysis Today*, Vol. 160, pp. 3–10.
- Roh, H. S., H. S. Potdar, D. W. Jeong, K. S. Kim, J. O. Shim, W. J. Jang, K. Y. Koo, and W. L. Yoon, 2012, “Synthesis of Highly Active Nano-Sized (1 wt.% Pt/CeO₂) Catalyst for Water Gas Shift Reaction in Medium Temperature Application”, *Catalysis Today*, Vol. 185, pp. 113-118.
- Rowshanzamir, S., S. M. Safdarnejad, M. H. Eikani, 2012, “A CFD Model for Methane Autothermal Reforming on Ru/γ-Al₂O₃ Catalyst”, *Procedia Engineering*, Vol. 42, pp. 2 – 24.
- Sakurai, H., T. Akita, S. Tsubota, M. Kiuchi, and M. Haruta, 2005, “Low-Temperature Activity of Au/CeO₂ for Water Gas Shift Reaction, and Characterization by ADF-STEM, Temperature-Programmed Reaction, and Pulse Reaction”, *Applied Catalysis A: General*, Vol. 291, pp. 179–187.

- Sánchez, J.M., M. Maroño, D. Cillero, L. Montenegro, and E. Ruiz, 2013, “Laboratory and Bench-Scale Studies of a Sweet Water–Gas-Shift Catalyst for H₂ and CO₂ Production in Pre-combustion CO₂ Capture”, *Fuel*, Vol.114, pp.191–198.
- Saw, E.T., U. Oemar, X. R. Tan, Y. Du, A. Borgna, K. Hidajat, and S .Kawi, 2014, “Bimetallic Ni–Cu Catalyst Supported on CeO₂ for High-Temperature Water–Gas Shift Reaction: Methane Suppression via Enhanced CO Adsorption”, *Journal of Catalysis*, Vol. 314, pp. 32–46.
- Sawant, S. Y., R. S. Somani, H. C. Bajaj, and S. S. Sharma, 2012, “A Dechlorination Pathway for Synthesis of Horn Shaped Carbon Nanotubes and Its Adsorption Properties for CO₂, CH₄, CO and N₂”, *Journal of Hazardous Materials*, Vol. 227– 228, pp. 317– 326.
- Schadel, B. T., M. Duisberg and O. Deutschmann, 2009, “Steam Reforming of Methane, Ethane, Propane, Butane, and Natural Gas over a Rhodium-based Catalyst”, *Catalysis Today*, Vol. 142, pp. 42-51.
- Sevilla, M., and A. B. Fuertes, 2012, “CO₂ Adsorption by Activated Templated Carbons”, *Journal of Colloid and Interface Science*, Vol.366, pp.147–154.
- Shafeeyan, M. S., W. M. A. W. Daud, A. Houshmand, and A. Shamiri, 2010, “A review on Surface Modification of Activated Carbon for Carbon Dioxide Adsorption”, *Journal of Analytical and Applied Pyrolysis*, Vol. 89, pp. 143–151.
- Shafeeyan, M. S., W. M. A. W. Daud, A. Houshmand, and A. Arami-Niya, 2011, “Ammonia Modification of Activated Carbon to Enhance Carbon Dioxide Adsorption: Effect of Pre-oxidation”, *Applied Surface Science*, Vol. 257, pp. 3936–3942.
- Shen, C., C. A. Grande, P. Li, J. Yu, and A.E. Rodrigues, 2010, “Adsorption Equilibria and Kinetics of CO₂ and N₂ on Activated Carbon Beads”, *Chemical Engineering Journal*, Vol. 160, pp. 398-407.

- Shi, M., Z. Wang, Z. Zheng, 2013, “Effect of Na⁺ Impregnated Activated Carbon on the Adsorption of NH⁴⁺-N from Aqueous Solution”, *Journal of Environmental Sciences*, Vol. 25, pp. 1501- 1510.
- Siriwardane, R.V., M. S. Shen, E. P. Fisher, and J. A. Poston, 2001, “Adsorption of CO₂ on Molecular Sieves and Activated Carbon”, *Energy Fuels*, Vol. 15(2), pp. 279–284.
- Somy, A., M. R. Mehrnia, H. D. Amrei, A. Ghanizadeh, and M. Safari, 2009, “Adsorption of Carbon Dioxide Using Impregnated Activated Carbon Promoted by Zinc”, *International Journal of Greenhouse Gas Control*, Vol.3, pp. 249–254.
- Song, C.S., 2002, “Fuel Processing for Low-Temperature and High-Temperature Fuel Cells– Challenges, and Opportunities for Sustainable Development in the 21st Century, *Catalysis Today*, Vol.77, pp. 17–49.
- Sopeña, D., A. Melgar, Y. Briceño, Y. M. Navarro, M. C. Álvarez-Galvan, and F. Rosa, 2007, "Diesel Fuel Processor for Hydrogen Production for 5 kW Fuel Cell Application", *International Journal of Hydrogen Energy*, Vol. 32, pp. 1429-1436.
- Souza, M. M. V. M., N. F. P. Ribeiro, O. R. M. Neto, I. O. V. Cruz, and M. Schmal, 2007, “Autothermal Reforming of Methane over Nickel Catalysts Prepared from Hydrotalcite-Like Compounds”, *Studies in Surface Science and Catalysis*, Vol. 167, pp. 451-456.
- Sun, N., C. Suna, H. Liua, J. Liu, L. Stevens, T. Drage, C. E. Snape, K. Li, W. Wei, and Y. Sun, 2013, “ Synthesis, Characterization and Evaluation of Activated Spherical Carbon Materials for CO₂ Capture”, *Fuel*, Vol. 113, pp. 854–862.
- Swanson, M., V. V. Pushkarev, V. I. Kovalchuk, and J. L. d’Itri, 2008, “Evidence for CO Disproportionation over Ceria during Oxygen Storage Capacity Measurements: an in Situ Raman Spectroscopic Investigation”, *Journal of Siberian Federal University, Chemistry* 1, pp. 24-34.

- Tlili, N., G. Grévillet, and C. Vallières, 2009, “Carbon Dioxide Capture and Recovery by Means of TSA and/or VSA”, *International Journal of Greenhouse Gas Control*, Vol.3, pp. 519–527.
- Toledo, F., I.T. Ghampson, C. Sepúlveda, R. García, J .L. G. Fierro, A. Videla, R. Serpell, and N. Escalona, 2019, “Effect of Re Content and Support in the Liquid Phase Conversion of Furfural to Furfuryl Alcohol and 2-Methyl Furan over ReO_x Catalysts”, *Fuel*, Vol. 242, pp. 532–544.
- Tripathy, S. N., K. K. Mishra, S. Sen, and D. K. Pradhan, 2014, “Dielectric and Raman Spectroscopic Studies of $\text{Na}_{0.5}\text{Bi}_{0.5}\text{TiO}_3\text{--BaSnO}_3$ Ferroelectric System”, *Journal of American Ceramic Society*, Vol. 97, pp. 1846–1854.
- Vignatti, C., M. S. Avila, C. R. Apesteguia, and T.F. Garetto, 2010, “Catalytic and DRIFTS Study of the WGS Reaction on Pt-based Catalysts”, *International Journal of Hydrogen Energy*, Vol. 35, pp. 7302-7312.
- Vignatti, C. I., M. S. Avila, C. R. Apesteguia, and T. F. Garetto, 2011, “Study of the Water-Gas Shift Reaction over Pt Supported on $\text{CeO}_2\text{--ZrO}_2$ Mixed Oxides”, *Catalysis Today*, Vol.171, pp. 297– 303.
- Vita, A., G. Cristiano, C. Italiano, L. Pino, and S. Specchia, 2015, “Syngas production by methane oxy-steam reforming on Me/ CeO_2 (Me = Rh, Pt, Ni) catalyst lined on cordierite monoliths”, *Applied Catalysis B: Environmental*, Vol. 162, pp. 551–563.
- Vita, A., L. Pino, F. Cipiti, M. Lagana, and V. Recupero, 2010, “Structured Reactors as Alternative to Pellets Catalyst for Propane Oxidative Steam Reforming”, *International Journal of Hydrogen Energy*, Vol. 35, No. 18, pp. 9810-9817.
- Wang, B., B. Chen, Y. Sun, H. Xiao, X. Xu, M. Fu, J. Wu, L. Chen, and D. Ye, 2018, “Effects of Dielectric Barrier Discharge Plasma on the Catalytic Activity of Pt/ CeO_2 Catalysts”, *Applied Catalysis B: Environmental*, Vol. 238, pp. 328–338.

- Wang, J., V. F. Kispersky, W. N. Delgass, and F. H. Ribeiro, 2012, “Determination of the Au Active Site and Surface Active Species via Operando Transmission FTIR and Isotopic Transient Experiments on 2.3 wt.% Au/TiO₂ for the WGS Reaction”, *Journal of Catalysis*, Vol. 289, pp.171–178.
- Wang, L., M. Huang, B. Li, L. Dong, G. Jin, J. Gao, J. Ma, and T. Liu, 2015, “Enhanced Hydrothermal Stability and Oxygen Storage Capacity of La³⁺ Doped CeO₂- γ -Al₂O₃ Intergrowth Mixed Oxides” *Ceramics International*, Vol. 41, pp. 12988–12995.
- Wang, T., M. D. Porosoff, and J. G. Chen, 2014, “Effects of Oxide Supports on the Water-Gas Shift Reaction over Pt Ni Bimetallic Catalysts: Activity and Methanation Inhibition”, *Catalysis Today*, Vol. 233, pp. 61-69.
- Wang, X., and R.J. Gorte, 2003, “The Effect of Fe and Other Promoters on the Activity of Pd/Ceria for the Water-Gas Shift Reaction”, *Applied Catalysis A: General*, Vol. 247, pp.157–162.
- Wang, Y., K. S. Chen, J. Misshler, S. C. Cho, and X. C. Adroher, 2011, “A Review of Polymer Electrolyte Membrane Fuel Cells: Technology, Applications, and Needs on Fundamental Research”, *Applied Energy*, Vol. 88, pp. 981-1007.
- Wei, Z. H., J. M. Sun, Y. Li, A. K. Datye, and Y. Wang, 2012, “Bimetallic Catalysts for Hydrogen Generation”, *Chemical Society Reviews*, Vol. 41, pp. 7994–8008.
- Wu, Z., A. J. Rondinone, I. N. Ivanov, and S. H. Overbury, 2011, “Structure of Vanadium Oxide Supported on Ceria by Multiwavelength Raman Spectroscopy”, *The Journal of Physical Chemistry C*, Vol. 115, pp. 25368-25378.
- Xu, D., J. Zhang, G. Li, P. Xiao, P. Webley, and Y. Zhai, 2011, “Effect of Water Vapor from Power Station Flue Gas on CO₂ Capture by Vacuum Swing Adsorption with Activated Carbon”, *Journal of Fuel Chemistry and Technology*, Vol. 39, pp. 169-174.

- Xu, D., P. Xiao, J. Zhang, G. Li, G. Xiao, P. A. Webley, and Y. Zhai, 2013, "Effects of Water Vapour on CO₂ Capture with Vacuum Swing Adsorption Using Activated Carbon", *Chemical Engineering Journal*, Vol. 230, pp. 64–72.
- Xu, W., R. Si, S. D. Senanayake, J. Llorca, H. Idriss, D. Stacchiola, J. C. Hanson, and J. A. Rodriguez, 2012, "In situ Studies of CeO₂-supported Pt, Ru, and Pt–Ru Alloy Catalysts for the Water–Gas Shift Reaction: Active Phases and Reaction Intermediates", *Journal of Catalysis*, Vol.291, pp.117–126.
- Yang, H., M. Gong, and Y. Chen, 2011, "Preparation of Activated Carbons and Their Adsorption Properties for Greenhouse Gases: CH₄ and CO₂", *Journal of Natural Gas Chemistry*, Vol. 20, pp. 460–464.
- Yang, H., Z. Xu, M. Fan, R. Gupta, R. B. Slimane, A. E. Bland, and I. Wright, 2008, "Progress in Carbon Dioxide Separation and Capture: A Review", *Journal of Environmental Sciences*, Vol. 20, pp.14–27.
- Yao, H. C., and Y. F. Y. Yao, 1984, "Ceria in Automotive Exhaust Catalysts", *Journal of Catalysis*, Vol. 86, pp. 254-265.
- Yi, H., F. Li, P. Ning, X. Tang, J. Peng, Y. Li, and H. Deng, 2013, "Adsorption Separation of CO₂, CH₄, and N₂ on Microwave Activated Carbon", *Chemical Engineering Journal*, Vol. 215–216, pp. 635–642.
- Yin, G., Z. Liu, Q. Liu, and W. Wu, 2013, "The Role of Different Properties of Activated Carbon in CO₂ Adsorption", *Chemical Engineering Journal*, Vol. 230, pp. 133–140.
- Yu, Q., W. Chen, Y. Li, M. Jin, and Z. Suo, 2010, "The Action of Pt in Bimetallic Au–Pt/CeO₂ Catalyst for Water-Gas Shift Reaction", *Catalysis Today*, Vol. 158, pp. 324–328.

- Yu, L., and Y. Luo, 2014, "The Adsorption Mechanism of Anionic and Cationic Dyes by Jerusalem Artichoke Stalk-Based Mesoporous Activated Carbon", *Journal of Environmental Chemical Engineering*, Vol. 2, pp. 220-229.
- Zeng, G., Y. Tian, and Y. Li, 2010, "Thermodynamic Analysis of Hydrogen Production for Fuel Cell via Oxidative Steam Reforming of Propane", *International Journal of Hydrogen Energy*, Vol.35, pp. 6726-6737.
- Zhou, A., J. Wang, H. Wang, H. Li, J. Wang, and M. Shen, 2018, "Effect of Active Oxygen on the Performance of Pt/CeO₂ Catalysts for CO Oxidation", *Journal of Rare Earths*, Vol. 36, pp. 257-264.
- Zhu, X., M. Shen, L. L. Lobban, and R. G. Mallinson, 2011, "Structural Effects of Na Promotion for High Water Gas Shift Activity on Pt–Na/TiO₂", *Journal of Catalysis*, Vol. 278, pp. 123–132.
- Zhu, X., T. Hoang, L. L. Lobban, and R. G. Mallinson, 2009, "Significant Improvement in Activity and Stability of Pt/TiO₂ Catalyst for Water Gas Shift Reaction via Controlling the Amount of Na Addition", *Catalysis Letters*, Vol. 129, pp. 135–141.

APPENDIX A: TIME-ON-STREAM ACTIVITY DATA OF INDIVIDUAL WGS TESTS

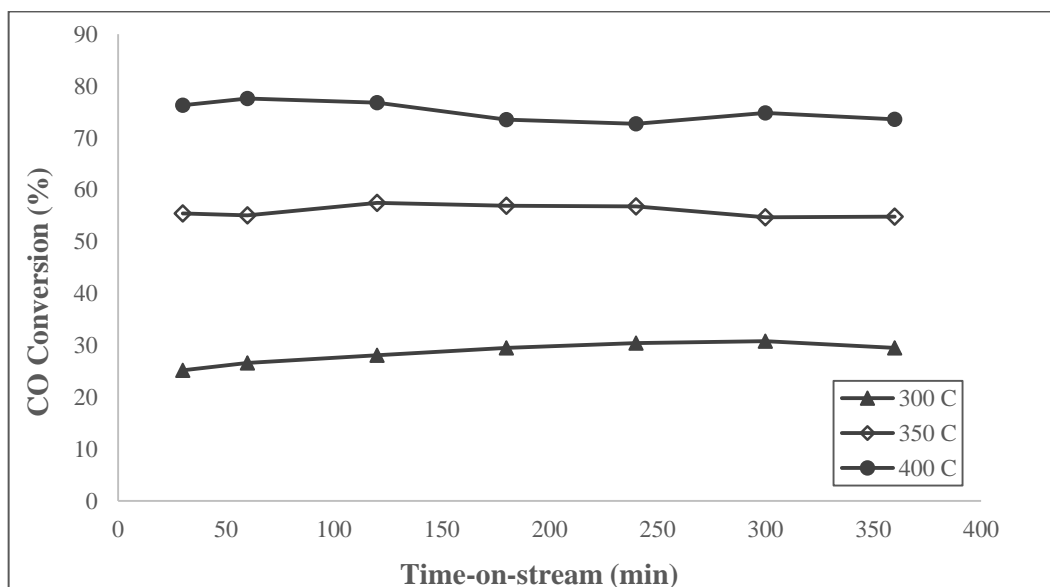


Figure A.1. Temperature dependence of time-on-stream activity data for coimpregnated 1%Pt-1%Re-1%Na/CeO₂ catalyst under ideal feed #1 (H₂O/CO=5).

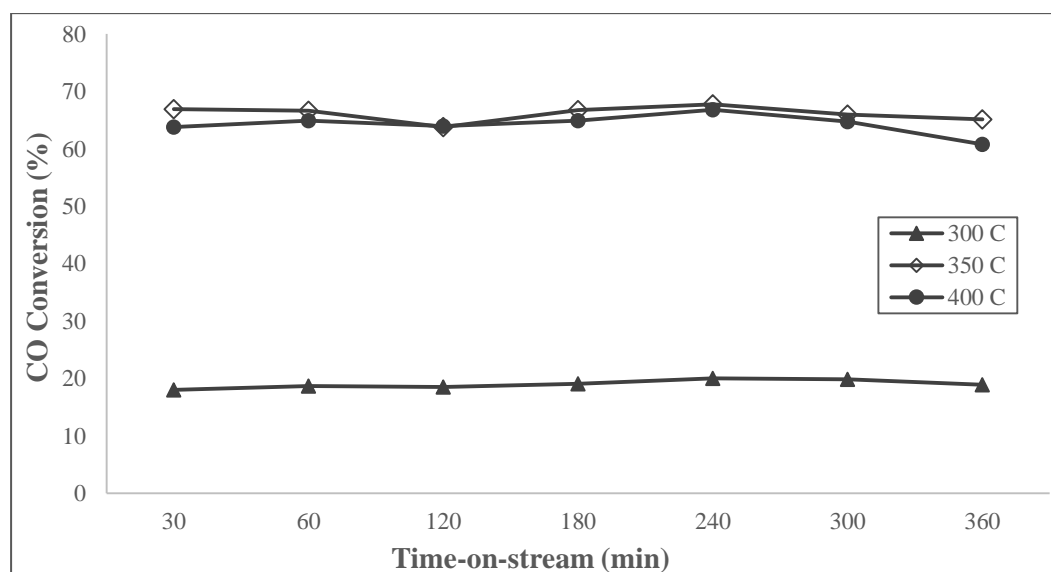


Figure A.2. Temperature dependence of time-on-stream activity data for coimpregnated 1%Pt-1%Re-1%Na/CeO₂ catalyst under ideal feed #2 (H₂O/CO=2).

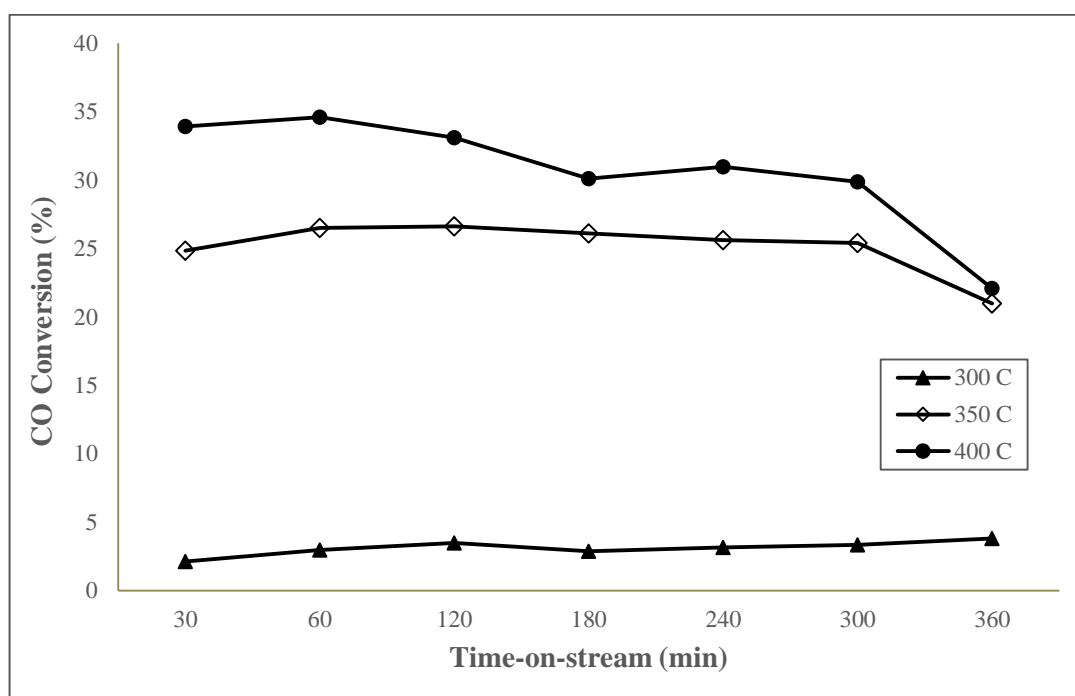


Figure A.3. Temperature dependence of time-on-stream activity data for coimpregnated 1%Pt-1%Re-1%Na/CeO₂ catalyst under realistic feed #1 (H₂O/CO=6.7).

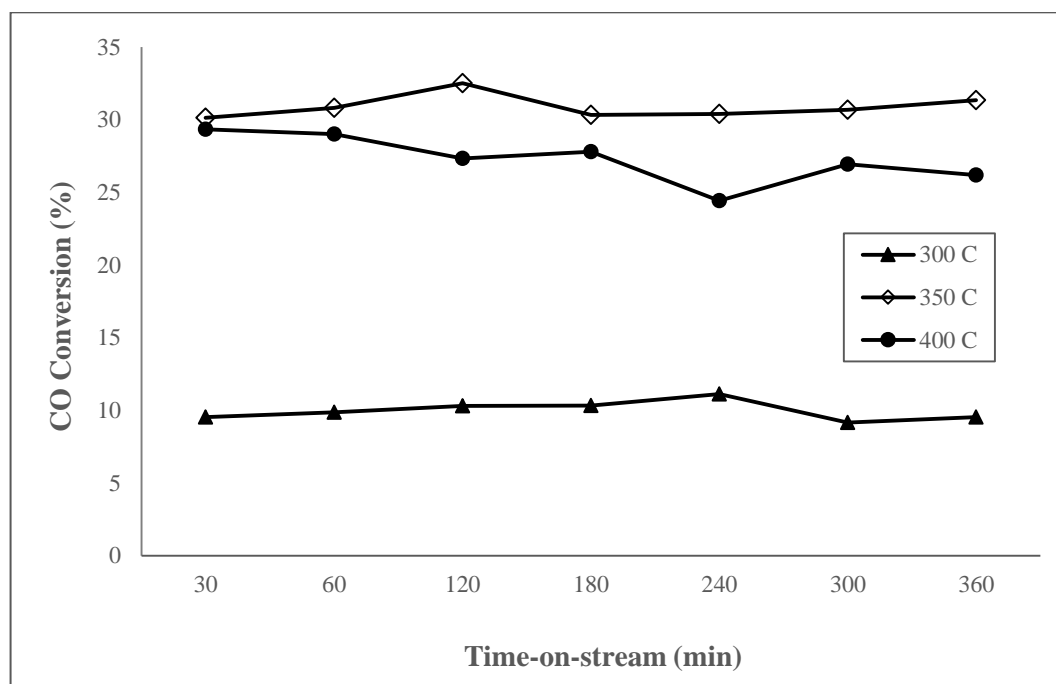


Figure A.4. Temperature dependence of time-on-stream activity data for coimpregnated 1%Pt-1%Re-1%Na/CeO₂ catalyst under realistic feed #2 (H₂O/CO=16.2).

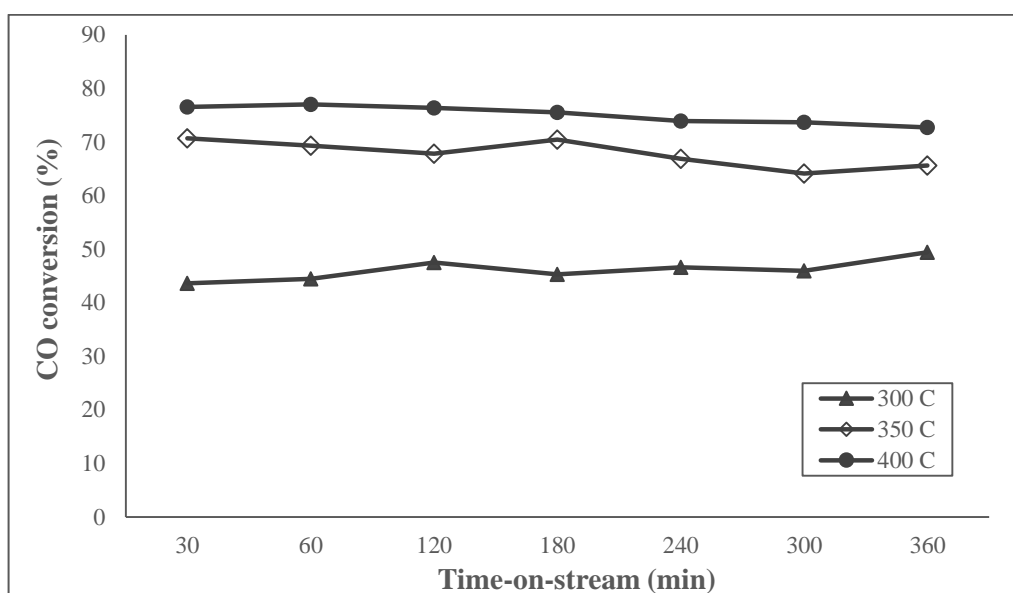


Figure A.5. Temperature dependence of time-on-stream activity data for sequentially impregnated 1%Pt-1%Re-1%Na/CeO₂ catalyst under ideal feed #1 (H₂O/CO=5).

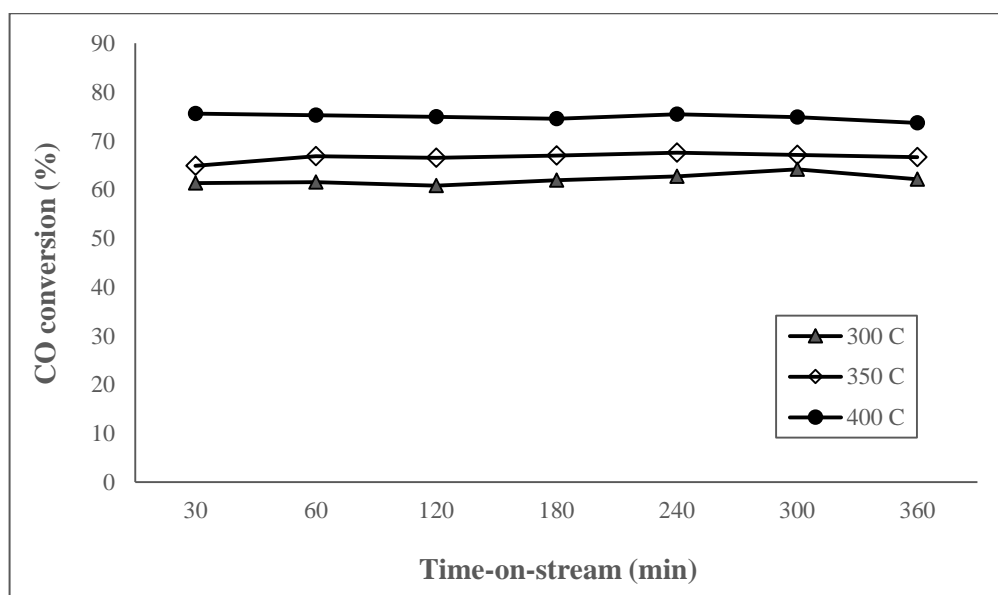


Figure A.6. Temperature dependence of time-on-stream activity data for sequentially impregnated 1%Pt-1%Re-1%Na/CeO₂ catalyst under ideal feed #2 (H₂O/CO=2).

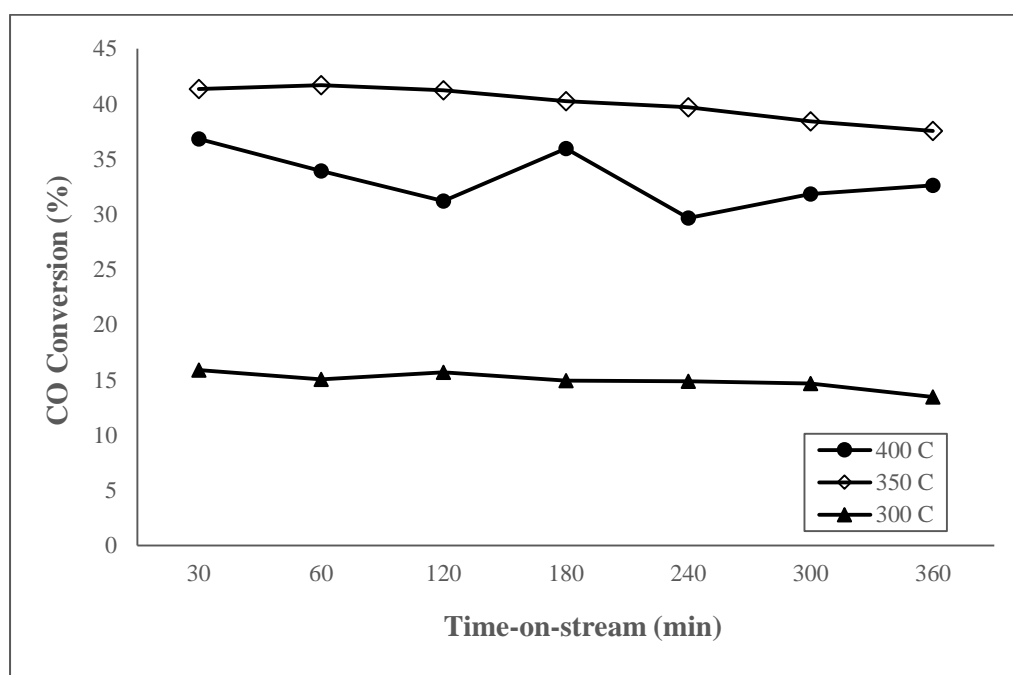


Figure A.7. Temperature dependence of time-on-stream activity data for sequentially impregnated 1%Pt-1%Re-1%Na/CeO₂ catalyst under realistic feed #1 (H₂O/CO=6.7).

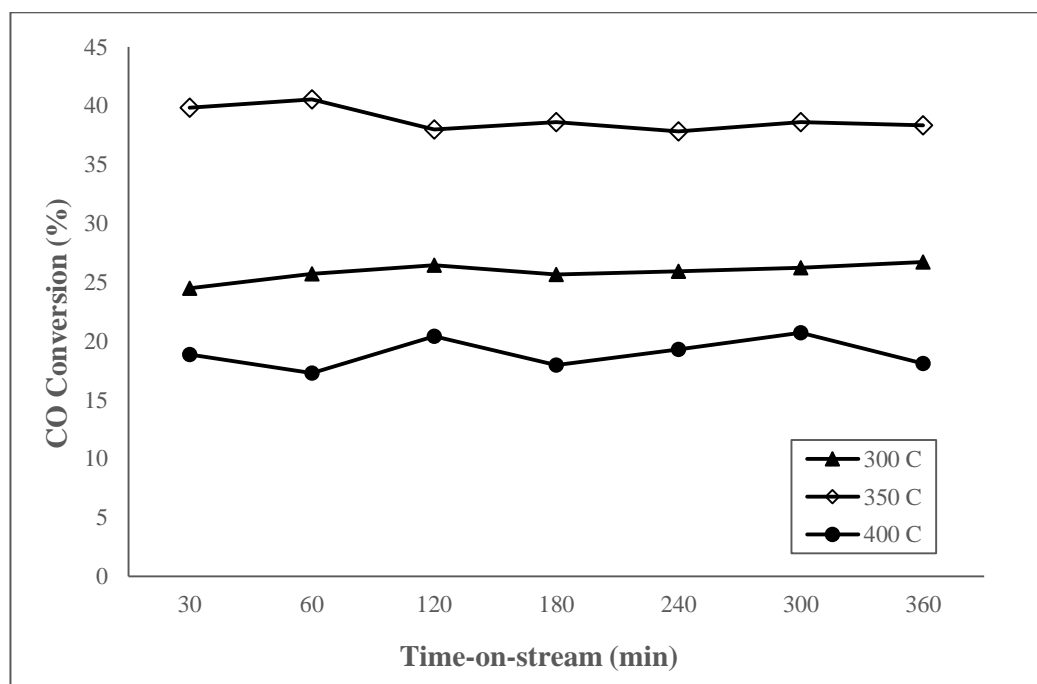


Figure A.8. Temperature dependence of time-on-stream activity data for sequentially impregnated 1%Pt-1%Re-1%Na/CeO₂ catalyst under realistic feed #2 (H₂O/CO=16.2).

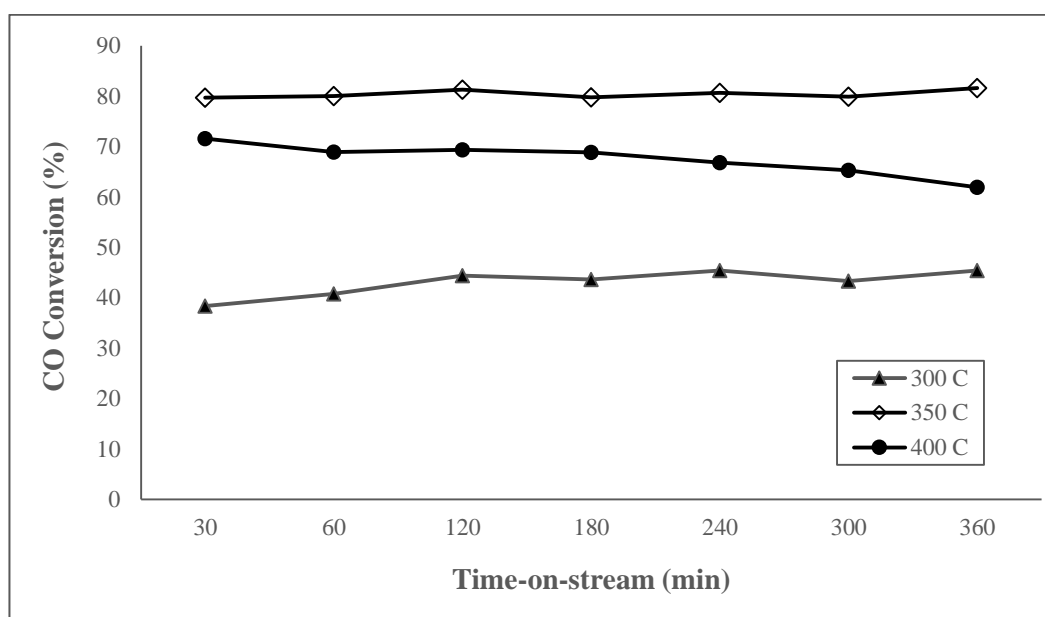


Figure A.9. Temperature dependence of time-on-stream activity data for sequentially impregnated 1%Pt-1%Re-2%Na/CeO₂ catalyst under ideal feed #1 (H₂O/CO=5).

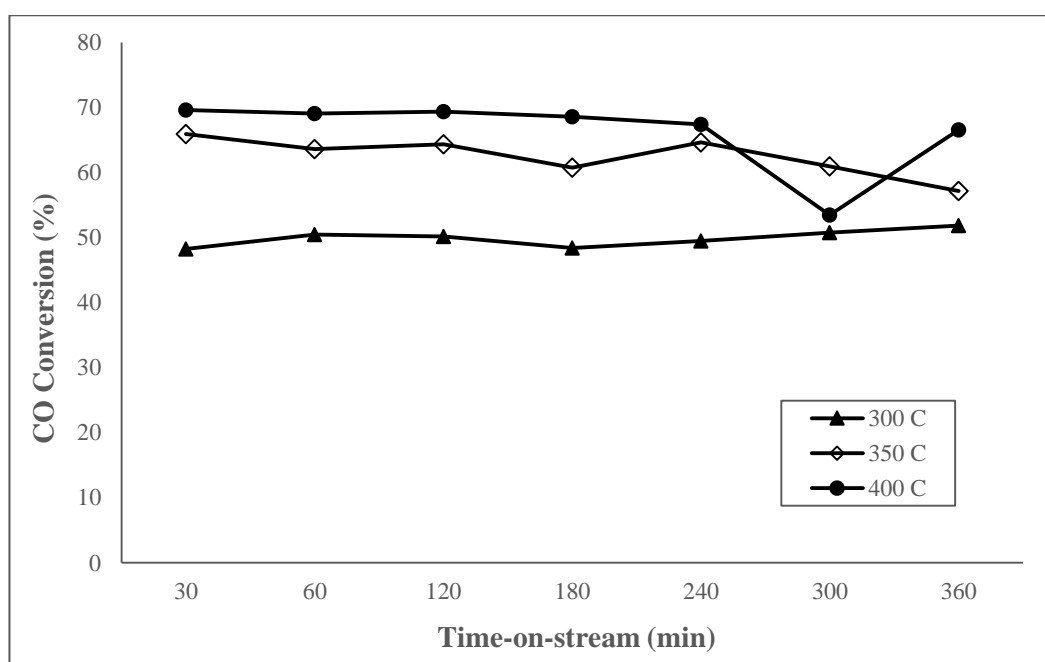


Figure A.10. Temperature dependence of time-on-stream activity data for sequentially impregnated 1%Pt-1%Re-2%Na/CeO₂ catalyst under ideal feed #2 (H₂O/CO=2).

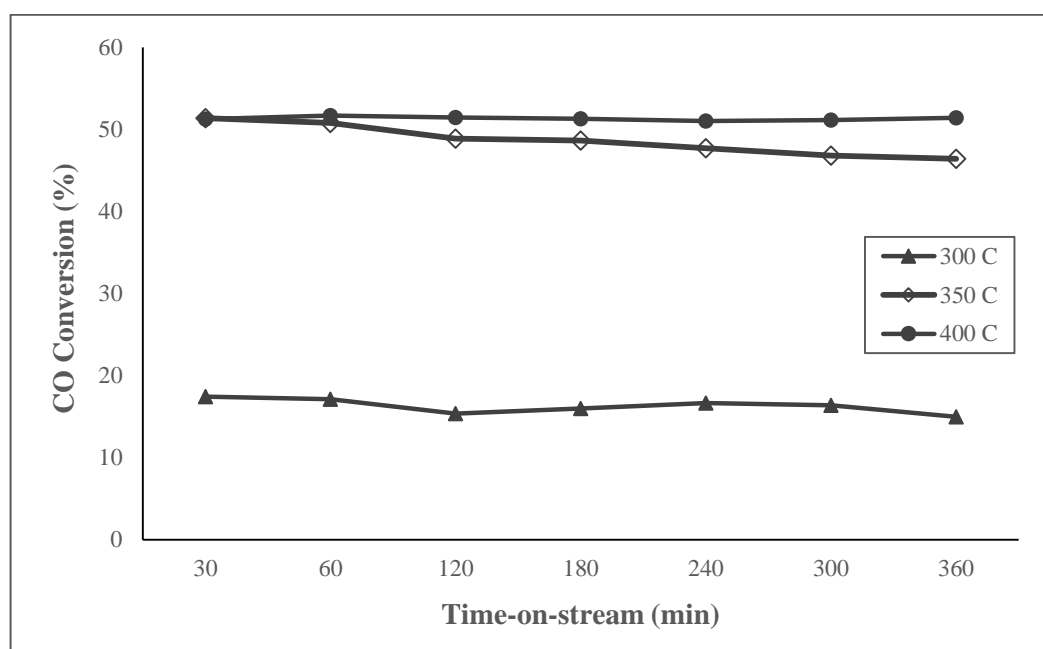


Figure A.11. Temperature dependence of time-on-stream activity data for sequentially impregnated 1%Pt-1%Re-2%Na/CeO₂ catalyst under realistic feed #1 (H₂O/CO=6.7).

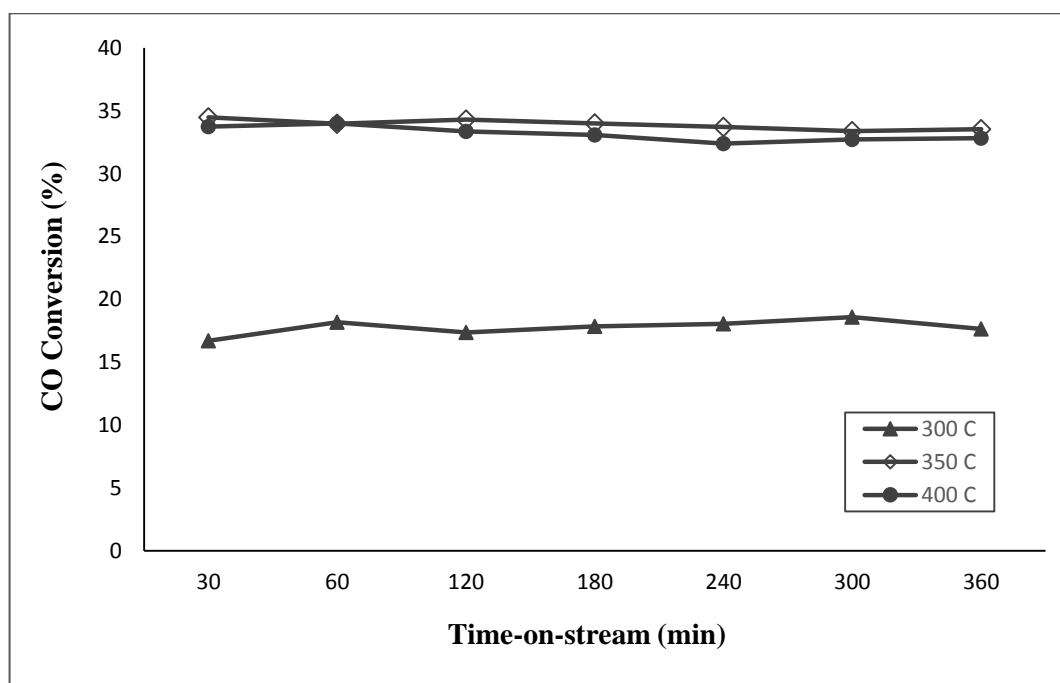


Figure A.12. Temperature dependence of time-on-stream activity data for sequentially impregnated 1%Pt-1%Re-2%Na/CeO₂ catalyst under realistic feed #2 (H₂O/CO=16.2).

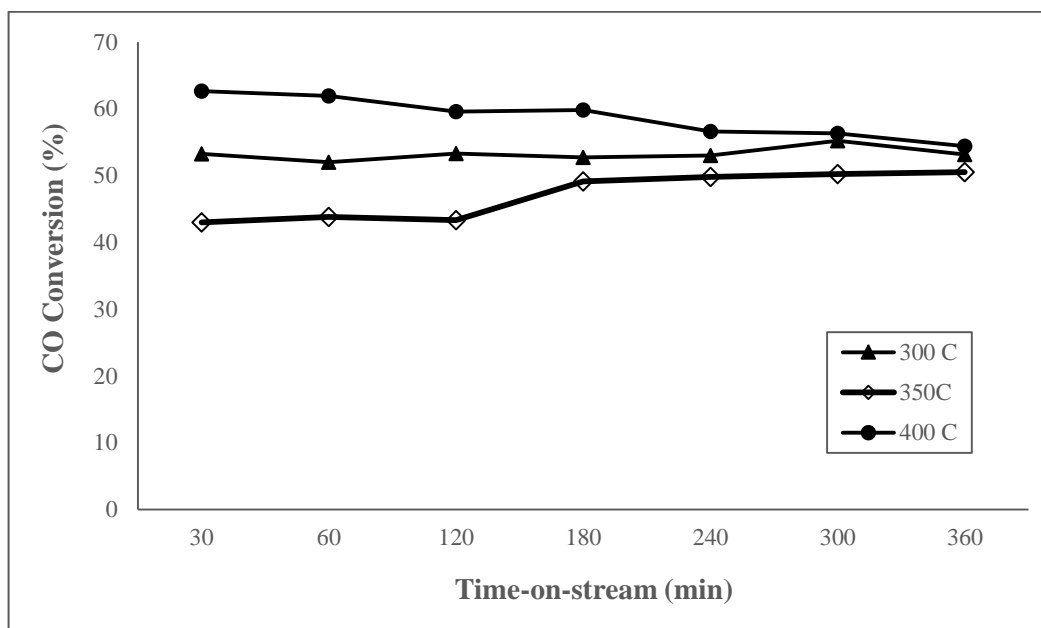


Figure A.13. Temperature dependence of time-on-stream activity data for sequentially impregnated 1%Pt-1%Re-1%Na/TiO₂ catalyst under ideal feed #1 (H₂O/CO=5).

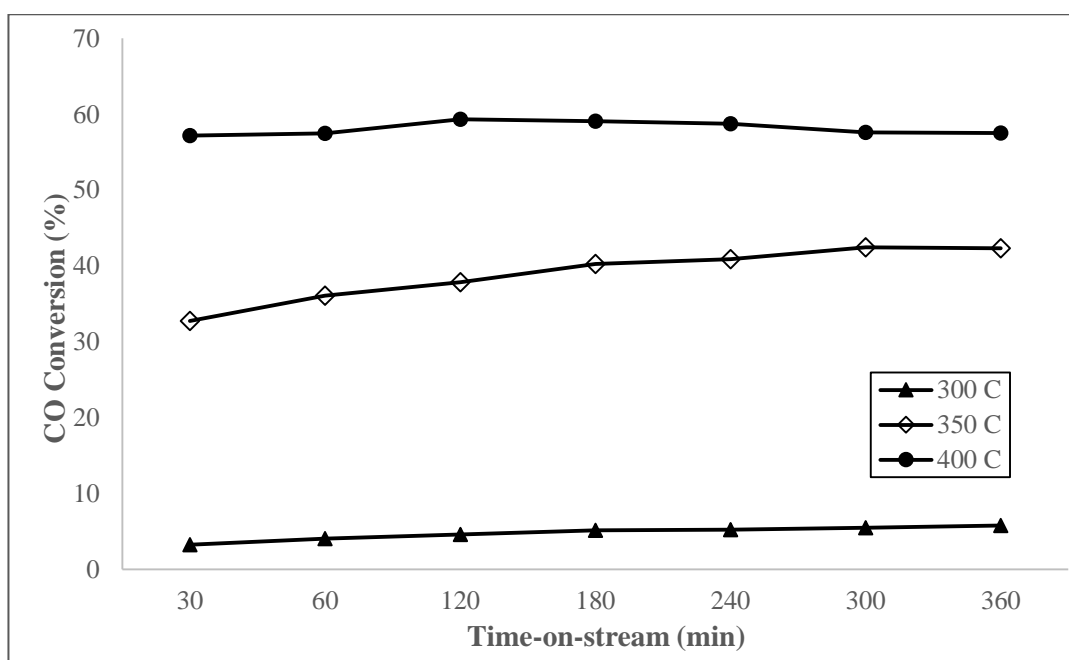


Figure A.14. Temperature dependence of time-on-stream activity data for sequentially impregnated 1%Pt-1%Re-1%Na/TiO₂ catalyst under ideal feed #2 (H₂O/CO=2).

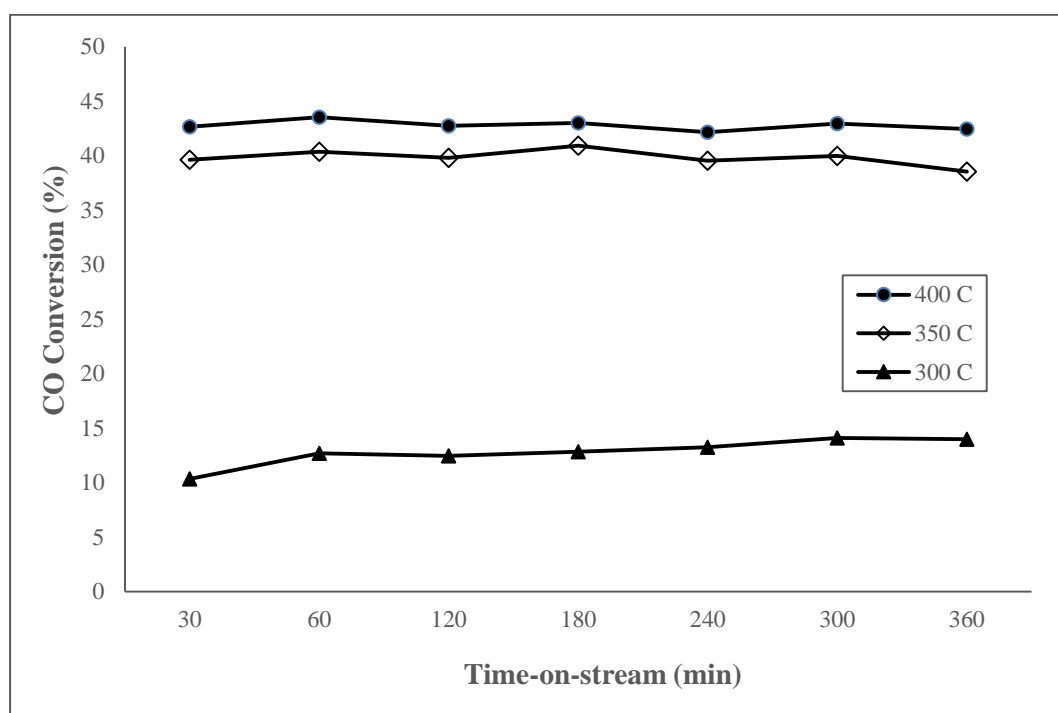


Figure A.15. Temperature dependence of time-on-stream activity data for sequentially impregnated 1%Pt-1%Re-1%Na/TiO₂ catalyst under realistic feed #1 (H₂O/CO=6.7).

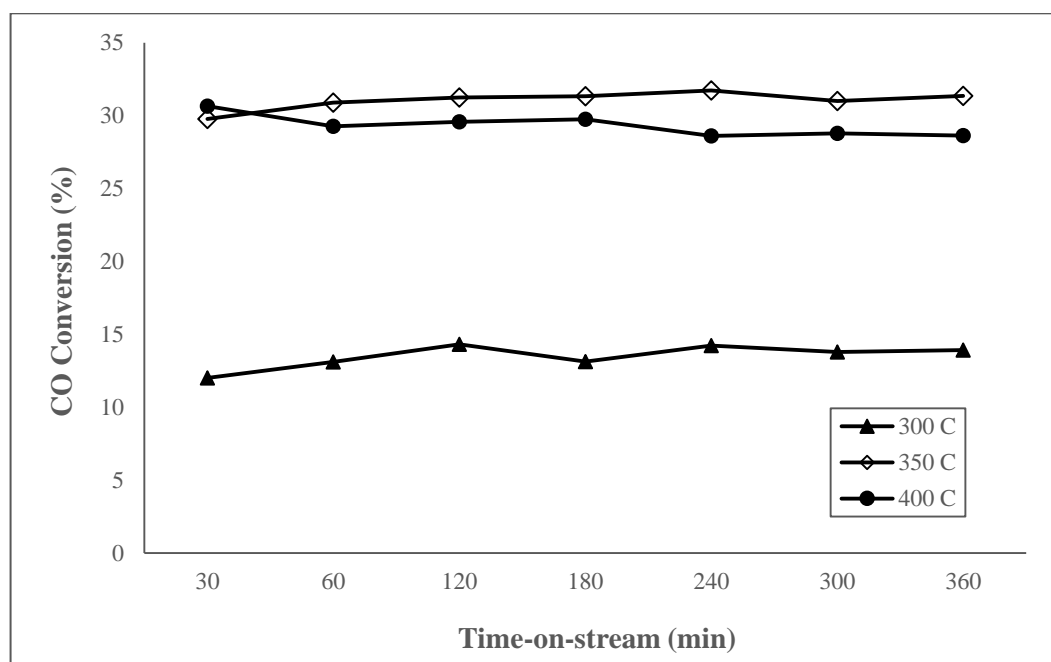


Figure A.16. Temperature dependence of time-on-stream activity data for sequentially impregnated 1%Pt-1%Re-1%Na/TiO₂ catalyst under realistic feed #2 (H₂O/CO=16.2).

APPENDIX B: TIME-ON-STREAM ACTIVITY DATA OF SERIAL OSR- WGS TESTS

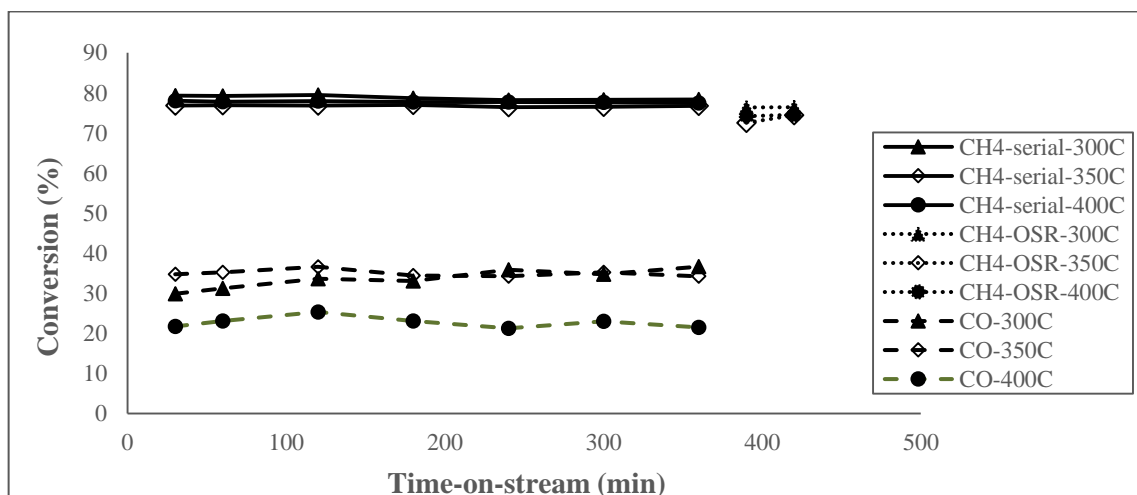


Figure B.1. 6 h TOS OSR and WGS activities over coimpregnated 1%Pt-1%Re-1%Na/CeO₂ under 14% CH₄, 9.3% O₂, 56% H₂O, 20.7% Ar (H₂O/CO=4, O/C=1.33) feed flow at 300°C, 350°C and 400°C.

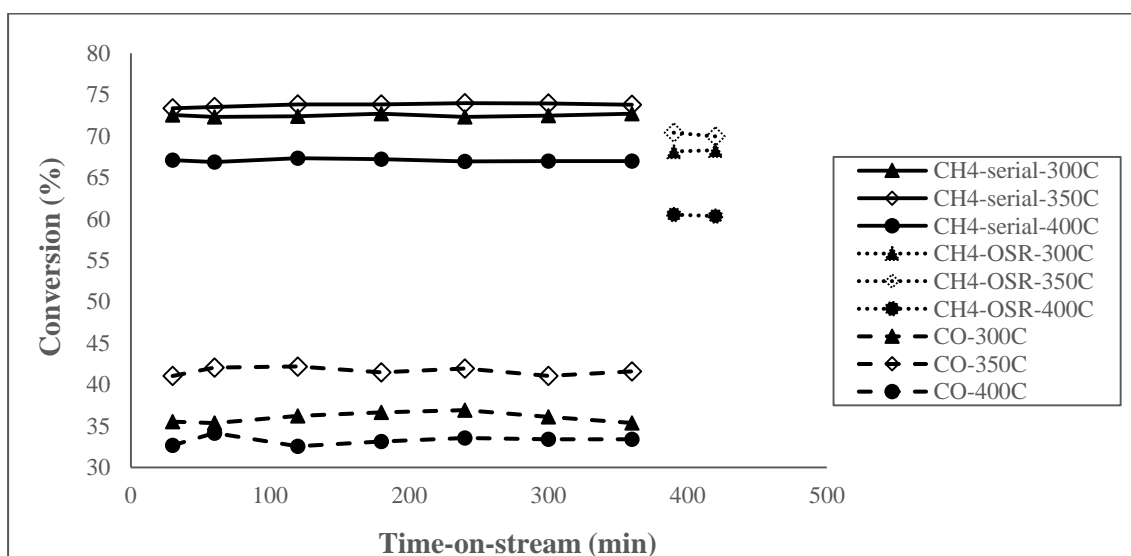


Figure B.2. 6 h TOS OSR and WGS activities over coimpregnated 1%Pt-1%Re-1%Na/CeO₂ under 14% CH₄, 6.7% O₂, 56% H₂O, 23.3% Ar (H₂O/CO=4, O/C=0.95) feed flow at 300°C, 350°C and 400°C.

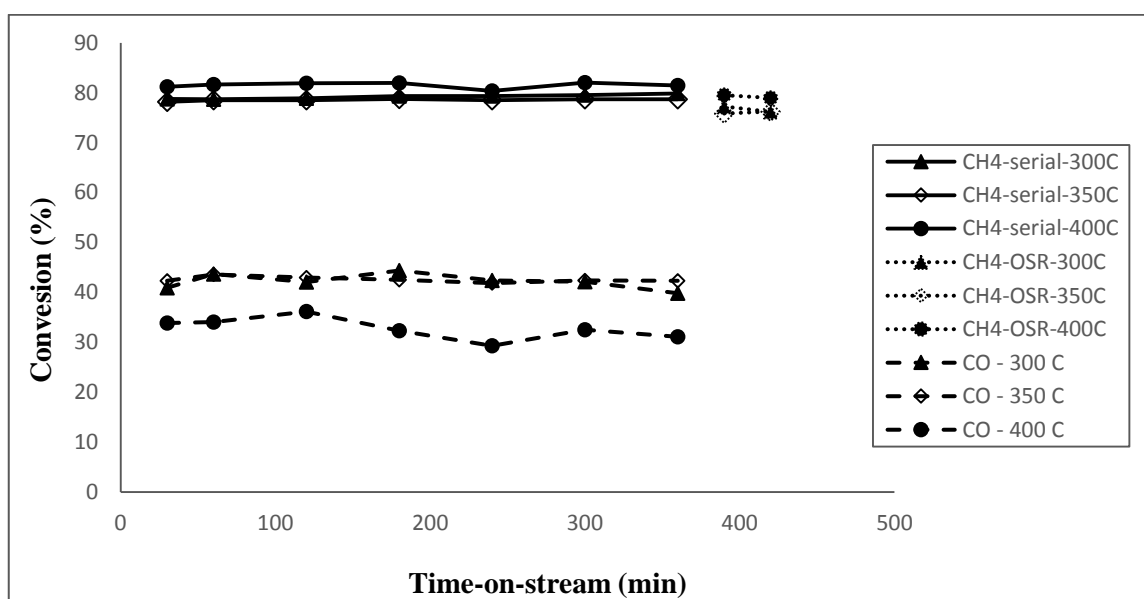


Figure B.3. 6 h TOS OSR and WGS activities over sequentially impregnated 1%Pt-1%Re-1%Na/CeO₂ under 14% CH₄, 9.3% O₂, 56% H₂O, 20.7% Ar (H₂O/CO=4, O/C=1.33) feed flow at 300°C, 350°C and 400°C.

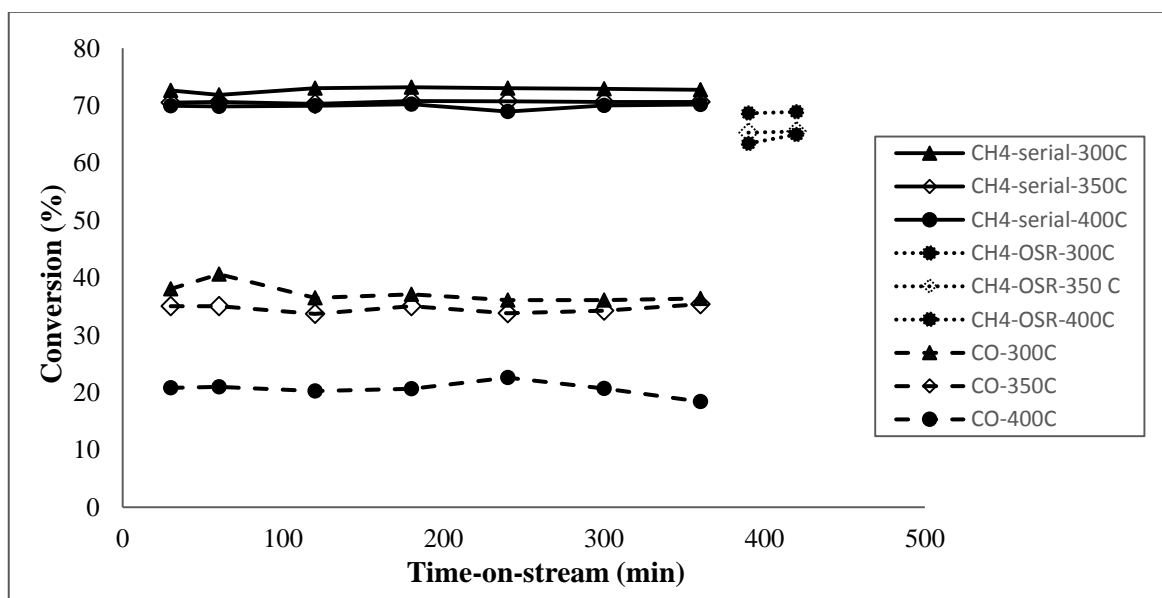


Figure B.4. 6 h TOS OSR and WGS activities over sequentially impregnated 1%Pt-1%Re-1%Na/CeO₂ under 14% CH₄, 6.7% O₂, 56% H₂O, 23.3% Ar (H₂O/CO=4, O/C=0.95) feed flow at 300°C, 350°C and 400°C.

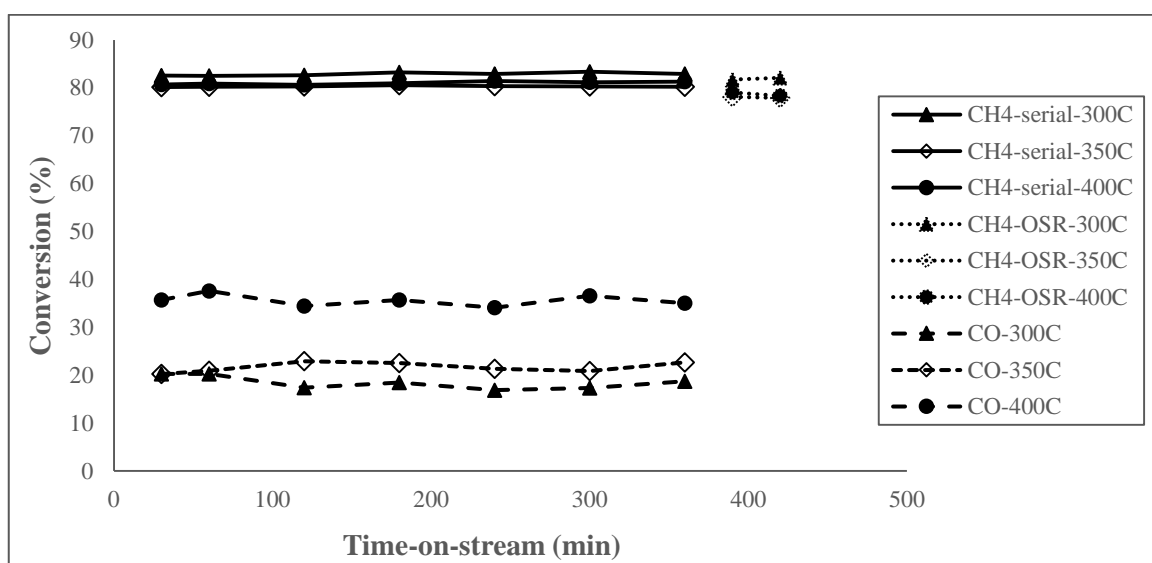


Figure B.5. 6 h TOS OSR and WGS activities over sequentially impregnated 1%Pt-1%Re-2%Na/CeO₂ under 14% CH₄, 9.3% O₂, 56% H₂O, 20.7% Ar (H₂O/CO=4, O/C=1.33) feed flow at 300°C, 350°C and 400°C.

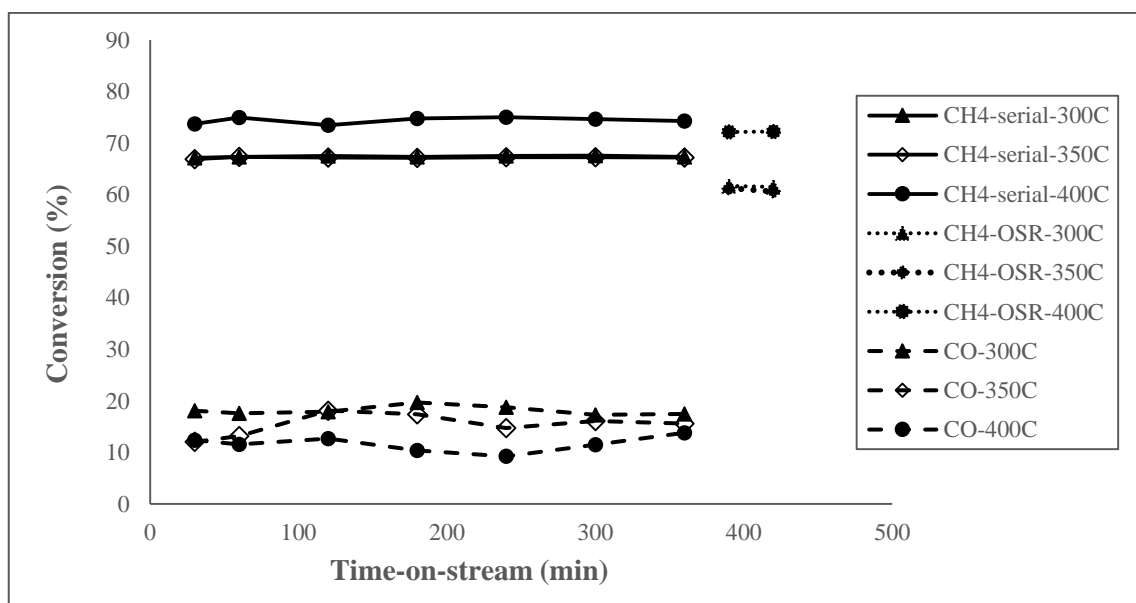


Figure B.6. 6 h TOS OSR and WGS activities over sequentially impregnated 1%Pt-1%Re-2%Na/CeO₂ under 14% CH₄, 6.7% O₂, 56% H₂O, 23.3% Ar (H₂O/CO=4, O/C=0.95) feed flow at 300°C, 350°C and 400°C.

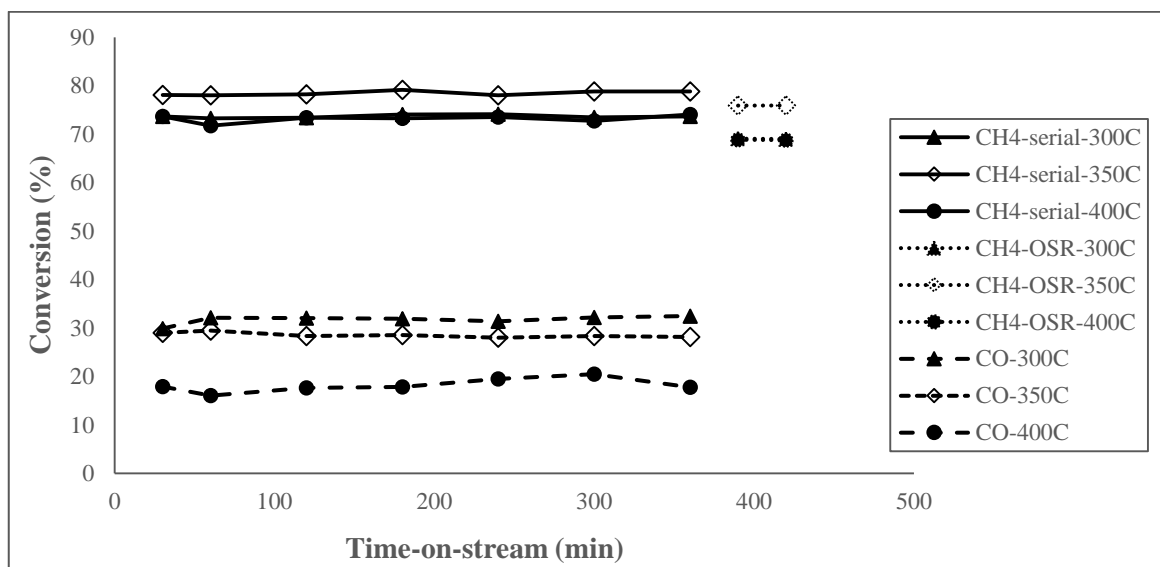


Figure B.7. 6 h TOS OSR and WGS activities over sequentially impregnated 1%Pt-1%Re-1%Na/TiO₂ under 14% CH₄, 9.3% O₂, 56% H₂O, 20.7% Ar (H₂O/CO=4, O/C=1.33) feed flow at 300°C, 350°C and 400°C.

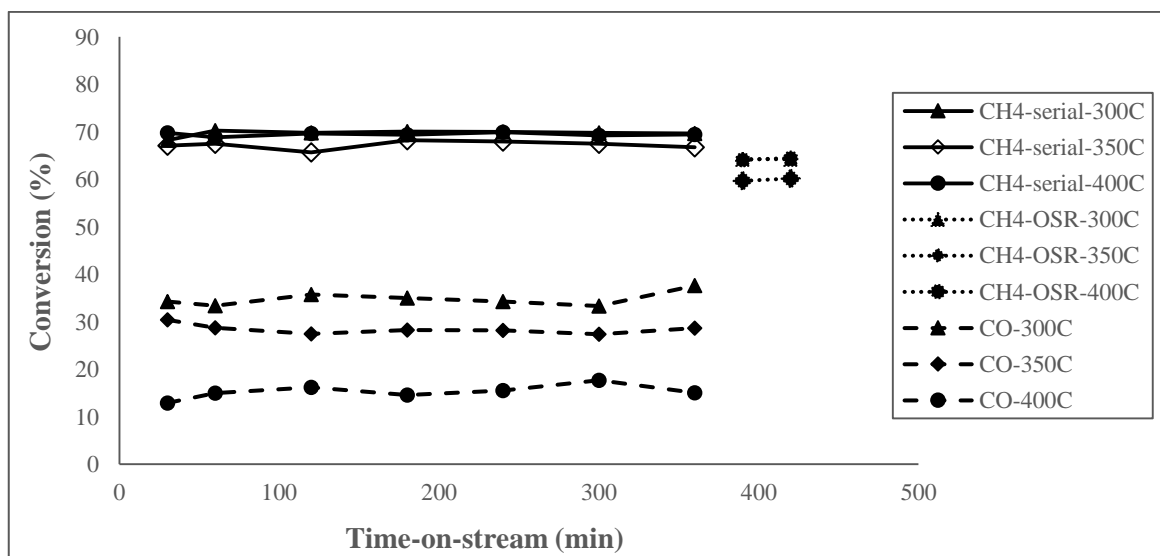


Figure B.8. 6 h TOS OSR and WGS activities over sequentially impregnated 1%Pt-1%Re-1%Na/TiO₂ under 14% CH₄, 6.7% O₂, 56% H₂O, 23.3% Ar (H₂O/CO=4, O/C=0.95) feed flow at 300°C, 350°C and 400°C.